Acta Technica *63* No. 6/2018, 763–774

Natural vibration of parallelogram plate with circular variation in density

Amit Sharma[1]

Abstract. In this paper, author studies the natural vibration of non-homogeneous tapered parallelogram plate along with temperature variation. For tapering and non-homogeneity, author considered two-dimensional linear thickness variations and one-dimensional circular variation in density parameter. Author also assumed two-dimensional linear temperature variation on the plate. In order to solve differential equation of motion for vibrational frequencies, Rayleigh–Ritz technique is used on clamped boundary conditions. The results are presented in tabular form. Comparison of results with existing results are also given to support the present study.

Key words. Parallelogram plate, natural vibration, circular variation, density.

1. Introduction

The non-homogeneous plates with variable thickness have the vast applications in engineering like aeronautical engineering, mechanical engineering, marine engineering, and ocean engineering because of versatility, usability and high tensile strength. In order to make trustworthy design, it is essential to study vibrational characteristics of plates because first few modes of vibration play tremendous role. Almost all engineering structure worked under great influence of temperature. Therefore, without consideration of temperature effect, the study of vibration means nothing. A significant work has been reported in these directions.

Leissa [1] provided plate vibration of different geometry with different edges in his excellent monograph. Sharma and Verma [2] studied free vibration of tapered square plate (orthotropic and non-homogeneous) on clamped edge under temperature field by using Rayleigh–Ritz method. The effect of non-homogeneity on natural vibration of orthotropic rectangular plates with variable thickness resting of Pasternak foundation has been analyzed by Lal and Dhanpati [3]. The effect of elastic foundation on the mode shapes and natural vibration of rectangular plates on simply supported edges have been discussed by Raju and Rao [4]. Wang and Xu [5] presented an analysis on natural vibration of beams and rectangular plates with free edges us-

[1]Amity University Haryana, Gurgaon, India; e-mail: dba.amitsharma@gmail.com

ing discrete singular convolution. Gupta and Bhardwaj [6] investigated vibration of orthotropic rectangular elliptic tapered (quadratic variation in thickness) plates resting on elastic foundation. A differential quadrature analysis of vibration and buckling of rectangular plate loaded by linearly varying in-plane stress have been analyzed by Wang et al. [7] on SS-C-SS-C condition. Huanga et al. [8] discussed free vibration of rectangular plates with variable thickness and point support. A study of free vibration of non-homogeneous trapezoidal plates with variable thickness under temperature field has been presented by Gupta and Sharma [9]. Reddy [10] discussed a simple higher order theory for laminated composite plates. An analysis of free vibration of non-uniform and non-homogeneous parallelogram plate under temperature field has been discussed by Sharma and Sharma [11] with the help of mathematical model. Itakura [12] provided natural vibration of thick skewed plates having arbitrary boundary conditions. Sharma and Sharma [13] applied Rayleigh–Ritz method to study the natural vibration of orthotropic rectangular plate with two dimensional thickness and temperature variation. Sharma [14] studied the effect of circular variation in thickness on vibrational frequencies of parallelogram plate on clamped edges using Rayleigh–Ritz method. Sharma et al. [15] also studied the effect of circular variation in thickness on vibrational frequencies of non-homogeneous rectangular plate using Rayleigh–Ritz method.

Here, author tries to find the effect of circular variation as a non-homogeneity effect on vibrational frequencies of non-uniform parallelogram plate on clamped edges. Author also emphasizes on the effect of other variation of plate parameters such as thickness variation, temperature variation, skew angle variation and aspect ratio on the frequency modes.

2. Analysis

2.1. Model description

A non uniform and non-homogeneous parallelogram (thin) plate having skew angle θ is shown in Fig. 1.

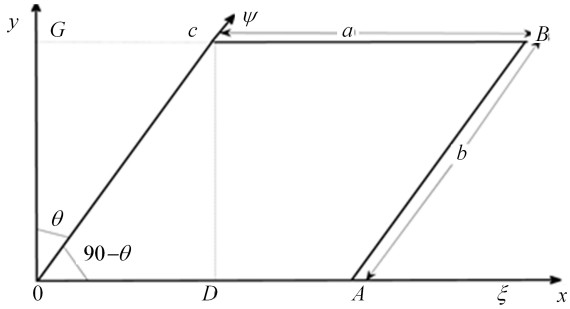

Fig. 1. Parallelogram plate with skew angle θ

The skew coordinates for the parallelogram plate are

$$\zeta = x - y\tan\theta\,, \quad \psi = y\sec\theta\,. \tag{1}$$

The boundaries of the plate in skew coordinates are

$$\zeta = 0,\, a, \quad \text{and} \quad \psi = 0,\, b\,. \tag{2}$$

For natural (free) vibration of the plate, deflection (displacement) is assumed

$$\phi\,(\zeta,\,\psi,\,t) = \Phi\,(\zeta,\,\psi)\cdot T(t)\,, \tag{3}$$

where $\Phi\,(\zeta,\,\psi)$ and $T(t)$ are known as maximum deflection (displacement) at time t and time function, respectively.

The differential equation of motion (kinetic energy T_s and strain energy V_s) for natural frequency of non-uniform parallelogram plate is given by [1] as

$$T_{\mathrm{s}} = \frac{1}{2}\omega^2\rho\cos\theta\int\int l\,\Phi^2\,\mathrm{d}\zeta\;\mathrm{d}\psi \tag{4}$$

and

$$V_{\mathrm{s}} = \frac{1}{2\cos^3\theta}\int\int D\left[\begin{array}{l}\left(\frac{\partial^2\Phi}{\partial\zeta^2}\right)^2 - 4\sin\theta\left(\frac{\partial^2\Phi}{\partial\zeta^2}\right)\left(\frac{\partial^2\Phi}{\partial\zeta\,\partial\psi}\right) + \\ +\,2\left(\sin^2\theta + \nu\cos^2\theta\right)\left(\frac{\partial^2\Phi}{\partial\zeta^2}\right)\left(\frac{\partial^2\Phi}{\partial\psi^2}\right) + \\ +\,2\left(1 + \sin^2\theta - \nu\cos^2\theta\right)\left(\frac{\partial^2\Phi}{\partial\zeta\,\partial\psi}\right)^2 - \\ -\,4\sin\theta\left(\frac{\partial^2\Phi}{\partial\zeta\,\partial\psi}\right)\left(\frac{\partial^2\Phi}{\partial\psi^2}\right) + \left(\frac{\partial^2\Phi}{\partial\psi^2}\right)^2\end{array}\right]\mathrm{d}\zeta\;\mathrm{d}\psi\,, \tag{5}$$

where ρ, ν and l represent the density, Poisson's ratio and thickness of the plate. Here, $D = \frac{El^3}{12(1-\nu^2)}$ is the known flexural rigidity (E being Young's modulus).

2.2. Assumptions required for the model

As the vibration is very vast area of research, therefore we require little limitations in the form of assumptions in this study.

1. For tapering in plate, author assumed a bilinear thickness variation, i.e., linear in the ζ-direction and linear in the ψ-direction as shown in Fig. 2 as

$$l = l_0\left(1 + \beta_1\frac{\zeta}{a}\right)\left(1 + \beta_2\frac{\psi}{b}\right)\,, \tag{6}$$

   where $\beta_1,\ \beta_2,\ (0 \le \beta_1, \beta_2 \le 1)$ are known as the tapering parameters. The thickness of the plate becomes constant, i.e., $l = l_0$ at $\zeta = \psi = 0$.

2. For non-homogeneity in plate's material, author takes into consideration that

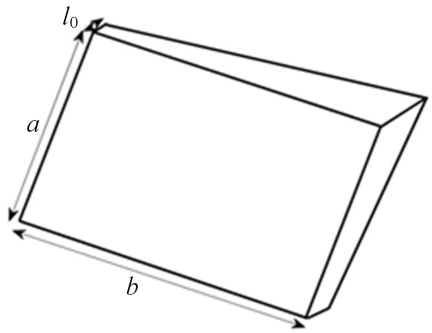

Fig. 2. Parallelogram plate with bilinear thickness variation

the density varies circular in the ζ-direction as

$$\rho = \rho_0 \left[1 - m\left(1 - \sqrt{1 - \frac{\zeta^2}{a^2}}\right)\right], \tag{7}$$

where $(0 \leq m < 1)$ is known as the non-homogeneity constant.

3. The variation of temperature on the plate is considered as bilinear, i.e., linear in the ζ direction and linear in ψ direction as

$$\tau = \tau_0 \left(1 - \frac{\zeta}{a}\right)\left(1 - \frac{\psi}{b}\right), \tag{8}$$

where τ and τ_0 denote the temperature excess above the reference temperature on the plate at any point and at the origin, respectively. The temperature dependence modulus of elasticity for engineering structures is given by

$$E = E_0 \left(1 - \gamma\tau\right), \tag{9}$$

where E_0 is the Young's modulus at the mentioned temperature (i.e., $\tau = 0$) and γ is called the slope of variation.

Using equation (8), equation (9) becomes

$$E = E_0 \left[1 - \alpha\left\{1 - \frac{\zeta}{a}\right\}\left\{1 - \frac{\psi}{b}\right\}\right], \tag{10}$$

where $\alpha,\ (0 \leq \alpha < 1)$ is called the temperature gradient, which is the product of temperature at the origin and slope of variation, i.e., $\alpha = \gamma\tau_0$.

Using equations (6) and (10), the flexural rigidity of the plate becomes

$$D = \frac{E_0 l_0^3 \left[1 - \alpha\left\{1 - \frac{\zeta}{a}\right\}\left\{1 - \frac{\psi}{b}\right\}\right]\left[\left(1 + \beta_1 \frac{\zeta}{a}\right)\left(1 + \beta_2 \frac{\psi}{b}\right)\right]^3}{12\left(1 - \nu^2\right)}. \tag{11}$$

Also, using equations (6), (7) and (11), equations (4) and (5) become

$$V_{\mathrm{s}} = \frac{E_0 l_0^3}{24\,(1-\nu^2)\cos^4\theta}\cdot$$

$$\cdot\int_0^a\int_0^b \left\{ \begin{array}{l} \left[1-\alpha\left\{1-\frac{\zeta}{a}\right\}\left\{1-\frac{\psi}{b}\right\}\right]\left[\left(1+\beta_1\frac{\zeta}{a}\right)\left(1+\beta_2\frac{\psi}{b}\right)\right]^3\cdot \\ \cdot\left[\begin{array}{l} \left(\frac{\partial^2\Phi}{\partial\zeta^2}\right)^2 - 4\left(\frac{a}{b}\right)\sin\theta\left(\frac{\partial^2\Phi}{\partial\zeta^2}\right)\left(\frac{\partial^2\Phi}{\partial\zeta\,\partial\psi}\right) + \\ +2\left(\frac{a}{b}\right)^2\left(\sin^2\theta+\nu\cos^2\theta\right)\left(\frac{\partial^2\Phi}{\partial\zeta^2}\right)\left(\frac{\partial^2\Phi}{\partial\psi^2}\right) + \\ +2\left(\frac{a}{b}\right)^2\left(1+\sin^2\theta-\nu\cos^2\theta\right)\left(\frac{\partial^2\Phi}{\partial\zeta\,\partial\psi}\right)^2 - \\ -4\left(\frac{a}{b}\right)^3\sin\theta\left(\frac{\partial^2\Phi}{\partial\zeta\,\partial\psi}\right)\left(\frac{\partial^2\Phi}{\partial\psi^2}\right)+\left(\frac{a}{b}\right)^4\left(\frac{\partial^2\Phi}{\partial\psi^2}\right)^2 \end{array}\right] \end{array}\right\} \mathrm{d}\psi\ \mathrm{d}\zeta \tag{12}$$

and

$$T_{\mathrm{s}} = \frac{1}{2}\omega^2\rho_0 l_0\cdot$$

$$\cdot\int_0^a\int_0^b\left\{\left[1-m\left(1-\sqrt{1-\frac{\zeta^2}{a^2}}\right)\right]\left[\left(1+\beta_1\frac{\zeta}{a}\right)\left(1+\beta_2\frac{\psi}{b}\right)\right]\right\}\Phi^2\,\mathrm{d}\psi\ \mathrm{d}\zeta\,. \tag{13}$$

4. In this model, author is computing frequency on clamped (along all the four edges) condition (i.e., on C-C-C-C), therefore, the boundary conditions are

$$\begin{aligned} \Phi(\zeta,\psi) &= \tfrac{\partial\Phi(\zeta\,\psi)}{\partial\zeta} = 0, \quad \text{at}, \quad \zeta = 0,\, a\,, \\ \Phi(\zeta\,\psi) &= \tfrac{\partial\Phi(\zeta\,\psi)}{\partial\psi} = 0, \quad \text{at}, \quad \psi = 0,\, b\,. \end{aligned} \tag{14}$$

Therefore, two term deflection (i.e., maximum displacement) which satisfy equation (14) could be represented by

$$\Phi(\zeta\,\psi) = \left(\frac{\zeta}{a}\right)^2\left(\frac{\psi}{b}\right)^2\left(1-\frac{\zeta}{a}\right)^2\cdot$$

$$\cdot\left(1-\frac{\psi}{b}\right)^2\left[\Omega_1+\Omega_2\left(\frac{\zeta}{a}\right)\left(\frac{\psi}{b}\right)\left(1-\frac{\zeta}{a}\right)\left(1-\frac{\psi}{b}\right)\right], \tag{15}$$

where Ω_1 and Ω_2 are arbitrary constants.

3. Solution of model for vibrational frequency

To obtain equation of frequency and vibrational frequency, author uses Rayleigh–Ritz technique (i.e., maximum strain energy V_{s} must equal to the maximum kinetic energy T_{s}). Therefore, we have

$$\delta\left(V_{\mathrm{s}} - T_{\mathrm{s}}\right) = 0\,. \tag{16}$$

Using equations (12) and (13), equation (16) becomes

$$\delta\left(V_{\mathrm{s}}^{*} - \lambda^2 T_{\mathrm{s}}^{*}\right) = 0\,, \tag{17}$$

where

$$V_{\mathrm{s}}^{*} = \frac{1}{\cos^4\theta}\cdot$$

$$\cdot\int_0^a\int_0^b \left\{ \begin{array}{l} \left[\left[1-\alpha\left\{1-\frac{\zeta}{a}\right\}\left\{1-\frac{\psi}{b}\right\}\right]\left[\left(1+\beta_1\frac{\zeta}{a}\right)\left(1+\beta_2\frac{\psi}{b}\right)\right]^3\right]\cdot \\ \cdot\left[\begin{array}{l} \left(\frac{\partial^2\Phi}{\partial\zeta^2}\right)^2 - 4\left(\frac{a}{b}\right)\sin\theta\left(\frac{\partial^2\Phi}{\partial\zeta^2}\right)\left(\frac{\partial^2\Phi}{\partial\zeta\,\partial\psi}\right) + \\ +2\left(\frac{a}{b}\right)^2\left(\sin^2\theta+\nu\cos^2\theta\right)\left(\frac{\partial^2\Phi}{\partial\zeta^2}\right)\left(\frac{\partial^2\Phi}{\partial\psi^2}\right) + \\ +2\left(\frac{a}{b}\right)^2\left(1+\sin^2\theta-\nu\cos^2\theta\right)\left(\frac{\partial^2\Phi}{\partial\zeta\,\partial\psi}\right)^2 - \\ -4\left(\frac{a}{b}\right)^3\sin\theta\left(\frac{\partial^2\Phi}{\partial\zeta\,\partial\psi}\right)\left(\frac{\partial^2\Phi}{\partial\psi^2}\right) + \left(\frac{a}{b}\right)^4\left(\frac{\partial^2\Phi}{\partial\psi^2}\right)^2 \end{array}\right] \end{array}\right\}\,\mathrm{d}\psi\,\mathrm{d}\zeta$$

and

$$T_{\mathrm{s}}^{*} = \int_0^a\int_0^b\left\{\left[1-m\left(1-\sqrt{1-\frac{\zeta^2}{a^2}}\right)\right]\left[\left(1+\beta_1\frac{\zeta}{a}\right)\left(1+\beta_2\frac{\psi}{b}\right)\right]\right\}\Phi^2\,\mathrm{d}\psi\,\mathrm{d}\zeta$$

.

Here, $\lambda^2 = 12\rho_0\omega^2 a^4\left(1-\nu^2\right)/E_0 l_0^2$ is known as the frequency parameter. Equation (17) consists of two unknown constants Ω_1 and Ω_2 (because of substitution of deflection function $\Phi(\zeta,\,\psi)$). These two unknowns can be calculated as follows

$$\frac{\partial}{\partial\Omega_n}\left(V_{\mathrm{s}}^{*} - \lambda^2 T_{\mathrm{s}}^{*}\right) = 0,\ n = 1, 2\,. \tag{18}$$

After simplifying equation (18), we get system of homogeneous equations as

$$\begin{array}{l} r_{11}\Omega_1 + r_{12}\Omega_2 = 0\,, \\ r_{21}\Omega_2 + r_{22}\Omega_2 = 0\,. \end{array} \tag{19}$$

To obtain a nonzero solution (frequency equation), the determinant of the coefficient matrix (symmetric matrix) in equation (19) must zero i.e.,

$$\left|\begin{array}{cc} r_{11} & r_{12} \\ r_{21} & r_{22} \end{array}\right| = 0\,. \tag{20}$$

Equation (20) is a quadratic equation from which we get two modes as λ_1 (first mode) and λ_2 (second mode).

4. Results and discussion

The first two modes of vibration of parallelogram plate on clamped edges is calculated for various values of plate parameters (non-homogeneity m, tapering parameters β_1, β_2, temperature gradient α, skew angle θ and aspect ratio a/b) and tabulated in Tables 1–5. The value of Poisson's ratio ν is taken 0.345.

Table 1 provides the vibrational frequency corresponding to non-homogeneity constant m with fixed value of skew angle $\theta = 30^\circ$ and aspect ratio $a/b = 1.5$ for three different values of taper constants β_1, β_2, i.e., $\beta_1 = \beta_2 = 0$, 0.2, 0.4 and temperature gradient α, i.e., $\alpha = 0.2$, 0.4, 0.6. From Table 1, author concludes that with the increasing value of non-homogeneity m, the frequencies for both modes increase for all the three above mentioned value of taper constants β_1, β_2 and temperature gradient α. When the combined value of taper constants β_1, β_2 increases from 0 to 0.4 and temperature gradient α increases from 0.2 to 0.6, the frequency modes also increase. The rate of increment in case of non-homogeneity is less (due to circular variation) than the rate of increment in case of combined value of taper constants β_1, β_2 and temperature gradient α.

Table 1. Non-homogeneity m versus frequency parameter (λ) for $\theta = 30^\circ$ and $a/b = 1.5$

m	$\beta_1 = \beta_2 = 0$, $\alpha = 0.2$		$\beta_1 = \beta_2 = 0.2$, $\alpha = 0.4$		$\beta_1 = \beta_2 = 0.4$, $\alpha = 0.6$	
	λ_1	λ_2	λ_1	λ_2	λ_1	λ_2
0.0	72.16	287.33	86.24	343.50	102.60	409.21
0.2	76.07	302.87	90.86	361.74	108.06	430.59
0.4	80.68	321.24	96.32	383.23	114.50	455.72
0.6	86.25	343.42	102.89	409.07	122.25	485.83
0.8	93.16	370.94	111.03	440.95	131.81	522.83

Table 2 gives the frequency modes corresponding to tapering parameters β_1, β_2 with fixed value of skew angle $\theta = 30^\circ$ and aspect ratio $a/b = 1.5$ for three different values of temperature gradient α and non-homogeneity constant m i.e., $\alpha = m = 0$, 0.4, 0.8. From Table 2, one can easily see that vibrational frequency increases with increasing values of tapering parameters β_1, β_2 for all the three mentioned values of temperature gradient α and non-homogeneity constant m. The frequency also increases when the combined value of temperature gradient α and non-homogeneity constant m varies from 0 to 0.8. The rate of increment in case of combined values of temperature gradient α and non-homogeneity constant m are less (due to circular variation in density) when compared with rate of increment in case of increasing value tapering parameters.

Table 3 displays the frequency modes corresponding to thermal gradient α with fixed value of skew angle $\theta = 30^\circ$ and aspect ratio $a/b = 1.5$ for three different values of tapering constants β_1, β_2, i.e., $\beta_1, \beta_2 = 0$, 0.2, 0.4 and non-homogeneity constant

m, i.e., $m = 0.2, 0.4, 0.6$. From Table 3 author enlightens the fact that the frequency for both modes decreases, when the temperature gradient α increases from 0 to 0.8. On the other hand, the frequency increases when the combined value of tapering constants β_1, β_2 increases from 0 to 0.4 and non-homogeneity m increases from 0.2 to 0.6.

Table 2. Tapering constants (β_1, β_2) versus frequency parameter (λ) for $\theta = 30^\circ$ and $a/b = 1.5$

$\beta_1 = \beta_2$	$\alpha = m = 0.0$		$\alpha = m = 0.4$		$\alpha = m = 0.8$	
	λ_1	λ_2	λ_1	λ_2	λ_1	λ_2
0.0	74.00	294.60	78.58	312.90	85.67	341.23
0.2	90.10	385.75	96.32	383.23	105.81	420.47
0.4	108.80	433.33	116.86	464.85	129.04	512.14
0.6	130.03	518.31	140.13	557.69	155.27	616.15
0.8	153.75	613.24	166.08	661.71	184.46	732.44
1.0	179.93	719.27	194.68	776.85	216.57	860.95

Table 3. Thermal gradient (α) versus frequency parameter (λ) for $\theta = 30^\circ$ and $a/b = 1.5$

α	$\beta_1 = \beta_2 = 0$, $m = 0.2$		$\beta_1 = \beta_2 = 0.2$, $m = 0.4$		$\beta_1 = \beta_2 = 0.4$, $m = 0.6$	
	λ_1	λ_2	λ_1	λ_2	λ_1	λ_2
0.0	78.00	310.53	100.64	400.24	129.63	514.48
0.2	76.07	302.87	98.50	391.82	127.22	505.11
0.4	74.08	295.00	96.32	383.23	124.76	495.56
0.6	72.04	286.92	94.08	374.43	122.25	485.83
0.8	69.95	278.61	91.79	365.43	119.67	475.90

Table 4 provides the frequency modes corresponding to skew angle θ with fixed value of tapering parameters $(\beta_1 = \beta_2 = 0)$, thermal gradient $(\alpha = 0.2)$, aspect ratio $(a/b = 1.5)$ and variable values of non-homogeneity constant m, i.e., $m = 0.2, 0.4, 0.6$. From Table 4, one can easily demonstrate that the frequency mode increases with the increasing value of skew angle θ. When the non-homogeneity m in plate's material varies from 0.2 to 0.6, frequency modes also increase with less rate of the increment.

Table 4. Skew angle (θ) versus frequency parameter (λ) for $\beta_1 = \beta_2 = 0$, $\alpha = 0.2$ and $a/b = 1.5$

θ	$m = 0.2$		$m = 0.4$		$m = 0.6$	
	λ_1	λ_2	λ_1	λ_2	λ_1	λ_2
0	55.64	223.50	59.01	237.06	63.09	253.43
30	76.07	302.87	80.68	321.24	86.25	343.82
60	238.81	936.43	253.30	993.24	270.79	1061.81

Finally, Table 5 accommodates the frequency modes corresponding to aspect ratio a/b with fixed value tapering parameters $(\beta_1 = \beta_2 = 0)$, thermal gradient $(\alpha = 0.2)$, skew angle $(\theta = 30^\circ)$ and variable values of non-homogeneity constant m, i.e., $m = 0.2, 0.4, 0.6$. From table 5, it is interesting to note that when aspect ratio a/b

varies from 0.5 to 1.5, the frequency modes increase. On the other hand, when non-homogeneity m in plate's material varies from 0.2 to 0.6, the frequency modes also increase with less rate of the increment.

Table 5. Aspect ratio (a/b) versus frequency parameter (λ) for $\beta_1 = \beta_2 = 0,\ \alpha = 0.2$ and $\theta = 30°$

a/b	$m = 0.2$		$m = 0.4$		$m = 0.6$	
	λ_1	λ_2	λ_1	λ_2	λ_1	λ_2
0.5	31.57	128.13	33.48	135.90	35.79	145.28
1.0	51.99	200.36	55.15	212.52	58.95	227.19
1.5	76.07	302.87	80.68	321.24	86.25	343.42

5. Comparison of results

A comparison of frequency modes with [11] is presented in Table 6. It compares the frequencies corresponding to density m with fixed value of tapering parameters $\beta_1 = 0.4,\ \beta_2 = 0.6$, skew angle $\theta = 30°$, aspect ratio $a/b = 1$ and variable values of thermal gradient α i.e., $\alpha = 0, 0.4$. It is noticed that the frequency modes in the present paper are less when compared with [11] for above mentioned values of the thermal gradient α.

Table 6. Comparison of frequency parameter (λ) for present paper and [11] corresponding to non-homogeneity m for $\theta = 30°,\ \beta_1 = 0.4,\ \beta_2 = 0.6$ and $a/b = 1$

m	$\alpha = 0.0$		$\alpha = 0.4$	
	λ_1	λ_2	λ_1	λ_2
0.0	81.16**{81.16}**	312.01**{312.01}**	78.28**{78.28}**	300.98**{300.98}**
0.2	85.47**{85.63}**	328.32**{329.47}**	82.45**{82.60}**	316.70**{317.81}**
0.4	90.56**{90.92}**	347.49**{350.22}**	87.36**{87.70}**	335.18**{337.82}**
0.6	96.69**{97.33}**	370.47**{375.46}**	93.26**{93.88}**	357.34**{362.17}**
0.8	104.25**{105.32}**	398.71**{407.08}**	100.56**{101.59}**	384.58**{392.69}**

Values in bold brackets are from [11].

6. Conclusion

In this paper, author computes the frequency modes corresponding to different values of plate parameters on clamped edges. From the discussion and comparison of results, author would like to record the following conclusions.

1. Frequency modes are less in case of circular variation in density (present paper) when compared to linear variation in density [11] as shown in Table 6. The frequency modes coincide with [11] when $\beta_1 = 0.4,\ \beta_2 = 0.6,\ m = 0,\ \alpha = 0$ and $\beta_1 = 0.4,\ \beta_2 = 0.6,\ m = 0,\ \alpha = 0.4$.

2. Frequency modes increase with less rate of increment with the increasing value

of non-homogeneity m constant due to circular variation in density as shown in Table 1.

3. Due to bilinear variation in thickness parameters β_1, β_2, frequency of both modes increase in linear fashion as shown in Table 2.

4. As the temperature gradient α varies on the plate, vibrational frequencies decrease as shown in Table 3.

5. The vibrational frequencies also increase (in non-linear fashion) with increasing value of skew angle θ and aspect ratio a/b as shown in Tables 4 and 5.

References

[1] A. W. Leissa: *Vibration of plates (NASA SP-160)*. NASA, Government Office, Washington, DC, USA (1969).

[2] A. K. Sharma, V. Verma: *Inspection of vibration using Rayleigh Ritz method for orthotropic non-homogeneous plate with varying thickness and thermal effect*. Romanian Journal of Acoustics and Vibration *14* (2017), No. 1, 33–37.

[3] R. Lal, Dhanpati: *Effect of nonhomogeneity on vibration of orthotropic rectangular plates of varying thickness resting on Pasternak foundation*. Journal of Vibration and Acoustics *131* (2009), No. 1, 1–9.

[4] K. K. Raju, G. V. Rao: *Effect of elastic foundation on the mode shapes in stability and vibration problems of simply supported rectangular plates*. Journal of Sound and Vibration *139* (1990), No. 1, 170-173.

[5] X. Wang, S. Xu: *Free vibration analysis of beams and rectangular plates with free edges by the discrete singular convolution*. Journal of Sound and Vibration *329* (2010), No. 10, 1780–1792.

[6] P. Gupta, N. Bhardwaj: *Vibration of rectangular orthotropic elliptic plates of quadratically varying thickness resting on elastic foundation*. Journal of Vibration and Acoustics *126* (2004), No. 1, 132–140.

[7] X. Wang, L. Gan, Y. Wang: *A differential quadrature analysis of vibration and buckling of an SS-C-SS-C rectangular plate loaded by linearly varying in-plane stresses*. Journal of Sound and Vibration *298* (2006), Nos. 1–2, 420–431.

[8] M. Huang, X. Q. Ma, T. Sakiyama, H. Matsuda, C. Morita: *Free vibration analysis of rectangular plates with variable thickness and point supports*. Journal of Sound and Vibration *300* (2007), Nos. 3–5, 435–452.

[9] A. K. Gupta, P. Sharma: *Vibration study of non-homogeneous trapezoidal plates of variable thickness under thermal gradient*. Journal of Vibration and Control *22* (2016), No. 5, 1369–1379.

[10] J. N. Reddy: *A simple higher-order theory for laminated composite plates*. Journal of Applied Mechanics *51* (1984), No. 4, 745–752.

[11] A. Sharma, A. K. Sharma: *Mathematical modeling of vibration on parallelogram plate with non-homogeneity effect*. Romanian Journal of Acoustics and Vibration *13* (2016), No. 1, 53–57.

[12] K. Itakura: *Free vibration analysis of thick skewed plates having arbitrary boundary conditions*. Journal of Structural and Construction Engineering (Transactions of AIJ) *62* (1997), No. 492, 37–45.

[13] S. K. Sharma, A. K. Sharma: *Rayleigh-Ritz method for analyzing free vibration of orthotropic rectangular plate with 2D thickness and temperature variation*. Journal of Vibroengineering *17* (2015), No. 4, 1989–2000.

[14] A. Sharma: *Vibrational frequencies of parallelogram plate with circular variations in thickness*. Soft Computing: Theories and Applications, Part: Advances in Intelligent Systems and Computing, Book Series (AISC) *583* (2018), 317–326.

[15] A. Sharma, A. K. Raghav, V. Kumar, A. K. Sharma: *Effect of circular variation in thickness and linear variation in density on vibrational frequencies*. Progress in Advanced Computing and Intelligent Engineering, Part: Advances in Intelligent Systems and Computing, Book Series (AISC) *564* (2018), 501–509.

Received February 6, 2018

Acta Technica *63* No. 6/2018, 775–794

Effects of slip on nanofluid flow over an exponentially stretched permeable sheet[1]

Sudipta Ghosh[2], Swati Mukhopadhyay[2,3]

Abstract. This article aims to present the steady boundary layer flow of nanofluid over an exponentially stretching permeable sheet in presence of slips at the boundary. The effects of Brownian motion and thermophoresis on heat and mass transfer are considered. Similarity transformations are used to transform the governing partial differential equations into ordinary ones. The self-similar equations are then solved numerically using shooting technique with fourth order Runge–Kutta method. It is noted that the governing parameters, viz. the suction/blowing parameter, velocity slip, thermal and mass slip parameters, Brownian motion parameter, thermophoresis parameter, Prandtl number, Lewis number significantly affect the flow field, heat transfer and the nanoparticle volume fraction. Suction through the porous sheet causes reduction in velocity, temperature and also in concentration. With the increase in velocity slip, fluid velocity decreases whereas increase in both temperature and concentration are noted. Due to increase in thermal slip and mass slip both temperature and concentration decrease. Temperature is found to increase but the nanoparticle volume fraction decreases due to the Brownian motion. With the increase in Lewis number, the rate of heat transfer decreases. For thermospheric effect the thermal boundary layer becomes larger.

Key words. Nanofluid, exponentially stretching sheet, slip boundary conditions, suction/blowing.

1. Introduction

Recently, the study of boundary layer flow of nanofluid has acquired momentum due to its various applications in engineering/industrial disciplines. The term nanofluid was first proposed by Choi [1] and he mentioned the dispersions of nanoparticles in the base fluid such as water, ethylene glycol and propylene glycol. Masuda et

[1]One of the authors, S. Ghosh, (SRF, CSIR) acknowledges the financial assistance from CSIR, New Delhi, India. The other author (S. Mukopadhyay) acknowledges the financial support received from SERB (New Delhi, India) through Young Scientist Project.

[2]Department of Mathematics, The University of Burdwan, Burdwan-713104, West Bengal, India

[3]Corresponding author; email: swati_bumath@yahoo.co.in

al. [2] observed the enhancement characteristics of thermal conductivity of nanofluid. The high thermal conductivity of nanoparticles suspended in the base fluid with a low thermal conductivity, remarkably increase thermal conductivity of nanofluids. So, researchers developed many models to report how much that increase would be and many experiments have been conducted to compare experimental data with those analytical models. A comprehensive survey of convective transport in nanofluid was made by Buongiorno [3] by developing a non homogeneous equilibrium model for convective transport. He explained that the abnormal increase in the thermal conductivity occurs due to the presence of two main effects, namely, the Brownian diffusion and the thermophoretic diffusion of nanoparticles. The materials with sizes of nanometers possess sole physical and chemical properties. They can flow easily through microchannels without creating any obstruction as they are sufficiently small to act in the same way to the liquid molecules [4]. Later, employing Buongiorno model, Kuznetsov and Nield [5] investigated the natural convective boundary layer flow of a nanofluid.

The viscous fluid flows due to a stretching sheet have enormous applications in a variety of manufacturing processes. Flow past a stretching sheet is usually encountered in extrusion process in which melt is stretched into a cooling fluid. Crane [6] first studied the boundary layer flow due to linearly stretching sheet. Later on, a lot of researchers extended the work of Crane [6] to analyze a range of features of the flow and/ or heat transfer problems due to a stretching surface where the velocity of the stretching surface is assumed linearly proportional to the distance from the fixed origin. However, it is often argued that (Gupta and Gupta [7]) practically stretching of plastic sheet may not essentially be linear. The boundary layer flow and heat transfer due to an exponentially stretching sheet was considered by Magyari and Keller [8]. Bearing in mind wall mass suction, Elbashbeshy [9] investigated the flow and heat transfer over an exponentially stretching surface. Khan and Sanjayanand [10] presented the boundary layer flow of viscoelastic fluid and heat transfer over an exponentially stretching sheet with viscous dissipation effect and Partha et al. [11] obtained a similarity solution for mixed convection flow passed an exponentially stretching surface. Recently, Bhattacharyya and Vajravelu [12] described the stagnation point boundary layer flow due to exponentially shrinking sheet for Newtonian fluid. Mandal and Mukhopadhyay [13] investigated the flow and heat transfer due to an exponentially stretching sheet in porous medium taking the variable heat flux. Bachok et al. [14] investigated the same problem for nanofluid. The boundary layer flow of nanofluid past a linearly stretching sheet was studied by Khan and Pop [15]. The boundary layer flow induced in a nanofluid due to a linearly stretching sheet with convective boundary condition was described by Makinde and Aziz [16]. Kandasamy et al. [17] investigated the MHD boundary layer flow of a nanofluid past a vertical stretching permeable surface. Mustafa et al. [18] reported the flow of a nanofluid near a stagnation point towards a stretching surface. Rana and Bhargava [19] illustrated the steady, laminar boundary layer flow due to the nonlinear stretching of a flat surface in a nanofluid. Later Hady et al. [20] investigated the boundary layer flow and heat transfer characteristics of a viscous nanofluid over a nonlinearly stretching sheet in presence of thermal radiation and variable wall

temperature. Makinde et al. [21] discussed the combined effects of buoyancy force and magnetic field on stagnation point flow and heat transfer in a nanofluid flow towards a stretching sheet. A theoretical study of unsteady boundary layer flow of a nanofluid over a permeable stretching/shrinking sheet was investigated by Bachok et al. [22]. Recently, using homotopy analysis method (HAM), Nadeem and Lee [23] obtained analytical solutions of boundary layer flow of nanofluid over an exponentially stretching surface. Bhattacharyya and Layek [24] analysed the effects of magnetic field on nanofluid flow over an exponentially stretching permeable surface assuming the no-slip condition at the boundary.

All the studies mentioned above, continued their discussions by considering no-slip boundary condition. In no-slip-flow, the flow velocity is zero at the solid–fluid interface. But in case of slip-flow, the flow velocity at the solid wall is non-zero. Even if the separation of individual molecules is obvious at the nanoscales, it is still possible to explain main transport phenomena in nanofluidic systems using continuum hypothesis (Nandy and Mahapatra [25]). The nanofluidic flow generally exhibits partial slip against the solid surface, which can be characterized by slip-length (around 3.4–68 mm for different liquids) (Majumder et al. [26]).

The fluids exhibiting slip at the boundary have important technological applications such as in the polishing of the artificial heart valves and internal cavities. Sometimes the assumption of no-slip flow is not applicable and should be replaced by the partial slip boundary conditions. Partial slips occur for fluid with particulate such as emulsion suspensions, foams and polymer solutions. With a slip at the wall boundary, the flow behavior and the shear stress in the fluid are quite different from the no-slip flow. Wang [27] discussed the effects of partial slip on flow due to the stretching surface. Noghrehabadi et al. [28] investigated the effects of slip on the boundary layer flow and heat transfer over a stretching sheet. Mukhopadhyay [29] analyzed the combined effects of slip and magnetic field on flow and heat transfer past an exponentially stretching surface.

In the present paper, the boundary layer nanofluid flow due to an exponentially stretching porous sheet in presence of partial slips at the boundary is considered. Velocity, thermal as well as mass slip conditions at the boundary are considered. So this work can be considered as an extension of the problem considered by Bhattacharyya and Layek [24]. With the help of appropriate similarity transformations the governing partial differential equations are reduced into a set of nonlinear ordinary differential equations and these equations are then solved numerically using fourth order Runga–Kutta method with the help of shooting technique. Effects of different pertinent parameters are analyzed in detail with their graphical representations.

2. Mathematical formulation

Consider the steady boundary layer flow of nanofluid over an exponentially stretching sheet in presence of partial slip. The governing equations for this problem

may be written in usual notation as

$$\frac{\partial u}{\partial x}+\frac{\partial v}{\partial y}=0\,, \tag{1}$$

$$u\frac{\partial u}{\partial x}+\upsilon\frac{\partial u}{\partial y}=\nu\frac{\partial^2 u}{\partial y^2}\,, \tag{2}$$

$$u\frac{\partial T}{\partial x}+\upsilon\frac{\partial T}{\partial y}=\alpha\frac{\partial^2 T}{\partial y^2}+\frac{(\rho c)_{\mathrm{P}}}{(\rho c)_{\mathrm{f}}}\left[D_{\mathrm{B}}\frac{\partial C}{\partial y}\frac{\partial T}{\partial y}+\frac{D_{\mathrm{T}}}{T_\infty}\left(\frac{\partial T}{\partial y}\right)^2\right], \tag{3}$$

$$u\frac{\partial C}{\partial x}+\upsilon\frac{\partial C}{\partial y}=D_{\mathrm{B}}\frac{\partial^2 C}{\partial y^2}+\frac{D_{\mathrm{T}}}{T_\infty}\frac{\partial^2 T}{\partial y^2}\,, \tag{4}$$

where u and υ are the velocity components in directions x and y, respectively, ν is the kinematic viscosity, ρ_{f} is the density of the base fluid, T is the temperature, T_∞ denotes the constant temperature of the fluid in the inviscid free stream, α is the thermal diffusivity, $(\rho c)_{\mathrm{p}}$ is the effective heat capacity of nanoparticles, $(\rho c)_{\mathrm{f}}$ is the heat capacity of the base fluid, C stands for the nanoparticle volume fraction, D_{B} denotes the Brownian diffusion coefficient and D_{T} is the thermophoretic diffusion coefficient. The boundary conditions are given by the formulae

$$u=U_{\mathrm{w}}+B_1\nu\frac{\partial u}{\partial y},\quad \upsilon=\upsilon_{\mathrm{w}}\ \text{at}\ \ y=0\ \ \text{and}\ \ u\to 0\ \ \text{as}\ \ y\to\infty,$$

$$T=T_{\mathrm{w}}+D_1\frac{\partial T}{\partial y}\ \ \text{at}\ \ y=0\ \ \text{and}\ \ T\to T_\infty\ \ \text{as}\ \ y\to\infty,$$

$$C=C_{\mathrm{w}}+N_1\frac{\partial C}{\partial y}\ \ \text{at}\ \ y=0\ \ \text{and}\ \ C\to C_\infty\ \ \text{as}\ \ y\to\infty. \tag{5}$$

Here, $U_{\mathrm{w}}=U_0\exp(x/L)$ is the stretching velocity where $U_0>0$ denotes the stretching constant, T_{w} is the uniform wall temperature, T_∞ is the free stream temperature, C_w is the uniform wall nanoparticles volume fraction and C_∞ is the nanoparticle volume fraction in free stream, υ_{w} is the variable velocity for suction/blowing with $\upsilon_w=\upsilon_0\exp(x/2L)$, where υ_0 is a constant ($\upsilon_0>0$ indicates suction and $\upsilon_0<0$ stands for blowing). Further, $B_1=B_0\exp(-x/2L)$ is the velocity slip factor which changes with space co-ordinate x, B_0 denotes the initial value of velocity slip factor, $D_1=D_0\exp(-x/2L)$ is the thermal slip factor which changes with space co-ordinate x, D_0 denotes the initial value of thermal slip factor, $N_1=N_0\exp(-x/2L)$ is the mass slip factor which changes with space co-ordinate x, and N_0 denotes the initial value of the velocity slip factor.

Let us introduce the following similarity transformations

$$\psi=\sqrt{2\nu U_0 L}\,f(\eta)\,\exp\left(\frac{x}{2L}\right),\quad \eta=y\sqrt{\frac{U_0}{2\nu L}}\,\exp\left(\frac{x}{2L}\right),$$

$$\theta(\eta) = \frac{T - T_\infty}{T_\mathrm{w} - T_\infty}, \quad \phi(\eta) = \frac{C - C_\infty}{C_\mathrm{w} - C_\infty}, \tag{6}$$

where ψ is the stream function and $u = \frac{\partial \psi}{\partial y}$, $v = -\frac{\partial \psi}{\partial x}$ and η is the similarity variable.

Equation (1) is automatically satisfied by this. Using the relations (6) in equations (2)–(4), we get the following equations

$$f''' + ff'' - 2f'^2 = 0, \tag{7}$$

$$\theta'' + \mathrm{Pr}\ f\theta' + \mathrm{Pr}\ (\mathrm{Nb}\,\phi' + \mathrm{Nt}\,\theta')\,\theta' = 0, \tag{8}$$

$$\phi'' + \mathrm{Le}\, f\phi' + \frac{\mathrm{Nt}}{\mathrm{Nb}}\theta'' = 0. \tag{9}$$

Here $\mathrm{Pr} = \nu/\alpha$ is the Prandtl number and $\mathrm{Le} = \nu/D_\mathrm{B}$ is the Lewis number. The two dimensionless parameters Nb (Brownian motion parameter) and Nt (thermophoresis parameter) are defined as

$$\mathrm{Nb} = D_\mathrm{B}\frac{(\rho c)_\mathrm{p}}{(\rho c)_\mathrm{f}}\frac{C_\mathrm{w} - C_\infty}{\nu}, \quad \mathrm{Nt} = \frac{D_\mathrm{T}}{T_\infty}\frac{(\rho c)_\mathrm{p}}{(\rho c)_\mathrm{f}}\frac{T_\mathrm{w} - T_\infty}{\nu}.$$

The boundary conditions take the following forms

$$f(\eta) = S,\ f'(\eta) = 1 + Bf''(\eta) \text{ at } \eta = 0, \quad f'(\eta) \to 0 \text{ as } \eta \to \infty\,, \tag{10}$$

$$\theta(\eta) = 1 + D\theta'(\eta) \text{ at } \eta = 0, \quad \theta(\eta) \to 0 \text{ as } \eta \to \infty\,, \tag{11}$$

$$\phi(\eta) = 1 + N\phi'(0) \text{ at } \eta = 0 \quad \phi(\eta) \to 0 \text{ as } \eta \to \infty\,. \tag{12}$$

Here, $S = -\frac{v_0}{\sqrt{(\nu c)/(2L)}}$ is the suction/blowing parameter; $S > 0$ ($v_0 < 0$) corresponds to suction and $S < 0$ ($v_0 > 0$) corresponds to blowing. Symbols B, D, and N are respectively velocity slip, thermal slip and mass slip parameters which are given as

$$B = B_0\sqrt{U_0\nu/(2L)},\ D = D_0\sqrt{U_0/(2\nu L)},\ N = N_0\sqrt{U_0/(2\nu L)}\,.$$

The quantities of physical interest for this problem are the local skin friction coefficient

$$C_\mathrm{f} = \frac{\nu}{U_\mathrm{w}^2}\left.\frac{\partial u}{\partial y}\right|_{y=0}, \ \mathrm{Nu}_x = -\frac{x}{(T_\mathrm{w} - T_\infty)}\left.\frac{\partial T}{\partial y}\right|_{y=0}, \ \mathrm{Sh}_x = -\frac{x}{C_\mathrm{w} - C_\infty}\left.\frac{\partial C}{\partial y}\right|_{y=0},$$

i.e.,

$$\sqrt{2\mathrm{Re}_x C_\mathrm{f}} = f''(0),\ \frac{\mathrm{Nu}_x}{\sqrt{2\mathrm{Re}_x}} = -\sqrt{\frac{x}{2L}}\theta'(0),\ \frac{\mathrm{Sh}_x}{\sqrt{2\mathrm{Re}_x}} = -\sqrt{\frac{x}{2L}}\phi'(0)\,. \tag{13}$$

The highly nonlinear coupled ODEs (7–9) along with the boundary conditions (10–12) form a two-point boundary value problem (BVP) and those are solved using the shooting method.

3. Results and discussion

The accuracy of the employed numerical method is tested by direct comparisons with the available results of $f''(0)$ reported by Magyari and Keller [8], Elbashbeshy [9], Sahoo and Poncet [30] and found $f''(0) = -1.281812$ correct to six decimal places which is in good agreement with $f''(0)$= -1.28180, $f''(0)$= 1.28181 and $f''(0)$= -1.281811, reported by Magyari and Keller [8], Elbashbeshy [9] and Sahoo and Poncet [30], respectively.

To validate our numerical results obtained in this study, the values of the skin friction coefficient $-f''(0)$ and heat transfer coefficient $-\theta'(0)$ are compared with the available data obtained by Elbashbeshy [9] and Hafidzuddin et al. [31] for no-slip case. Our results agree completely with their results which are presented in Table 1.

To analyze the results numerical computations for various values of the pertaining parameters are made and presented graphically in Figs. 1–11.

Figs. 1(a)–1(c) present the effects of mass suction parameter on velocity, temperature and concentration field, respectively. It is found that the velocity, temperature and nanoparticle volume fraction decrease with the increase of mass suction parameter. Due to the increase of mass suction, the flow is closer to the boundary layer. So the velocity boundary layer thickness becomes thinner. The same effect is noted for the thermal and nanoparticle volume boundary layer thicknesses. On the other hand, an opposite effect is observed for the blowing case. That is due to increase of blowing the velocity, thermal and nanoparticle volume boundary layer thicknesses increase.

The effects of velocity slip parameter B is shown in Figs .2(a)–(c). It is found that with increasing velocity slip, fluid velocity decreases and so the velocity boundary layer thickness decreases (Fig. 2(a)). Due to the slip, the flow velocity near the sheet is no longer equal to the stretching velocity at the sheet. With the increase in B, such a slip velocity increases and consequently fluid velocity decreases because under the slip condition at the boundary, the pulling of the stretching sheet can only partly be transmitted to the fluid. The opposite effect is observed for the temperature (Fig. 2(b)) and nanoparticle volume (Fig. 2(c)), that is due to the increase of velocity slip parameter, while the temperature (Fig. 2(b)) and nanoparticle volume (Fig. 2(c)) both increase with increasing values of slip parameter B. Consequently, thermal and nanoparticle volume boundary layer thicknesses increase.

Fig. 3(a) shows that with the increase of thermal slip parameter, less heat is transferred to the fluid. As a result, temperature decreases. So the thermal boundary

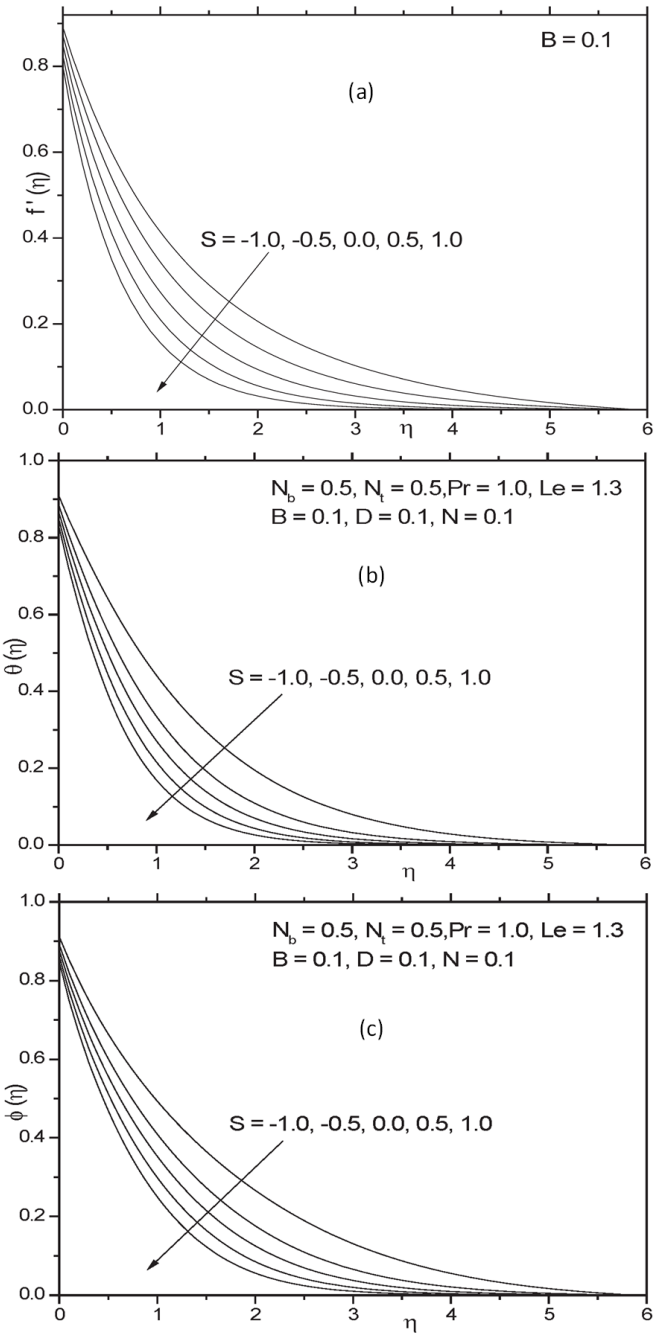

Fig. 1. Effects of suction/blowing parameter S on (a) velocity $f'(\eta)$, (b) temperature $\theta(\eta)$ and (c) nanoparticle volume fraction $\phi(\eta)$

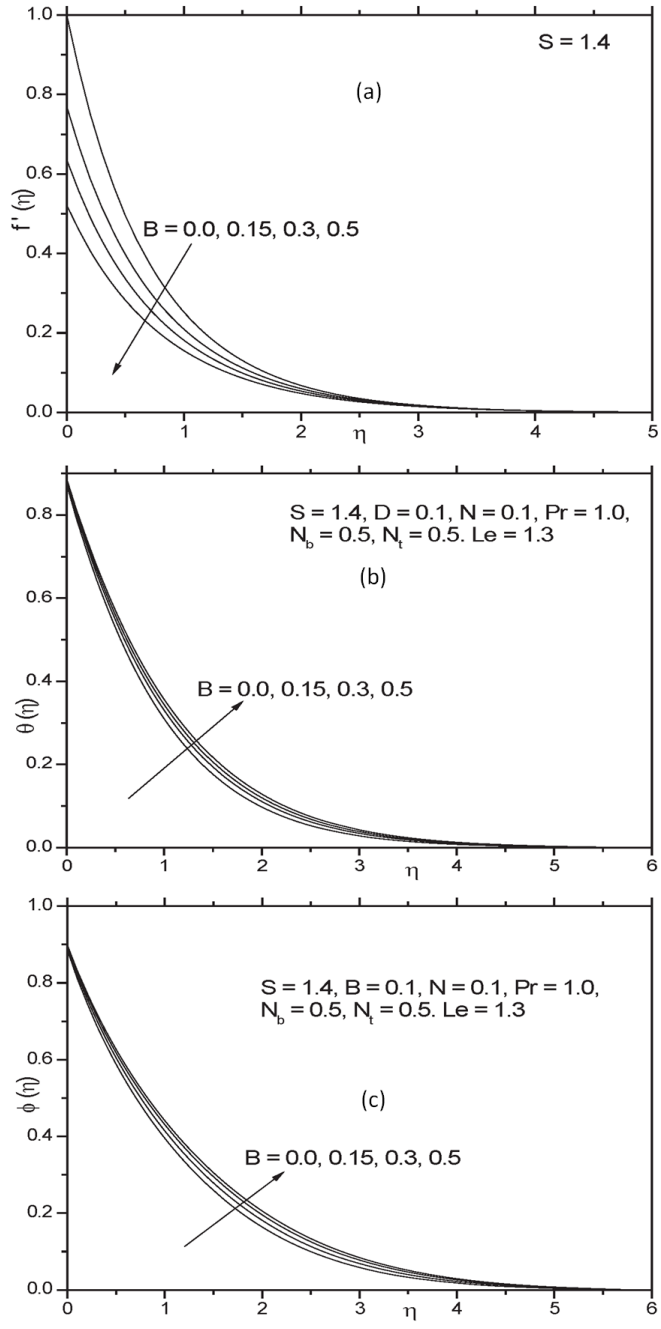

Fig. 2. Effects of velocity slip parameter B on (a) velocity $f'(\eta)$, (b) temperature $\theta(\eta)$ and (c) nanoparticle volume fraction $\phi(\eta)$

layer thickness also decreases with the increase of thermal slip parameter. With the increase of thermal slip parameter, the nanoparticle volume fraction also decreases (Fig. 3(b)).

In Figs. 4(a)–(b), the variations of temperature and nanoparticle volume fraction due to the variation in nanoparticle volume slip parameter N are exhibited. Temperature decreases with increasing N (Fig. 4(a)), but the effect is not pronounced. The nanoparticle volume fraction decreases significantly with the increase of nanoparticle volume slip parameter near the sheet (Fig. 4(b)), but away from the sheet, this feature is smeared out. So the boundary layer thicknesses of temperature and nanoparticle volume fraction decrease.

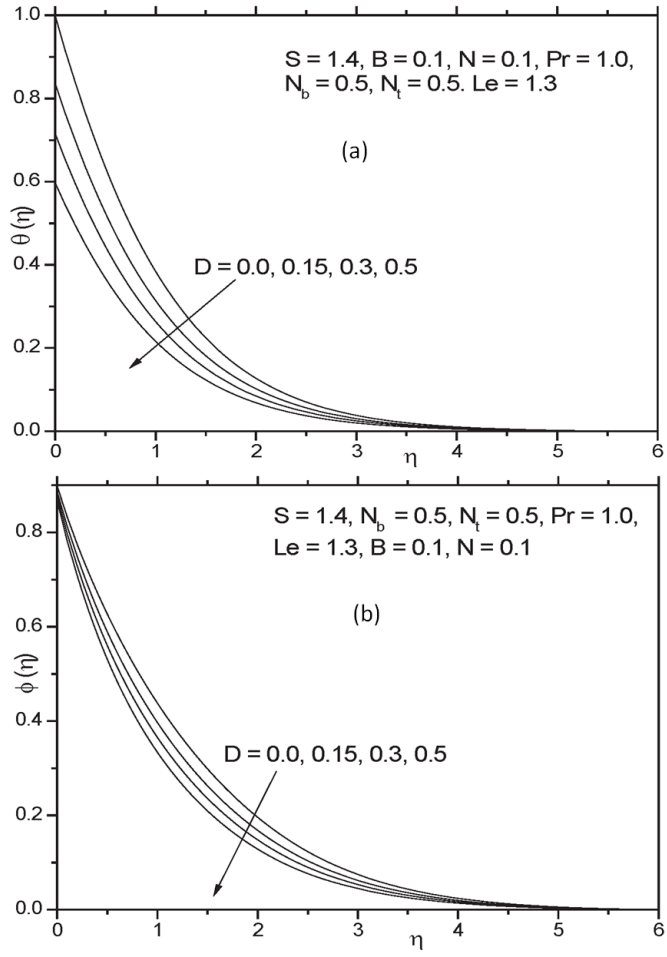

Fig. 3. Effects of thermal slip parameter D on (a) temperature $\theta(\eta)$ and (b) nanoparticle volume fraction $\phi(\eta)$

The fluid temperature decreases with increasing values of Lewis number Le (Fig. 5(a)). But the effect of Lewis number Le on temperature is not significant.

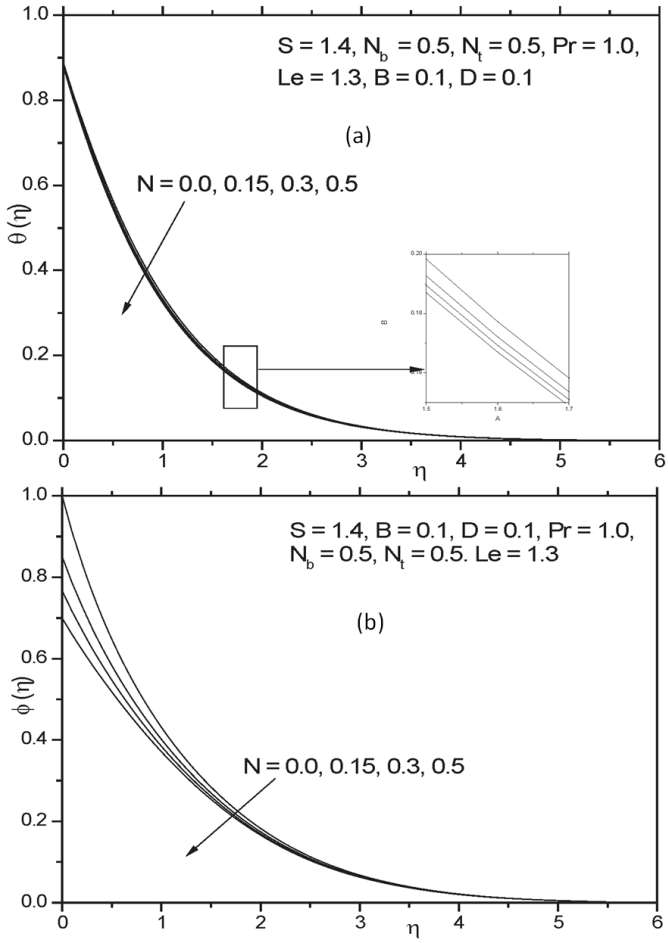

Fig. 4. Effects of nanoparticle volume slip parameter N on (a) temperature $\theta(\eta)$ and (b) nanoparticle volume fraction $\phi(\eta)$

The nanoparticle volume fraction is also found to decrease significantly with increasing Lewis number Le (Fig. 5(b)]. With the increase in Le, mass transfer rate increases and, consequently, concentration boundary layer thickness decreases.

The effects of Prandtl number Pr are exhibited in Figs. 6(a)–(b). Temperature decreases with increasing Pr (Fig. 6(a)). The nanoparticle volume fraction initially increases with increasing Pr (Fig. 6(b)) but away from the sheet it decreases. This is due to the Brownian motion of the nanoparticles. So the thermal and concentration boundary layer thicknesses decrease in both cases. Actually, fluid with higher Prandtl number has lower thermal conductivity which causes to decrease the thickness of thermal boundary layer.

In Fig. 7(a)–(b), the effects due to the Brownian motion parameter Nb are exhibited. Due to increase of Brownian motion parameter, temperature increases

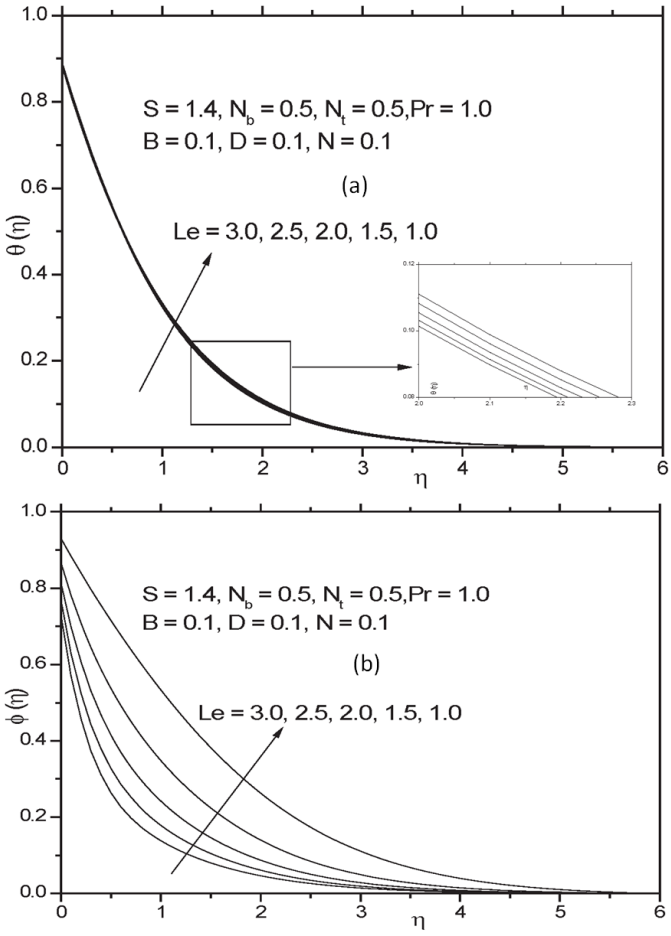

Fig. 5. Effects of Lewis number Le on (a) temperature $\theta(\eta)$ and (b) nanoparticle volume fraction $\phi(\eta)$

(Fig. 7(a)). But opposite behavior is observed in case of nanoparticle volume fraction (Fig. 7(b)). With the rise in Nb, nanoparticle volume boundary layer thickness decreases.

From Figs. 8(a)–(b) effects due to thermophoresis parameter Nt on temperature and nanoparticle volume fraction are observed. Due to increase of thermophoresis parameter, both the temperature (Fig. 8(a)) and nanoparticle volume fraction (Fig. 8(b)) increase significantly. Overshoot in case of nanoparticle volume fraction near the sheet is noted for higher values of Nt (Fig. 8(b). This physically means that with the continuous thermophoretic particle deposition, the nanoparticle volume fraction becomes higher in the fluid adjacent to the sheet than the value at the wall. Actually with the increase in Nt, thermophoresis force increases and this helps to move the nanoparticles from hot to cold areas. As a result, both the temperature

and concentration increase.

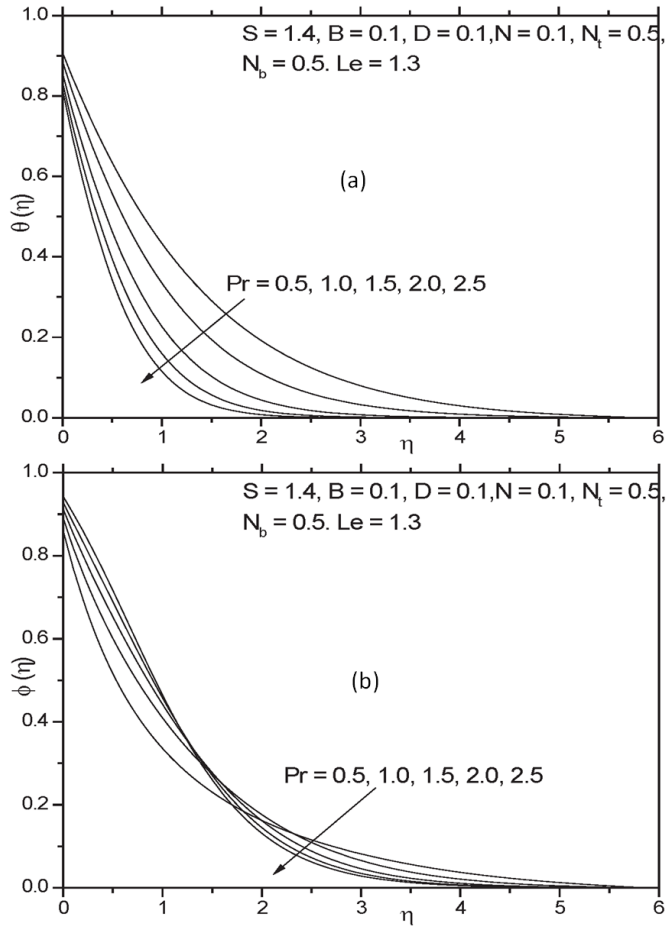

Fig. 6. Effects of Prandtl number Pr on (a) temperature $\theta(\eta)$ and (b) nanoparticle volume fraction $\phi(\eta)$

Skin friction coefficient, Nusselt number and Sherwood number are of great importance. We now discuss the variations of these physical quantities, i.e., the local skin friction coefficient C_{f}, the local nusselt number Nu_x and the local Sherwood number Sh_x for different values of the parameters S, B, D, N, Pr, Le, Nb and Nt. The variations of the quantities $-f''(0)$, $-\theta'(0)$, $-\phi'(0)$ related to local skin friction coefficient, the local Nusselt number, and the local Sherwood number, respectively, are presented in the Figs. 9–11 for various values of those parameters. The values of $-f''(0)$, $-\theta'(0)$, $-\phi'(0)$ versus the suction/blowing parameter S are plotted in Fig. 9 for different values of velocity slip parameter B, thermal slip parameter D and the nanoparticle volume slip parameter N, respectively. The local skin friction coefficient decreases with increasing velocity slip parameter B but increases with the increasing values of suction/blowing parameter S (Fig.9(a)). Local

Nusselt number decreases with increasing values of thermal slip parameter D but increases with suction/blowing parameter S (Fig. 9(b)) and local Sherwood number is found to decrease with nanoparticle volume slip parameter N but increases with suction/blowing parameter S (Fig. 9(c)).

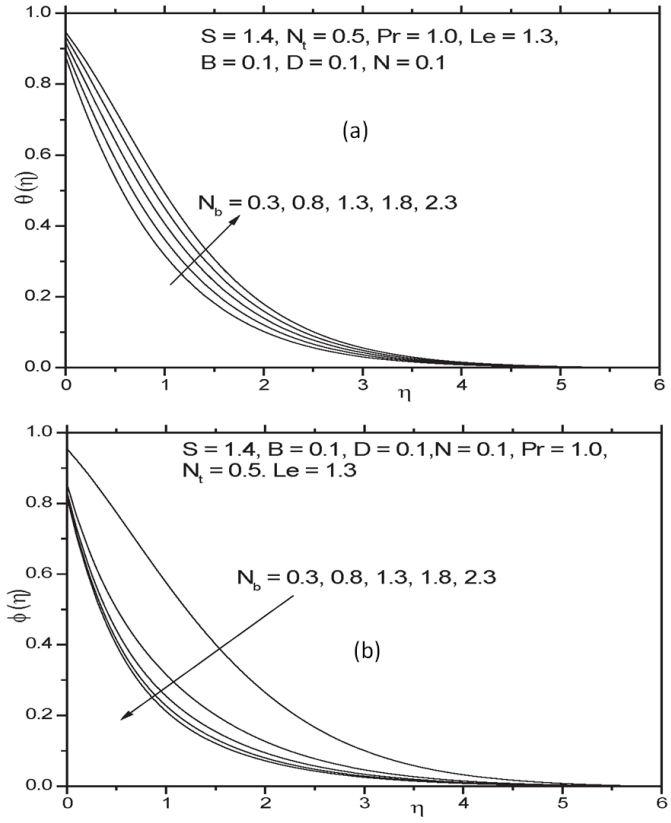

Fig. 7. Effects of Brownian motion parameter Nb on (a) temperature $\theta(\eta)$ and (b) nanoparticle volume fraction $\phi(\eta)$

Local Nusselt number decreases with the Brownian motion parameter Nb (Fig. 10(a)) and also with thermophoresis parameter Nt (Fig.10(a)). With the Lewis number Le, local Nusselt number decreases but increases with increasing Prandtl number Pr (Fig. 10(b)). Brownian diffusion effect increases with the decrease in Lewis number Le. As a result heat transfer is higher for lower values of Lewis number Le.

Local Sherwood number increases with the Brownian motion parameter Nb but decreases with thermophoresis parameter Nt (Fig. 11(a)) whereas local Sherwood number increases with the Lewis number Le but decreses with Pr (Fig. 11(b)). One can conclude that Lewis number Le affects temperature and concentration field in opposite way compared to that of Prandtl number Pr.

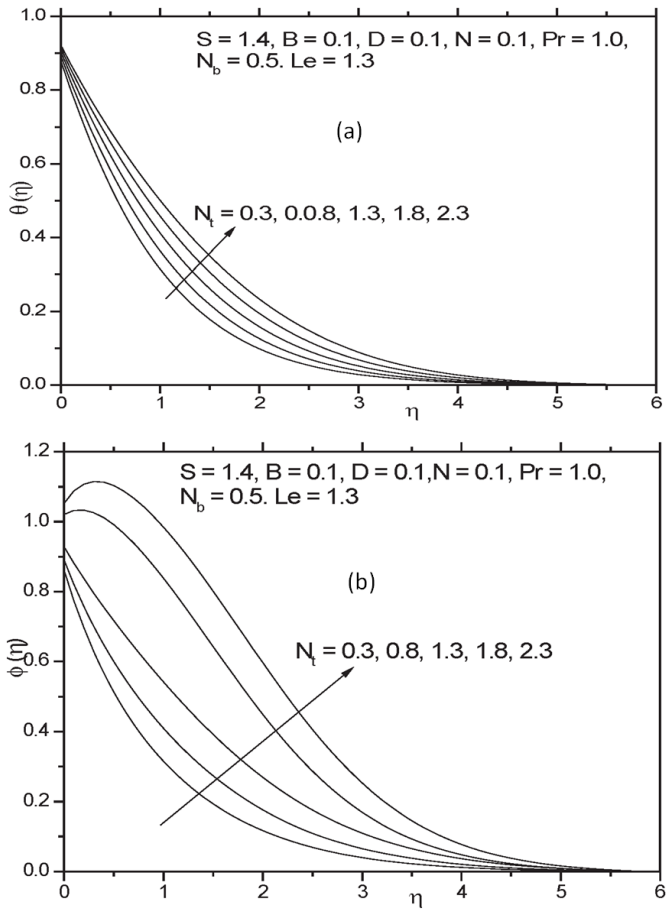

Fig. 8. Effects of thermophoresis parameter Nt on (a) temperature $\theta(\eta)$ and (b) nanoparticle volume fraction $\phi(\eta)$

4. Conclusions

Boundary layer nanofluid flow past an exponentially stretching porous sheet in presence of slip at the boundary has been considered. The findings of this investigation can be summarized as follows:

1. Velocity slip significantly affect the flow, thermal and concentration fields. Velocity decreases but the temperature and concentration increase are noted with increasing velocity slip.

2. Due to suction, fluid velocity, temperature and nanoparticle volume fraction are found to decrease. Opposite nature is noted for blowing.

3. Temperature is found to increase but the nanoparticle volume fraction decreases due to Brownian motion.

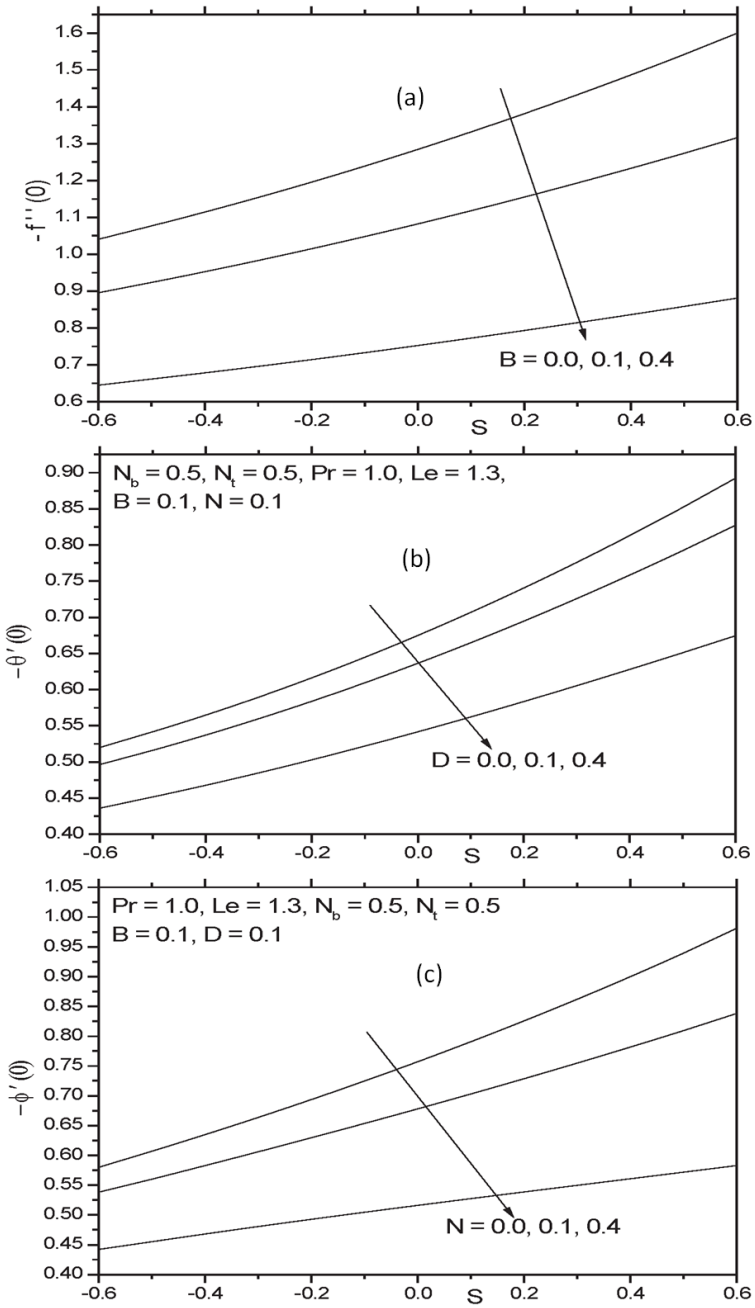

Fig. 9. Variations of (a) $-f''(0)$ with velocity slip parameter B (b) $-\theta'(0)$ with thermal slip parameter D and (c) $-\phi'(0)$ with the nanoparticle volume slip parameter N for different values of mass transfer parameter S

4. Due to thermophoresis, both the temperature and nanoparticle volume fraction significantly increase in the boundary layer region.

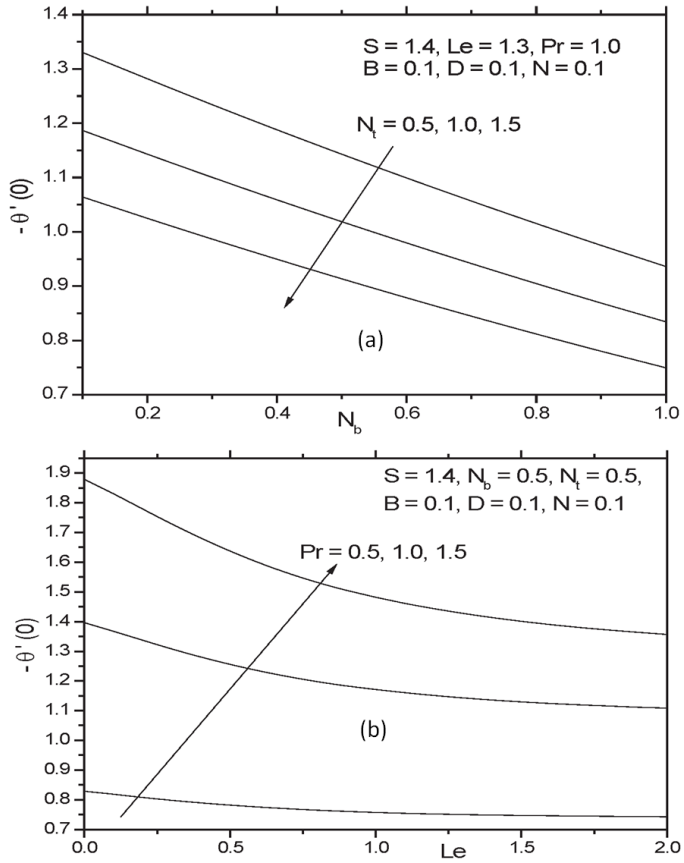

Fig. 10. Variations of $-\theta'(0)$ with (a) Brownian motion parameter Nb for different values of thermophoresis parameter Nt, (b) Lewis number Le for different values of Prandtl number Pr

References

[1] S. U. S. Choi, J. A. Eastman: *Enhancing thermal conductivity of fluids with nanoparticles.* ASME International Mechanical Engineering Congress & Exposition, 12–17 November 1995, San Francisco, CA, Proceedings of the ASME (1995), No. 66, 99–105.

[2] H. Masuda, A. Ebata, K. Teramae, N. Hishinuma: *Alteration of thermal conductivity and viscosity of liquid by dispersing ultra-fine particles.* Netsu Bussei *7* (1993), No. 4, 227–233.

[3] J. Buongiorno: *Convective transport in nanofluids.* Journal of Heat Transfer *128* (2005), No. 3, 240–250.

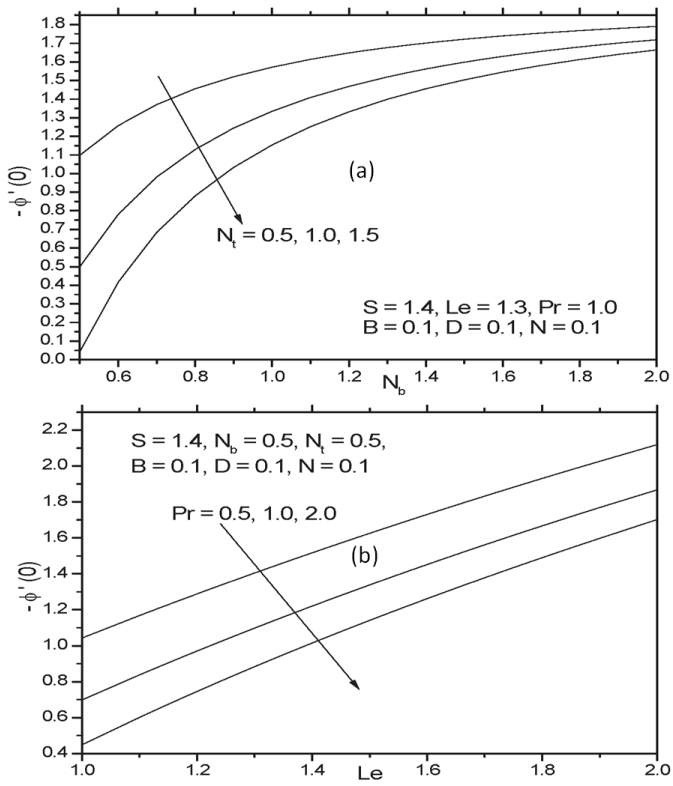

Fig. 11. Variations of $-\phi'(0)$ with (a) Brownian motion parameter Nb for different values of thermophoresis parameter Nt (b) Lewis number Le for different values of Prandtl number Pr

[4] F. Mabood, W. A. Khan, M. M. Rashidi: *The new analytical study for boundary-layer slip flow and heat transfer of nanofluid over a stretching sheet.* Thermal Science (2015) DOI: 10.2298/TSCI140424035M.

[5] A. V. Kuznetsov, D. A. Nield: *Natural convective boundary-layer flow of a nanofluid past a vertical plate.* International Journal of Thermal Sciences *49* (2010), No. 2, 243–247.

[6] L. J. Crane: *Flow past a stretching plate.* Zeitschrift für angewandte Mathematik und Physik ZAMP *21* (1970), No. 4, 645–647.

[7] P. S. Gupta, A. S. Gupta: *Heat and mass transfer on a stretching sheet with suction or blowing.* Canadian Journal of Chemical Engineering *55* (1977), No. 6, 744–746.

[8] E. Magyari, B. Keller: *Heat and mass transfer in the boundary layers on an exponentially stretching continuous surface.* Journal of Physics D: Applied Physics *32* (1999), No. 5, 577–585.

[9] E. M. A. Elbashbeshy: *Heat transfer over an exponentially stretching continuous surface with suction.* Archives of Mechanics *53* (2001), No. 6, 643–651.

[10] S. K. Khan, E. Sanjayanand: *Viscoelastic boundary layer flow and heat transfer over an exponential stretching sheet.* International Journal of Heat and Mass Transfer *48* (2005), No. 8, 1534–1542.

[11] M. K. Partha, P. V. S. N. Murthy, G. P. Rajasekhar: *Effect of viscous dissipa-*

tion on the mixed convection heat transfer from an exponentially stretching surface. Heat and Mass Transfer *41* (2005), No. 4, 360–366.

[12] K. Bhattacharyya, K. Vajravelu: *Stagnation-point flow and heat transfer over an exponentially shrinking sheet.* Communications in Nonlinear Science and Numerical Simulation *17* (2012), No. 7, 2728–2734.

[13] I. C. Mandal, S. Mukhopadhyay: *Heat transfer analysis for fluid flow over an exponentially stretching porous sheet with surface heat flux in porous medium.* Ain Shams Engineering Journal *4* (2013), No. 1, 103–110.

[14] N. Bachok, A. Ishak, I. Pop: *Boundary layer stagnation-point flow and heat transfer over an exponentially stretching/shrinking sheet in a nanofluid.* International Journal of Heat and Mass Transfer *55* (2012), Nos. 25–26, 8122–8128.

[15] W. A. Khan, I. Pop: *Boundary-layer flow of a nanofluid past a stretching sheet.* International Journal of Heat and Mass Transfer *53* (2010), Nos. 11–12, 2477–2483.

[16] O. D. Makinde, A. Aziz: *Boundary layer flow of a nanofluid past a stretching sheet with a convective boundary condition.* International Journal of Thermal Sciences *50* (2011), No. 7, 1326–1332.

[17] R. Kandasamy, P. Loganathan, P. Puvi Arasu: *Scaling group transformation for MHD boundary-layer flow of a nanofluid past a vertical stretching surface in the presence of suction/injection.* Nuclear Engineering and Design *241* (2011), No. 6, 2053–2059.

[18] M. Mustafa, T. Hayat, I. Pop, S. Asghar, S. Obaidat: *Stagnation-point flow of a nanofluid towards a stretching sheet.* International Journal of Heat and Mass Transfer *54* (2011), Nos. 25–26, 5588–5594.

[19] P. Rana, R. Bhargava: *Flow and heat transfer of a nanofluid over a nonlinearly stretching sheet: A numerical study.* Communications in Nonlinear Science and Numerical Simulation *17* (2012), No. 1, 212–226.

[20] F. M. Hady, F. S. Ibrahim, S. M. Abdel-Gaied, M. R. Eid: *Radiation effect on viscous flow of a nanofluid and heat transfer over a nonlinearly stretching sheet.* Nanoscale Research Letters *7* (2012), No. 1, Article 229.

[21] O. D. Makinde, W. A. Khan, Z. H. Khan: *Buoyancy effects on MHD stagnation point flow and heat transfer of a nanofluid past a convectively heated stretching/shrinking sheet.* International Journal of Heat and Mass Transfer *62* (2013), 526–533.

[22] N. Bachok, A. Ishak, I. Pop: *Unsteady boundary-layer flow and heat transfer of a nanofluid over a permeable stretching/shrinking sheet.* International Journal of Heat and Mass Transfer *55* (2012), Nos. 7–8, 2102–2109.

[23] S. Nadeem, C. Lee: *Boundary layer flow of nanofluid over an exponentially stretching surface.* Nanoscale Research Letters *7* (2012), No. 1, Article 94, 1–15.

[24] K. Bhattacharyya, G. C. Layek: *Magnetohydrodynamic boundary layer flow of nanofluid over an exponentially stretching permeable sheet.* Physics Research International *2014* (2014), Article ID 592536.

[25] S. K. Nandy, T. R. Mahapatra: *Effects of slip and heat generation/absorption on MHD stagnation flow of nanofluid past a stretching/shrinking surface with convective boundary conditions.* International Journal of Heat and Mass Transfer *64* (2013), 1091–1100.

[26] M. Majumder, N. Chopra, R. Andrews, B. J. Hinds: *Nanoscale hydrodynamics: Enhanced flow in carbon nanotubes.* Nature *438* (2005), No. 3, 44–44.

[27] C. Y. Wang: *Flow due to a stretching boundary with partial slip—an exact solution of the Navier–Stokes equations.* Chemical Engineering Science *57* (2002), No. 17, 3745–3747.

[28] A. Noghrehabadi, R. Pourrajab, M. Ghalambaz: *Effect of partial slip boundary condition on the flow and heat transfer of nanofluids past stretching sheet prescribed constant wall temperature.* International Journal of Thermal Sciences *54* (2012), 253–261.

[29] S. Mukhopadhyay: *Slip effects on MHD boundary layer flow over an exponentially stretching sheet with suction/blowing and thermal radiation.* Ain Shams Engineering Journal *4* (2013), No. 3, 485–491.

[30] B. Sahoo, S. Poncet: *Flow and heat transfer of a third grade fluid past an exponentially stretching sheet with partial slip boundary condition.* International Journal of Heat and Mass Transfer *54* (2011), Nos. 23–24, 5010–5019.

[31] E. H. Hafidzuddin, R. Nazar, NN. M. Arifin, I. Pop: *Numerical solutions of boundary layer flow over an exponentially stretching/shrinking sheet with generalized slip velocity.* International Journal of Mathematical and Computational Sciences *9* (2015), No. 4, 233–238.

Received April 23, 2018

Acta Technica *63* No. 6/2018, 795–808

Effect of radiation on heat and mass transfer in fluid flow in the presence of inclined magnetic field through a vertical channel[1]

Khushbu Bhaskar[1], Kalpna Sharma[1]

Abstract. The objective of this paper is to examine effects of radiation on unsteady magnetohydrodynamic fluid flow through a vertical channel filled with porous medium. Influence of radiation is also studied on heat and mass transfer in the presence of heat generation/absorption. Governing equations are solved by using the perturbation method. Velocity and temperature field profiles are obtained for various dimensionless parameters such as Grashoff number, modified Grashoff number, radiation parameter, porosity parameter, Prandtl number, Schmidt number, magnetic parameter and heat generation/absorption coefficient. Effects of various dimensionless parameters are also discussed for shear stress and Nusselt number.

Key words. Magnetohydrodynamic, porous medium, heat generation/absorption parameter, Couette flow, shearing stress and Nusselt number.

1. Introduction

Study of fluid flow with heat and mass transfer through a channel partially filled with porous medium has become more important in recent years because of its varied applications in engineering, agriculture, petroleum industries, biological sciences, physical chemistry, plasma physics, metrology, oceanography and scores of other disciplines. Radiative free convection MHD Couette flows are used in many environmental and scientific processes, such as thermal insulation, astrophysical flows, solar power technology and heating or cooling of chambers.

Singh [1] investigated natural convection in unsteady Couette motion. Jha, Prasad and Rai [2] studied mass transfer effects on the flow past an exponentially accelerated vertical plate with constant heat flux.

Transient MHD free convection flow of an incompressible viscous dissipative fluid is discussed by Sreekanth, Nagarajan and Ramana [3]. Effect of mass transfer on free

[1]Department of Mathematics, Manipal University Jaipur, Jaipur-303007, Rajasthan, India

convection in MHD flow of a viscous fluid is explained by Singh [4]. MHD steady flow in a channel with slip at the permeable boundaries is presented by Makinde and Osalusi [5]. Radiation and mass transfer effects on an unsteady MHD free convection flow past a heated vertical plate in a porous medium with various dissipation is described by Prasad and Reddy [6]. Thermal radiation effect on a transient MHD flow with mass transfer past an impulsively fixed infinite vertical plate is analyzed by Ahmed and Sarmah [7]. Unsteady MHD convective flow within a parallel plate rotating channel with thermal source/sink in a porous medium under slip boundary conditions is derived by Seth, Nandkeolyar and Ansari [8]. Unsteady hydrodynamic Couette flow within a porous channel is explained by Seth, Ansari and Nandkeolyar [9]. Transient convection fluid flow with heat and mass flux in a fixed vertical plate with radiation is obtained by Uwanta, Sani and Ibrahim [10]. Radiation and mass transfer effects on transient free convection flow of a dissipative fluid past semi-infinite vertical plate with uniform heat and mass flux is considered by Vasu, Prasad and Reddy [11]. Heat source and mass transfer effects on MHD flow of an elasto-viscous fluid through a porous medium is investigated by Rajesh [12]. Radiation effects on MHD flow past an impulsively started vertical plate with variable heat and mass transfer is presented by Rajput and Kumar [13]. Radiation effects on unsteady MHD free convective Couette flow of heat generation/absorbing fluid is obtained by Das, Guchhait and Jana [14]. Radiation effects on free convection MHD Couette flow started exponentially with variable wall temperature in presence of heat generation is discussed by Das, Sarkar and Jana [15]. Heat and mass transfer flow past an infinite vertical plate with variable thermal conductivity is studied by Uwanta and Sani [16]. Effects of radiation and time dependent permeability on unsteady two-dimensional hydromagnetic free convective flow and heat transfer through porous medium bounded between parallel plates is derived by Sharma and Sharma [17]. Radiative and free convective effects on MHD flow through a porous medium with periodic wall temperature and heat generation or absorption is investigated by Sharma, Sharma and Mehta [18]. Effect of radiation on free convection heat and mass transfer flow through porous medium in a vertical channel with heat absorption/generation is derived by Mishra, Menon and Shanfari [19]. Unsteady MHD oscillatory free convective and chemical reactive fluid flow through porous medium between parallel plates with radiation and temperature gradient dependent heat source is studied by Sharma and Mehta [20]. Dar and Elangovan [21] studied the thermal diffusion, radiation and inclined magnetic field effects on oscillatory flow in an asymmetric channel in presence of heat source and chemical reaction. Sobamowo [22] investigated on the analysis of laminar flow of viscous fluid through a porous channel with suction/injection at slowly expending or contracting walls. Lavanya [23] provided the effect of radiation on free convection heat and mass transfer flow through porous medium in a vertical channel with heat absorption/generation and chemical reaction. Sasikumar, Gayathri and Govindarajan [24] also discussed heat and mass transfer effects on MHD oscillatory flow of a couple stress fluid in an asymmetric tapered channel. Kiruthika [25] showed heat source and chemical effects on MHD flow in the presence of Soret.

The aim of this paper is to analyze effect of radiation on MHD flow along with

heat and mass transfer through a vertical channel filled with porous medium with oscillatory wall temperature and heat generation/absorption.

2. Mathematical formulation

In Cartesian coordinate system $(x,\, y,\, z)$, consider an unsteady Couette flow of a viscous incompressible electrically conducting optically thin fluid bounded by two vertical parallel porous plates filled with porous medium. A uniform transverse magnetic field B_0 is applied perpendicularly to the plates. Let axis x^* is assumed to be in the direction of the flow and axis y^* is perpendicular to it. The temperature of both the walls is assumed high enough to induce radiative heat transfer. By using Boussinesq's approximation, the flow is described by following equations for electrically conductive optically thin fluid

$$\frac{\partial u^*}{\partial t^*} = \nu \frac{\partial^2 u^*}{\partial y^{*2}} + g\beta\left(T^* - T_0^*\right) + g\beta\left(C^* - C_0^*\right) - \frac{\nu}{K^*} u^* - \frac{\sigma}{\rho} B_0^2 u^*\,, \tag{1}$$

$$\rho c_{\mathrm{P}} \frac{\partial T^*}{\partial t^*} = \kappa \frac{\partial^2 T^*}{\partial y^{*2}} - \frac{\partial q}{\partial y^*} - Q_0\left(T^* - T_0^*\right)\,, \tag{2}$$

$$\frac{\partial C^*}{\partial t^*} = D \frac{\partial^2 C^*}{\partial y^{*2}}\,. \tag{3}$$

Here u^* is the axial velocity, t^* denotes the time, ν stands for the kinematic viscosity, g represents the acceleration due to gravity, β is the coefficient of thermal expansion, T^* denotes the fluid temperature, T_0^* represents the reference temperature of free stream, C^* is the concentration of the fluid, C_0^* denotes the concentration of the species at wall, K^* stands for the permeability of porous medium, σ represents the electric conductivity, ρ is the fluid density, c_{P} represents the specific heat at constant pressure, κ stands for the thermal conductivity, q is the radiative heat flux in the y^*-direction, Q_0 denotes the heat generation/absorption constant and D is the thermal diffusivity of fluid.

The boundary conditions are given as

$$y^* = 0: \quad u^*\left(y^*, t^*\right) = U_0\left(1 + \varepsilon \mathrm{e}^{\mathrm{i}\omega^* t^*}\right), \quad T^*\left(y^*, t^*\right) = T_1^* + \varepsilon\left(T_1^* - T_0^*\right)\mathrm{e}^{\mathrm{i}\omega^* t^*},$$

$$C^*\left(y^*, t^*\right) = C_1^*,$$

$$y^* = h: \quad u^*\left(y^*, t^*\right) = 0, \quad T^*\left(y^*, t^*\right) = T_1^*, \quad C^*\left(y^*, t^*\right) = C_0^*\,. \tag{4}$$

Following Cogley et al. [26] and assuming that the fluid is optically thin with relatively low density, then

$$\frac{\partial q}{\partial y^*} = 4\alpha^2\left(T^* - T_0^*\right) \tag{5}$$

Introducing the following non-dimensional variables

$$y^* = yh,\ t^* = \frac{h^2 t}{\nu},\ \omega^* = \frac{\nu\omega}{h^2},\ u^* = U_0 u,\ \theta = \frac{T^* - T_0^*}{T_1^* - T_0^*},\ C = \frac{C^* - C_0^*}{C_1^* - C_0^*},$$

$$\mathrm{Gr} = \frac{g\beta h^2 \left(T_1^* - T_0^*\right)}{\nu U_0},\ \mathrm{Gc} = \frac{g\beta h^2 \left(C_1^* - C_0^*\right)}{\nu U_0},\ K^2 = \frac{h^2}{K^*},\ \mathrm{Sc} = \frac{\nu}{D},$$

$$M^2 = \frac{\sigma B_0^2 h^2}{\rho\nu},\ R^2 = \frac{4\alpha^2 h^2}{\kappa},\ S = \frac{Q_0 h^2}{\kappa},\ \mathrm{Pr} = \frac{\rho\nu C_\mathrm{P}}{\kappa} \tag{6}$$

into equations (1) to (3) along with equation (5), we get

$$\frac{\partial u}{\partial t} = \frac{\partial^2 u}{\partial y^2} + \mathrm{Gr}\theta + \mathrm{Gc}C - \left(K^2 + M^2\right) u\,, \tag{7}$$

$$\mathrm{Pr}\,\frac{\partial \theta}{\partial t} = \frac{\partial^2 \theta}{\partial y^2} - \left(R^2 + S\right)\theta, \tag{8}$$

$$\mathrm{Sc}\frac{\partial C}{\partial t} = \frac{\partial^2 C}{\partial y^2}\,, \tag{9}$$

where y is the dimensionless coordinate axis normal to the plates, t denotes the dimensionless time, u stands for the dimensionless velocity, θ represents the dimensionless temperature, C is the dimensionless concentration, Gr denotes the thermal Grashoff number, Gc represents the modified Grashoff number, K stands for the porosity parameter, Sc is the Schmidt number, M denotes the magnetic parameter, R represents the radiation parameter, S stands for the heat generation/absorption parameter, Pr is Prandtl number and α denotes the mean radiation absorption coefficient.

The corresponding boundary conditions for the above set of equations in non-dimensional form read

$$y = 0: \quad u\left(y,t\right) = 1 + \varepsilon \mathrm{e}^{\mathrm{i}\omega t},\ \theta\left(y,t\right) = 1 + \varepsilon \mathrm{e}^{\mathrm{i}\omega t}, C\left(y,t\right) = 1;$$

$$y = 1: \quad u\left(y,t\right) = 0,\ \theta\left(y,t\right) = 1,\ C\left(y,t\right) = 0. \tag{10}$$

3. Method of solution

Equations (7), (8) and (9) are coupled second-order partial differential equations. The velocity, temperature and mass distributions are separated into steady and unsteady parts with the help of expansion given below

$$u\left(y,t\right) = u_0\left(y\right) + \varepsilon u_1 \mathrm{e}^{\mathrm{i}\omega t} + o\left(\varepsilon^2\right)\,,$$

$$\theta\left(y,t\right) = \theta_0\left(y\right) + \varepsilon \theta_1 \mathrm{e}^{\mathrm{i}\omega t} + o\left(\varepsilon^2\right)\,,$$

$$C(y,t) = C_0(y) + \varepsilon C_1 \mathrm{e}^{\mathrm{i}\omega t} + o\left(\varepsilon^2\right) . \tag{11}$$

Substituting equations given by (11) into (7) to (9) and neglecting the coefficients of $o\left(\varepsilon^2\right)$, we obtain the following system

$$\frac{\mathrm{d}^2 u_0}{\mathrm{d}y^2} - \left(K^2 + M^2\right) u_0 = -\mathrm{Gr}\theta_0 - \mathrm{Gc}C_0 , \tag{12}$$

$$\frac{\mathrm{d}^2 u_1}{\mathrm{d}y^2} - \left(K^2 + M^2 + \mathrm{i}\omega\right) u_1 = -Gr\theta_1 - \mathrm{Gc}C_1 , \tag{13}$$

$$\frac{\mathrm{d}^2 \theta_0}{\mathrm{d}y^2} - \left(R^2 + S\right)\theta_0 = 0 , \tag{14}$$

$$\frac{\mathrm{d}^2 \theta_1}{\mathrm{d}y^2} - \left(R^2 + S + \mathrm{i}\omega\,\mathrm{Pr}\right)\theta_1 = 0 , \tag{15}$$

$$\frac{\mathrm{d}^2 C_0}{\mathrm{d}y^2} = 0 , \tag{16}$$

$$\frac{\mathrm{d}^2 C_1}{\mathrm{d}y^2} - \mathrm{i}\omega \mathrm{Sc} C_1 = 0 . \tag{17}$$

The corresponding boundary conditions are reduced to

$$\begin{aligned} y = 0: &\quad u_0 = 1,\ u_1 = 1,\ \theta_0 = 1,\ \theta_1 = 1,\ C_0 = 1,\ C_1 = 0 , \\ y = 1: &\quad u_0 = 0,\ u_1 = 0,\ \theta_0 = 1,\ \theta_1 = 0,\ C_0 = 0,\ C_1 = 0 . \end{aligned} \tag{18}$$

Equations (12) to (17) are ordinary second-order coupled differential equations. They can be solved using an analytical method with the help of the boundary conditions stated in (18). The solutions of $u_0(y), u_1(y), \theta_0(y), \theta_1(y), C_0(y)$ and $C_1(y)$ are obtained as follows:

$$u_0(y) = A_8 \mathrm{e}^{m_3 y} + A_9 \mathrm{e}^{m_4 y} - A_5 \mathrm{e}^{m_1 y} - A_6 \mathrm{e}^{m_2 y} + A_7 (1 - y) ,$$

$$u_1(y) = A_{12} \mathrm{e}^{(B_3 + \mathrm{i}B_4)y} + A_{13} \mathrm{e}^{-(B_3 + \mathrm{i}B_4)y} + A_{10} \mathrm{e}^{(B_1 + \mathrm{i}B_2)y} + A_{11} \mathrm{e}^{-(B_1 + \mathrm{i}B_2)y} ,$$

$$\theta_0(y) = A_1 \mathrm{e}^{m_1 y} + A_2 \mathrm{e}^{m_2 y} ,$$

$$\theta_1(y) = A_3 \mathrm{e}^{(B_1 + \mathrm{i}B_2)y} + A_4 \mathrm{e}^{-(B_1 + \mathrm{i}B_2)y} ,$$

$$C(y) = 1 - y .$$

Finally, the expression of $u(y,t), \theta(y,t)$ and $C(y,t)$ are given as below

$$u(y,t) = A_8 \mathrm{e}^{m_3 y} + A_9 \mathrm{e}^{m_4 y} - A_5 \mathrm{e}^{m_1 y} - A_6 \mathrm{e}^{m_2 y} + A_7 (1-y)$$

$$+ \varepsilon \mathrm{e}^{\mathrm{i}\omega t} \left(A_{12} \mathrm{e}^{(B_3 + \mathrm{i}B_4)y} + A_{13} \mathrm{e}^{-(B_3 + \mathrm{i}B_4)y} + A_{10} \mathrm{e}^{(B_1 + \mathrm{i}B_2)y} + A_{11} \mathrm{e}^{-(B_1 + iB_2)y} \right) , \tag{19}$$

$$\theta(y,t) = A_1 \mathrm{e}^{m_1 y} + A_2 \mathrm{e}^{m_2 y} + \varepsilon \mathrm{e}^{i\omega t} \left(A_3 \mathrm{e}^{(B_1 + \mathrm{i}B_2)y} + A_4 \mathrm{e}^{-(B_1 + \mathrm{i}B_2)y} \right) , \tag{20}$$

$$C(y) = 1 - y \, . \tag{21}$$

The expressions of shear stress τ and Nusselt number Nu on the lower wall are given by:

Shear stress

$$\tau = \left(\frac{\partial u}{\partial y} \right)_{y=0} = (m_3 A_8 + m_4 A_9 - m_1 A_5 - m_2 A_6 - A_7)$$

$$+ \varepsilon \mathrm{e}^{\mathrm{i}\omega t} \left((B_3 + \mathrm{i}B_4)(A_{12} - A_{13}) + (B_1 + \mathrm{i}B_2)(A_{10} - A_{11}) \right) . \tag{22}$$

and Nusselt number

$$\mathrm{Nu} = - \left(\frac{\partial \theta}{\partial y} \right)_{y=0} = (m_1 A_1 + m_2 A_2) + \varepsilon \mathrm{e}^{\mathrm{i}\omega t} \left((B_1 + \mathrm{i}B_2)(A_3 - A_4) \right) . \tag{23}$$

4. Results and discussion

To study the effect of non-dimensional parameters such as Grashoff number, Prandtl number, magnetic parameter, radiation parameter, porosity parameter and heat generation/absorption parameter on fluid velocity and temperature, shearing stress and Nusselt number at the walls are discussed numerically.

Figures 1–5 show the influence of different values of Grashoff number Gr, porosity parameter K, magnetic parameter M, radiation parameter R and heat generation or absorption parameter S on velocity. In Fig. 1, it is observed that by increasing the value of the Grashoff number, the fluid velocity also increases. It is due to the fact that an increasing value of in Grashoff number gives rise to buoyancy force which increases the fluid velocity. Figure 2 shows that the velocity increases with decrease in porosity parameter. Porosity is a ratio of void volume to the total volume and represents a measure of the void spaces in a porous medium. Figure 3 displays the result of velocity profile for different values of magnetic field parameter. It shows that the velocity increases with decrease in magnetic parameter because magnetic force generates a resistance force called the Lorentz force which acts in the opposite direction of flow; that is why the velocity decreases. It is observed from Fig. 4 that the velocity increases with the decrease in radiation parameter. Figure 5 depicts the effects of heat generation/absorption parameter on velocity. By increasing the value of heat generation parameter the velocity slows down.

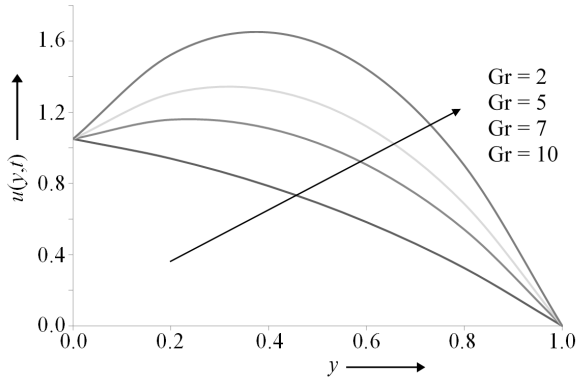

Fig. 1. Velocity profiles for various values of Gr for $K = 0.3$, $M = 1$, $R = 0.5$, $S = 0$, Pr=0.7, Gc $= 0.1$, $\omega = 0.5$, and $\varepsilon = 0.1$

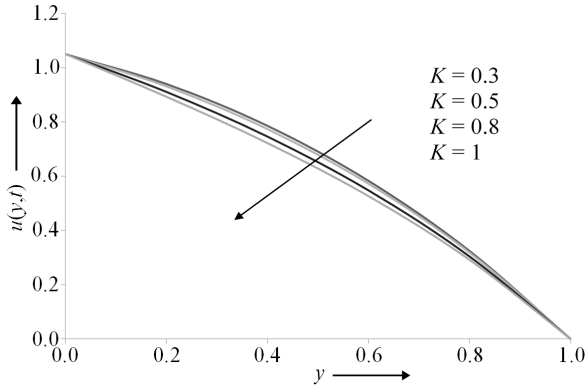

Fig. 2. Velocity profiles for various values of K for Gr $= 2$, $M = 1$, $R = 0.5$, $S = 0$, Pr=0.7, Gc $= 0.1$, $\omega = 0.5$, and $\varepsilon = 0.1$

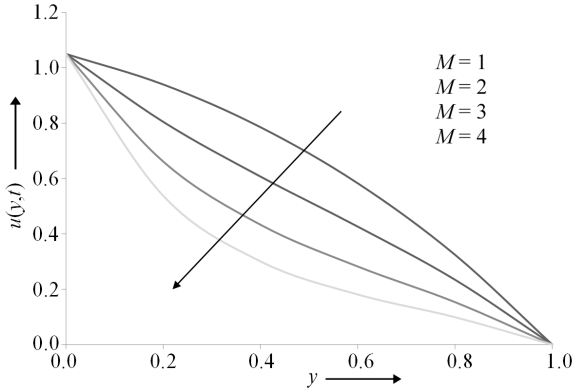

Fig. 3. Velocity profiles for various values of M for Gr $= 2$, $K = 0.3$, $R = 0.5$, $S = 0$, Pr=0.7, Gc $= 0.1$, $\omega = 0.5$, and $\varepsilon = 0.1$

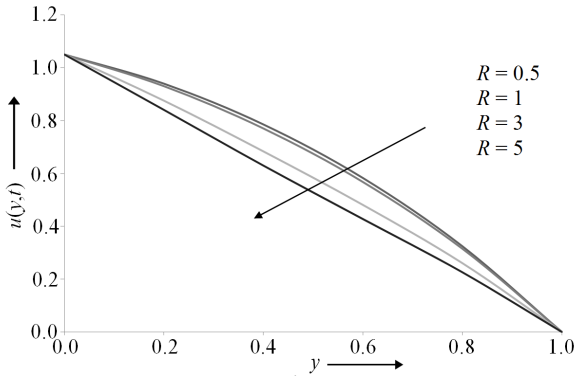

Fig. 4. Velocity profiles for various values of R for Gr $= 2$, $K = 0.3$, $M = 1$, $S = 0$, Pr=0.7, Gc $= 0.1$, $\omega = 0.5$, and $\varepsilon = 0.1$

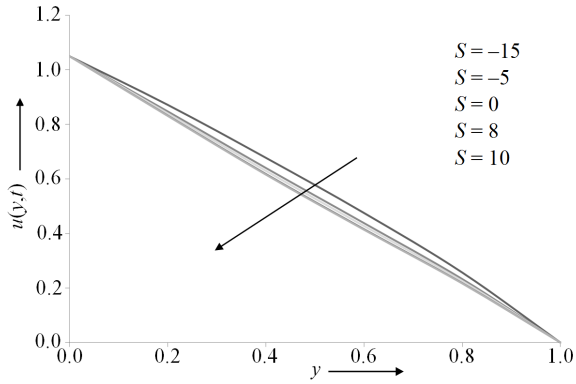

Fig. 5. Velocity profiles for various values of S for Gr $= 2$, $K = 0.3$, $M = 1$, $R = 0.5$, Pr=0.7, Gc $= 0.1$, $\omega = 0.5$, and $\varepsilon = 0.1$

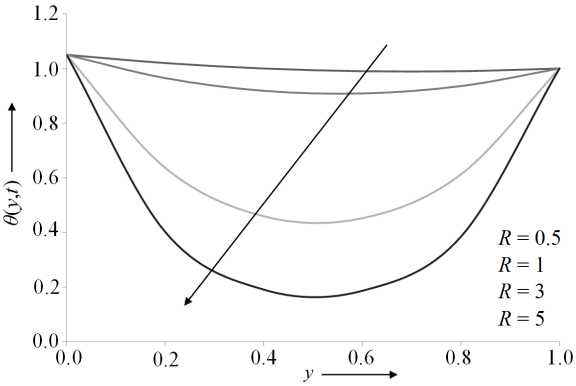

Fig. 6. Temperature profiles for various values of R for Gr $= 2$, $K = 0.3$, $M = 1$, $S = 0$, Pr=0.7, Gc $= 0.1$, $\omega = 0.5$, and $\varepsilon = 0.1$

Figures 6–8 present the effects of radiation parameter, heat generation/absorption parameter and Prandtl number on temperature. Figure 6 reveals that the temperature decreases with an increase in radiation parameter. The increase in radiation parameter means heat energy release from the fluid region and so the fluid temperature significantly decreases. Figure 7 represents that decrease of the value of heat generation parameter, the fluid temperature increases. Figure 8 shows the effect of Prandtl number on temperature. Increase in the Prandtl number causes temperature decrease. Numerical values of shear stress at the wall for different values of non-dimensional parameters are listed in Table 1.

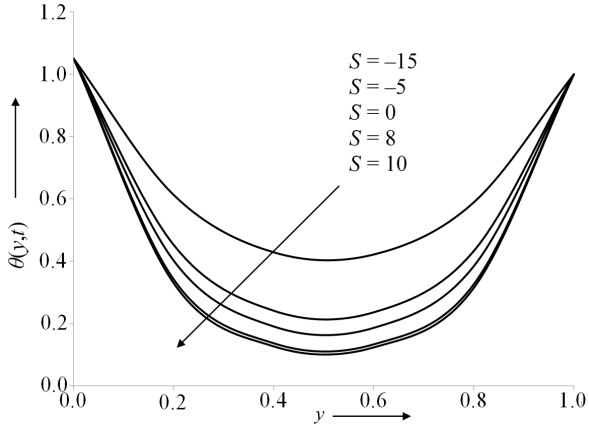

Fig. 7. Temperature profiles for various values of S for Gr $= 2$, $K = 0.3$, $M = 1$, $R = 0.5$, Pr=0.7, Gc $= 0.1$, $\omega = 0.5$, and $\varepsilon = 0.1$

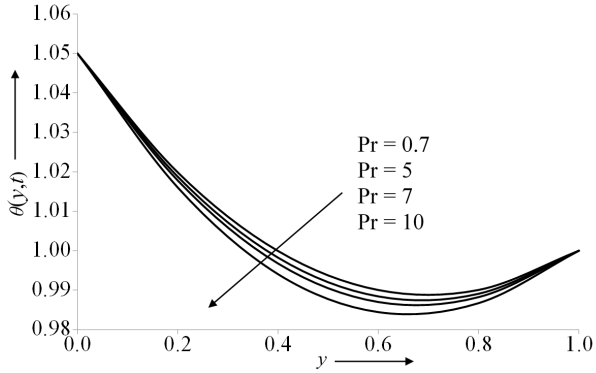

Fig. 8. Temperature profiles for various values of Pr for Gr $= 2$, $K = 0.3$, $M = 1$, $R = 0.5$, $S = 0$, Gc $= 0.1$, $\omega = 0.5$, and $\varepsilon = 0.1$

It is observed from Table 1 that the shear stress at the wall increases as the value of the Grashoff number increases, and it decreases due to increase on the value of porosity parameter, magnetic parameter, radiation parameter, heat generation/absorption parameter or Prandtl number. The Nusselt numbers for different

values of R, S and Pr when $M = 1$, Gr $= 2$, $K = 0.3$ and Gc $= 0.1$ are given in Table 2.

Table 1. Numerical values of shear stress τ at the wall for different values of non-dimensional parameters

Gr	K	M	R	S	Pr	τ
2	0.3	1	0.5	0	0.7	–0.445130371
5	0.3	1	0.5	0	0.7	0.950336819
7	0.3	1	0.5	0	0.7	1.880648278
10	0.3	1	0.5	0	0.7	3.276115468
2	0.5	1	0.5	0	0.7	–0.504648671
2	0.8	1	0.5	0	0.7	–0.64494951
2	1	1	0.5	0	0.7	–0.768882128
2	0.3	2	0.5	0	0.7	–1.402906557
2	0.3	3	0.5	0	0.7	–2.546071827
2	0.3	4	0.5	0	0.7	–3.704372298
2	0.3	1	1	0	0.7	–0.496474343
2	0.3	1	3	0	0.7	–0.794219137
2	0.3	1	5	0	0.7	–0.989361108
2	0.3	1	0.5	0	5	–0.446316166
2	0.3	1	0.5	0	7	–0.447275959
2	0.3	1	0.5	0	10	–0.448980526
2	0.3	1	0.5	0	0.7	–0.476268241
2	0.3	1	5	-15	0.7	–0.81502497
2	0.3	1	5	-5	0.7	–0.949498558
2	0.3	1	5	0	0.7	–0.9893611077
2	0.3	1	5	8	0.7	–1.035257518
2	0.3	1	5	10	0.7	–1.0444144365

Table 2. Nusselt numbers for different values of R, S and Pr when $M = 1$, Gr $= 2$, $K = 0.3$ and Gc $= 0.1$

R	S	Pr	Nu
0.5	0	0.7	0.176684882
1	0	0.7	0.527872688
3	0	0.7	2.866214462
0.5	0	5	0.182686369
0.5	0	10	0.197749403
5	–15	0.7	3.064138927
5	–5	0.7	4.594793963
5	8	0.7	5.995151235

It can be seen from Table 2 that the Nusselt number at the wall increases with increase in radiation parameter, heat generation parameter and Prandtl number when the other parameters are kept fixed.

5. Conclusion

In this paper, we have intended the effect of radiation and heat source on a viscous, incompressible and electrically conducting optically thin fluid bounded by two vertical plates filled with porous medium in the presence of transverse magnetic field. The nonlinear and coupled governing equations are solved analytically by using regular perturbation method. From the present investigation, we sort the following conclusions-

1. Enhancement in the velocity of the fluid is observed due to increase in Grashoff number.

2. Decline in the fluid velocity is deduced due to increase in porosity parameter or magnetic parameter.

3. Fluid velocity and temperature both show the same behavior i.e. decline for increment in radiation parameter or heat generation/absorption parameter.

4. Fluid temperature decreases due to increase in Prandtl number.

5. The shearing stress at the wall increases due to increase in Grashoff number and indicate the opposite behavior due to increase in porosity parameter, radiation parameter, magnetic parameter or heat generation/absorption parameter.

6. An increase in radiation parameter, heat generation/absorption parameter or Prandtl number decline is observed in Nusselt number at the wall.

References

[1] A. K. Singh: *Natural convection in unsteady Couette motion.* Defence Science Journal *38* (1988), No. 1, 35–41.

[2] B. K. Jha, R. Prasad, S. Rai: *Mass transfer effects on the flow past an exponentially accelerated vertical plate with constant heat flux.* Astrophysics and Space Science *181* (1991), No. 1, 125–134.

[3] S. Sreekanth, A. S. Nagarajan, S. V. Ramana: *Transient MHD free convection flow of an incompressible viscous dissipative fluid.* Indian Journal of Pure and Applied Mathematics *32* (2001), No. 7, 1051–1058.

[4] A. K. Singh: *Effect of mass transfer on free convection in MHD flow of a viscous fluid.* Indian Journal of Pure & Applied Physics *41* (2003), No. 4, 262–274.

[5] O. D. Makinde, E. Osalusi: *MHD steady flow in a channel with slip at the permeable boundaries.* General Physics, Romanian Journal of Physics *51* (2006), Nos. 3–4, 319–328.

[6] V. R. Prasad, N. B. Reddy: *Radiation and mass transfer effects on an unsteady MHD free convection flow past a heated vertical plate in a porous medium with various dissipation.* Theoretical and Applied Mechanics *34* (2007), No. 2, 135–160.

[7] N. Ahmed, H. K. Sarmah: *Thermal radiation effect on a transient MHD flow with mass transfer past an impulsively fixed infinite vertical plate.* International Journal of Applied Mathematics and Mechanics *5* (2009), No. 5, 87–98.

[8] G. S. Seth, R. Nandkeolyar, Md. S. Ansari: *Unsteady MHD convective flow within a parallel plate rotating channel with thermal source/sink in a porous medium under slip boundary conditions.* International Journal of Engineering, Science and Technology *2* (2010), No. 11, 1–16.

[9] G. S. Seth, Md. S. Ansari, R. Nandkeolyar: *Unsteady hydrodynamic Couette flow within a porous channel.* Tamkang Journal of Science and Engineering *14* (2011), No. 1, 7–14.

[10] I. J. Uwanta, M. Sani, M. O. Ibrahim: *Transient convection fluid flow with heat and mass flux in a fixed vertical plate with radiation.* International Journal of Computer Applications *36* (2011), No. 2, 33–40.

[11] B. Vasu, V. R. Prasad, N. B. Reddy: *Radiation and mass transfer effects on transient free convection flow of a dissipative fluid past semi-infinite vertical plate with uniform heat and mass flux.* Journal of Applied Fluid Mechanics *4* (2011), No. 1, 15–26.

[12] V. Rajesh: *Heat source and mass transfer effects on MHD flow of an elasto-viscous fluid through a porous medium.* Annals of the Faculty of Engineering Hunedoara-International Journal of Engineering *9* (2011), No. 2, 205–212.

[13] U. S. Rajput, S. Kumar: *Radiation effects on MHD flow past an impulsively started vertical plate with variable heat and mass transfer.* International Journal of Applied Mathematics and Mechanics *8* (2012), No. 1, 66–85.

[14] S. Das, S. K. Guchhait, R. N. Jana: *Radiation effects on unsteady MHD free convective Couette flow of heat generation/absorbing fluid.* International Journal of Computer Applications *39* (2012), No. 3, 42–51.

[15] S. Das, B. C. Sarkar, R. N. Jana: *Radiation effects on free convection MHD Couette flow started exponentially with variable wall temperature in presence of heat generation.* Open Journal of Fluid Dynamics *2* (2012), No. 1, 14–27.

[16] I. J. Uwanta, M. Sani: *Heat and mass transfer flow past an infinite vertical plate with variable thermal conductivity.* International Journal of Applied Information Systems *6* (2013), No. 1, 16–24.

[17] P. R. Sharma, P. Sharma: *Effects of radiation and time dependent permeability on unsteady two-dimensional hydromagnetic free convective flow and heat transfer through porous medium bounded between parallel plates.* Journal of International Academy Of Physical Sciences *17* (2013), No. 1, 27–38.

[18] P. R. Sharma, K. Sharma, T. Mehta: *Radiative and free convective effects on MHD flow through a porous medium with periodic wall temperature and heat generation or absorption.* International Journal of Mathematical Archive *5* (2014), No. 9, 119–128.

[19] A. K. Mishra, R. K. Menon, S. A. A. A. Shanfari: *Effect of radiation on free convection heat and mass transfer flow through porous medium in a vertical channel with heat absorption/generation.* International Journal of Advanced Research in Computer Engineering & Technology *4* (2015), No. 7, 3254–3262.

[20] P. R. Sharma, T. Mehta: *Unsteady MHD oscillatory free convective and chemical reactive fluid flow through porous medium between parallel plates with radiation and temperature gradient dependent heat source.* IOSR Journal of Mathematics *11* (2015), No. 1, 66–82.

[21] A. A. Dar, K. Elangovan: *Thermal diffusion, radiation and inclined magnetic field effects on oscillatory flow in an asymmetric channel in presence of heat source and chemical reaction.* Journal of the Nigerian Mathematical Society *35* (2016), 488–509.

[22] M. G. Sobamowo: *On the analysis of laminar flow of viscous fluid through a porous channel with suction/injection at slowly expanding or contracting walls.* Journal of Computational Applied Mechanics *48* (2017), No. 2, 319–330.

[23] B. Lavanya: *Effect of radiation on free convection heat and mass transfer flow through porous medium in a vertical channel with heat absorption/generation and chemical reaction.* AIP Conference Proceedings *1859* (2017), No. 1.

[24] J. Sasikumar, R. Gayathri, A. Govindarajan: *Heat and mass transfer effects on MHD oscillatory flow of a couple stress fluid in an asymmetric tapered channel.* IOP Conference Series: Materials Science and Engineering *402* (2018), No. 1.

[25] R. Kiruthika: *Heat source and chemical effects on MHD flow in the presence of Soret*. International Research Journal of Engineering and Technology *5* (2013), No. 9, 229–237.

[26] A. C. Cogley, W. G. Vincenti, S. E. Gill: *Differential approximation for relative transfer in a non-gray gas near equilibrium*. The American Institute of Aeronautics and Astronautics Journal *6* (1968), No. 3, 551–553.

Received June 12, 2018

Acta Technica *63* No. 6/2018, 809–828

Radiation absorption, heat generation and chemical reaction effects on MHD heat and mass transfer flow past a vertical porous plate in the presence of slip

Ruchika Mehta[1], Tripti Mehta[2]

Abstract. The present study describes the effect of Heat and Mass transfer on unsteady MHD flow of an electrically conducting, incompressible, heat generating / absorbing fluid in the presence of pressure gradient, thermal radiation and chemical reaction along a semi-infinite moving porous plate in a porous medium. The permeable plate is assumed to move with a constant velocity in the flow direction in the presence of transverse magnetic field and surrounded by a uniform porous medium. The governing system of partial differential equations is transformed to dimensionless equations using dimensionless variables. The dimensionless equations are then solved analytically using regular perturbation technique. The expressions for the velocity, temperature distribution, concentration, Skin-friction, Nusselt number and Sherwood number are derived, discussed numerically and shown through graphs.

Key words. Incompressible flow, electrically conducting, heat generation/absorption, thermal radiation, chemical reaction, porous, concentration, skin-friction, Nusselt number, Sherwood number.

1. Introduction

The study of magneto hydrodynamic flows have stimulated considerable interest due to its applications in cosmic fluid dynamics, aerodynamics, metrology, solar physics, MHD generators, plasma studies, geothermal energy extraction etc. In the past few years, several simple flow problems associated with classical hydrodynamics have received attention within the more general context of magneto hydrodynamics.

[1]Department of Mathematics & Statistics, Manipal University Jaipur-303007 (Raj.), India; e-mail: ruchika.mehta1981@gmail.com

[2]S. S. Jain Subodh P. G. College, Jaipur-302004 (Raj.), India; e-mail: m.tripti24@gmail.com

Heat losses from hot pipes, ovens etc. surrounded by cooled air, are at least in part, due to free convection.

The study of the effect of chemical reaction on heat and mass transfer in a flow is of great practical importance to the engineers and scientists because of its universal occurrence of many branches of science and technology. Chemical reactions are characterized by chemical changes that are involved in rearrangement of molecular structure of fluids. Therefore, investigation of heat and mass transfer in the presence of chemical reaction is of keen interest for research community due to their various prospective engineering applications which include underground disposal of radioactive waste materials, nuclear fuel debris and storage of food stuffs etc. In addition, chemical reactions play a significant role in many chemical engineering processes, namely manufacturing of ceramics or glassware, polymer production, food processing, etc. The phenomenon of chemical reaction occurs due to the physical interaction of foreign mass and working fluid. Thus, the order analysis of chemical reaction in various physical processes is of superb eminence. Radiation is a process of heat transfer through electromagnetic waves. Radiative and convective flows are encountered in countless industrial and environmental process. Radiative heat and mass transfer play an important role in space related technology. Many investigators have studied the effect of radiation and chemical reactions in different convective heat and mass transfer flows.

In recent years, free convective flow and heat transfer problems in the presence of magnetic field, chemical reactions and radiation absorption through a porous medium have attracted the attention of a number of scholars because of their possible application in many branches of science and technology. The phenomena of heat and mass transfer are also very common in theory of stellar structure and observable effects are detectable on the solar structure. Analytical solutions of the problem of convective flows, which arise in the fluids due to interaction of the force of gravity and density differences caused by simultaneous diffusion of thermal energy and chemical species, have been presented by many authors due to application of such problems in Geophysics and Engineering including Ahmed et al. [1] discussed MHD free convective Poiseuille flow and mass transfer through a porous medium bounded by two infinite vertical porous plates. Singh et al. [2] described effect of volumetric heat generation/absorption on mixed convection stagnation point flow on an isothermal vertical plate in porous media. Srinivas and Muthuraj [3] presented MHD flow with slip effects and temperature dependent heat source in a vertical wavy porous space. Babu and Reddy [4] investigated Mass transfer effects on MHD mixed convective flow from a vertical surface with ohmic heating and viscous dissipation. Chamkha and Ahmed [5] discussed similarity solution for unsteady MHD flow near a stagnation point of a three dimensional porous body with heat and mass transfer, heat generation/absorption and chemical reaction. Makinde [6] explained on MHD mixed convection with Soret and Dufour effects past a vertical plate embedded in a porous medium. Raju and Varma [7] investigated Unsteady MHD free convection oscillatory couette flow through a porous medium with periodic wall temperature. Muthucumaraswamy and Amutha [8] described Thermal diffusion effects on MHD flow past an oscillating vertical plate with chemical reaction of first order.

Pal and Talukdar [9] presented influence of fluctuating thermal and mass diffusion on unsteady MHD buoyancy-driven convection past a vertical surface with chemical reaction and Soret effects. Raju et al. [10] discussed Radiation and mass transfer effects on a free convection flow through a porous medium bounded by a vertical surface. Ravikumar et al. [11] described Heat and mass transfer effects on MHD flow of viscous fluid through non-homogeneous porous medium in presence of temperature dependent heat source. Sharma and Dadheech [12] explained effect of volumetric heat generation/absorption on convective heat and mass transfer in porous medium between two vertical porous plates. Satya Narayana and Sravanthi [13] investigated simultaneous effects of soret and ohmic heating on MHD free convective heat and mass transfer flow of micropolar fluid with porous medium.

Ibrahim Mohammed [14] presented effects of mass transfer, radiation, Joule heating and viscous dissipation on steady MHD marangoni convection flow over a flat surface with suction and injection. Ahmed and Batin [15] discussed magneto hydrodynamic heat and mass transfer flow with induced magnetic field and viscous dissipative effects. Sarma et al. [16] studied MHD free convection and mass transfer flow past an accelerated vertical plate with chemical reaction in presence of radiation. Arthur Maurice et al. [17] explained MHD convective boundary layer flow towards a vertical surface in a porous medium with radiation , chemical reaction and internal heat generation. Mohammed Ibrahim and Suneetha [18] analyzed Chemical reaction and Soret effects on unsteady MHD flow of a viscoelastic fluid past an impulsively stated infinite vertical plate with heat source/sink. Mahdy and Ahmed [19] considered Thermosolutal Marangoni boundary layer magnetohydrodynamic flow with the soret and dufour effects past a vertical flat plate. Ibrahim Mohammed and Suneetha [20] described heat source and chemical effects on MHD convection flow embedded in a porous medium with soret, viscous and Joules dissipation. Gurivireddy et al. [21] discussed thermal diffusion effect on MHD heat and mass transfer flow past a semi infinite moving vertical porous plate with heat generation and chemical reaction. Keeping in view the wide range of applications an attempt is made to analyze the unsteady MHD flow of an incompressible, electrically conducting, heat generating/absorbing fluid along a semi-infinite moving porous plate embedded in a porous medium with the presence of pressure gradient, thermal radiation and chemical reaction.

2. Mathematical analysis

Consider an unsteady two-dimensional flow of an incompressible electrically conducting and heat generating/absorbing fluid with mass transfer past a vertical porous plate embedded in a porous medium. A uniform magnetic field is applied in perpendicular direction of the plate. Let axis x^* be directed along the plate in upward direction and let axis y^* be normal to it. The induced magnetic field is assumed to be negligible compared to the applied magnetic field. Since the motion is two dimensional and length of plate is large, all the physical variables are independent of x^*. Due to the assumption of infinite plane surface, the flow variables are function of y^* and t^* only. The plate is subjected to a constant suction velocity v_0, which is

a non-zero positive constant.

On the above conditions and usual Boussinesq's approximation the governing equations of continuity, momentum, energy and mass for a flow of an electrically conducting fluid are given by the following equations:

Continuity equation:

$$\frac{\partial v^*}{\partial y^*} = 0 \Rightarrow v^* = -v_0, \quad v_0 > 0\,. \tag{1}$$

Momentum equation:

$$\frac{\partial u^*}{\partial t^*} + v^* \frac{\partial u^*}{\partial y^*} = -\frac{1}{\rho}\frac{\partial p}{\partial x} + \vartheta \frac{\partial^2 u^*}{\partial y^{*2}} + g\beta_{\mathrm{T}}^* \left(T^* - T_\infty\right) +$$

$$+ g\beta_{\mathrm{C}}^* \left(C^* - C_\infty\right) - \frac{\sigma}{\rho} B_0^2 u^* - \frac{\vartheta}{k^*} u^*\,. \tag{2}$$

Energy equation:

$$\frac{\partial T^*}{\partial t^*} + v^* \frac{\partial T^*}{\partial y^*} = \frac{k}{\rho C_{\mathrm{p}}} \frac{\partial^2 T^*}{\partial y^{*2}} - \frac{1}{\rho C_{\mathrm{p}}} \frac{\partial q_{\mathrm{r}}}{\partial y^*} + \frac{D_{\mathrm{m}} k_{\mathrm{T}}}{C_{\mathrm{s}} C_{\mathrm{p}}} \frac{\partial^2 C^*}{\partial y^{*2}} +$$

$$+ \frac{Q_{\mathrm{T}}}{\rho C_{\mathrm{p}}} \left(T^* - T_\infty\right) + \frac{Q_{\mathrm{c}}}{\rho C_{\mathrm{p}}} \left(C^* - C_\infty\right)\,. \tag{3}$$

Mass equation:

$$\frac{\partial C^*}{\partial t^*} + v^* \frac{\partial C^*}{\partial y^*} = D_{\mathrm{m}} \frac{\partial^2 C^*}{\partial y^{*2}} - k_1 \left(C^* - C_\infty\right)\,. \tag{4}$$

Here, u^*, v^* are the velocity components along the axes x^* and y^*, respectively, ϑ is the kinematic viscosity of the fluid, g is the acceleration due to gravity, β_{T}^* is the coefficient of thermal expansion, $\beta{*}_{\mathrm{C}}$ is the coefficient of mass expansion, T^* is the dimensional temperature of the fluid, T_∞ is the temperature far away from the plate, T_{w} is the temperature near the plate, C^* is the dimensional concentration of the fluid, C_∞ is the concentration far away from the plate, C_{w} is the concentration near the plate, σ is the electrical conductivity of the fluid, k^* is the permeability of porous medium, ρ is the fluid density, q_{r} is the radiative heat flux, k is the thermal conductivity of the medium, B_0 is the magnetic field coefficient, C_{p} is the specific heat of the fluid at a constant pressure, C_{s} is the concentration susceptibility, Q_{T} is the additional constant heat source/sink, Q_{c} is the radiation absorption rate constant, D_{m} is the molecular diffusivity, k_{T} is the thermo-diffusion ratio, and k_1 is the rate of chemical reaction.

Following the Rosseland approximation, the radiative heat flux q_{r} is modeled as

$$q_{\mathrm{r}} = \frac{4\sigma_{\mathrm{s}}}{3k_{\mathrm{e}}} \frac{\partial T^{*4}}{\partial y^*}\,, \tag{5}$$

where σ_{s} and k_{e} are the Stefan-Boltzmann constant and the mean absorption coefficient, respectively. By using the Rosseland approximation we restrict our analysis to optically thick fluids. By assuming that the difference in temperature within the flow is small such that T^{*4} can be expressed as a linear combination of the temperature, we expand T^{*4} in the Taylor series about T_{∞}^{*4} as follows:

$$T^{*4} = T_{\infty}^{*4} + 4T_{\infty}^{*3}\left(T^{*} - T_{\infty}^{*}\right) + 6T_{\infty}^{*2}\left(T^{*} - T_{\infty}^{*}\right)^{2} + \dots , \tag{6}$$

and neglecting higher order terms after the first degree in $(T^{*} - T_{\infty}^{*})$, we have

$$T^{*4} \approx -3T_{\infty}^{*4} + 4T_{\infty}^{*3}T^{*} . \tag{7}$$

Differentiating equation (5) with respect to y^{*} and using equation (7) we obtain

$$\frac{\partial q_{\mathrm{r}}}{\partial y^{*}} = -\frac{16T^{*4}}{\sigma_{\mathrm{s}}} 3k_{\mathrm{e}} \frac{\partial^{2} T^{*}}{\partial y^{*2}} . \tag{8}$$

The initial and boundary conditions for the velocity, temperature and concentration fields are

$$u^{*} = L^{*}\frac{\partial u^{*}}{\partial y^{*}},\ T^{*} = T_{\mathrm{w}} + \varepsilon\left(T_{\mathrm{w}} - T_{\infty}\right)\mathrm{e}^{n^{*}t^{*}},\ C^{*} = C_{\mathrm{w}} + \varepsilon\left(C_{\mathrm{w}} - C_{\infty}\right)\mathrm{e}^{n^{*}t^{*}}$$

at $y^{*} = 0$ and

$$u^{*} \to U_{\infty}^{*} = U_{0}\left(1 + \mathrm{e}^{n^{*}t^{*}}\right),\ T^{*} \to T_{\infty},\ C^{*} \to C_{\infty} . \tag{9}$$

at $y^{*} \to \infty$.

Outside the boundary layer, equation (2) gives

$$-\frac{1}{\rho}\frac{\partial p}{\partial x} = \frac{\mathrm{d}U_{\infty}^{*}}{\mathrm{d}t^{*}} + \frac{\vartheta}{k^{*}}U_{\infty}^{*} + \frac{\sigma}{\rho}B_{0}^{2}U_{\infty}^{*} . \tag{10}$$

Let us introduce the following non-dimensional variables

$$u = \frac{u^{*}}{v_{0}},\ v = \frac{v^{*}}{v_{0}},\ U_{\infty} = \frac{U_{\infty}^{*}}{v_{0}},\ y = \frac{v_{0}y^{*}}{\vartheta},\ t = \frac{v_{0}^{2}t^{*}}{\vartheta},\ n^{*} = \frac{nv_{0}^{2}}{\vartheta},\ \theta = \frac{T^{*} - T_{\infty}}{T_{\mathrm{w}} - T_{\infty}},$$

$$C = \frac{C^{*} - C_{\infty}}{C_{\mathrm{w}} - C_{\infty}},\ k = \frac{k^{*}v_{0}^{2}}{\vartheta^{2}},\ \mathrm{Sc} = \frac{\vartheta}{D},\ \mathrm{Kr} = \frac{k_{1}\vartheta}{v_{0}^{2}},\ \mathrm{Pr} = \frac{\rho\vartheta C_{\mathrm{p}}}{K} = \frac{\vartheta}{\alpha},$$

$$\mathrm{Gr} = \frac{\vartheta\beta_{\mathrm{T}}^{*}g(T_{\mathrm{w}} - T_{\infty})}{v_{0}^{3}},\ \mathrm{Gm} = \frac{\vartheta\beta_{\mathrm{c}}^{*}g(C_{\mathrm{w}} - C_{\infty})}{v_{0}^{3}},\ R = \frac{kk_{\mathrm{e}}}{4\sigma_{\mathrm{s}}T_{\infty}^{3}},\ M = \frac{\sigma\vartheta B_{0}^{2}}{\rho v_{0}^{2}},$$

$$\mathrm{Nm} = \frac{1}{k} + M,\ N_{\mathrm{r}} = \frac{16}{3}\frac{T_{\infty}^{*}\sigma^{*}}{kk^{*}},\ D_{\mathrm{u}} = \frac{D_{\mathrm{m}}k_{\mathrm{T}}}{C_{\mathrm{s}}C_{\mathrm{p}}\vartheta}\frac{C_{\mathrm{w}} - C_{\infty}}{T_{\mathrm{w}} - T_{\infty}},\ Q = \frac{Q_{\mathrm{T}}}{\rho C_{\mathrm{p}}}\frac{\vartheta}{v_{0}^{2}},$$

$$N = \frac{1 + N_{\mathrm{r}}}{\mathrm{Pr}},\ Q_{1} = \frac{Q_{\mathrm{C}}}{\rho C_{\mathrm{p}}}\frac{\vartheta}{v_{0}^{2}}\frac{C_{\mathrm{w}} - C_{\infty}}{T_{\mathrm{w}} - T_{\infty}},\ \lambda = \frac{L^{*}v_{0}}{\vartheta} , \tag{11}$$

where L^* is the characteristic dimension of the flow fluid, Sc is the Schmidt number, Kr is the chemical reaction parameter, Pr is the Prandtl number, Gr is the thermal Grashoff number, Gm is the mass Grashoff number, R is the radiation parameter, M is the magnetic parameter, k is the peremeability parameter, N_{r} is the thermal radiation parameter, D_{u} is the Dufour number, Q is the heat source/sink parameter, Q_1 is the radiation/absorption parameter and λ is the slip parameter.

Substituting equation (11) into equations (2)–(4) and (9) by using equations (1), (8) & (10) yields the following dimensionless equations:

$$\frac{\partial u}{\partial t} - \frac{\partial u}{\partial y} = \frac{\mathrm{d}U_\infty}{\mathrm{d}t} + \frac{\partial^2 u}{\partial y^2} + \mathrm{Gr}\theta + \mathrm{Gm}C + (U_\infty - u)\,\mathrm{Nm}\,, \tag{12}$$

$$\frac{\partial \theta}{\partial t} - \frac{\partial \theta}{\partial y} = N\frac{\partial^2 \theta}{\partial y^2} + D_{\mathrm{u}}\frac{\partial^2 C}{\partial y^2} + Q\theta + Q_1 C\,, \tag{13}$$

$$\frac{\partial C}{\partial t} - \frac{\partial C}{\partial y} = \frac{1}{\mathrm{Sc}}\frac{\partial^2 C}{\partial y^2} - \mathrm{Kr}C\,. \tag{14}$$

The corresponding boundary conditions are

$$u = \lambda\frac{\partial u}{\partial y},\ \theta = 1 + \varepsilon \mathrm{e}^{nt},\ C = 1 + \varepsilon \mathrm{e}^{nt} \text{ at } y = 0,$$

$$u \to U_\infty,\ \theta \to 0,\ C \to 0 \text{ as } y \to \infty\,. \tag{15}$$

3. Solution of the problem

The above system of partial differential equations cannot be solved in closed form. So it can be transformed to a system of ordinary differential equations in dimensionless form that can be solved analytically, for $\varepsilon \ll 1$. The expressions for the velocity, temperature and concentration represented by a regular perturbation technique are as follows:

$$u = U_0(y) + \varepsilon \mathrm{e}^{nt} U_1(y) + O\left(\varepsilon^2\right) + \dots\,, \tag{16}$$

$$\theta = \theta_0(y) + \varepsilon \mathrm{e}^{nt}\theta_1(y) + O\left(\varepsilon^2\right) + \dots\,, \tag{17}$$

$$C = C_0(y) + \varepsilon \mathrm{e}^{nt} C_1(y) + O\left(\varepsilon^2\right) + \dots\,, \tag{18}$$

$$U_\infty = 1 + \varepsilon \mathrm{e}^{nt} + \dots\,. \tag{19}$$

Substituting these equations (16) to (19) into equations (12) to (14) and equating the harmonic and non-harmonic terms, also neglecting the coefficient of ε^2, we get

the following pair of equations for $u_0,\ u_1,\ \theta_0,\ \theta_1,\ C_0$ and C_1.

$$\frac{\mathrm{d}^2u_0}{\mathrm{d}y^2} + \frac{\mathrm{d}u_0}{\mathrm{d}y} - \mathrm{Nm}u_0 = -\left(\mathrm{Gr}\theta_0 + \mathrm{Gm}C_0 + \mathrm{Nm}\right), \tag{20}$$

$$\frac{\mathrm{d}^2u_1}{\mathrm{d}y^2} + \frac{\mathrm{d}u_1}{\mathrm{d}y} - (\mathrm{Nm}+n)u_1 = -(n + \mathrm{Gr}\theta_1 + \mathrm{Gm}C_1 + \mathrm{Nm}), \tag{21}$$

$$N\frac{\mathrm{d}^2\theta_0}{\mathrm{d}y^2} + \frac{\mathrm{d}\theta_0}{\mathrm{d}y} + Q\theta_0 = D_\mathrm{u}\frac{\partial^2 C_0}{\partial y^2} - Q_1C_0, \tag{22}$$

$$N\frac{\mathrm{d}^2\theta_1}{\mathrm{d}y^2} + \frac{\mathrm{d}\theta_1}{\mathrm{d}y} + (Q-n)\theta_1 = D_\mathrm{u}\frac{\partial^2 C_1}{\partial y^2} - Q_1C_1, \tag{23}$$

$$\frac{1}{\mathrm{Sc}}\frac{\mathrm{d}^2C_0}{\mathrm{d}y^2} + \frac{\mathrm{d}C_0}{\mathrm{d}y} - \mathrm{Kr}C_0 = 0, \tag{24}$$

$$\frac{1}{\mathrm{Sc}}\frac{\mathrm{d}^2C_1}{\mathrm{d}y^2} + \frac{\mathrm{d}C_1}{\mathrm{d}y} - (\mathrm{Kr}+n)C_1 = 0. \tag{25}$$

The corresponding boundary conditions can be written as

$$u_0 = \frac{\lambda\,\mathrm{d}u_0}{\mathrm{d}y},\ u_1 = \frac{\lambda\,\mathrm{d}u_1}{\mathrm{d}y},\ \theta_0 = 1,\ \theta_1 = 1,\ C_0 = 1,\ C_1 = 1$$

at $y = 0$ and

$$u_0 = 1,\ u_1 = 1,\ \theta_0 = 0,\ \theta_1 = 0,\ C_0 = 0,\ C_1 = 0 \tag{26}$$

at $y \to \infty$.

The solutions of equations (20) to (25) with satisfying boundary conditions (26) are given as

$$u_0(y) = H_6\mathrm{e}^{-b_9y} + H_3\mathrm{e}^{-b_5y} + H_4\mathrm{e}^{-b_1y} + 1, \tag{27}$$

$$u_1(y) = H_{10}\mathrm{e}^{-b_{11}y} + H_7\mathrm{e}^{-b_7y} + H_8\mathrm{e}^{-b_3y} + 1, \tag{28}$$

$$\theta_0(y) = (1-H_1)\,\mathrm{e}^{-b_5y} + H_1\mathrm{e}^{-b_1y}, \tag{29}$$

$$\theta_1(y) = (1-H_2)\,\mathrm{e}^{-b_7y} + H_2\mathrm{e}^{-b_3y}, \tag{30}$$

$$C_0(y) = \mathrm{e}^{-b_1y}, \tag{31}$$

$$C_1(y) = \mathrm{e}^{-b_3y}. \tag{32}$$

Substituting equations (27) to (32) in equations (16) to (18), we obtain expres-

sions for the velocity, temperature and concentration as follows

$$u\,(y,t) = H_6\mathrm{e}^{-b_9 y} + H_3\mathrm{e}^{-b_5 y} + H_4\mathrm{e}^{-b_1 y} + 1 + \\ + \varepsilon\mathrm{e}^{nt}(H_{10}\mathrm{e}^{-b_{11} y} + H_7\mathrm{e}^{-b_7 y} + H_8\mathrm{e}^{-b_3 y} + 1)\,, \tag{33}$$

$$\theta\,(y,t) = (1-H_1)\,\mathrm{e}^{-b_5 y} + H_1\mathrm{e}^{-b_1 y} + \varepsilon\mathrm{e}^{nt}\left((1-H_2)\,\mathrm{e}^{-b_7 y} + H_2\mathrm{e}^{-b_3 y}\right)\,, \tag{34}$$

$$C\,(y,t) = \mathrm{e}^{-b_1 y} + \varepsilon\mathrm{e}^{nt}(\mathrm{e}^{-b_3 y})\,, \tag{35}$$

where

$$b_1 = \frac{\mathrm{Sc} + \sqrt{\mathrm{Sc}^2 + 4\mathrm{Kr}\cdot\mathrm{Sc}}}{2},\ b_2 = \frac{-\mathrm{Sc} + \sqrt{\mathrm{Sc}^2 + 4\mathrm{Kr}\cdot\mathrm{Sc}}}{2},$$

$$b_3 = \frac{\mathrm{Sc} + \sqrt{\mathrm{Sc}^2 + 4(n+\mathrm{Kr})}}{2},\ b_4 = \frac{-\mathrm{Sc} + \sqrt{\mathrm{Sc}^2 + 4(n+\mathrm{Kr})}}{2},$$

$$b_5 = \frac{1+\sqrt{1-4QN}}{2},\ b_6 = \frac{-1+\sqrt{1-4QN}}{2},\ b_7 = \frac{1+\sqrt{1-4N(-n+Q}}{2},$$

$$b_8 = \frac{-1+\sqrt{1-4N(-n+Q}}{2},\ b_9 = \frac{1+\sqrt{1+4\mathrm{Nm}}}{2},\ b_{10} = \frac{-1+\sqrt{1+4\mathrm{Nm}}}{2},$$

$$b_{11} = \frac{1+\sqrt{1+4(\mathrm{Nm}+n)}}{2},\ b_{12} = \frac{1-\sqrt{1+4(\mathrm{Nm}+n)}}{2},\ H_1 = \frac{-\mathrm{Du}b_1^2 - Q_1}{\mathrm{Nb}^2{}_1 - b_1 + Q}$$

$$H_2 = \frac{-\mathrm{Du}b_3^2 - Q_1}{(\mathrm{Nb}_2^2 - b_2 - n + Q)},\ H_3 = \frac{-\mathrm{Gr}(1-H_1)}{b_5^2 - b_5 - \mathrm{Nm}},$$

$$H_4 = \frac{-(\mathrm{Gr}H_1 + \mathrm{Gm})}{b_1^2 - b_1 - \mathrm{Nm}},\ H_5 = -\lambda H_3 b_5 - \lambda H_4 b_1 - H_3 - H_4 - 1\,,$$

$$H_6 = \frac{H_5}{1+\lambda b_9} = H_6,\ H_7 = \frac{-\mathrm{Gr}(1-H_2)}{b_7^2 - b_7 - (\mathrm{Nm}+n)},\ H_8 = \frac{-(\mathrm{Gr}H_2 + \mathrm{Gm})}{b_3^2 - b_3 - (\mathrm{Nm}+n)},$$

$$H_9 = -\lambda H_7 b_7 - \lambda H_8 b_3 - H_7 - H_8 - 1,\ H_{10} = \frac{H_9}{1+\lambda b_{11}} = H_{10}\,.$$

The skin friction coefficient, Nusselt number and Sherwood number are important physical quantities of engineering interest.

3.1. Skin-friction

For the velocity field, the skin friction coefficient at the plate can be obtained, which in non-dimensional form is given by

$$\tau_{\mathrm{w}} = \left(\frac{\partial u}{\partial y}\right)_{y=0} = -(H_6 b_9 + H_3 b_5 + H_4 b_1) - \varepsilon\mathrm{e}^{nt}(H_{10}b_{11} + H_7 b_7 + H_8 b_3)\,. \tag{36}$$

3.2. Nusselt number

For the temperature field, the rate of heat transfer coefficient can be obtained, which in non-dimensional form is given in terms of the Nusselt number as

$$\mathrm{Nu} = \left(\frac{\partial\theta}{\partial y}\right)_{y=0} = -[b_5\,(1-H_1) + b_1 H_1] - \varepsilon \mathrm{e}^{nt}\,[b_7\,(1-H_2) + b_3 H_7]\,. \tag{37}$$

3.3. Sherwood number

For the concentration field, the rate of mass transfer coefficient can be obtained, which in non-dimensional form is given in terms of Sherwood number as

$$\mathrm{Sh} = \left(\frac{\partial C}{\partial y}\right)_{y=0} = -b_1 - \varepsilon \mathrm{e}^{nt} b_3\,. \tag{38}$$

4. Result and discussion

An unsteady three dimensional flow of an incompressible electrically conducting and chemically reacting slip flow regime over an infinite vertical porous plate through a porous medium in the presence of radiation absorption and heat source/sink was studied. Numerical evaluation of the analytical solutions reported in the previous section was performed and the result are presented in graphical forms. In this study, we have chosen $t = 1$, $n = 0.5$ and $\varepsilon = 0.2$, while other parameters are varied over a range.

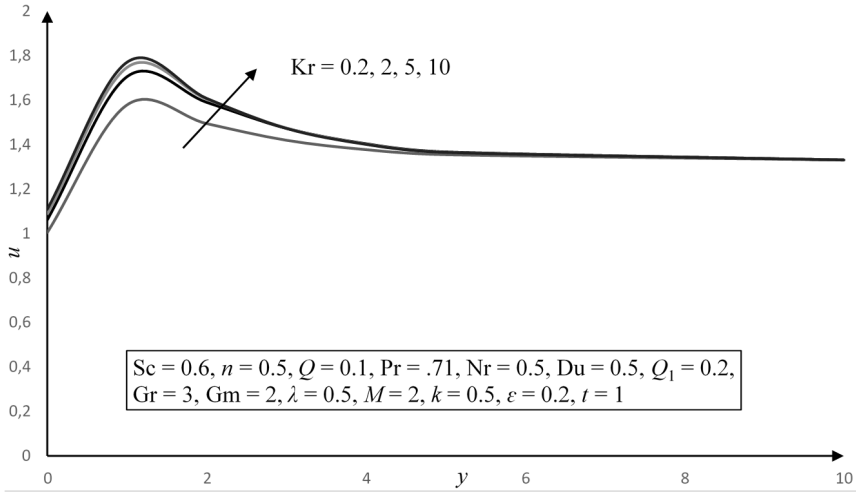

Fig. 1. Effect of chemical reaction parameter on velocity

Figure 1 displays the behavior of the velocity for different values of chemical reaction parameter Kr. It is seen that the velocity increases with increasing chemical

reaction parameter Kr. For large value of y effect of chemical reaction parameter on velocity remains the same.

Figure 2 depicts the behavior of the velocity for different values of magnetic parameter M while other parameters are kept fixed. The effect of magnetic field parameter M results in a decreasing velocity distribution across the boundary layer. This is due to the fact that the effect of a transverse magnetic field give rise to a resistive type force called the Lorentz force. The force has the tendency to slow the motion of the fluid. But the opposite behavior is noted at $y = 0$. For large values of y velocity remains the same.

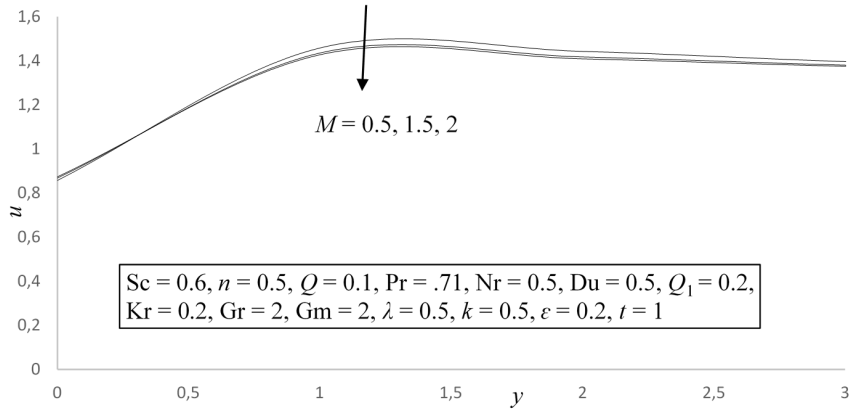

Fig. 2. Effect of magnetic parameter on velocity

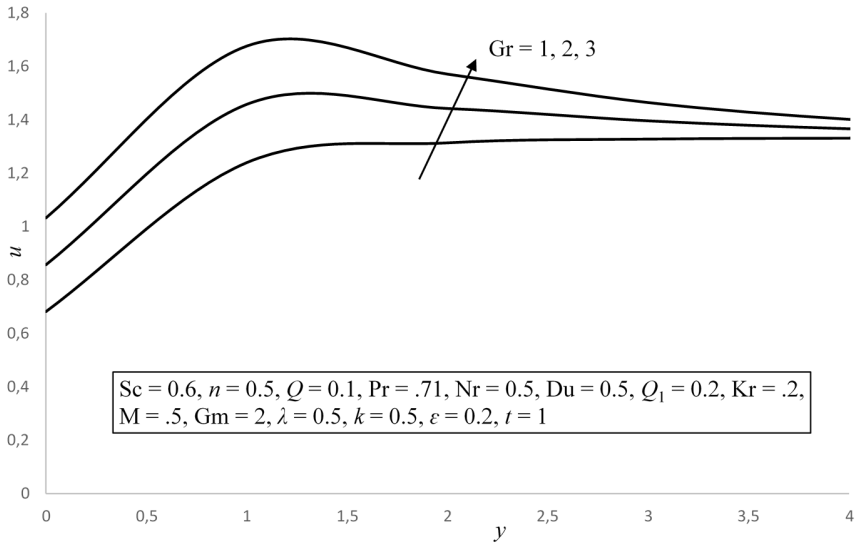

Fig. 3. Effect of thermal Grashoff number on velocity

Figure 3 illustrates the behavior of the velocity for different values of thermal

Grashoff number Gr while other parameters are kept fixed. It is seen that the velocity decreases with increasing Grashoff number Gr. Physically, Gr > 0 implies heating of the fluid of cooling of the boundary surface, while Gr < 0 implies cooling of the fluid of heating of the boundary surface.

Figure 4 shows the mass Grashoff number Gm defines the ratio of the species buoyancy force to the viscous hydrodynamic force. Effect of increasing values of the mass Grashoff number results in a decreasing velocity distribution across the boundary layer.

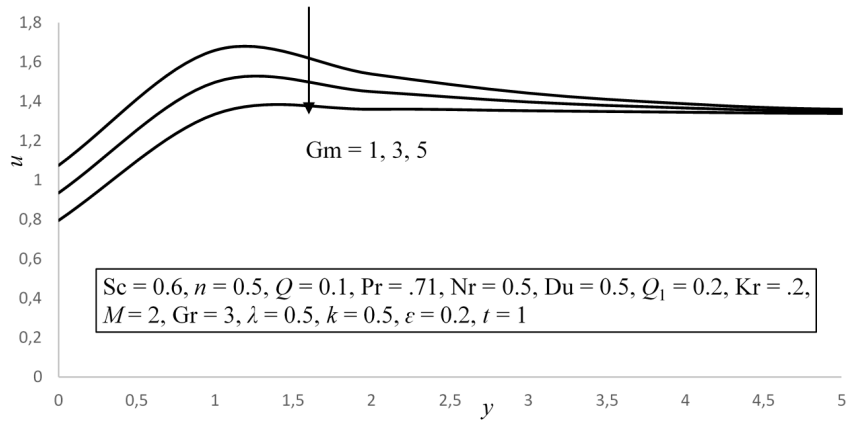

Fig. 4. Effect of mass Grashoff number Gm on velocity

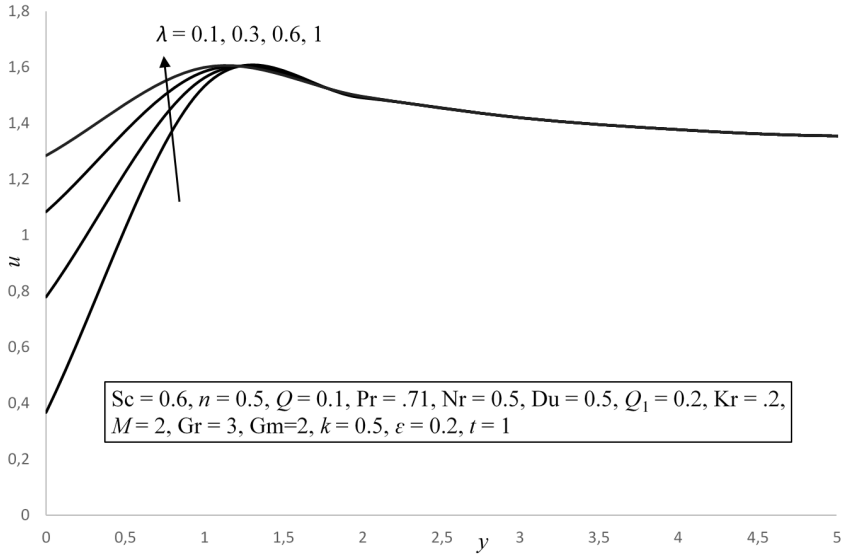

Fig. 5. Effect of slip parameter on velocity

Figure 6 indicates the effect of thermal radiation Parameter Nr on the velocity

profile. Here we find that, as the value of Nr increases the velocity increases, with an increasing in the flow boundary layer thickness. Thus, thermal radiation enhances the convective flow.

Figure 7 shows the velocity profiles across the boundary layer for different values of Prandtl number Pr. The results show that the effect of increasing values of Pr results in a decreasing the velocity. Prandtl number is the ratio of kinematic viscosity and thermal diffusivity. As we increase Prandtl number, it gives increment in the viscosity of the fluid which makes the fluid thick and hence decrease in velocity.

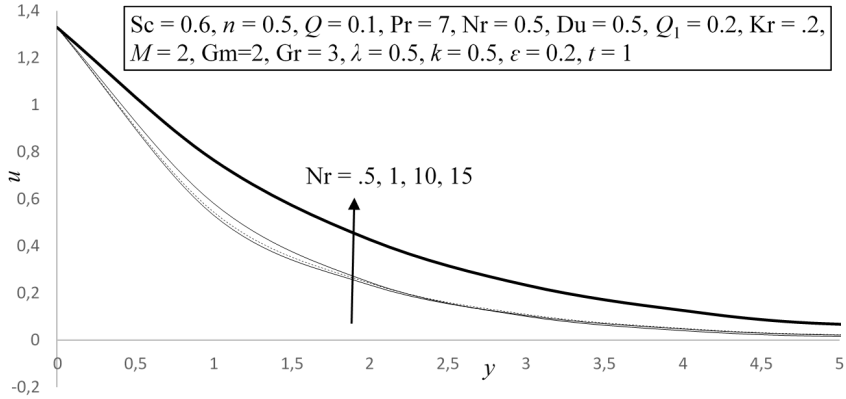

Fig. 6. Effect of thermal radiation parameter on velocity

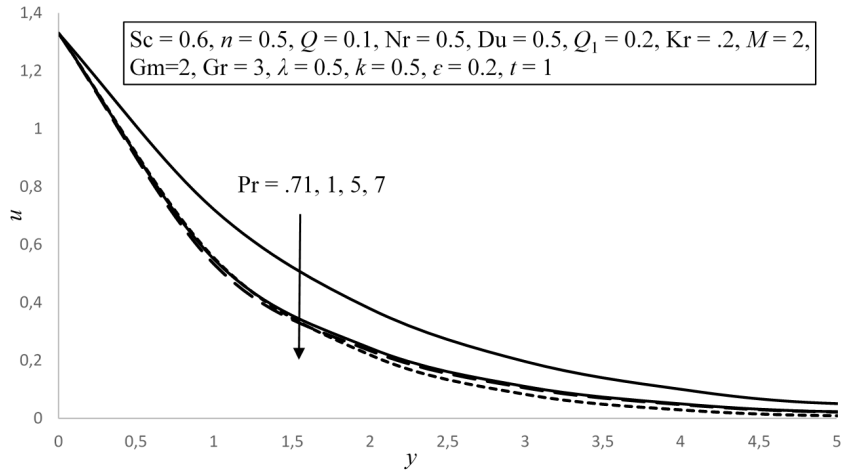

Fig. 7. Effect of Prandtl number on velocity

Figure 8 depictes the effect of heat sink parameter on velocity field. It is seen from this figure that the heat sink parameter Q leads the fluid motion to retard.

The plot of velocity profile for different values of radiation absorption parameter in presence of sink is given in Fig. 9. It is observed that velocity increases for the

increment in radiation absorption parameter.

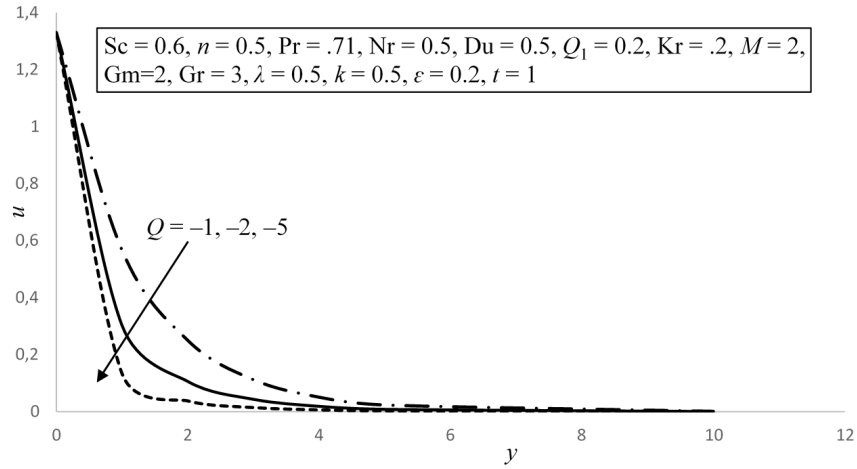

Fig. 8. Effect of heat sink parameter on velocity

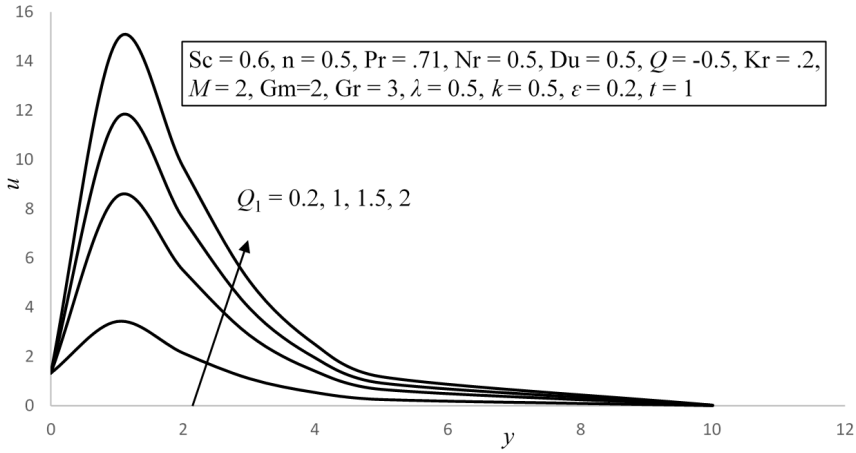

Fig. 9. Effect of radiation absorption parameter on velocity

Figure 10 depicts the effect of permeability of the porous medium parameter K on velocity distribution profiles and it is obvious that permeability parameter isa measure of the porosity of medium. As the porosity of medium increases, the value of K increases. For large porosity of the medium fluid gets more space to flow as a consequence its velocity increases. It shows that the resistance posed by the porous medium reduces, the permeability of the medium because of which velocity increases. These results could be very useful in deciding the applicability of enhanced oil recovery in reservoir engineering.

Figure 11 depicts the variation of thermal boundary layer with the Dufour number. The thermal boundary layer increases with an increase in the Dufour number.

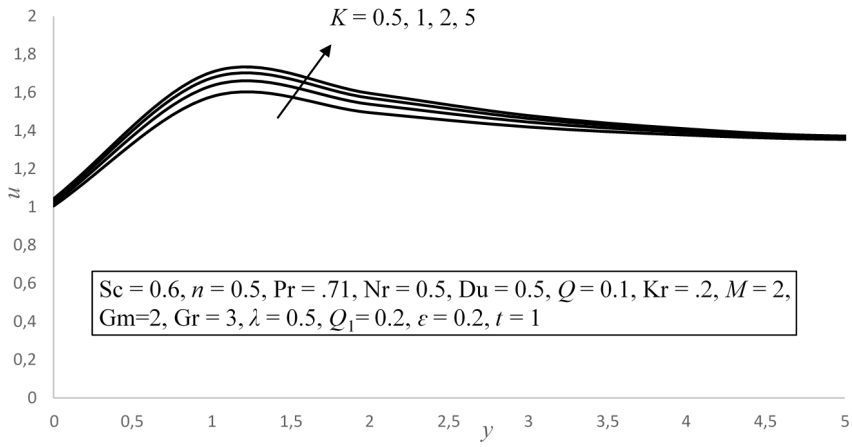

Fig. 10. Effect of Dufour number on temperature

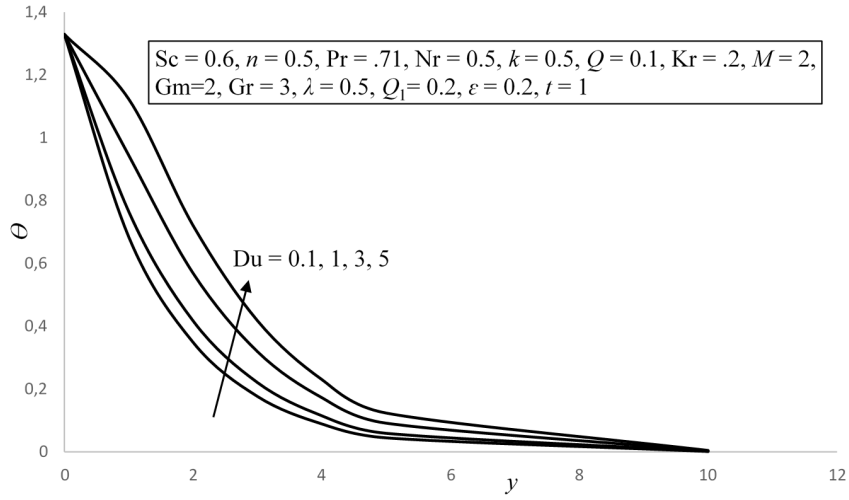

Fig. 11. Effect of thermal radiation parameter on temperature

Figure 12 illustrates the effect of thermal radiation parameter Nr on the temperature. Fluid temperature increases due to increase in thermal radiation parameter.

Figure 13 shows the effect of heat sink parameter on temperature profile. It is noticed that as the heat sink parameter increases the temperature of fluid decreases.

The effect of radiation absorption parameter on temperature profile is given in Fig. 14. It is noticed that the thermal boundary layer thickness increases with an increase in the radiation absorption parameter.

The effect of Schmidt number Sc on concentration profiles is seen from Fig. 15. The figure shows that an increase in Sc result in a decrease in the concentration distribution, because the smaller values of Sc are equivalent to increasing the chemical molecular diffusivity. Physically, the Schmidt number is inversely proportional to

the diffusion coefficient. Hence the concentration decreases with increasing Sc.

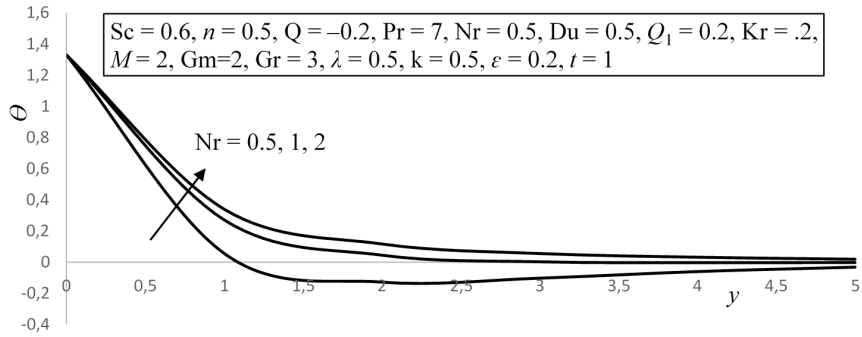

Fig. 12. Effect of thermal radiation parameter on temperature

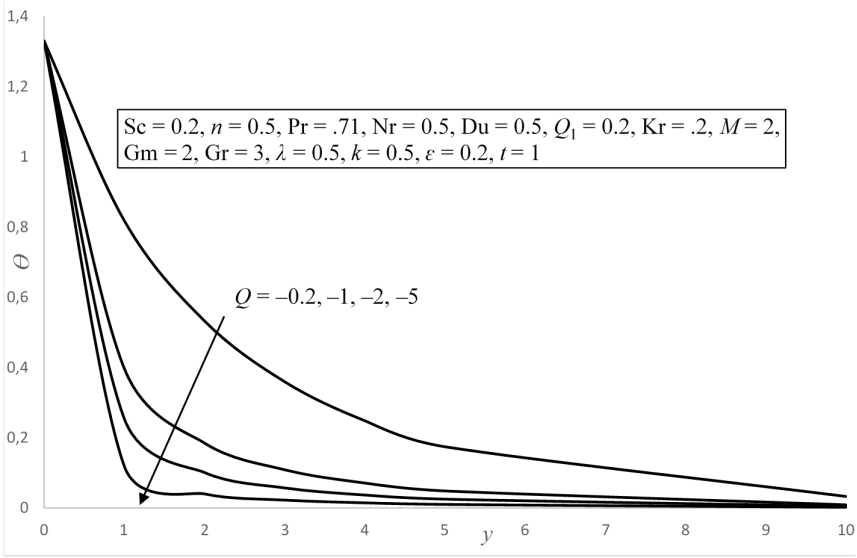

Fig. 13. Effect of heat sink parameter on temperature

Figure 16 shows the effect of chemical reaction parameter Kr on concentration profiles. The concentration decreases as the chemical reaction parameter Kr increases. This shows that the buoyancy effects (due to concentration and temperature difference) are important in the plate. Moreover it is observed that the fluid motion is retarded on the account of chemical reaction.

The variation in skin-friction coefficient, the rate of heat transfer in the form of Nusselt number and the rate of mass transfer in the form of Sherwood number for various parameters are studied through Tables 1–3.

Skin friction increases due to increase in chemical reaction parameter, Grashoff number and porosity parameter while it decreases due to increase in mass Grashoff number and magnetic parameter.

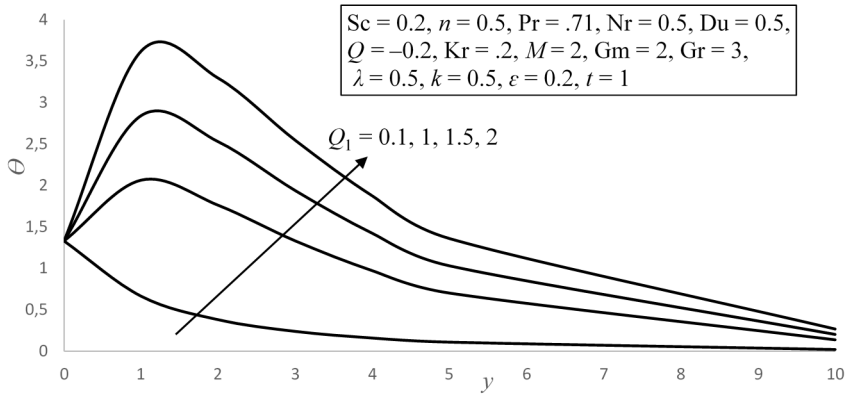

Fig. 14. Effect of radiation absorption parameter on temperature

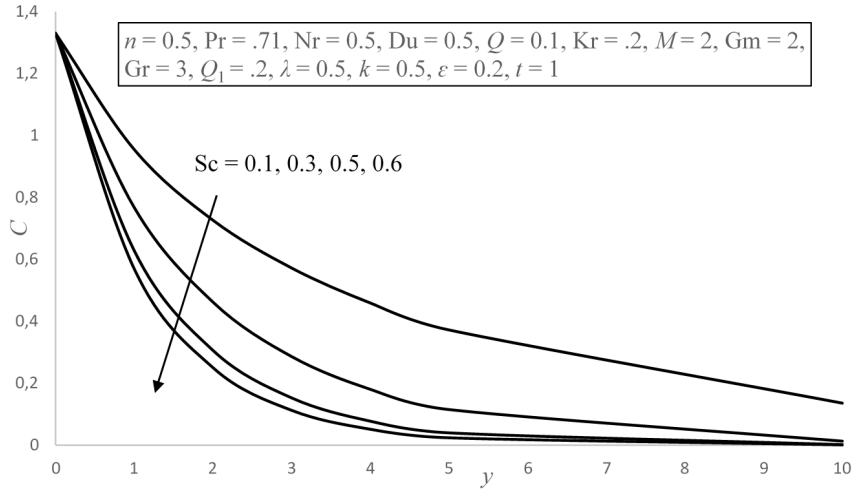

Fig. 15. Effect of Schmidt number on concentration

The rate of Nusselt number decreases due to increase in sink parameter Q, radiation absorption parameter Q_1, Dufour number Du and radiation parameter Nr while it increases due to increase in Prandtl number. The Sherwood number decreases due to increase in Schmidt number and chemical reaction parameter in presence of sink.

5. Conclusion

In this paper, the effect of heat and mass transfer on unsteady MHD flow of an incompressible, electrically conducting, heat generating/absorbing fluid along a semi-infinite moving porous plate embedded in a porous medium with the presence of pressure gradient, thermal radiation and chemical reaction has been studied numerically. The present investigation brings out the following interesting features of

physical interest on the flow velocity, temperature and concentration:

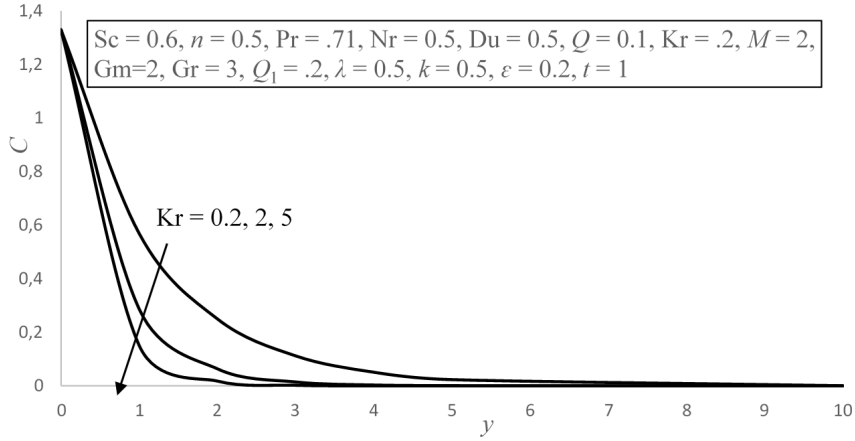

Fig. 16. Effect of chemical reaction parameter on concentration

Table 1. Effect of various physical parameter on skin friction for Sc = 0.6, $n = 0.5$, $Q = 0.1$, Pr =.71, Nr = 0.5, Du = 0.5, $Q_1 = .2$, $\lambda = 0.5$, $\varepsilon = 0.2$, $t = 1$

Kr	Gr	Gm	M	K	C_{f0}
0.1	3	2	2	0.5	1.984089192
0.2	3	2	2	0.5	2.010398906
0.3	3	2	2	0.5	2.028066725
0.4	3	2	2	0.5	2.041341592
0.2	1	2	2	0.5	1.484130332
0.2	2	2	2	0.5	1.747264619
0.2	3	2	0.5	0.5	2.064653448
0.2	3	2	1.5	0.5	2.02205219
0.2	3	2	2	0.1	2.015220521
0.2	3	2	2	1.5	2.055010921
0.2	3	1	2	0.5	2.150265024
0.2	3	3	2	0.5	1.870532788

1. The fluid velocity decreases with increase in magnetic field parameter, thermal Grashoff number, mass Grashoff number, Prandtl number and heat sink parameter.

2. The fluid velocity increases with increase in chemical reaction parameter, slip parameter, thermal radiation parameter, radiation absorption parameter and permeability of porous medium.

3. The fluid temperature decreases with increase in heat sink parameter while it increases due to increase in Dufour number, thermal radiation parameter and radiation absorption parameter.

4. It is marked that a decreases in concentration with the increasing of Schmidt number as well as chemical reaction parameter is observed.

Table 2. Effect of various physical parameter on Nusselt number for Sc = 0.6, $n = 0.5$, Kr = 0.2, Gr = 3, Gm = 2, $M = 2$, $K = 0.5$, $\lambda = 0.5$, $\varepsilon = 0.2$, $t = 1$

Q	Pr	Nr	Du	Q_1	Nu_0
–0.2	0.71	0.5	0.5	0.2	–3.370286958
–0.2	1	0.5	0.5	0.2	–1.874104832
–0.2	7	0.5	0.5	0.2	–1.594676934
–0.2	0.71	1	0.5	0.2	–2.568371193
–0.2	0.71	10	0.5	0.2	–2.773852987
–0.2	0.71	15	0.5	0.2	–3.08707725
–0.1	0.71	0.5	0.5	0.2	–2.67456224
–0.3	0.71	0.5	0.5	0.2	–4.617831191
–0.2	0.71	0.5	0.5	1	–5.515169471
–0.2	0.71	0.5	0.5	2	–8.196272613
–0.2	0.71	0.5	1	0.2	–4.346519024
–0.2	0.71	0.5	3	0.2	–8.251447289

Table 3. Effect of various physical parameter on Sherwood number for Sc = 0.6, $n = 0.5$, $Q = -0.2$, Pr = 0.71, Nr = 0.5, Du = 0.5, $Q_1 = 0.2$, Gr = 3, Gm = 2, $M = 2$, $K = 0.5$, $\lambda = 0.5$, $\varepsilon = 0.2$, $t = 1$

Sc	Kr	Sh
1	0.2	–1.657087463
2	0.2	–2.942894118
3	0.2	–4.249165038
4	0.2	–5.565247246
0.6	0.1	–1.06012776
0.6	0.3	–1.229618626
0.6	0.4	–1.301470931

References

[1] N. Ahmed, D. Kalitha, D. Barman: *MHD free convective Poiseuille flow and mass transfer through a porous medium bounded by two infinite vertical porous plates.* International Journal of Applied Engineering Research *5* (2010), No. 1, 25–35.

[2] G. Singh, P. R. Sharma, A. J. Chamkha: *Effect of volumetric heat generation/absorption on mixed convection stagnation point flow on an iso-thermal vertical plate in porous media.* International Journal Industrial Mathematics *2* (2010), No. 2, 59–71.

[3] S. Srinivas, R. Muthuraj: *MHD flow with slip effects and temperature dependent heat source in a vertical wavy porous space.* Chemical Engineering Communications *197* (2010), No. 11, 1387–1403.

[4] V. S. Babu, G. V. R. Reddy: *Mass transfer effects on MHD mixed convective flow from a vertical surface with ohmic heating and viscous dissipation.* Advances in Applied Science Research *2* (2011), No. 4, 138–146.

[5] A. J. Chamkha, S. E. Ahmed: *Similarity solution for unsteady MHD flow near a stagnation point of a three-dimensional porous body with heat and mass transfer, heat generation/absorption and chemical reaction.* Journal of Applied Fluid Mechanics *4* (2011), No. 3, 24–31.

[6] O. D. Makinde: *On MHD mixed convection with Soret and Dufour effects past a vertical plate embedded in a porous medium.* Latin American Applied Research *41* (2011), No. 1, 63–68.

[7] M. C. Raju, S. V. K. Varma: *Unsteady MHD free convection oscillatory couette flow through a porous medium with periodic wall temperature.* Journal on Future Engineering and Technology *6* (2011), No. 4, 7–12.

[8] R. Muthucumaraswamy, K. Amutha: *Thermal diffusion effects on MHD flow past an oscillating vertical plate with chemical reaction of first order.* International Journal of Mathematical Archive *3* (2012), No. 12, 4989–4996.

[9] D. Pal, B. Talukdar: *Influence of fluctuating thermal and mass diffusion on unsteady MHD buoyancy-driven convection past a vertical surface with chemical reaction and Soret effects.* Communications in Nonlinear Science and Numerical Simulation *17* (2012), No. 4, 1597–1614.

[10] P. R. Sharma, I. K. Dadheech: *Effect of volumetric heat generation/absorption on convective heat and mass transfer in porous medium between two vertical porous plates.* International Journal of Engineering Research and Technology *1* (2012), 1–7.

[11] M. C. Raju, S. V. K. Varma, N. A. Reddy: *Radiation and mass transfer effects on a free convection flow through a porous medium bounded by a vertical surface.* Journal on Future Engineering and Technology *7* (2012), No. 2, 7–12.

[12] V. R. Ravikumar, M. C. Raju, G. S. S. Raju: *Heat and mass transfer effects on MHD flow of viscous fluid through non-homogeneous porous medium in presence of temperature dependent heat source.* International Journal of Contemporary Mathematical Sciences *7* (2012), No. 32, 1597–1604.

[13] P. V. S. Narayana, C. S. Sravanthi: *Simultaneous effects of Soret and ohmic heating on MHD free convective heat and mass transfer flow of micropolar fluid with porous medium.* Elixir International Journal Applied Mathematics *48* (2012), 9379–9386.

[14] S. M. Ibrahim: *Effects of mass transfer, radiation, Joule heating and viscous dissipation on steady MHD Marangoni convection flow over a flat surface with suction and injection.* International Journal of Engineering Mathematics (2013), ID No. 903818.

[15] S. Ahmed, A. Batin: *Magnetohydrodynamic heat and mass transfer flow with induced magnetic field and viscous dissipative effects.* Latin American Applied Research *44* (2014), 9–17.

[16] D. Sarma, N. Ahmed, H. Deka: *MHD free convection and mass transfer flow past an accelerated vertical plate with chemical reaction in presence of radiation.* Latin American Applied Research *44* (2014), No. 1, 1.

[17] E. M. Arthur, T. Ayando, I. Y. Seini: *MHD convective boundary layer flow towards a vertical surface in a porous medium with radiation , chemical reaction and internal heat generation.* Frontiers in Heat and Mass Transfer *6* (2015), No. 1, 1–10.

[18] S. M. Ibrahim, K. Suneetha: *Chemical reaction and Soret effects on unsteady MHD flow of a viscoelastic fluid past an impulsively stated infinite vertical plate with heat source/sink.* International Journal of Mathematics and Computational Science *1* (2015), No. 1, 5–14.

[19] A. Mahdy, S. E. Ahmed: *Thermosolutal Marangoni boundary layer magnetohydrodynamic flow with the Soret and Dufour effects past a vertical flat plate.* Engineering Science and Technology *18* (2015), No. 1, 24–31.

[20] S. M. Ibrahim, K. Suneetha: *Heat source and chemical effects on MHD convection flow embedded in a porous medium with Soret, viscous and Joules dissipation.* Ain Shams Engineering Journal *7* (2016), No. 2, 811–818.

[21] P. Gurivireddy, M. C. Raju, B. Mamatha, S. V. K. Varma: *Thermal diffusion effect on MHD heat and mass transfer flow past a semi-infinite moving vertical porous plate with heat generation and chemical reaction.* Applied Mathematics *7* (2016), 638–649.

Received June 15, 2018

Acta Technica *63* No. 6/2018, 829–844

Vibration analysis of clamped and simply supported non-homogeneous trapezoidal plate of varying thickness and density under thermal gradient

Kavita[1], Deepak Gupta[1], Pragati Sharma[2,3]

Abstract. The objective of present paper is to study the effect of non-homogeneity on thermally induced vibrations of non-homogeneous trapezoidal plate whose thickness varies linearly in one and parabolically in other direction. Parabolic variation in density in x-direction is taken because of the behavior of non-homogeneity. Using Rayleigh-Ritz method governing differential equations has been attained by taking two term deflection function corresponding to clamped-simply supported- clamped- simply supported (C-S-C-S) boundary condition. Effect of non-homogeneity constant, aspect ratios, thermal gradient and taper constants on the frequencies has been studied for first and second mode of vibration. All the numerical results are presented graphically.

Key words. Trapezoidal plate, non-homogeneous problem, thickness, density, frequencies.

1. Introduction

In engineering and mechanical structures the occurrence of vibration is an ordinary fact even though not constantly discarded. The effect of vibration plays a fundamental role in engineering as many machines and structures undergo vibrations. To minimize vibration and noise in structures, plate theory has been applied. Ultimately, in modern technology, the significance of elastic behavior of plates, in addition to, the natural frequency and mode shapes have made engineers aware. In general, tapered plates are applied in structure modeling. Plates with variability in thickness are applied in different engineering applications such as naval structures, nuclear reactor structures, aeronautical fields etc.

Taken into account the practical significance of these plates, vibration analysis has become very important for evading resonance agitated by internal and exter-

[1]Department of Mathematics, M. M. University, Mullana, Haryana, India
[2]Department of Mathematics, N. I. T. Kurukshetra, Haryana, India
[3]Corresponding author; e-mail: prgt.shrm@gmail.com

nal forces. Not only science and engineering but our daily life is also affected by vibration. Numerous authors deal in vibration phenomena of plates by taking into consideration their shapes, thickness, homogeneity or non-homogeneity. Considerable change occurs in material properties because such structures are exposed to high intensity heat fluxes. Vibration of non-homogeneous plate's temperature effect can be considered also for enhanced designing of space craft, gas turbines, jet engines and nuclear power projects. So, it is necessary to study the temperature variations on plates. Above all, thermal effect cannot be taken as insignificant.

Trapezoidal plates of variable thickness are commonly used in several engineering applications such as aircraft, ships and bridges etc. To economize plate material they are more efficient than the uniform thickness plates. Many researchers are inspired to work in this direction. Some of them are: Laura and Grossi [1] analyzed the transverse vibration of rectangular plates with thickness varying in two directions and with edges elastically restrained against rotation. Malhotra et al. [2] discussed the vibrations of orthotropic square plates having variable thickness, i.e., parabolic variation. Kukreti et al. [3] determined the fundamental frequencies of simply supported rectangular plates with linearly varying thickness by Differential Quadrature and Rayleigh–Ritz methods. Bhasker and Kaushik [4] gave the simple and exact series solutions for flexure of orthotropic rectangular plates with any combination of clamped and simply supported edges. Kumar and Tomar [5] worked on the free transverse vibrations of monoclinic rectangular plates with continuously varying thickness and density. Gupta et al. [6] studied the vibration of visco-elastic parallelogram plate with parabolic thickness variation. Gupta and Kumud [7] analyzed the thermal effect on vibration of non-homogeneous parallelogram plate of parabolically varying thickness. Khanna and Arora [8] did the theoretical analysis on thermally induced vibration of tapered parallelogram plate with mixed boundary conditions. Singh and Chakraverty [9] discussed the transverse vibration of circular and elliptic plates with variable thickness. Gupta and Sharma [10] provided the forced axisymmetric response of an annular plate of parabolically varying thickness. Gupta et al. [11] analyzed the vibration of non-homogeneous circular plate of nonlinear thickness variation by differential quadrature method. Tomar et al. [13] studied the free vibrations of an isotropic non homogeneous infinite plate of parabolically varying thickness. Chakraverty et al. [14] observed the effect of non-homogeneity on natural frequencies of vibration of elliptic plates. Liew and Lim [15] studied the transverse vibration of trapezoidal plates of variable thickness considering symmetric trapezoids. Qatu [16] calculated the natural frequencies for cantilevered laminated composite right triangular and trapezoidal plates. Gupta and Sharma [17] studied the thermal gradient effect on frequencies of a trapezoidal plate of linearly varying thickness. Gupta and Sharma [18] presented an analysis for frequencies of thermally induced vibration of non-homogeneous trapezoidal plate of variable thickness and density. Gupta and Sharma [19] observed the effect of thermal gradient on vibration of non-homogeneous orthotropic trapezoidal plate of linearly varying thickness. Shokrollahi and Shafaghat [20] suggested a global Ritz formulation for the free vibration analysis of hybrid metal-composite thick trapezoidal plates. Kavita et al. [21] studied the temperature behavior on thermally induced

vibration of non-homogeneous trapezoidal plate with bi-linearly varying thickness. Kavita et al. [22] observed the thermal effect on vibration of non-homogeneous trapezoidal plate with bilinear thickness variation and parabolic density variation.

In this work, the effect of non-homogeneity on thermally induced vibration of non-homogeneous trapezoidal plate with variable thickness linearly in one and parabolically in other direction is analyzed. Parabolic variation in density in x-direction and linear variation in temperature along length of the plate is assumed. Fundamental frequencies of C-S-C-S trapezoidal plate for different values of taper constants, aspect ratios, thermal gradient and non-homogeneity constant have been calculated for both modes of vibration by using Rayleigh-Ritz method. All the results are displayed graphically.

2. Equation of motion and analysis

2.1. Geometry of the plate

The geometry of symmetric non-homogeneous trapezoidal plate is shown in Fig. 1.

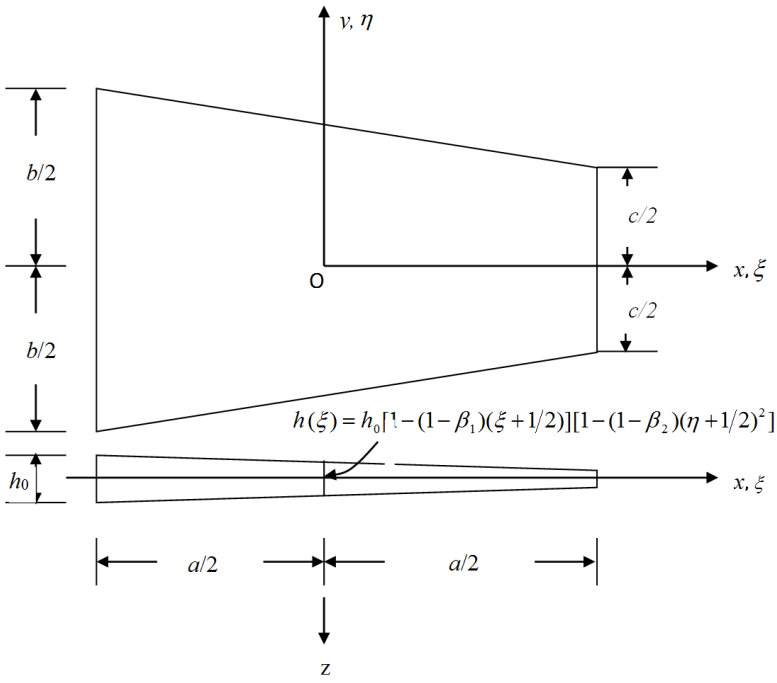

Fig. 1. Geometry of C-S-C-S trapezoidal plate

2.2. Temperature

Temperature of non-homogeneous trapezoidal plate is assumed to vary linearly along x-axis as

$$\tau = \tau_0 \left(\frac{1}{2} - \xi \right) , \tag{1}$$

where τ denotes the excess above the reference temperature at a distance $\xi = \frac{x}{a}$ and τ_0 denotes the temperature excess above the reference temperature at the end $\xi = -\frac{1}{2}$.

The modulus of elasticity is described as a function of temperature for most of the structural materials by Nowacki [12], as

$$E = E_0 \left(1 - \gamma\tau\right) , \tag{2}$$

where E_0 is the value of Young's modulus at the reference temperature $\tau = 0$ and γ is the slope of variation of E with τ.

Putting eq. (1) into eq. (2), the modulus of E becomes

$$E = E_0 \left(1 - \alpha \left(\frac{1}{2} - \xi \right) \right) , \tag{3}$$

where $\alpha = \gamma\tau_0$ $(0 \leq \alpha \leq 1)$ is known as the thermal gradient.

2.3. Thickness and density variation

Proper variations in thickness have considerably better efficiency on vibration on the contrary of uniform thickness of plate. As a result variation in thickness of trapezoidal plate is assumed linearly in x-direction and parabolically in y-direction as

$$h(\xi) = h_0 \left[1 - (1 - \beta_1) \left(\xi + \frac{1}{2} \right) \right] \left[1 - (1 - \beta_2) \left(\eta + \frac{1}{2} \right)^2 \right] , \tag{4}$$

where $h_0 = h$ at $\xi = \eta = -\frac{1}{2}$ and β_1, β_2 are taper constants.

Because of parabolic variation in density in x-direction, non-homogeneity occurs in plate which can be expressed as

$$\rho = \rho_0 \left[1 - (1 - \beta) \left(\xi + \frac{1}{2} \right)^2 \right] , \tag{5}$$

where $\rho_0 = \rho$ is the mass density at $\xi = -\frac{1}{2}$ and β is the non-homogeneity constant.

2.4. Deflection function and corresponding boundary condition

With clamped simply-supported clamped simply- supported (C-S-C-S) boundary condition a two term deflection function has been considered for vibration analysis

and can be written as

$$w = A_1 \left\{ \left(\xi + \frac{1}{2}\right)\left(\xi - \frac{1}{2}\right) \right\}^2 \left\{ \eta - \left(\frac{b-c}{2}\right)\xi + \left(\frac{b+c}{4}\right) \right\} \cdot$$

$$\cdot \left\{ \eta + \left(\frac{b-c}{2}\right)\xi - \left(\frac{b+c}{4}\right) \right\} + A_2 \left\{ \left(\xi + \frac{1}{2}\right)\left(\xi - \frac{1}{2}\right) \right\}^3 \cdot$$

$$\left\{ \eta - \left(\frac{b-c}{2}\right)\xi + \left(\frac{b+c}{4}\right) \right\}^2 \left\{ \eta + \left(\frac{b-c}{2}\right)\xi - \left(\frac{b+c}{4}\right) \right\}^2 , \tag{6}$$

where A_1 and A_2 are two unknown constants to be determined.

Thus, for a non-homogeneous trapezoidal plate eq. (6) is considered in such a way to satisfy the following (C-S-C-S) boundary conditions that are represented by the four straight lines

$$\eta = \frac{c}{4b} - \frac{\xi}{2} + \frac{1}{4} + \frac{c\xi}{2b} ,$$

$$\eta = -\frac{c}{4b} + \frac{\xi}{2} - \frac{1}{4} - \frac{c\xi}{2b} ,$$

$$\xi = -\frac{1}{2} ,$$

$$\xi = \frac{1}{2} , \tag{7}$$

introducing the following non-dimensional variables as $\xi = \frac{x}{a}$ and $\eta = \frac{y}{b}$.

2.5. Governing differential equations

Expressions for kinetic energy T and strain energy V are given by [15] as

$$T = \frac{a\,b}{2}\omega^2 \int_A h(\xi)\rho w^2 \,\mathrm{d}A , \tag{8}$$

$$V = \frac{ab}{2} \int_A D(\xi) I \,\mathrm{d}A ,$$

$$I = \left\{ \left(\frac{1}{a^2}\frac{\partial^2 w}{\partial \xi^2} + \frac{1}{b^2}\frac{\partial^2 w}{\partial \eta^2} \right)^2 - 2\,(1-\nu)\left(\frac{1}{a^2 b^2}\frac{\partial^2 w}{\partial \xi^2}\frac{\partial^2 w}{\partial \eta^2} - \left(\frac{1}{ab}\frac{\partial^2 w}{\partial \xi \partial \eta} \right)^2 \right) \right\} , \tag{9}$$

where A is the area of the plate, ω is the angular frequency of vibration, ν is the Poisson ratio, and the flexural rigidity $D(\xi)$ of the plate can be defined as

$$D(\xi) = D_0 \left[\left[1 - (1-\beta_1)\left(\xi + \frac{1}{2}\right) \right] \cdot \left[1 - (1-\beta_2)\left(\eta + \frac{1}{2}\right)^2 \right] \right]^3 , \tag{10}$$

where

$$D_0 = \frac{Eh_0^3}{12\,(1-\nu^2)}\,. \tag{11}$$

Inserting the value of E from (3) to (11), we get

$$D_0 = \frac{E_0 h_0^3\left(1-\alpha\left(\frac{1}{2}-\xi\right)\right)}{12\,(1-\nu^2)}\,. \tag{12}$$

After putting the value of D_0 from (12) into (10), flexural rigidity of the plate becomes

$$D(\xi) = \frac{E_0 h_0^3}{12\,(1-\nu^2)}\left(1-\alpha\left(\frac{1}{2}-\xi\right)\right)\cdot$$

$$\cdot\left[\left[1-(1-\beta_1)\left(\xi+\frac{1}{2}\right)\right]\left[1-(1-\beta_2)\left(\eta+\frac{1}{2}\right)^2\right]\right]^3\,. \tag{13}$$

Insertion of the equations (4), (5) and (13) in equations (8) and (9) gives the following values of the following values of kinetic energy T and strain energy V as

$$T = \frac{ab}{2}\rho_0 h_0 \omega^2 \int_A I w^2\,\mathrm{d}A\,,$$

$$I = \left[1-(1-\beta_1)\left(\xi+\frac{1}{2}\right)\right]\cdot\left[1-(1-\beta_2)\left(\eta+\frac{1}{2}\right)^2\right]\cdot\left[1-(1-\beta)\left(\xi+\frac{1}{2}\right)^2\right] \tag{14}$$

and

$$V = \tfrac{ab}{2}\tfrac{E_0 h_0^3}{12(1-\nu^2)}\int_A\left[\left[1-(1-\beta_1)\left(\xi+\tfrac{1}{2}\right)\right]\left[1-(1-\beta_2)\left(\eta+\tfrac{1}{2}\right)^2\right]\right]^3\times I\,\mathrm{d}A\ \ , \tag{15}$$

where

$$I = \left(\frac{1}{a^2}\frac{\partial^2 w}{\partial\xi^2}+\frac{1}{b^2}\frac{\partial^2 w}{\partial\eta^2}\right)^2 - 2\,(1-\nu)\left(\frac{1}{a^2 b^2}\frac{\partial^2 w}{\partial\xi^2}\frac{\partial^2 w}{\partial\eta^2}-\left(\frac{1}{ab}\frac{\partial^2 w}{\partial\xi\,\partial\eta}\right)^2\right).$$

After applying (7) of boundary condition, (14) and (15) can be expressed as

$$T = \tfrac{ab}{2}\rho_0 h_0\omega^2\int_{-\frac{1}{2}}^{\frac{1}{2}}\int_{-\frac{c}{4b}+\frac{\xi}{2}-\frac{1}{4}-\frac{c\xi}{2b}}^{\frac{c}{4b}-\frac{\xi}{2}+\frac{1}{4}+\frac{c\xi}{2b}}\left[1-(1-\beta_1)\left(\xi+\tfrac{1}{2}\right)\right]\left[1-(1-\beta_2)\left(\eta+\tfrac{1}{2}\right)^2\right]\times$$

$$\times\left[1-(1-\beta)\left(\xi+\tfrac{1}{2}\right)^2\right]w^2\,\mathrm{d}\eta\,\mathrm{d}\xi \tag{16}$$

and

$$V = \frac{ab}{2}\frac{E_0 h_0^3}{12\,(1-\nu^2)}\int_{-\frac{1}{2}}^{\frac{1}{2}}\int_{-\frac{c}{4b}+\frac{\xi}{2}-\frac{1}{4}-\frac{c\xi}{2b}}^{\frac{c}{4b}-\frac{\xi}{2}+\frac{1}{4}+\frac{c\xi}{2b}} I\times J\,\mathrm{d}\eta\,\mathrm{d}\xi\,, \tag{17}$$

where

$$I = \left[\left[1-(1-\beta_1)\left(\xi+\frac{1}{2}\right)\right]\ \left[1-(1-\beta_2)\left(\eta+\frac{1}{2}\right)^2\right]\right]^3 \left(1-\alpha\left(\frac{1}{2}-\xi\right)\right)$$

and

$$J = \left(\frac{1}{a^2}\frac{\partial^2 w}{\partial\xi^2}+\frac{1}{b^2}\frac{\partial^2 w}{\partial\eta^2}\right)^2 - 2(1-\nu)\left(\frac{1}{a^2b^2}\frac{\partial^2 w}{\partial\xi^2}\frac{\partial^2 w}{\partial\eta^2}-\left(\frac{1}{a\,b}\frac{\partial^2 w}{\partial\xi\,\partial\eta}\right)^2\right).$$

2.6. Method of solution and frequency equation

Rayleigh-Ritz technique requires that the maximum strain energy must be equal to the maximum kinetic energy. It is, therefore, necessary for the problem under consideration that

$$\delta(V-T)=0\,. \tag{18}$$

On placing the values of T and V from equations (14) and (15) into equation (18), one obtains

$$\delta\left(V_1-\lambda^2 T_1\right)=0\,, \tag{19}$$

where

$$\lambda^2=\frac{12\omega^2\rho_0 a^4\left(1-\nu^2\right)}{E_0 h_0^2} \tag{20}$$

is the frequency parameter.

Then

$$\begin{aligned} T_1 = {} & \int_{-\frac{1}{2}}^{\frac{1}{2}}\int_{-\frac{c}{4b}+\frac{\xi}{2}-\frac{1}{4}-\frac{c\xi}{2b}}^{\frac{c}{4b}-\frac{\xi}{2}+\frac{1}{4}+\frac{c\xi}{2b}}\left[1-(1-\beta_1)\left(\xi+\tfrac{1}{2}\right)\right]\left[1-(1-\beta_2)\left(\eta+\tfrac{1}{2}\right)^2\right]\times \\ & \times\left[1-(1-\beta)\left(\xi+\tfrac{1}{2}\right)^2\right]w^2\,\mathrm{d}\eta\,\mathrm{d}\xi\,, \end{aligned} \tag{21}$$

$$\begin{aligned} V_1 = {} & \int_{-\frac{1}{2}}^{\frac{1}{2}}\int_{-\frac{c}{4b}+\frac{\xi}{2}-\frac{1}{4}-\frac{c\xi}{2b}}^{\frac{c}{4b}-\frac{\xi}{2}+\frac{1}{4}+\frac{c\xi}{2b}}\left[\left[1-(1-\beta_1)\left(\xi+\tfrac{1}{2}\right)\right]\left[1-(1-\beta_2)\left(\eta+\tfrac{1}{2}\right)^2\right]\right]^3\times \\ & \times\left(1-\alpha\left(\tfrac{1}{2}-\xi\right)\right)\times \\ & \times\left\{\left(\tfrac{1}{a^2}\tfrac{\partial^2 w}{\partial\xi^2}+\tfrac{1}{b^2}\tfrac{\partial^2 w}{\partial\eta^2}\right)^2-2(1-\nu)\left(\tfrac{1}{a^2b^2}\tfrac{\partial^2 w}{\partial\xi^2}\tfrac{\partial^2 w}{\partial\eta^2}-\left(\tfrac{1}{ab}\tfrac{\partial^2 w}{\partial\xi\,\partial\eta}\right)^2\right)\right\}\mathrm{d}\eta\,\mathrm{d}\xi\,. \end{aligned} \tag{22}$$

It is essential to consider the following method to estimate the values of two unknown constants, i.e. A_1 and A_2 involved in (19) on the account of the deflection function

$$\frac{\partial}{\partial A_1}\left(V_1-\lambda^2 T_1\right)=0\,,$$

$$\frac{\partial}{\partial A_2}\left(V_1 - \lambda^2 T_1\right) = 0\,. \tag{23}$$

The solution of (23) presents the following form

$$b_{m1}A_1 + b_{m2}A_2 = 0, \quad m = 1, 2\,, \tag{24}$$

where b_{m1}, b_{m2} $(m = 1, 2)$ involves parametric constants and frequency parameters.

Now the determinant of coefficient of (24) must be zero for a non-trivial solution. As a result, one finds the frequency equation, which can be written as

$$\begin{vmatrix} b_{11} & b_{12} \\ b_{21} & b_{22} \end{vmatrix} = 0\,. \tag{25}$$

The solution of equation (25) gives a quadratic equation in λ^2. Thus two roots of λ^2 can be obtained which represent the first and second modes of vibration.

3. Results and discussion

Here, a non-homogeneous clamped simply-supported clamped simply-supported (C-S-C-S) trapezoidal plate with varying thickness and density has been taken in order to examine the behavior of frequency for the first two modes of vibration. Numerical values have been computed by using Mathematica software for different values of parameters such as taper constant β_1, β_2, thermal gradient α, aspect ratios a/b and c/b and non-homogeneity constant β. The value of Poisson ratio ν is taken 0.33 here and all numerical results are plotted graphically in Figs. 2–6. Every of these figures depicts results obtained for both first and second modes of vibration.

In case of taper constant β_1 (varying from 0.0 to 1.0), frequencies are obtained for both modes of vibration by using different values of plate parameters such as $\beta_2 = 0.6$, $a/b = 1.0$, $c/b = 0.5$, $\alpha = 0.0$ and 0.4, and $\beta = 0.4$ and 1.0. Afterwards, the effect of taper constant β_1 on frequency parameter λ is shown in Fig. 2 for the first and second modes of vibration respectively. So, one can observe from this figure that increase in the taper constant β_1 increases the value of frequency parameter λ for both the modes of vibration.

In case of taper constant β_2 (varying from 0.0 to 1.0), frequencies are obtained for both modes of vibration by using different values of plate parameters such as $\beta_1 = 0.6$, $a/b = 1.0$, $c/b = 0.5$, $\alpha = 0.0$ and 0.4, and $\beta = 0.4$ and 1.0. After that, the effect of taper constant β_1 on the frequency parameter λ, is shown in Fig. 3 for the first and second modes of vibration, respectively. Thus, from this figure one can observe that increase in taper constant β_2 causes an increase in the value of frequency parameter λ for both the modes of vibration.

Figure 4 shows the graph regarding the effect of thermal gradient α (varying from 0.0 to 1.0) on the frequency parameter λ for the first and second modes of vibration. Therefore, the numerical results are shown there for aspect ratio $a/b = 1.0$, $c/b = 0.5$ with four combinations of taper constants β_1, β_2 and non-homogeneity constant β

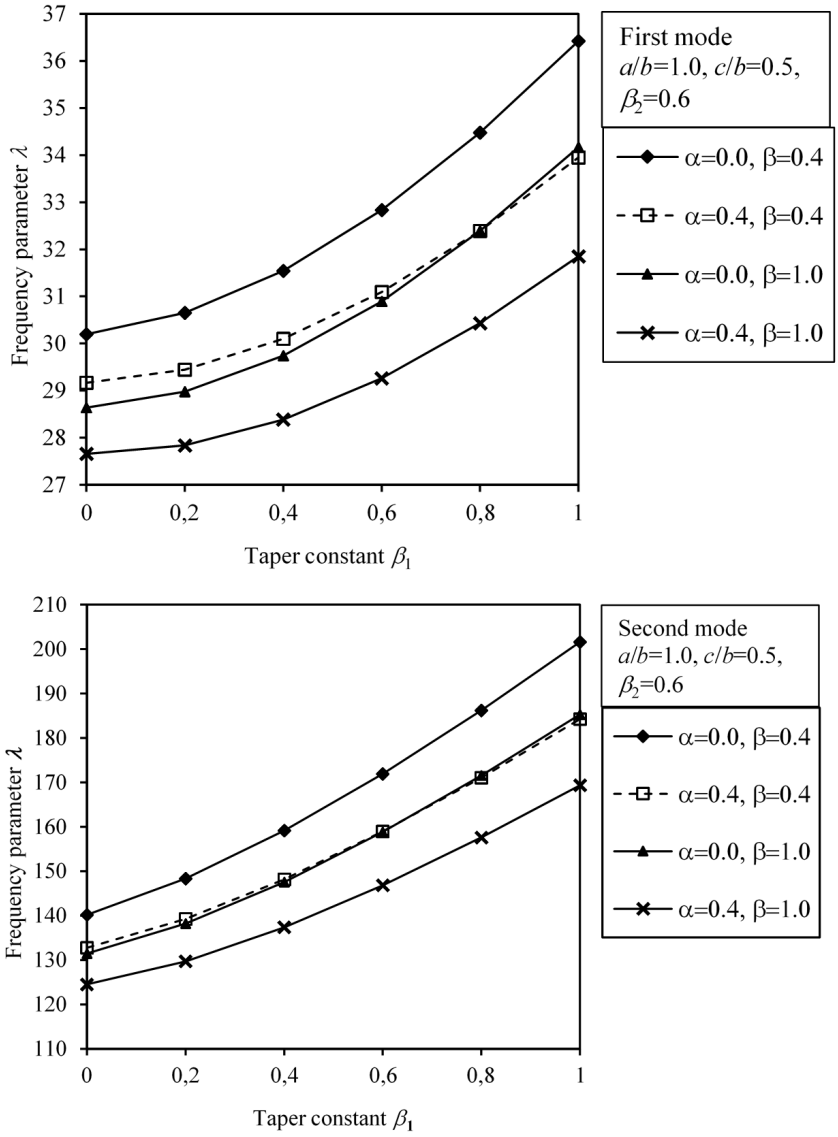

Fig. 2. Variation of frequency parameter with taper constant β_1 for a non-homogeneous trapezoidal plate: top–first mode, bottom–second mode

as

1. $\beta_1 = \beta_2 = 0.0,\ \beta = 0.4,$
2. $\beta_1 = \beta_2 = 0.0,\ \beta = 1.0,$
3. $\beta_1 = 0.2,\ \beta_2 = 0.6,\ \beta = 0.4,$

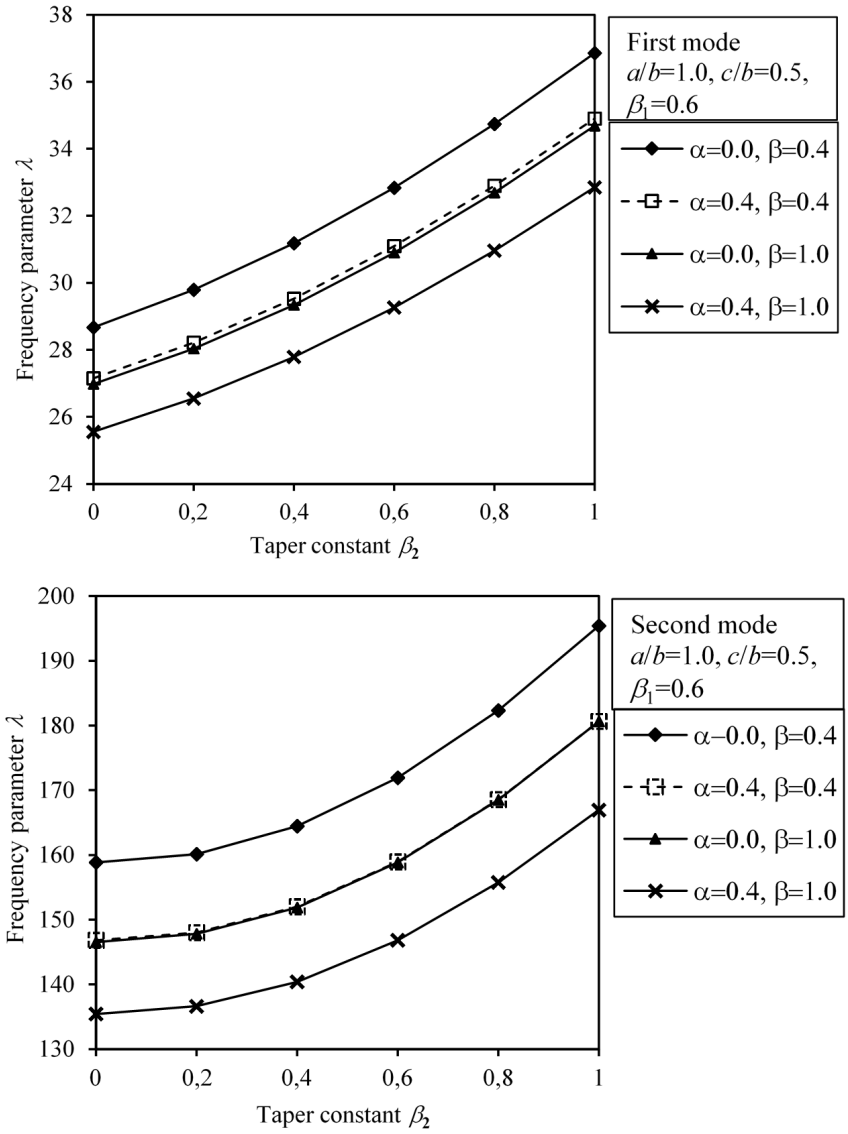

Fig. 3. Variation of frequency parameter with taper constant β_2 for a non-homogeneous trapezoidal plate: top–first mode, bottom–second mode

4. $\beta_1 = 0.2,\ \beta_2 = 0.6,\ \beta = 1.0$.

In case of thermal gradient, the behavior of frequency parameter λ can be examined from the above Fig. 4. So, it can be concluded that as thermal gradient α increases, frequency parameter λ decreases for both first and second modes of vibration.

Fig. 5 represents the effect of aspect ratio c/b (varying from 0.25 to 1.0) on fre-

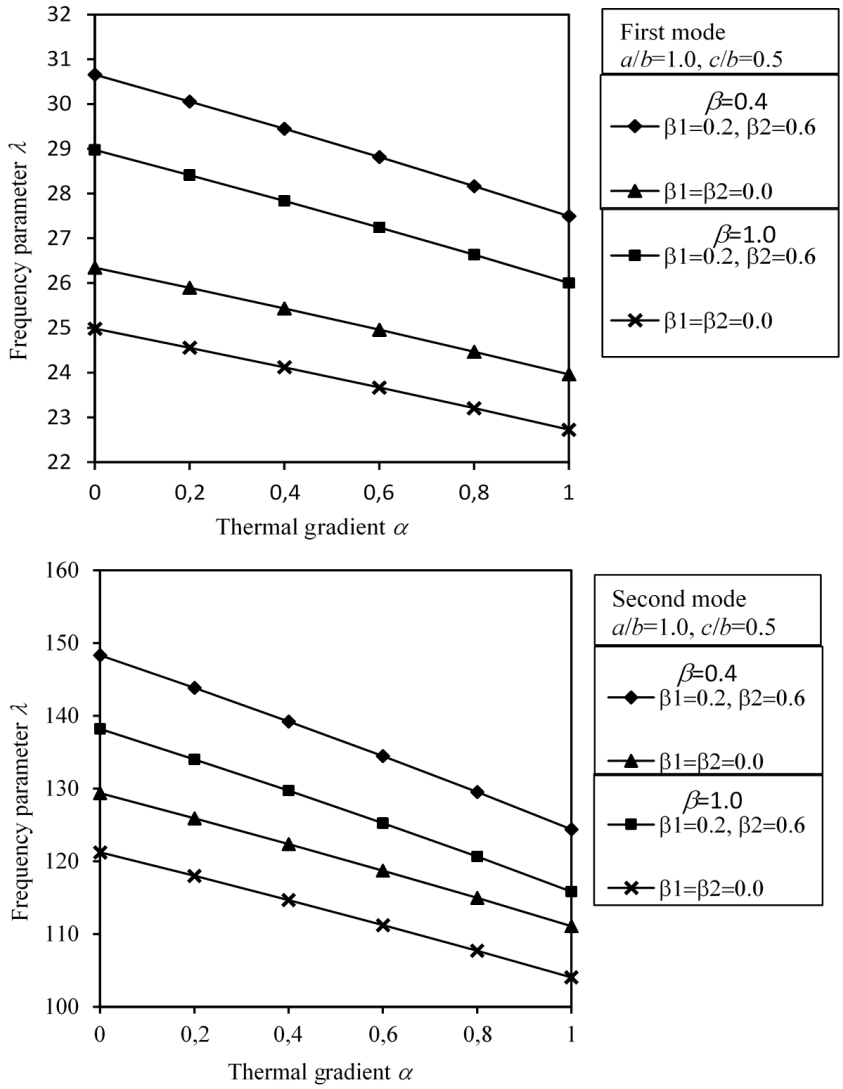

Fig. 4. Variation of frequency parameter with thermal gradient α for a non-homogeneous trapezoidal plate: top–first mode, bottom–second mode

quency parameter λ for both first and second modes of vibration for the following values (i) Aspect ratio $a/b = 0.75$ and 1.0 and (ii) taper constant $\beta_1 = \beta_2 = 0.6$) has been taken by considering four combinations of thermal gradient and non-homogeneity constant as $\alpha = 0.0$ and $\beta = 0.0$, $\alpha = 0.4$ and $\beta = 0.0$, $\alpha = 0.0$ and $\beta = 0.4$ and $\alpha = 0.4$ and $\beta = 0.4$. These figures make clear that as aspect ratio c/b increases, the frequency parameter decreases. It is also noticed that as aspect ratio a/b increases from 0.75 to 1.0, the frequency parameter also increases for both the modes of vibration.

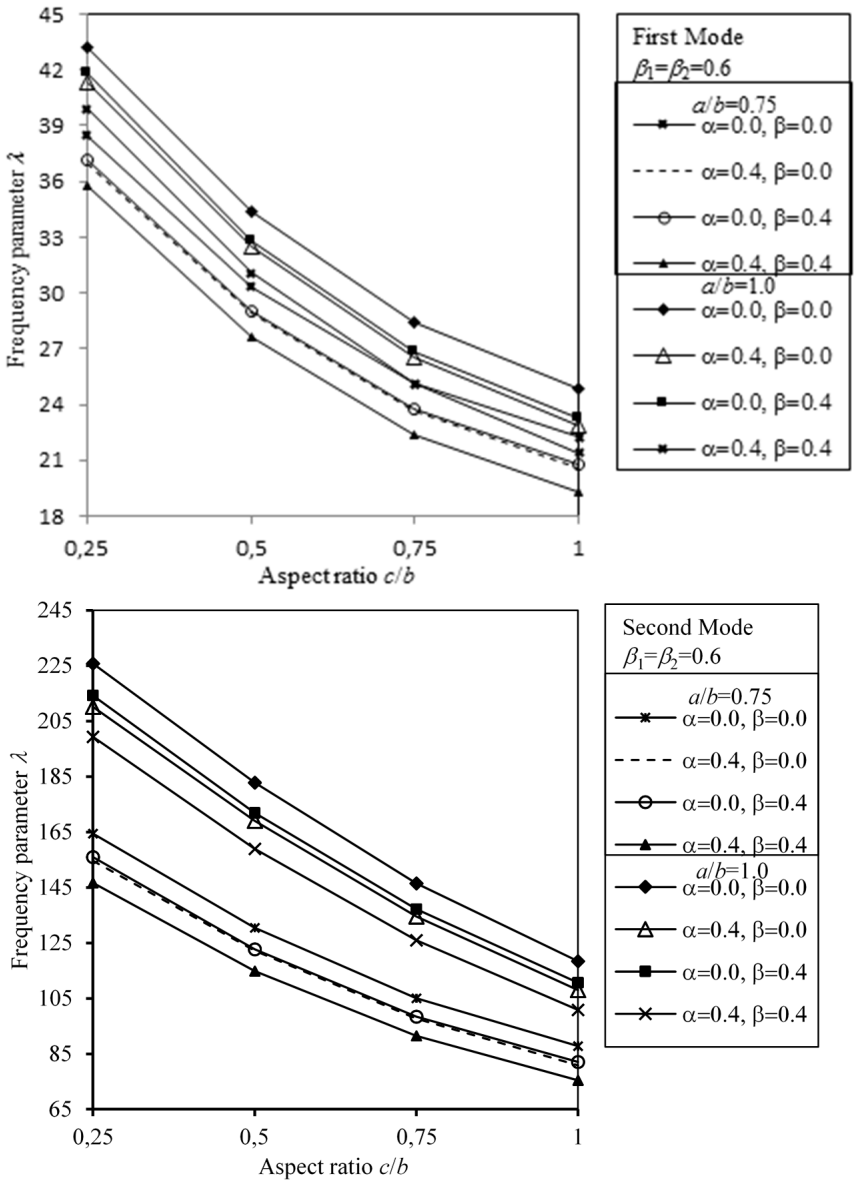

Fig. 5. Variation of frequency parameter with aspect ratio c/b for a non-homogeneous trapezoidal plate: top–first mode, bottom–second mode

Fig. 6 displays the effect of non-homogeneity constant β varying from 0.0 to 1.0 on the frequency parameter λ for different combinations of thermal gradient α and taper constants β_1 and β_2 as follows: (i) $\beta_1 = \beta_2 = 0.0$ and $\alpha = 0.0$, (ii) $\beta_1 = \beta_2 = 0.0$ and $\alpha = 0.4$, (iii) $\beta_1 = 0.2,\ \beta_2 = 0.6$ and $\alpha = 0.0$, (iv) $\beta_1 = 0.2,\ \beta_2 = 0.6$ and $\alpha = 0.4$.

Thus, Fig. 6 shows that on increasing the values of non-homogeneity constant the frequency parameter decreases and furthermore, as taper constants values increases the frequencies also increase for both modes of vibration.

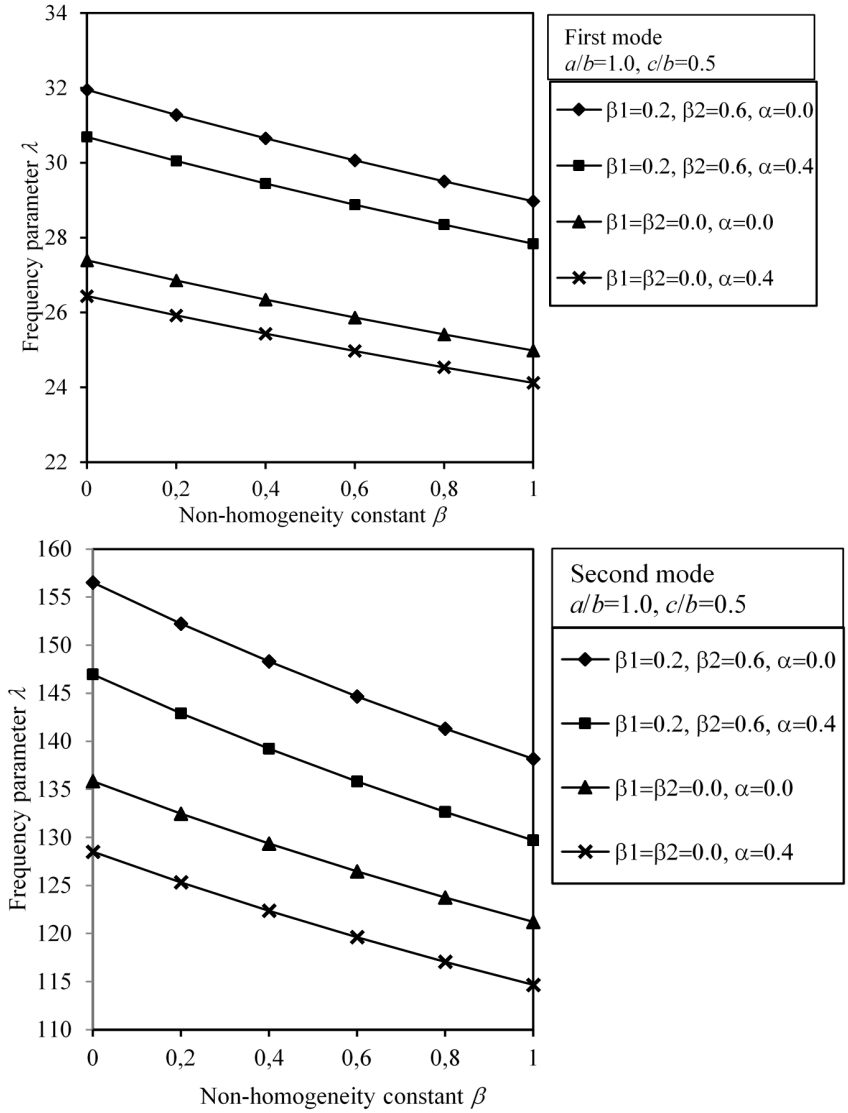

Fig. 6. Variation of frequency parameter with non-homogeneity constant β for a non-homogeneous trapezoidal plata: top–first mode, bottom–second mode

4. Conclusion

In the present study, through graphical representation the following results are given as follows:

1. For both modes of vibration frequency parameter λ increases on increasing the taper constants β_1 and β_2.

2. For both modes of vibration frequency parameter λ decreases on increasing the thermal gradient α, aspect ratio c/b and non-homogeneity constant β.

3. From graphs in Fig. 5, it is concluded that as aspect ratio a/b increases from 0.75 to 1.0, the frequency parameter λ also increases for both modes of vibration. In case of aspect ratio a/b taken as 0.75 and non-homogeneity constant β increases from 0.0 to 0.4, the frequencies decrease and the same in the case when aspect ratio a/b is taken as 1.0.

4. From graphs in Fig. 6, it is concluded that as taper constants increases, the frequency parameter also increases.

References

[1] P. A. A. Laura, R. O. Grossi, G. I. Carneiro: *Transverse vibrations of orthotropic rectangular plates with thickness varying in two directions and with edges elastically restrained against rotation.* Journal of Sound and Vibration *63* (1979), No. 4, 499–505.

[2] S. K. Malhotra, N. Ganesan, M. A. Veluswami: *Vibrations of orthotropic square plates having variable thickness (parabolic variation).* Journal of Sound and Vibration *119* (1987), No. 1, 184–188.

[3] A. R. Kukreti, J. Farsa, C. W. Bert: *Differential quadrature and Rayleigh–Ritz methods to determine the fundamental frequencies of simply supported rectangular plates with linearly varying thickness.* Journal of Sound and Vibration *189* (1996), No. 1, 103–122.

[4] K. Bhasker, B. Kaushik: *Simple and exact series solutions for flexure of orthotropic rectangular plates with any combination of clamped and simply supported edges.* Composite Structures *63* (2004), No. 1, 63–68.

[5] Y. Kumar, S. K. Tomar: *Free transverse vibrations of monoclinic rectangular plates with continuously varying thickness and density.* International Journal of Applied Mechanics and Engineering *11* (2006), No. 4, 881–900.

[6] A. K. Gupta, A. Kumar, Y. K. Gupta: *Vibration of visco-elastic parallelogram plate with parabolic thickness variation.* Applied Mathematics *1* (2010), No. 2, 128–136.

[7] A. K. Gupta, Kumud Rana: *Thermal effect on vibration of non-homogeneous parallelogram plate of parabolically varying thickness.* Asian Journal of Applied Sciences *1* (2013), No. 1, 50–58.

[8] Anupam Khanna, Pratibha Arora: *Theoretical analysis on thermally induced vibration of tapered parallelogram plate with mixed boundary conditions.* Journal of Vibroengineering *16* (2014), No. 3, 1276–1283.

[9] B. Singh, S. Chakraverty: *Transverse vibration of circular and elliptic plates with quadratically varying thickness.* Indian Journal of Pure and Applied Mathematics *22* (1991), No. 9, 787–803.

[10] A. P. Gupta, N. Sharma: *Forced axisymmetric response of an annular plate of parabolically varying thickness.* International Journal of Mechanical Sciences *41* (1999), No. 1, 71–83.

[11] U. S. Gupta, R. Lal, S. Sharma: *Vibration analysis of non-homogeneous circular plate of nonlinear thickness variation by differential quadrature method.* Journal of Sound and Vibration *298* (2006), Nos. 4–5, 892–906.

[12] W. Nowacki: *Thermo Elasticity.* Pergamon Press, New York (1962).

[13] J. S. Tomar, D. C. Gupta, N. C. Jain: *Free vibrations of an isotropic nonhomogeneous infinite plate of parabolically varying thickness.* Indian Journal of Pure and Applied Mathematics *15* (1984), No. 2, 211–220.

[14] S. Chakraverty, R. Jindal, V. K. Agarwal: *Effect of non-homogeneity on natural frequencies of vibration of elliptic plates.* Meccanica *42* (2007), No. 6, 585–599.

[15] K. M. Liew, M. K. Lim: *Transverse vibration of trapezoidal plates of variable thickness: Symmetric trapezoids.* Journal of Sound and Vibration *165* (1993), No. 1, 45–67.

[16] M. S. Qatu: *Natural frequencies for cantilevered laminated composite right triangular and trapezoidal plates.* Composites Science and Technology *51* (1994), No. 3, 441–449.

[17] A. K. Gupta, P. Sharma: *Study the thermal gradient effect on frequencies of a trapezoidal plate of linearly varying thickness.* Applied Mathematics *1* (2010), No. 5, 357–365.

[18] A. K. Gupta, P. Sharma: *Thermal analysis on frequencies of non-homogeneous trapezoidal plate of variable thickness and density.* Acta Technica CSAV *58* (2013), No. 2, 189–205.

[19] A. K. Gupta, S. Sharma: *Effect of thermal gradient on vibration of non-homogeneous orthotropic trapezoidal plate of linearly varying thickness.* Ain Shams Engineering Journal *4* (2013), No. 3, 523–530.

[20] S. Shokrollahi, S. Shafaghat: *A global Ritz formulation for the free vibration analysis of hybrid metal-composite thick trapezoidal plates.* Scientia Iranica *23* (2016), No. 1, 249–259.

[21] Kavita, S. Kumar, P. Sharma: *Study of temperature behaviour on thermally induced vibration of non-homogeneous trapezoidal plate with bi-linearly varying thickness.* Journal of Applied Mathematics and Physics *4* (2016), No. 10, 1936–1948.

[22] Kavita, P. Sharma, S. Kumar: *Thermal effect on vibration of non-homogeneous trapezoidal plate with bilinear thickness variation and parabolic density variation.* Acta Technica CSAV *62* (2012), No. 1, 57–70.

Received June 15, 2018

Acta Technica *63* No. 6/2018, 845–856

A mathematical model of dynamical processes in multi-mass transport systems[1]

Victor Zviadauri[2], Giorgi Tumanishvili[3], Tamaz Morchadze[4], Nunu Rusadze[5]

Abstract. Inertial loads in the transport systems have a significant influence on their normal operation and durability. In this connection, in spite of wide spectrum of the researches, the existent dynamical models need perfection for identical mapping of the real processes; for example, inertial interaction of the masses being in the direct contact is not considered properly. A new systemic approach to drawing up a generalized mathematical model of spatial oscillatory movement of the transport means (locomotive, vibratory transportation and technological machine etc.) as a multi-mass system is considered in the work. At obtaining a mathematical model of the locomotive vibrations the movements of the wheel-set relative to the rail and drive were considered as relative and translatory. This allowed us to present variation of the rail inertial force as depending on the sign of the wheel-set vibrations, likewise the gear wheels interaction between the wheel-set and motor. The methods of development of the noted mathematical model and some results of the mathematical modeling, including those showing reduction of dynamical loads depending on the type of connection of the drive to the wheel-set (rigid connection, elastic suspension) are given. With the help of the locomotive dynamical model is shown that at using the wheel-set of new construction developed by the authors the lateral loads decrease significantly.

Key words. Multi-mass system, decrease of the unsprung masses, mathematical model, oscillations of the masses, systemic approach.

[1]This work was supported by Shota Rustaveli National Science Foundation of Georgia (SRNSFG) N FR17_292, "Mathematical modeling of the vibratory technological processes and design of the new, highly effective machines."

[2]R. Dvali Institute of Machine Mechanics, 0186, Georgia, Tbilisi, Mindeli st. No. 10; e-mail: v_zviadauri@yahoo.com

[3]R. Dvali Institute of Machine Mechanics, 0186, Georgia, Tbilisi, Mindeli st. No. 10; e-mail: gukagio@yahoo.com

[4]Faculty of Technical Engineering, Akaki Tsereteli State University, 59 Tamara Mepe, Kutaisi, 4600 Georgia; e-mail: tamazmor@mail.ru, corresponding author

[5]Faculty of Technical Engineering, Akaki Tsereteli State University, 59 Tamara Mepe, Kutaisi, 4600 Georgia; e-mail: nunukarus@mail.ru

1. Introduction

Dynamical loads caused by the oscillations significantly affect locomotive operation and cause heavy wear of its moving members and their early breakdown.

Inertial interaction of the masses is not fully reflected in the existing dynamic and mathematical models of railway vehicles [1, 2, 3] describing the oscillatory processes that are the main sources of the damage. The given paper describes interaction of teeth of the driving gear "connecting rod—wheel-set" in the connection with the rest of the locomotive masses, as well as the inertial effect of the mounted wheels on rails.

Based on the above mentioned, the oscillations of the mounted wheels are considered as relative [4, 5] with regard to both the rail and connecting rod; therewith, besides the elastic forces, their inertial interactions also contribute to the formation of the oscillations of each of them.

2. Construction of the dynamic and mathematical models

A spatial dynamic model of the locomotive, as a multi-mass oscillatory system with the concentrated masses and elastic-damping connections between them, is presented in Fig. 1, left part, which includes traction motor m_6 with a driving gear. The rotational movements are expressed by the Euler's angles (Fig. 1, right part).

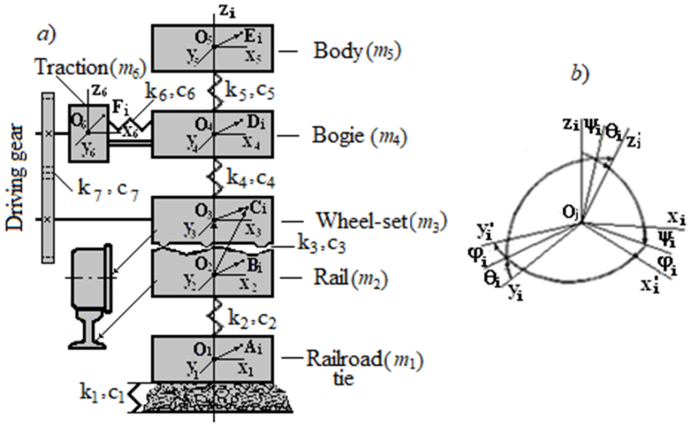

Fig. 1. Dynamic model of locomotive: left–a general (multi-mass) scheme, right–Euler's angles of the rotational movement

The elastic linkages between the masses are provided by the elastic elements with rigidities $\boldsymbol{k}_1$, $\boldsymbol{k}_2$, $\boldsymbol{k}_3$, $\boldsymbol{k}_4$, $\boldsymbol{k}_5$, $\boldsymbol{k}_6$ and $\boldsymbol{k}_7$, as well as by inertial interactions between the wheel-set and rail and between the teeth of the wheel-set and traction engine. Particularly, $\boldsymbol{k}_3$ and $\boldsymbol{k}_7$ are the contact rigidities between the wheel and rail and between the teeth of the drive and wheel-set gear wheels.

When deriving equations of the spatial oscillatory motion a method of the systematic approach [4, 5] was used.

For description of spatial movement of the system given in Fig. 1 we draw up kinetic energies for all mass. For this purpose we determine vector expressions of velocities of free points $A_i,\ B_i,\ C_i,\ D_i,\ E_i,\ F_i$ of masses $m_1,\ m_2,\ m_3, m_4, m_5, m_6$:

$$V_{\mathrm{A}i} = V_{\mathrm{O}1} + \omega_{\mathrm{O}1} \times r_{1i}, \quad V_{\mathrm{B}i} = V_{\mathrm{O}1} + \omega_{\mathrm{O}2} \times r_{2i}\,,$$

$$V_{\mathrm{C}i} = V_{\mathrm{O}2} + \omega_{\mathrm{O}2} \times R_{3i} + V_{\mathrm{O}3} + \omega_{\mathrm{O}3} \times r_{3i}\,,$$

$$V_{\mathrm{D}i} = V_{\mathrm{O}4} + \omega_{\mathrm{O}4} \times r_{4i}, \quad V_{\mathrm{E}i} = V_{\mathrm{O}5} + \omega_{\mathrm{O}5} \times r_{5i}\,,$$

$$V_{\mathrm{F}i} = V_{\mathrm{O}6} + \omega_{\mathrm{O}6} \times R_{6i} + V_{\mathrm{O}6} + \omega_{\mathrm{O}6} \times r_{6i}\,.$$

Here, $V_{\mathrm{A}i}, ..., V_{\mathrm{F}i}$ are the absolute velocities of points $\mathrm{A}_i, ..., \mathrm{F}_i$, $V_{\mathrm{O}1}, ..., V_{\mathrm{O}6}$ are linear velocities of the centers of masses $m_1, ..., m_6$, $\omega_{\mathrm{O}_1}, ..., \omega_{\mathrm{O}6}$ stand for the rotary velocities of masses $m_1, ..., m_6$ and $r_{1i}, ..., r_{6i}$ represent the position vectors of the free points of masses relative to the proper centers.

Kinetic energies will correspondingly have the forms:

$$T_1 = \sum_i^{n_1} M_{1i} \frac{V_{\mathrm{A}i}^2}{2},\ T_2 = \sum_i^{n_2} M_{1i} \frac{V_{\mathrm{B}i}^2}{2},\ T_3 = \sum_i^{n_3} M_{3i} \frac{V_{\mathrm{C}i}^2}{2}\,,$$

$$T_4 = \sum_i^{n_4} M_{4i} \frac{V_{\mathrm{D}i}^2}{2},\ T_5 = \sum_i^{n_5} M_{5i} \frac{V_{\mathrm{E}i}^2}{2},\ T_6 = \sum_i^{n_6} M_{6i} \frac{V_{\mathrm{F}i}^2}{2}\,.$$

A movement of the wheel-set relative to the rail and traction motor is regarded as relative, but movements of the rail and traction motor are considered to be the bulk motions. By this approach, along with the elastic and resistive forces the inertial interactions between the teeth and between the wheel-set and rail will appear in the equations.

To illustrate the sequence in which the equations are obtained, we shall consider spatial oscillatory motion of one of the units—a wheel-set as a complex movement relative to the rail performing in its turn a bulk motion.

At oscillatory motion of the wheel-set m_3 relative to the rail m_2, the vector expression of the absolute velocity of spatial motion of its free point C_i (Fig. 2, right part) would be

$$V_{\mathrm{C}_1 i} = V_{\mathrm{O}2} + \omega_{\mathrm{O}2} \times R_{3i} + V_{\mathrm{O}3} + \omega_{\mathrm{O}3} \times r_{3i}\,, \tag{1}$$

where $V_{\mathrm{O}2}$ is the linear velocity of the center of gravity of the rail, $V_{\mathrm{O}3}$ is the linear velocity of the center of gravity of the wheel-set, $\omega_{\mathrm{O}1}$ and $\omega_{\mathrm{O}3}$ denote the velocities of the rail and wheel-set rotary movements, r_{3i} and R_{3i} represent the position vectors of the wheel-set free point relative to the own coordinate system and that of the rail accordingly (see Fig. 2).

The expression of kinetic energy of the wheel-set will take the form:

$$T_3 = \sum_{i=1}^{n_3} M_{3i} \frac{V_{\mathrm{C}i}^2}{2} = \frac{1}{2} \sum_{i=1}^{n_3} M_{3i} [V_{\mathrm{O}_2} + \omega_{\mathrm{O}_2} (\mathrm{O}_2\mathrm{O}_3 + r_{3i}) + V_{\mathrm{O}_3} + \omega_{\mathrm{O}_3} \times r_{3i}]^2\,, \tag{2}$$

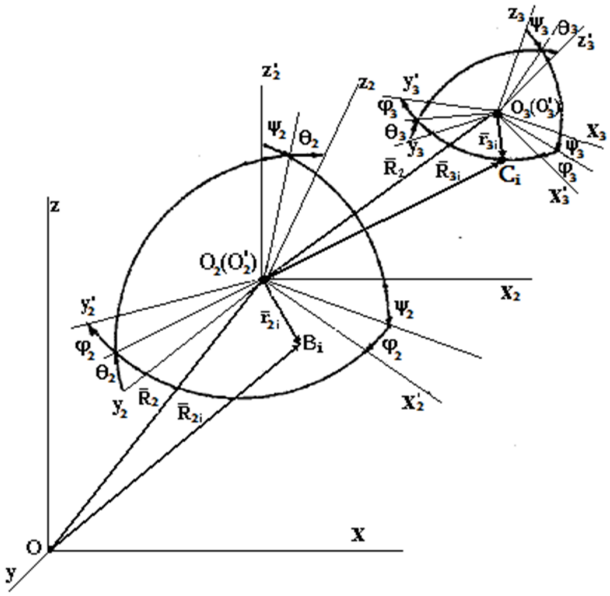

Fig. 2. Oscillatory movement of the wheel-set in relation to the rail

where $O_2O_3 + r_{3i} = R_{3i}$ (Fig. 2).

To obtain analytical expressions for kinetic energy, the expression (2) is decomposed relative to the coordinate system connected to any mass by means of direction cosines; the latter ones, for their part, are decomposed into the Euler's angles with various approximations depending on the values of oscillations.

After decomposition of the total kinetic energy of all the masses along the coordinate axes of one of the masses, the Lagrange equation is applied in relation to this amount; this results in obtaining a system of differential equations of spatial oscillations of the locomotive as an integrated mechanical system "cross-tie—rail—wheel-set—bogie—body—traction motor".

For the instant case, Lagrange equation will have the following form:

$$\frac{\mathrm{d}}{\mathrm{d}t}\left(\frac{\partial T}{\partial \dot{q}_i}\right) - \frac{\partial U}{\partial q_i} + \frac{\partial \Phi}{\partial \dot{q}_i} = Q_{q_i}\,, \tag{3}$$

where T and U are the sums of the kinetic and potential energies [6], [7], [8] of the masses

$$T = \sum_{j=1}^{6} T_j, \quad U = \sum_{j=1}^{6} U_j, \quad j = 1, ..., 6 \tag{4}$$

and q_i accepts the values of the coordinates of motion (oscillation) of the masses in the space

$$q_i = x_1, y_1, z_1, \theta_1, \psi_1, \varphi_1, ..., x_6, y_6, z_6, \theta_6, \psi_6, \varphi_6\,.$$

If we consider a linear form of the vibratory movement, then a general expression

of the potential energy will have the form

$$U = \frac{1}{2}\sum_{i,k=1}^{n} k_{i,k} q_i q_k$$

or in the quadrature form

$$U_i = \frac{1}{2}\sum_{i=1}^{6}(k_x^i x_i^2 + k_y^i y_i^2 + k_z^i z_i^2 + k_\theta^i \theta_i^2 + k_\psi^i \psi_i^2 + k_\varphi^i \varphi_i^2)\,.$$

At oscillatory motions, the forces of resistance are usually regarded as proportional to the motion speeds. In this case, the dissipative function will take the form

$$\Phi_i = \Phi_i(\dot{x}_i, \dot{y}_i, \dot{z}_i, \dot{\theta}_i, \dot{\psi}_i, \dot{\varphi}_i)$$

and for each mass it can be put in equation (3) as

$$\Phi_i = \frac{1}{2}\sum_{i=1}^{6} h_i \dot{q}_i^2$$

or

$$\Phi_i = \frac{1}{2}\sum_{i=1}^{6}(h_x^i \dot{x}_i^2 + h_y^i \dot{y}_i^2 + h_z^i \dot{z}_i^2 + h_\theta^i \dot{\theta}_i^2 + h_\psi^i \dot{\psi}_i^2 + h_\varphi^i \dot{\varphi}_i^2)\,, \tag{5}$$

where q_i for the first mass, for example, accepts the values x_1, y_1, z_1, θ_1, ψ_1, φ_1. Partial velocity derivatives of this function will produce the components of the forces of resistance.

Resistance factors h_i are determined either experimentally, or by coordinates of the attachment points of the elastic elements to the masses [5].

The total dissipative function for the whole locomotive will be

$$\Phi = \sum_{i=1}^{6} \Phi_i\,.$$

External forces that cause oscillatory movements of the locomotive may arise due to damage of the wheel or rail [9, 10], which have a periodic effect of certain frequency depending on the locomotive speed, as well as on the type of damage. The source of the onset of oscillations may also be the violations in the driving gear from traction motor on the wheel-set. In both cases, these forces directly act on the wheel-set, and therefore, they will be presented in the equations of oscillations as the exciting forces.

Decomposition (or "projection") of kinetic energy [11, 12, 13] onto the coordinate axes is carried out by using direction cosines, where the decomposition of sines and cosines of the Euler–Krylov [5] angles is performed by a linear or non-linear approximation depending on the values of the oscillations and required accuracy.

If we confine ourselves to the oscillations, when the angles θ, ψ, φ do not exceed $\pm 30°$, then it would be sufficient to use the first two terms of the decomposition of trigonometric functions of the Euler angles [4, 5] in power series, i.e. $\sin\theta = \theta - \theta^2/$, $\cos\theta = 1 - \theta^2/2$ and so on.

The masses are considered in two positions (Fig. 1 right): I–fixed $O_i x_i y_i z_i$, defined according to design drawings, II–dynamic $O_i' x_i' y_i' z_i'$, displaced under action of the exciting forces.

Rotational movement of the axes of coordinate systems is described by Euler's angles (see Table 1), where α_{ij} denote the direction cosines between the axes. Their expansions by Euler's angles at linear approximations are given in Table 2, and at quadratic approximations in Table 3.

Table 1. Euler's angles describing rotational movement

	x_j	y_j	z_j
x_i	α_{11}	α_{12}	α_{13}
y_i	α_{21}	α_{22}	α_{23}
z_i	α_{31}	α_{32}	α_{33}

Table 2. Direction cosines expanded by Euler's angles with linear approximations

	x_i'	y_i'	z_i'
x_i	1	$-\varphi_i$	ψ_i
y_i	φ_i	1	$-\theta_i$
z_i	$-\psi_i$	θ_i	1

Table 3. Direction cosines expanded by Euler's angles with quadratic approximations

	x_i'	y_i'	z_i'
x_i	$1 - \frac{\psi_i^2}{2} - \frac{\varphi_i^2}{2}$	$-\varphi_i + \psi_i\theta_i$	ψ_i
y_i	φ_i	$1 - \frac{\theta_i^2}{2} - \frac{\varphi_i^2}{2}$	$-\theta_i$
z_i	$-\psi_i - \varphi_i\theta_i$	$-\varphi_i\psi_i + \theta_i$	$1 - \frac{\psi_i^2}{2} - \frac{\theta_i^2}{2}$

For obtaining a system of interconnected differential equations of movement of the system given in Fig. 1 it is necessary to replace vector expressions of kinetic energies of each mass by their projections on the corresponding coordinate axes.

We give here incomplete (because of cumbersomeness) analytical expression of kinetic energy of the wheelset movement relative to the rail that is obtained by expansion of expression (2) and projection on the coordinate axes.

$$T_3 = \frac{1}{2}M_3(\dot{x}_2^2 + \dot{y}_2^2 + \dot{z}_2^2) + \frac{1}{2}M_3(\dot{x}_3^2 + \dot{y}_3^2 + \dot{z}_3^2) +$$

$$+ M_3(\dot\theta_2\dot z_2 y_3 + \dot\psi_2\dot x_2 z_3 - \dot\psi_2\dot z_2 x_3 - \dot\varphi_2\dot x_2 y_2 - \dot\theta_2\dot y_2 z_3 + \dot\varphi_2\dot y_2 x_3) +$$
$$+ M_3(\dot x_2\dot x_3 + \dot y_2\dot y_3 + \dot z_2\dot z_3) +$$
$$+ M_3(\dot y_3\dot z_2\dot\theta_2 - \dot z_3\dot y_2\dot\theta_2 + \dot z_3\dot x_2\dot\psi_2 - \dot x_3\dot z_2\dot\psi_2 + \dot x_3\dot y_2\dot\varphi_2 - \dot y_3\dot x_2\dot\theta_2) +$$
$$+ \frac{1}{2}J_{\mathrm{O}_3x_2}(\dot\theta_2^2 - 2\dot\theta_2\dot\psi_2\varphi_2) + \frac{1}{2}J_{\mathrm{O}_3y_2}(\dot\psi_2^2 - 2\dot\psi_2\dot\theta_2\varphi_2) +$$
$$\frac{1}{2}J_{\mathrm{O}_3z_2}(\dot\varphi_2^2 - 2\dot\varphi_2\dot\psi_2\vartheta_2) - J_{\mathrm{O}_3x_2y_2}(\dot\theta_2\dot\psi_2 - \dot\theta_2^2\varphi_2 + \dot\psi_2^2\varphi_2) -$$
$$- J_{\mathrm{O}_3x_2z_2}(\dot\theta_2\dot\varphi_2 - \dot\theta_2\psi_2 + \dot\varphi_2\dot\psi_2\varphi_2) - J_{\mathrm{O}_3x_2y_2}(\dot\psi_2\dot\varphi_2 - \dot\psi_2^2\theta_2 + \dot\varphi_2^2\theta_2)\,.$$

By substitution of the kinetic, potential and dissipative functions into Lagrange equation (3), a system of equations with proper nonlinearities is obtained.

The mentioned systemic approach allows for obtaining a system of the spatial interrelated equations of movement of the locomotive masses. The equations of the movement are interrelated by the products of forces of inertia, resistance and elasticity of varying degrees. The highest degree of nonlinearity (of the product) will be determined depending on the value of the oscillatory processes in the system (in this case in the locomotive).

Because of cumbersomeness we give for illustration only nonlinear differential equations of the rail spatial linear movement and one rotary movement considering movement of the wheelset (m_3) relative to the rail:

$$(m_2+m_3)\ddot x_2 + m_3\ddot x_3 + m_3(\ddot\psi_2 z_3 + \dot\psi_2\dot z_3 - \ddot\varphi_2 y_2 - \dot\varphi_2\dot y_2 + \ddot z_3\psi_2 + \dot z_3\dot\varphi_2) =$$
$$= (k_{2x}+k_{3x})x_2 - k_{2x}x_1 - k_{3x}x_3 + (c_{2x}+c_{3x})\dot x_2 - c_{2x}\dot x_1 - c_{3x}\dot x_3\,,$$
$$(m_2+m_3)\ddot y_2 + m_3\ddot y_3 + m_3(\ddot\varphi_2 x_3 - \dot\theta_2\dot z_3 - \ddot\theta_2 z_3 - \varphi_2\dot x_3 + \theta_2\ddot z_3 + \dot\varphi_2\dot z_3) =$$
$$= (k_{2x}+k_{3x})x_2 - k_{2x}x_1 - k_{3x}x_3 + (c_{2x}+c_{3x})\dot x_2 - c_{2x}\dot x_1 - c_{3x}\dot x_3\,,$$
$$(m_2+m_3)\ddot z_2 + m_3\ddot z_3 + m_3(\ddot\theta_2 y_3 - \ddot\psi_2\dot x_3 - \psi_2\ddot x_3 + \theta_2\dot y_3 + \psi_3\ddot z_3 + \dot\varphi_2\dot z_3) =$$
$$= (k_{2x}+k_{3x})x_2 - k_{2x}x_1 - k_{3x}x_3 + (c_{2x}+c_{3x})\dot x_2 - c_{2x}\dot x_1 - c_{3x}\dot x_3\,,$$
$$J_{x_2}\ddot\theta_2 + J_{x_2}^{\mathrm{O}_2}\ddot\theta_2 + (J_{x_2}^{\mathrm{O}_2} - J_{y_2}^{\mathrm{O}_2})(\ddot\psi_2\varphi_2 + \dot\varphi_2\dot\psi_2) - J_{y_2}^{\mathrm{O}_2}(\ddot\psi_3\varphi_2 + \dot\varphi_2\dot\psi_3) +$$
$$+ J_{x_2}^{\mathrm{O}_2}(\ddot\theta_2 + \ddot\varphi_3\psi_3 + \dot\varphi_3\dot\psi_3) + m_3(\ddot z_2 y_3 - \ddot y_2 z_3) =$$
$$= (k_{2\theta}+k_{3\theta})\theta_2 - k_{2\theta}\theta_1 - k_{3\theta}\theta_3 + (c_{2\theta}+c_{3\theta})\dot\theta_2 - c_{2\theta}\dot\theta_1 - c_{3\theta}\dot\theta_3\,, \qquad (6)$$

where $k_1, ..., k_6$, $c_1, ..., c_6$ are the coefficients of rigidity and resistance of each elastic system and $J_{x_2}^{\mathrm{O}_2}$, $J_{y_2}^{\mathrm{O}_2}$, $J_{z_2}^{\mathrm{O}_2}$ are the moments of inertia of a mass around the proper coordinate axes.

In equations (6), the nonlinear terms of inertial nature no greater than second order and elastic forces and forces of resistance in the linear form are retained.

As it is seen from the equations and methods for their obtaining, the rail is considered as "carrier" of the movement and the wheelset as a body of relative movement. Therefore, in the given equations the inertia force of the rail (m_2) is

obtained in combination of the wheelset mass $(m_2 + m_3)\ddot{q}_2$ where $q_2 = x_2, y_2, z_2$, as the wheelset is connected to it by the second order nonlinear terms of inertial nature.

The paper describes only linearized equations (7) of vertical (as predominant) oscillations z_i of masses m_1, m_2, m_3, m_4, m_5, m_6 and shows some results of solutions (Figs. 4 and 5). In the second, third and sixth equations, along with the elastic forces, the inertial forces of masses m_2, m_3 and m_6 are also involved, which are in the direct contact with each other. Force $F(t)$ is a periodic force transferred from the rail to the wheelset, and it can be approximately expressed as a sine function

$$\begin{cases} m_1\ddot{z}_1 = (k_1 + k_2)z_1 - k_2 z_2 + (c_1 + c_2)\dot{z}_1 - c_2\dot{z}_2, \\ (m_2 + \mu_1 m_3)\ddot{z}_2 - m_3\ddot{z}_3 = (k_2 + k_3)z_2 + k_2 z_1 - k_3 z_3 + (c_2 + c_3)\dot{z}_2 - c_2\dot{z}_1 - c_3\dot{z}_3, \\ m_3\ddot{z}_3 - m_3(\ddot{z}_2 + \ddot{z}_6) = k_4(z_3 - z_4) - c_4(\dot{z}_3 + \dot{z}_4) + F(t), \\ m_4\ddot{z}_4 = k_4(z_4 - z_3) + k_5(z_4 - z_5) - c_4(\dot{z}_4 - \dot{z}_3) - c_5(\dot{z}_4 - \dot{z}_5), \\ m_5\ddot{z}_5 = k_4(z_5 - z_4) - c_4(\dot{z}_5 - \dot{z}_4), \\ (m_6 + \mu_2 m_3)\ddot{z}_6 - m_6\ddot{z}_3 = k_6(z_6 - z_4) - c_6(\dot{z}_6 - \dot{z}_4), \end{cases} \tag{7}$$

$$F(t) = A\sin\omega t\,, \tag{8}$$

where A is the peak value of the force and ω is the frequency of the exciting force dependent on the locomotive speed. Contact rigidities k_3 and k_7 are absent in these equations between the masses m_2, m_3 and m_3, m_6. Connections between the mentioned masses are of inertial nature and interaction is realized by the terms $(m_2 + \mu_1 m_3)\ddot{z}_2$ and $(m_6 + \mu_2 m_3)\ddot{z}_6$ of the second and sixth equations of the system (7).

In contrast to the existing models [14], [15], [16], [17], equations (7) contain terms with sums of the contiguous masses that indicates their joint movement provided that coefficient μ may take various values between 0 and 1 and vary depending on the sign of vibration of the mass having a relative movement (e.g. a wheel relative to the rail) that is taken into account in modeling. The noted condition increases the degree of identity of the mathematical model and physical processes [18].

With the use of Runge–Kutta methods, on the basis of the mathematical model (7) the numerical experiments have been conducted for various values of rigidities of the elastic links, resistance forces and masses. The frequency of the exciting force was calculated for the locomotive speed 100 km/h, and the diameter of wheel 1 m, which, in the case of a single push per one rotation, generates oscillation frequency $\omega = 8.7$ Hz.

3. Some modeling results

At this stage, the research results are presented regarding the influence of a type of cushioning of the traction motor: partial (elastic—k_6 and rigid—k_1 fixing, see Fig. 3) and complete (without fixing). In the second case, the engine is attached to the bogie only by the elastic elements and, accordingly, the wheel-set mass and the inertial effect on the rail are reduced.

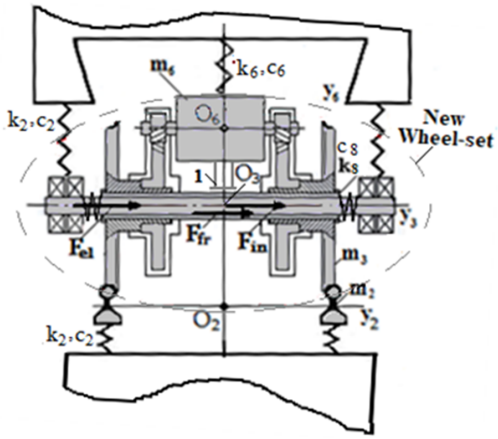

Fig. 3. New wheel-sat with a partially sprung traction motor

The figures below illustrate some oscillograms of solutions of the system of equations (7). Figure 4 illustrates the oscillogram of vertical oscillations of the wheel-set: 1) the natural oscillations (≈ 1, or 2 Hz) where z_3^*, $\dot{z}_3^*$ and $\ddot{z}_3^*$ are the trajectory, speed and acceleration, and 2) caused by the influence of the rail (≈ 8.7 Hz) where the same quantities are denoted as z_3, $\dot{z}_3$ and $\ddot{z}_3$.

Figure 5 shows the oscillograms of the wheel-set inertia force F_{in} with unsprung (2000 kg) and sprung (700 kg) traction motor.

The engine is connected to the new wheel-set [19] developed by the authors (Fig. 3), where lateral loads are decreased at movement in the curves. The lateral force in the curves is controlled by the springs (k_8). Later on, it is planned consideration of the mentioned dynamical process and preparation of the paper.

4. Conclusion

1. The proposed method and the obtained system of equations of the oscillatory movement of the locomotive masses allow for a study of the dynamic processes of interaction of the masses with the use of the mathematical modeling by variation of masses and other physical parameters.

2. Through the mathematical modeling, it has been demonstrated that at complete sprung of the traction motor a considerable reduction in dynamical loads on the wheel-set takes place.

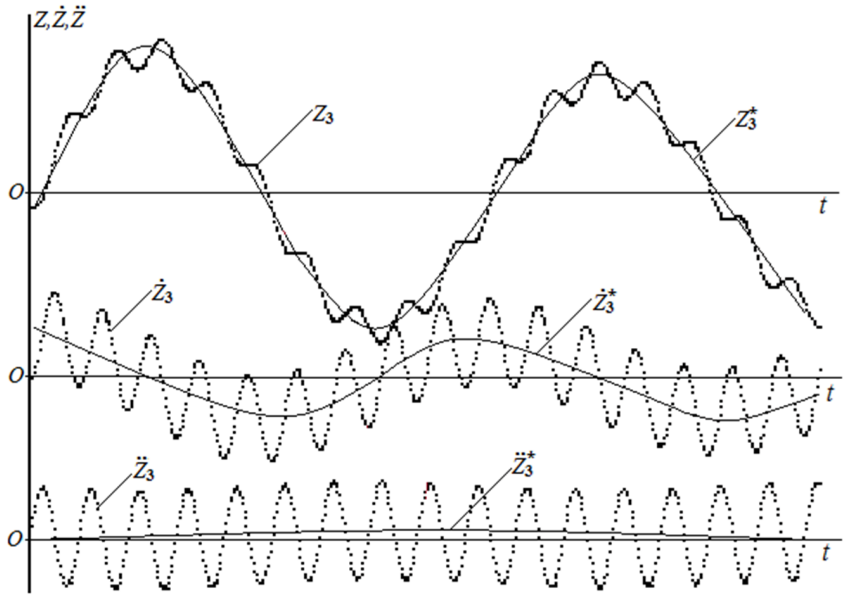

Fig. 4. Oscillograms of vertical oscillations of wheel-set

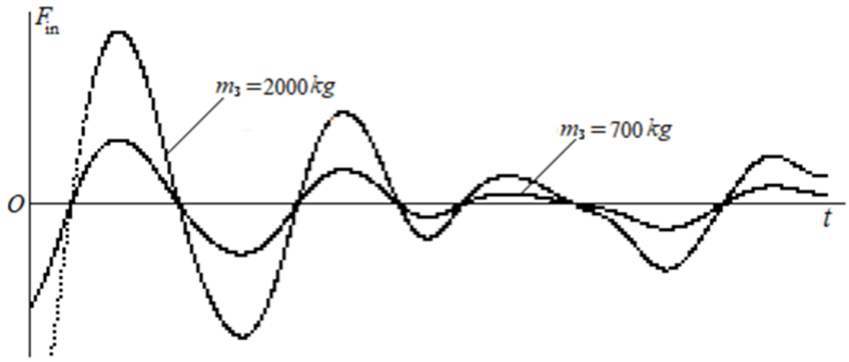

Fig. 5. Oscillograms of wheel-set inertia forces (damped) without sprung of the traction motor, and with a partial sprung

3. A generalized mathematical model developed on the basis of a systemic approach can be used for studying both the individual and linked masses of the railway transport, as well as similar multi-mass oscillatory systems (vibratory transportation and technological machine etc.).

4. Subsequently, the algorithm will be put together, comprehensive mathematical modeling of the dynamical process will be carried out and the results will be published.

References

[1] M. Verigo, A. Kogan: *Vzaimodejstvije dorogi i podvizhnogo sostava.* Book, Transport, Moscow (1986).

[2] O. Ahmedov, V. Zeman, M. Byrtus: *Modeling of vibration and modal properties of electric locomotive drive.* Engineering Mechanics *19* (2012), No. 2–3, 165–176.

[3] M. Antali, S. Gabor, S. J. Hogan: *Kinematic oscillations of railway wheelsets.* Multibody System Dynamics *34* (2015), No. 3, 259–274.

[4] V. S. Zviadauri: *Dinamika vibracionnych transportno-technologicheskich mashin.* Book, Metzniereba, Tbilisi (2001).

[5] R. Ganiev, V. Kononenko: *Dinamika tverdych tel.* Book, Nauka, Moscow (1986).

[6] `www.ellibs.com`.

[7] J. Taler, P. Duda: *Solving direct and inverse heat conduction problems.* Springer, Berlin, 2006.

[8] J. Krzyzanowski, J. Gluch: *Heat-flow diagnostics of energetic objects.* Polish Academy of Sciences, Gdansk, 2004.

[9] I. Blekhman, E. Kremer: *Vertical-longitudinal dynamics of vehicle on road with unevenness.* Procedia Engineering *199* (2017), 3278–3283.

[10] K. Oldknow: *Wheel-rail interaction fundamentals WRI 2017.* Principle course (2017).

[11] `www.Kortingboeken.nl`.

[12] `www.General-ebooks.com`.

[13] N. Chakraborty, S. Chakraborty: *A generalized object-oriented computational method for simulation of power and process cycles.* Proceedings of the Institution of Mechanical Engineers, Part A: Journal of Power and Energy *216* (2002), No. 2, 155–159.

[14] S. G. Zhang, W. H. Zhang, X. S. Jin: *Dynamics of high speed wheel/rail system and its modeling.* Chinese Science Bulletin *52* (2007), No. 11, 1566–1575.

[15] S. K. Sharma, R. C. Sharma, A. Kumar, S. Palli: *Challenges in rail vehicle-track modeling and simulation.* International Journal of Vehicle Structures & Systems *7* (2015), No. 1, 1–9.

[16] R. E. Roberson, R. Schwertassek: *Dynamics of multibody systems.* Book, Springer-Verlag, Berlin Heidelberg (1998).

[17] A. Sladkovski: *Rail vehicle dynamics and associated problems.* Silesian University of Technology, Gliwice, Poland (2005).

[18] A. Nagurney, J. F. Smith: *Matematical models of transportation and networks.* Mathematical Models in Economics (2007), `https://pdfs.semanticscholar.org/d7ec/ed5a4951a6686c4ceeaae448261b148b33a4.pdf`.

[19] G. Tumanishvili, T. Natriashvili, G. Goletiani, V. Zviadauri, T. Nadiradze: *Improvement of working conditions of the freight locomotive running gear.* Transport Problems *11* (2016), No. 3, 103–109.

Received June 12, 2018

Acta Technica *63* No. 6/2018, 857–876

Profiling and assessment of the wind power potential in Pakistan

Humaira Yasmeen[1], Ying Wang[1], Muhammad Mohsin[1], Hashim Zameer[1,2]

Abstract. Pakistan is facing a major energy shortage over the past two decades and needs to find new resources that could possibly relieve these energy crises. Currently, government is not only focusing on conventional energy resources like thermal, hydel but also emphasizing on massive potential of renewable energy like wind, solar and biogas. The recent worldwide concern on the environment and climate change has emphasized on the need of economically viable energy with low carbon emissions. However, to address the energy crises in Pakistan wind energy is prominent and viable option because it has low carbon emissions and it can generate cheaper electricity. The objective of this study is to precisely evaluate the wind characteristics and wind power potential of thirteen selected sites in Pakistan. It is worth mentioning that this kind of comprehensive analysis is hardly done for wind power assessment at any location in Pakistan. Results from comprehensive assessment reveal that only four sites comprising Kallar Kahar, Jamshoro, Nooriabad and Sardhi have potential for wind power installation. Our study provides adequate depiction about the actual wind speed and other wind characteristics, e.g., wind shape, scale parameters and capacity factor. In addition, this study provides guideline for policy implications to the government of Pakistan.

Key words. Wind energy, Weibull distribution, Rayleigh distribution, power density, capacity factor.

1. Introduction

Energy is one of the most important determinants of socio-economic development for any nation. Per capita energy supply is considered as a common indicator to determine the development situation of the nation worldwide. Pakistan is a developing nation with the population of almost 200 million suffering from the major energy crisis over the past two decades (Farooq & Shakoor [1]). Energy production in the country is static while the demand is continuously increasing (Khan & Ahmad [2]). Energy production is static because the energy sector of Pakistan is facing numerous

[1]College of Economics and Management, Nanjing University of Aeronautics and Astronautics Nanjing, China
[2]Corresponding author; e-mail: hashimzameer@yahoo.com

challenges like the burden of natural gas subsidies, insufficient revenue collection, line losses of electricity, low power generation, electricity theft and expensive furnace oil (Amer & Daim [3]). However, insufficient natural gas supply and older transmission network is also part of challenges for the energy sector in Pakistan (Kessides [4]). The natural gas production in the country has shown decline during past years, its production level was at the peak of 4.2 billion cubic feet (BCF) per day during the year 2012. The decline in natural gas production in the country is due to issues like security concerns, insufficient investment and regulatory challenges. Currently, the energy sector of Pakistan is majorly dependent on gas that contributes 45 % in overall energy production in the country. The other sources of electricity generation consist of 35 % from imported oil, hydroelectricity contribute 12 %, coal 6 % and the rest of the portion of electricity produced from nuclear energy at 2 %. The hydropower has seasonal drawbacks because the water in dams remains unavailable about four to five months of winter. On the other hand, thermal energy is foreign exchange strenuous and it is plummeting a nation into a long term crises regarding balance of payments.

To quick response the energy crisis, the country needs to take immediate decisions to bridge up the energy gap and to meet energy requirements of the country. No doubt coal is cheaper option to overcome the energy shortfall in the country but coal is not environment friendly option and world is shifting their energy production from coal to other available sources. However, the wind is an environment friendly source of energy production (Ghafoor, ur Rehman, Munir, Ahmad, & Iqbal [5]; Siddique & Wazir [6]). Wind power utilization primarily eradicate emissions of SO_2, NO_2 CO_2, and other injurious squander as compared to traditional harming coal energy plants, radioactive devastate in nuclear power plants and other damaging sources of society. Wind energy considerably decreases dependency on fossil fuels, which strengthen global energy security. Wind energy doesn't emit dangerous gases also it does not contribute to global climate change or global warming. Coal, gas, oil and other conventional sources of power generation produce greenhouse gases and other contaminant. Further, it has a minimum impact on livestock and crop production because it covers only a small area.

Wind energy is speedily increasing among all other renewable energy sources in both developing and developed countries (Bianco, Manca, & Nardini [7]). The energy policy of Pakistan also shows that the country has a keen interest to promote and adopt the renewable energy resources, for example installation of world largest solar project having a capacity of 100 MW. Quid-e-Azam solar park Bahawalput was completed during May, 2015 with mutual collaboration of China (Ali et al. [8]; Sher, Murtaza, Addoweesh, & Chiaberge[9]). Moreover, the reports from year 2011 have indicated that the government of Pakistan spent a huge amount to implement the renewable energy sources (Ahmed, Mahmood, Hasan, Sidhu, & Butt [10]; Sen & Ganguly [11]). These initiatives are significant for fulfilling the continuous increasing demand of electricity and will also reduce the cost of electricity generation. Further, renewable energy significantly reduces pollution and considered as vital for the sustainable environment (Glassley [12]; d'Artis Kancs & Wohlgemuth [13]). Pakistan's area consists of 1100 kilometers of a coastal line that has a huge potential of wind

energy but the country is still producing a small part of energy from the wind (Farooqui [14]; Sheikh [15]). Previous studies highlighted that the government should install more and more wind power plants (Mirza, Ahmad, Majeed, & Harijan [16]; Shoaib, Siddiqui, Amir, & Rehman [17]; Siddique & Wazir [6]; Ullah & Chipperfield [18]). However, to install wind power plant it is important to classify the feasible sites where wind power plants can be installed. The reason to classify the feasible sites is because wind energy varies with a cubic pattern with the average wind speed (Lawan, Abidin, Masri, Chai, & Baharun [19]).

So, a precise assessment of average wind speed is greatly significant to all variety of wind power utilization (Beurskens & Brand [20]; Burton, Sharpe, Jenkins, & Bossanyi [21]). Geographically and temporally wind is highly variable and it makes intricate to give a correct assessment of the wind speed. Traditionally, different mathematical models have been applied and introduced which have been experienced to illustrate the wind speed and wind characteristics. Especially, the Weibull probability distribution function that provide a reasonable demonstration about the variation of hourly wind speed over the year at a proposed site (Burton et al. [21]; de Andrade, Neto, Rocha, & da Silva [22]; Seguro & Lambert [23]). Authenticity and suitability of the Weibull distribution function has been confirmed and assessed by (Ghosh, Shawon, Rahman, & Nath [24]; Usta [25]). Lun & Lam [26] computed the parameters of Weibull probability and Weibull density distribution function for 3 different sites and found that mathematical values of scale and shape parameters for these stations are wide-ranging. The study of Celik [27] proposed the probability distribution function by time series data by estimating the distributional parameters of probability distribution function. Carta and Ramirez [28] demonstrate that the two component mixture of Weibull distribution function is considered as a useful estimation because it provides a heterogeneous wind regime. Yaniktepe, Koroglu, & Savrun [29] scrutinized the quality of wind power, wind characteristics through Rayleigh and Weibull distribution. Akdağ & Dinler [30] concluded that the accurate evaluation of Weibull shape and scale parameters is necessary for the wind energy potential estimation. Academic literature indicates that previous studies used different numerical methods to calculate the approximation of Weibull and Rayleigh distribution parameters (Chang [31]; Islam, Saidur, & Rahim [32]). Also, the latest studies done to estimate the wind power potential of different constituency with the help of Weibull and Rayleigh distribution functions and their results shows that the Weibull and Rayleigh distributions provide good estimates of wind power potential, wind characteristics and wind parameters.

Thus, to provide support for future energy projects and policy implications to the government of Pakistan, this study analyzed the data of thirteen prospective sites using modified Weibull probability distribution function. Although, researchers used suitability of wind speed to distribute the wind data at a Weibull distribution function but in our case, unlike others we defined the probability for given model of Weibull distribution and Rayleigh distribution function and we come up with a novel approach that distinguish our work from others. This study provides a comprehensive assessment of wind power potential, wind characteristics and wind parameters at prospective sites. In addition, to further ensure the validity of results,

this study reassesses the results using Rayleigh distribution function. Our study not only accompanied an empirical estimation of wind characteristics but this study also present a distinguish mechanism which adds a value to make a strong understanding of wind project installation.

Further parts of the paper are constructed as follows: Section two explains the background of wind energy, section 3 describes the data and methodology, section 4 is used to describe results and discussion and section 5 concludes the study and highlights some policy implications for the government of Pakistan.

2. Background of study

Pakistan is a developing country, facing severe energy crises from last two decades (Farooq & Shakoor [1]; Farooqui [14]). Electricity consumption in the country is increasing due to increase in the population (Shahbaz, Zeshan, & Afza [33]). With the passage of time, a nonstop increase in energy consumption is widening the gap of energy supply and demand (Farooqui [14]). The Pakistan energy sector is mostly dependent on fossil fuels (Anwar [34]; Mirza et al. [16]). The country has very limited resources of fossil fuels and Pakistan import the fossil fuel to fulfill the demand in the country. These imports put a huge burden on the government and it also create worse situation for foreign exchange reserves. Figure 1 below indicates the current energy mix in the country. Currently, Pakistan is producing most of its electricity from thermal that is continuously creating severe situation for the environment. Less than 1 % electricity in Pakistan is produced from the wind source. Major dependence of energy sector on fossil fuels has increased CO_2 emissions. Past studies have indicated that more than 32 % of CO_2 and 42 % SO_2 emissions in Pakistan are emitting from energy sector (Anwar [34]; Harijan, Uqaili, Memon, & Mirza [35]; Zaman, Abdullah, & Ali [36]).

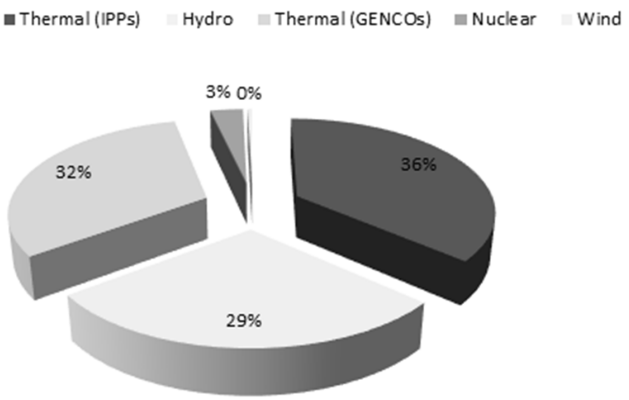

Fig. 1. Current energy mix of Pakistan

Globally the rising concern upon the effect of greenhouse gas emissions and climate change has influenced the governments to develop a sustainable economy that

should reduce the greenhouse gas emissions (Change [37]; Chaturvedi, Clarke, Edmonds, Calvin, & Kyle [38]). To tackle the concerns related to the environment sustainability, global communities are implementing energy saving targets and shifting toward alternate energy sources to minimize greenhouse gas emissions (Bhutto, Bazmi, Zahedi, & Klemeš [39]; Stigka, Paravantis, & Mihalakakou [40]). In this regard, most of the scholars have suggested the wind energy as an alternative source of electricity production (Hosenuzzaman et al. [41]; Özkale, Celik, Turkmen, & Cakmaz [42]). Wind energy is considered as commercially viable and it can significantly reduce environmental pollution.

Moreover, wind energy is reliable, clean and supplying competitive energy to fuel economic growth and to reduce emissions in developed countries. Further, it also enhances the energy security. The data of wind energy shows that 28 countries across the world have greater than 1 000 MW installed capacity of wind electricity, 8 countries having 10 GW installed capacity of wind power. However, 14 countries have the wind power capacity of greater than 5 000 MW (Dai, Herran, Fujimori, & Masui [43]; GWEC [44]; Kumar et al. [45]). A huge amount of $109 billion invested in the field of wind power globally. It is officially declared a sanction in the Paris Agreement that the 55 countries considered necessary to bring it into force and to adopt the strategic decision and implement the policies which can help globally to decrease the impact of global warming about less than 2 °C and idyllically reduce to 1.5 ° C over the next century. Wind energy has a pivotal role in reducing global warming and also it provides cheaper electricity.

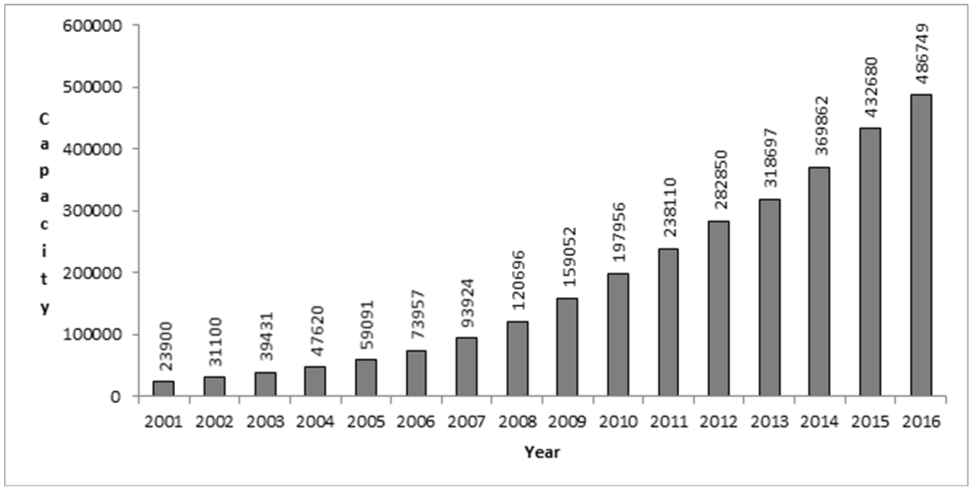

Fig. 2. Global cumulative installed capacity (MW)

Figure 2 shows the continuous increase in the installation of wind energy around the globe. As it can be seen that during year 2001 the installed capacity of wind energy worldwide was just 23 900 MW that reached at the level of 486 749 MW by the end of year 2016 that shows almost 2 000 % increase in the installed capacity of wind energy. The wind energy data of the world indicate that approximately 314 000

wind turbines were revolving around the globe at the end of 2016.

Profiling and assessment of wind energy worldwide is continuously increasing. The data of annual market statistics from Global Wind Energy Council shows that 54 GW wind energy installed worldwide in the year 2016 only. However, the wind energy market bringing world total installed capacity to nearly 487 GW. The wind energy data indicate that China has the capacity of 168 690 MW (34.7 % share) followed by the US with capacity of 82 184 MW (16.9 % share), Germany capacity is 50 018 MW (10.3 % share), Pakistan, India, Spain, United Kingdom, France, Canada, Brazil, Italy and rest of the world surprisingly shows the global market was nevertheless a lesser amount of 2015's record in the world (GWEC [46]).

Pakistan is a rich country in wind blowing geographic aspects and it has 4 weathers system and wind blows 24 hour in many areas of the country. According to NREL and USAID, Pakistan wind energy production capacity is 5 MW/km^2 in windy areas (Aman, Jasmon, Ghufran, Bakar, & Mokhlis [47]; Harijan, Uqaili, Memon, & Mirza [48]; Khahro et al. [49]). Wind measurement data of southern areas of Pakistan has been analyzed from 47 towers at a height of 30 m and 50 m because southern areas of Pakistan consist of mountains. According to area wise capacity of wind electricity production, Pakistan has been classified differently in the term of wind characteristics and availability of wind (Siddique & Wazir [6]). However, for profiling and assessment of wind power potential geographical distribution of wind speed, wind characteristics and wind flow are considered as important elements. Pakistan is located among the latitude of 24 and 37 ° North and longitude 62 and 75 ° East. The total area of the country is 803 950 km^2. Pakistan's coastline is estimated about 1 046 km long. The Alternative Energy Board of Pakistan argues that the wind power potential is 360 GW and this is supported by SWERA that estimated 349.3 GW.

Figure 3 given below is the wind map of Pakistan. The wind map is developed by the National Renewable Energy Laboratory (NREL) of the USA with collaboration of USAID. According to the map, Pakistan has potential of 346 GW. NREL and USAID classified that Pakistan has 3 % land that is in the category of 4+ and it have potential to produce 132 GW. This 3 % of land shows 24 hours availability of wind with excess wind speed and other wind characteristics. However, the energy mix of the country shows that wind power potential is not utilized significantly as the wind energy contribution in the total energy mix is less than 1 %. The government of Pakistan can fulfill the national demand of energy by utilizing the available wind energy potential and it can also promote electricity industry by introducing the cross border electricity trade in the region. In addition, wind energy is also favorable for environmental sustainability.

The first initiative of wind energy in Pakistan was taken during 1980s for water pumping. However, till the end of 2016 the wind energy did not show significant contribution in the energy sector of Pakistan. In addition, no efforts have been made in the country for effective and comprehensive assessment of wind power.

Thus, to add significant contribution of wind energy in the overall energy production mix of the country, it is highly important to comprehensively assess the wind power potential in the country. In addition, classify the potential sites for policy makers so that they can take initiatives for wind power project installation. For this

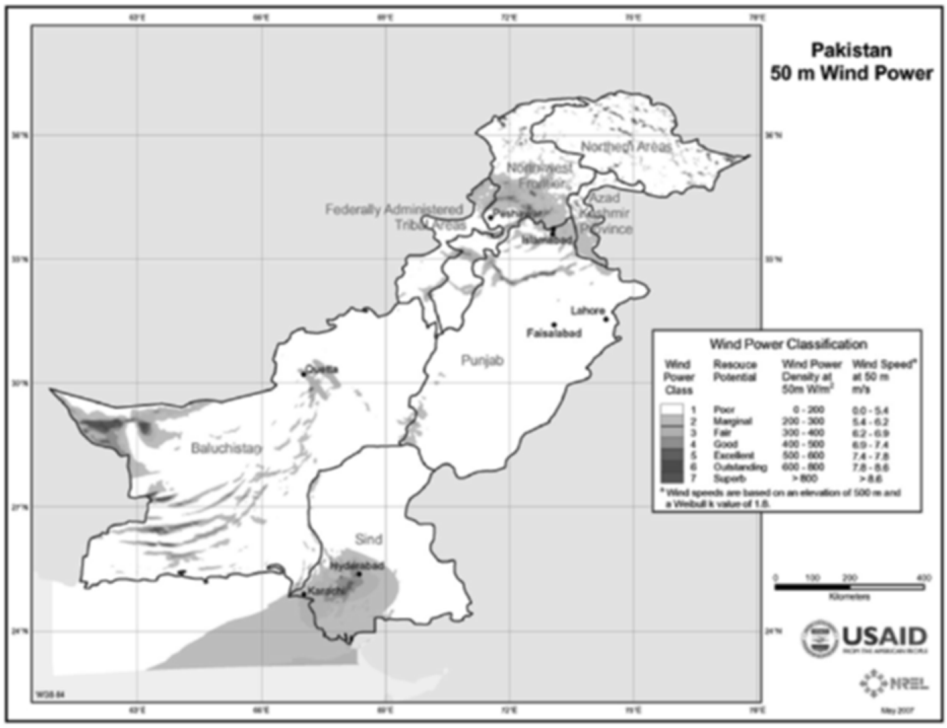

Fig. 3. Wind energy map designed by NREL USA with collaboration of USAID

objective creating a mechanism for profiling and assessment of wind power potential and picking optimal sites in the country is extremely vital.

2.1. Methodology

In most of the previous studies Weibull distribution function has been commonly used and recommended distribution that is used to determine the average wind speed distribution and wind characteristics, which are useful to estimate wind energy potential at prospective sites. Therefore, in this study the Weibull distribution function is used as a fundamental building block for estimation. In this section, we indicate how we estimate the suitability of Weibull function at wind speed data for thirteen sites proposed in this study. We defined $f(d)$ as a cumulative distribution function that is the probability of $X \leq d$, which implies that the probability x lies between $X_m in$ and d. Thus, we can model this cumulative distribution for Weibull and Rayleigh distribution as follows.

$$f(d) = P(X_{\min} \leq X \leq d) = \int_{X_{\min}}^{d} f(X)\,\mathrm{d}X\,. \tag{1}$$

We modified the mathematical model as (Lai, Xie, & Murthy [50]; Seguro &

Lambert [23]; Silva, Ortega, & Cordeiro [51]). The Shape parameter K and Scale parameter C can be calculated with the mean and standard deviation of wind speed. Although, researchers used suitability of wind speed to distribute the wind speed data at a Weibull distribution function but in our case, unlike others we defined the probability for a given model of Weibull distribution and Rayleigh distribution function and we come up with a novel model which distinguish our work from others as (2)

$$f(u) = \frac{2u}{C^2} \mathrm{e}^{-(u/C)^2}, \quad 0 \leq u < \infty\,. \tag{2}$$

The Weibull distribution consists of two parameters C and K, while the Rayleigh distribution has a single parameter C. However, the Rayleigh distribution function is considered as a special case of Weibull distribution having values of $K = 2$, which justifies that by putting the value of $K = 2$ in Weibull distribution function, we can get the Rayleigh distribution function (Pishgar-Komleh, Keyhani & Sefeedpari [52]) as a result so,

$$f(u) = \frac{K}{C} \cdot \left(\frac{u}{C}\right)^{K-1} \mathrm{e}^{-(u/C)^K}, \quad 0 \leq u < \infty\,, \tag{3}$$

where (3) in Weibull distribution setting $K = 2$ represents the Rayleigh distribution function (Pishgar-Komleh et al. [52]). For Weibull and Rayleigh distributions, $u_{\min} = 0$ and $u_{\max} = \infty$. The scale parameter C used in this context is the dimension of velocity. However, the K is dimensionless, so it is called the shape parameter. The following equation (4) is the Weibull distribution function; it is generated by substituting the value of equation (3) in equation (1).

$$f\,(d) = \int_{X_{\min}}^{d} f(u)\,\mathrm{d}u = \int_0^d \frac{K}{C} \left(\frac{u}{C}\right)^{k-1} \mathrm{e}^{-(u/C)^k}\,\mathrm{d}u = 1 - e^{-(d/C)^k} \quad \text{Weibull}\,. \tag{4}$$

If we put $k = 2$, we get the Rayleigh distribution

$$f\,(d) = 1 - \mathrm{e}^{-(d/C)^2} \quad \text{Rayleigh}\,. \tag{5}$$

The Gamma function $\Gamma(X)$ can be written as follows (Islam et al. [32]).

$$\mathit{\Gamma}\,(x) = \int_0^\infty \mathrm{e}^{-u} u^{x-1}\,\mathrm{d}u\,, \tag{6}$$

For calculation of Weibull and Rayleigh distributions we use the following parameters to quantify the actual wind speed data at these two distributions. Even many researcher use others distributions to measure the suitability of wind speed data with a traditional models but we, unlike others used these distributions to come up with a quite novel and holistic manners so that the results and wind characteristics represent a true picture of wind power potential at specific sites which has been ignored by others, so as a results we used these parameters to ease quantification of

the model,

$$\mu_{\text{Weibull}} = C\Gamma\left(\frac{1}{K}+1\right), \quad \mu_{\text{Rayleigh}} = C\frac{\sqrt{\pi}}{2}, \tag{7}$$

$$\sigma^2_{\text{Weibull}} = C^2\left[\Gamma\left(\frac{2}{k}+1\right) - \Gamma^2\left(\frac{1}{k}+1\right)\right], \quad \sigma^2_{\text{Rayleigh}} = c^2\left(2-\frac{\pi}{4}\right). \tag{8}$$

The following equations are used for the most probable value of velocity:

$$U_{\text{mp,Weibull}} = C\sqrt[K]{\left(\frac{K-1}{K}\right)}, \quad U_{\text{mp,Rayleigh}} = \frac{C}{\sqrt{2}}. \tag{9}$$

In the Rayleigh distribution function the scale parameter C relates with the following three characteristics:

$$C = U_{\text{mp}}\sqrt{2} = \frac{2\mu}{\sqrt{\pi}} = \sigma\sqrt{\frac{4}{8-\pi}}. \tag{10}$$

The Rayleigh distribution function can be written with U_{mp} (mean velocity). Substitute the value of equation (10) into (3), which gives the Rayleigh distribution function in the form

$$f(u) = \frac{2u}{C^2}\mathrm{e}^{-(u/C)^2} = \frac{u}{u^2_{\text{mp}}}\mathrm{e}^{-u^2/\left(2u^2_{\text{mp}}\right)} = \frac{\pi u}{2\mu^2}\mathrm{e}^{-\pi u^2/\left(4\mu^2\right)}. \tag{11}$$

Further, once the shape and scale parameters estimated for both of the distributions are known, the next important thing is the most probable wind speed V_{mp} and the wind carrying maximum energy. The most probable wind speed can be defined as the frequent wind speed for the probability distribution. Using the scale parameter and shape parameter from Weibull distribution, the most probable wind speed can be calculated with the following equation as suggested by (Islam et al. [32]; Pishgar-Komleh et al. [53]).

$$V_{\text{mp}} = C\left(1-1/k\right)^{1/k}. \tag{12}$$

The wind speed carrying maximum wind energy V_{mx} can also be calculated using the scale and shape parameters of the Weibull distribution function. To determine the wind speed carrying maximum wind energy the following equation can be used (Islam et al. [32]; Jamil [54]).

$$V_{\text{mx}} = C\left(1+2/k\right)^{1/k}. \tag{13}$$

The wind power density represents the wind power per unit area swept by the turbine blade. It can be expressed with the following equation as suggested by (Pimenta, Kempton, & Garvine [55]; Teetz, Harms, & Von Backström [56]).

$$P(v) = \frac{1}{2}\rho v^3 A. \tag{14}$$

Knowing the wind power density using (15), for comprehensive assessment this study used Weibull and Rayleigh distribution. So, when more than one distribution is being used, then the wind energy density can be calculated using the following equation as suggested by (Keyhani, Ghasemi-Varnamkhasti, Khanali, & Abbaszadeh [57]).

$$\frac{E}{A} = \frac{1}{2}\rho C^3 T \left(\frac{K+3}{K}\right) T\,. \tag{15}$$

3. Wind turbine performance

Wind turbine is operated with a maximum range of velocity which is called cut-out velocity. On the other hand the minimum range of velocity called cut-in velocity. Power coefficient C_{p}, is the fraction of the wind power which is actually captured. If wind power potential output is greater than maximum power input of the generator, the maximum generator power can be produced by controlling the turbine. Wind power is actually the product of mass stream rate sweeping over wind turbine blades ρ and per unit mass kinetic energy in the wind, U^2. The operating turbine pattern for a probability distribution function of the wind can be modeled with the average power output from the wind turbine. However, to measure the turbine efficiency, the wind speed and the number of hours at which wind speed blows are necessary to evaluate. Similar for other analysis of wind characteristics; it is necessary to measure the size of wind speed interval, direction of the wind speed and number of hours in which wind blows and swept over the area of blades (Carneiro, Melo, Carvalho, & Braga [58]; Seguro & Lambert [23]). Unfortunately, our study is based upon only a single type of turbine blade having capacity of 600 kWh power generations which is proposed by the metrological department of Pakistan.

$$\overline{P(u)} = \int_{u_{\mathrm{cut-in}}}^{u_{P\max}} \frac{C_{\mathrm{p}}\rho A u^3}{2} f(u)\,\mathrm{d}u = \int_{u_{P\max}}^{u_{\mathrm{cut-out}}} P_{\max} f(u)\,\mathrm{d}u\,. \tag{16}$$

Maximum wind velocity $u_{P\max}$ at which the power is distributed from the wind turbine to the generator at maximum capacity is called the rated wind speed of the turbine. Perspective of wind power definition, the wind power which is passing on wind turbine with wind velocity $u_{P\max}$ is $C_{\mathrm{p}}\rho A u_{P\max}^{3/2}$. So the description of $u_{P\max}$ depends on the definition of C_{p} and η_{gen} is the generator efficiency of turbine and $P_{\max}$ is the average output power of the generator

$$u_{P\max} = \begin{cases} \left(\frac{2P_{\max}}{C_{\mathrm{p}}\rho A}\right)^{1/3} & C_{\mathrm{p}} = \frac{\text{Turbine output}}{\text{Wind power}}, \\ \left(\frac{2P_{\max}}{C_{\mathrm{p}}\rho A\eta_{\mathrm{gen}}}\right)^{1/3} & C_{\mathrm{p}} = \frac{\text{Turbine input}}{\text{Wind power}}, \end{cases} \tag{17}$$

The capacity factor can be viewed in the equation (17), which clearly indicates that C_{p} depends upon turbine output and wind power potential which is considered as a wind input. It can be argued that the capacity factor of the wind turbine largely

depends upon the wind power potential further it is measured by wind density. Hence, two sites with same wind speed can generate different power due to wind power density. However, the capacity factor depends upon the wind power potential and wind turbine performance which makes the capacity factor dimensionless.

So for computation of capacity factors and other wind characteristics the data and information has been taken from the Pakistan Metrological Department, the National renewable energy research database (NREL), USAID reports for wind assessment and mapping for Afghanistan and Pakistan. Data and information has been processed using MATLAB, EasyFit and Microsoft Excel software to get results.

4. Results and findings

Wind speed and other wind characteristics such as scale and shape parameter, wind energy density and capacity factor are basic pillars to provide guidelines about wind power project installations. Wind turbines capacity factor is another measure of annually power output of a wind turbine at a specific location and it is an accumulated annual energy output of a wind energy project, which is called the capacity factor of a wind energy turbine. However, capacity factor varies from turbine to turbine and site to site. It depends mainly upon the capacity of the machine to produce electricity and the wind speed of proposed sites. The National Renewable Energy Laboratory (NREL) of the USA suggests that any site having capacity factor of 25 % is suitable to generate wind electricity (NREL). In addition, the understanding of wind energy density also has great importance to estimate the wind power potential and determining the suitability of wind power project sites in any region.

To determine the suitability of a wind project installation at prospective sites, in this study at first we analyzed the average wind speed. The NREL categorizes the average wind speed ranges from 6.2 to 6.9 as fair and if it ranges from 6.9 to 7.4 it is good. Above 7.4 is considered as excellent. So that generally we can say that, if the average wind speed is above 6.9 it can be considered as commercially viable. However, decision making based upon only wind speed data is an old concept. Practitioners believe that only wind speed data could not provide a good basis for making decision about wind project installation. Based upon the data we assessed the average wind speed at 50 meter height. Due to limitation of data, we assessed only on 50 meter height.

Figure 4 shows the average wind speed at prospective sites. As it can be seen that the average wind speed at Aghore is 4.7 m/s at 50 meter height, the highest wind speed noted at the Aghore station was 7.5 m/s during the month of July. The average wind speed at Kallar Kahar is 6.7 m/s at 50 meters height and the highest wind speed 8.6 m/s are observed during the month of June. According to wind frequency distribution records, during 76 % of the time the average wind speed is 6.8 m/s or above at Kallar Kahar. The average wind speed at Basol, Bella, Gaddani, Kot Sabzal, Shahida Sir, Chitral, Ayune and Tarbella has been noted as 4.3, 3.0, 5.1, 4.2, 4.6, 3.0, 3.9 and 3.8, respectively. The average wind speed at Jamshoro is 8.5 m/s at 50 meters height. Except March and October, the average wind speed is more than 8 m/s at this site. According to wind frequency distribution records,

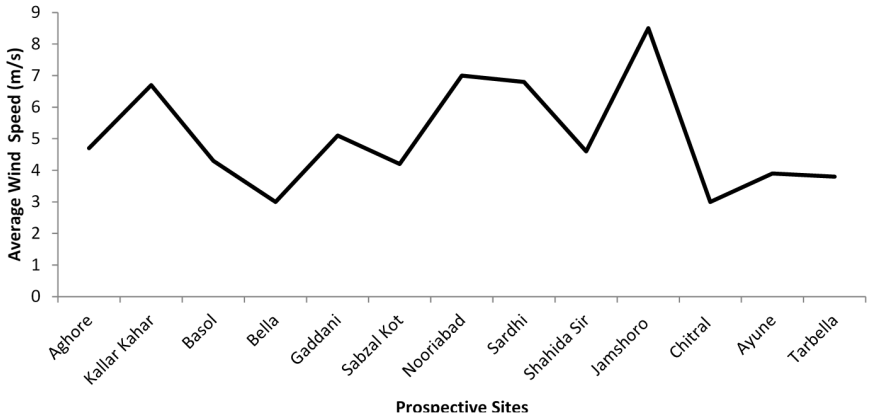

Fig. 4. Average wind speed

during 78 % of the time the average wind speed at Jamshoro is 7 m/s or above. The average wind speed at another potential site Sardhi is 6.8 m/s at 50 meters height and the highest wind speed 8.7 m/s are observed during the month of June. The data of wind frequency distribution shows that 75 % of the time the average wind speed noted at Sardhi was 6.8 m/s. Finally, the average wind speed at Nooriabad is 7.0 m/s at 50 meter height. From March to September, the highest wind speed 10.6 m/s is observed in June and the average wind speed is more than 5 m/s. Wind frequency distribution data indicate that 79 % of the time the wind speed at Nooriabad was noted above 5.1 m/s. Thus, based upon wind speed data Jamshoro and Nooriabad are highlighted as most potential sites for the installation of wind energy. But, Kallar Kahar and Sardhi also show the potential for wind energy production.

The wind energy stated in terms of area without taking into consideration the wind turbine area it is recognized as wind power density. Wind power density function indicates the amount of energy available at a specific location that can be converted into electricity using a wind turbine.

The wind power density represents the wind power per unit area swept by the wind turbine blade, theoretically it has a cubic relation with average wind speed and it used to determine the wind power potential of the prospective site. In this study, the highest wind power density at 50 meter height is 771 at the Jamshoro site with the lowest wind power density is found at the Bella site 91.9. Figure 5 shows the average wind power density at prospective sites used in the current context of study. The average wind power density at the Aghore site is 311.2 W/m^2, 309.0 W/m^2 at Kallar Kahar, 139.6 W/m^2 at Basol, 91.9 W/m^2 at Bella, 210.2 W/m^2 at Gaddani, 125.0 W/m^2 at Kot Sabzal, 454.29 W/m^2 at Nooriabad, 309.0 W/m^2 at Sardhi, 148.0 W/m^2 at Shahida Sir, 771.0 W/m^2 at Jamshoro, 126.4 W/m^2 at Chitral, 168.28 W/m^2 at Ayune and 150 W/m^2 at the Tarbella site. It is worth mentioning here that in our analysis we just found the difference of 1 % among the results of wind energy density from Weibull and Rayleigh distribution function.

According to NREL guideline for wind project installation, the class 3 category requires a power density of 200 W/m^2 or higher, in this study we found that Aghore,

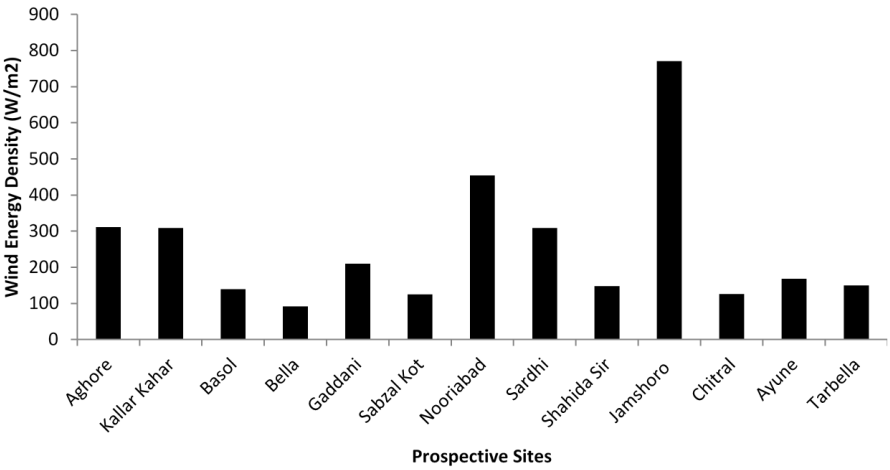

Fig. 5. Wind energy density

Kallar Kahar, Gaddani, Nooriabad, Sardhi and Jamshoro as potential sites for wind project installation. However, the most important element that must be taken into account is the capacity factor of a prospective site. The capacity factor of wind power project is the ratio of its actual output to potential output in a period of time.

Table 1. Weibull and Rayleigh distribution results for suitability of wind project

						W. distribution[1]		R. distribution[2]	
sites	Average wind speed	C	K	V_{mn} (m/s)	V_{mx} (m/s)	v/d[2]	Cap. factor[3]	v/d[2]	Cap. factor[3]
Aghore	4.7	5.7	1.4	2.29	10.555	311.2	0.19	311.6	0.19
Kallar Kahar	6.7	7.6	2.4	6.07	9.784	309	0.28	314.4	0.29
Basol	4.3	3.5	1.5	1.68	6.157	139.6	0.13	140	0.13
Bella	3	3.6	1.3	1.17	7.371	91.9	0.09	90.5	0.09
Gaddani	5.1	5.3	1.9	3.58	7.738	210.2	0.20	212	0.21
Kot Sabzal	4.2	4.9	1.7	2.91	7.742	125	0.12	128	0.13
Nooriabad	7	7.8	2.4	6.23	10.041	454.2	0.29	453	0.29
Sardhi	6.8	7.5	2.4	5.99	9.655	309	0.27	309	0.27
Shahida Sir	4.6	7.2	2.6	5.97	8.967	148	0.13	148	0.14
Jamshoro	8.5	9.6	1.9	6.48	14.017	771	0.41	770	0.40
Chitral	3	4.7	1.7	2.79	7.426	126.4	0.08	125	0.07
Ayune	3.9	6.1	2.2	4.63	8.184	168.3	0.09	166	0.08
Tarbella	3.8	6	2.1	4.41	8.251	150	0.10	150.5	0.10

[1]Weibull distribution, [2]Rayleigh distribution, [3]Capacity factor

We have measured the capacity factor of the selected thirteen sites on the bases of turbine model quality and the size of the wind turbine, wind speed and quality of the wind. The results from the Table 1 reveal that the capacity factors using the Weibull distribution vary from 0.41 at the Jamshoro to 0.08 at the Chitral site. The capacity factor at the Aghore and Gaddani is found to be comparatively better, like 0.19 and 0.20 respectively. But, it is insufficient to produce electricity as per criteria of the National Renewable Energy Laboratory (NREL) of the USA. Further, our results show that the sites Kallar Kahar, Jamshoro, Nooriabad and Sardhi have capacity factor of 0.28, 0.41, 0.29 and 0.27 respectively. Thus, these four sites are found to be viable for wind power project based on the criteria of capacity factor set by the NREL. However, the most powerful site for wind power project is Jamshoro followed by Nooriabad, Kallar Kahar and Sardhi respectively. While, the rest of the sites in our study did not show an acceptable capacity factors and do not fulfill the benchmark criteria of capacity factor. Even though, the average wind speed and power density is relatively acceptable at Gaddani and Aghore but these sites do not fulfill the benchmark criteria set by NREL because capacity factors of these sites is lessor than 0.25. The capacity factor of 600 kWh machine has been analyzed in the current context of study.

To further assure the validity of results, this study also used the Rayleigh distribution function to determine the capacity factor of the selected thirteen sites on the bases of turbine model quality and the size of the wind turbine, wind speed and quality of the wind. The results from Rayleigh distribution function reveal that the capacity factors vary from 0.40 at Jamshoro to 0.07 at the Chitral site. Rayleigh distribution also indicate similar results as it shows that the capacity factor at the Aghore and Gaddani is found to be comparatively better, like 0.19 and 0.21, respectively. But, similar to the Weibull model it also shows these places as insufficient to produce electricity. Further, parallel to Weibull distribution function, results from Rayleigh distribution also highlighted that the sites Kallar Kahar, Jamshoro, Nooriabad and Sardhi as potential sites for wind power installation. While, the rest of the sites in our study didn't shows an acceptable capacity factors from both models and don't fulfill the benchmark criteria.

Furthermore, the results from Table 1 show the Weibull parameters along with wind speed characteristics of prospective sites. The value of parameter K varies from 1.3 at Bella and 2.6 at Shahida Sir site. Also, the value of C varies from minimum 3.6 at Bella and maximum 9.6 at Jamshoro. Moreover, the V_{mp} (most probable wind speed) and V_{mx} (wind speed carrying maximum energy) were also calculated in present study. The V_{mp} ranged from minimum $1.17\,\mathrm{ms}^{-1}$ at Bella and maximum $6.48\,\mathrm{ms}^{-1}$ at Jamshoro. The V_{mx} ranged from minimum $6.15\,\mathrm{ms}^{-1}$ at Basol and maximum $10.55\,\mathrm{ms}^{-1}$ at Aghore site.

Figure 6 shows a graphical comparison of modified Weibull and Rayleigh distribution functions. Results show a similar trend between Weibull distribution and Rayleigh distribution function. From graphical representation we can see that both of the distributions show four similar potential sites where wind power can be installed.

The results from scale and parameters in our study also indicate that only four

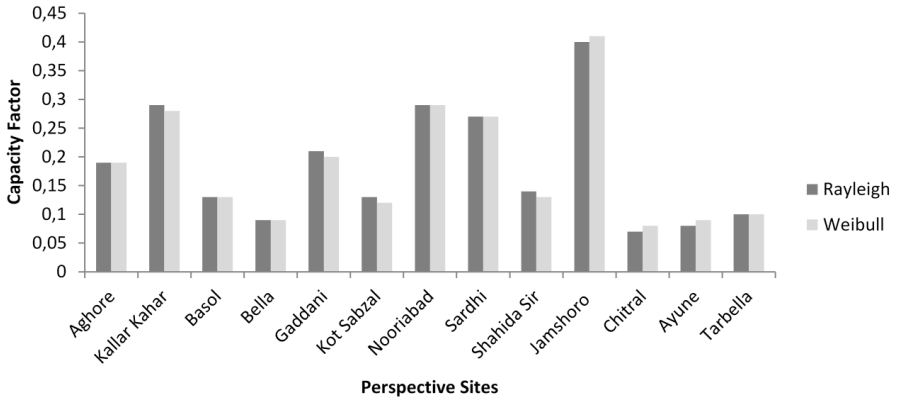

Fig. 6. Capacity factors from Weibull and Rayleigh distributions

sites comprise of Kallar Kahar, Jamshoro, Sardhi and Nooriabad have potential for wind power installation. The other prospective sites in this study don't show satisfactory results for wind power project installation.

According to the NREL's criteria the decision should not only taken based on the wind speed but also the shape parameter, scale parameter, capacity factor and wind energy density have major importance regarding wind energy project installation. The sites do not fulfill the criteria of NERL have not enough wind capacity to produce electricity, so these sites have no attraction to install wind grid of electricity production. This study used the classified standards provided by NREL to pick the optimal sites for wind project installation. The wind power densities for each of the prospective sites have been calculated with data for the entire duration and observation have been conducted and analyzed.

Furthermore, it has been also noted that the varying capacity factor is only due to the wind speed and quality of the wind because the stated capacity of 600 kWh turbines was used to measure the capacity factor of the all selected sites. Despite the consequences and availability of wind speed at specific location, some wind turbines machine performance is satisfactory such as Fuhrlander FL 2500 wind turbine machines generates maximum and highest magnitude of annual energy output. But some wind turbines generate minimum power. So among all prospective sites only four sites have the capacity factor of greater than 25 % which generate wind electricity and rest of the sites do not have potential to produce electricity.

5. Conclusion and policy implication

In the present study, we scrutinized the wind power project development at thirteen prospective sites in Pakistan. For the comprehensive assessment of these sites we modified the Weibull distribution function to get more precise results. Further, we also reassessed our findings using Rayleigh distribution function. We measured wind characteristics, wind power potential and energy utilization of prospective sites.

The basic objective of our study was to profile and assess the wind energy potential in Pakistan that can be used to address energy crises and at the same time to address environmental issues. The available wind resources in the country are vital to utilize, because the major part of CO_2 emissions in the country is emitting from the energy sector. Moreover, it is highly significant to consider the environmental sustainability while planning for future energy projects in the country. To make our results more feasible and easy to accept we discussed all of our findings with respect to the guidelines provided by the NREL.

Results from our study reveals that Kallar Kahar, Jamshoro, Nooriabad and Sardhi's average wind speed, scale and shape parameter, wind energy density and capacity factor are viable for wind power project installation according to the guidelines of the National Renewable Energy Laboratory (NREL) of USA. Further, results from Rayleigh distribution function also confirm that these four sites have potential for wind project installation.

While, the other sites used in this study does not provide acceptable wind characteristics and capacity factor to install a wind power project because Weibull shape & scale parameter and Rayleigh distribution of wind characteristics do not have satisfactory values to install wind power project. The presented values of other than four sites do not attract decision makers of the government of Pakistan to install wind power projects.

In addition, our study provides a guideline for policy makers, as we comprehensively assessed the wind power potential in the country and highlighted the potential sites where wind projects can be installed. So, the government of Pakistan can address energy crises by planning to install wind energy projects at the Kallar Kahar, Jamshoro, Nooriabad and Sardhi sites as these sites fulfill the international criteria for the wind project installation. These sites have more than 0.25 capacity factor that is viable for wind project installation as per guidelines of the National Renewable Energy Laboratory of USA. These sites also fulfill the standards set by the Kyoto protocol. The government of Pakistan can advertise these sites to attract foreign investors those are interested to invest in wind power projects that will ultimately result in fulfilling the energy demand of the country. Moreover, it would provide employment and enhance the economic and industrial growth in the country. We highly recommend policy makers to shift the energy system on the wind power as the country has huge potential of wind energy. By shifting the energy sector on wind, the government can address energy crises and it can also save the environment.

Based upon the profiling and assessment from this study, we believe that our study can be extended to generate hydrogen energy by using wind generated electricity to decompose water molecule into hydrogen and oxygen. Because hydrogen energy is also clean and it don't have any negative impact on climate and have no fuel cost. It can be extended to generate hybrid solar and wind energy together because the warm sunshine in Pakistan and enough temperature is available to generate energy through solar energy.

References

[1] M. Farooq, A. Shakoor: *Severe energy crises and solar thermal energy as a viable option for Pakistan.* Journal of Renewable and Sustainable Energy *5* (2013), No. 1, paper 013104.

[2] M. A. Khan, U. Ahmad: *Energy demand in Pakistan: A disaggregate analysis.* The Pakistan Development Review *47* (2008), No. 4, 437–455.

[3] M. Amer, T. U. Daim: *Selection of renewable energy technologies for a developing county: A case of Pakistan.* Energy for Sustainable Development *15* (2011), 420–435.

[4] I. N. Kessides: *Chaos in power: Pakistan's electricity crisis.* Energy Policy *55* (2013), 271–285.

[5] A. Ghafoor, T. ur Rehman, A. Munir, M. Ahmad, M. Iqbal: *Current status and overview of renewable energy potential in Pakistan for continuous energy sustainability.* Renewable and Sustainable Energy Reviews *60* (2016), 1332–1342.

[6] S. Siddique, R. Wazir: *A review of the wind power developments in Pakistan.* Renewable and Sustainable Energy Reviews *57* (2016), 315–361.

[7] V. Bianco, O. Manca, S. Nardini: *Electricity consumption forecasting in Italy using linear regression models.* Energy *34* (2009), No. 9, 1413–1421.

[8] M. Ali, S. A. Khan, N. A. Sheikh, M. Shehryar, S. I. Gilani, H. M. Ali, T. U. Rashid: *Performance analysis of a low capacity solar tower water heating system in climate of Pakistan.* Energy and Buildings *143* (2017), 84–99.

[9] H. A. Sher, A. F. Murtaza, K. E. Addoweesh, M. Chiaberge: *Pakistan's progress in solar PV based energy generation.* Renewable and Sustainable Energy Reviews *47* (2015), 213–217.

[10] S. Ahmed, A. Mahmood, A. Hasan, G. A. S. Sidhu, M. F. U. Butt: *A comparative review of China, India and Pakistan renewable energy sectors and sharing opportunities.* Renewable and Sustainable Energy Reviews *57* (2016), 216–225.

[11] S. Sen, S. Ganguly: *Opportunities, barriers and issues with renewable energy development – A discussion.* Renewable and Sustainable Energy Reviews *69* (2017), 1170–1181.

[12] W. E. Glassley: *Geothermal energy: Renewable energy and the environment.* CRC Press (2014).

[13] d'Artis Kancs, N. Wohlgemuth: *Evaluation of renewable energy policies in an integrated economic-energy-environment model.* Forest Policy and Economics *10* (2008), No. 3, 128–139.

[14] S. Z. Farooqui: *Prospects of renewables penetration in the energy mix of Pakistan.* Renewable and Sustainable Energy Reviews *29* (2014), 693–700.

[15] M. A. Sheikh: *Renewable energy resource potential in Pakistan.* Renewable and Sustainable Energy Reviews *13* (2009), No. 9, 2696–2702.

[16] U. K. Mirza, N. Ahmad, T. Majeed, K. Harijan: *Wind energy development in Pakistan.* Renewable and Sustainable Energy Reviews *11* (2007), No. 9, 2179–2190.

[17] M. Shoaib, I. Siddiqui, Y. M. Amir, S. U. Rehman: *Evaluation of wind power potential in Baburband (Pakistan) using Weibull distribution function.* Renewable and Sustainable Energy Reviews *70* (2017), 1343–1351.

[18] I. Ullah, Q. U. Z. Chaudhry, A. J. Chipperfield: *An evaluation of wind energy potential at Kati Bandar, Pakistan.* Renewable and Sustainable Energy Reviews *14* (2010), No. 2, 856–861.

[19] S. M. Lawan, W. A. W. Z. Abidin, T. Masri, W. Y. Chai, A. Baharun: *Wind power generation via ground wind station and topographical feedforward neural network (T-FFNN) model for small-scale applications.* Journal of Cleaner Production *143* (2017), 1246–1259.

[20] H. Beurskens, A. Brand: *Wind Energy.* Materials and Energy, The World Scientific Handbook of Energy *3* (2013), 307–341.

[21] T. Burton, D. Sharpe, N. Jenkins, E. Bossanyi: *Wind energy handbook.* John Wiley & Sons (2011).

[22] C. F. de Andrade, H. F. M. Neto, P. A. C. Rocha, M. E. V. da Silva: *An efficiency comparison of numerical methods for determining Weibull parameters for wind energy applications: A new approach applied to the northeast region of Brazil.* Energy Conversion and Management *86* (2014), 801–808.

[23] J. V. Seguro, T. W. Lambert: *Modern estimation of the parameters of the Weibull wind speed distribution for wind energy analysis.* Journal of Wind Engineering and Industrial Aerodynamics *85* (2000), No. 1, 75–84.

[24] S. K. Ghosh, M. H. Shawon, M. A. Rahman, S. K. Nath: *Wind energy assessment using Weibull Distribution in coastal areas of Bangladesh.* International Conference on the Developments in Renewable Energy Technology (ICDRET), 29–31 May 2014, Dhaka, Bangladesh, DOI: 10.1109/ICDRET.2014.6861731.

[25] I. Usta: *An innovative estimation method regarding Weibull parameters for wind energy applications.* Energy *106* (2016), 301–314.

[26] I. Y. F. Lun, J. C. Lam: *A study of Weibull parameters using long-term wind observations.* Renewable Energy *20* (2000), No. 2, 145–153.

[27] A. N. Celik: *A statistical analysis of wind power density based on the Weibull and Rayleigh models at the southern region of Turkey.* Renewable Energy *29* (2004), No. 4, 593–604.

[28] J. A. Carta, P. Ramirez: *Analysis of two-component mixture Weibull statistics for estimation of wind speed distributions.* Renewable Energy *32* (2007), No. 3, 518–531.

[29] B. Yaniktepe, T. Koroglu, M. M. Savrun: *Investigation of wind characteristics and wind energy potential in Osmaniye, Turkey.* Renewable and Sustainable Energy Reviews *21* (2003), 703–711.

[30] S. A. Akdağ, A. Dinler: *A new method to estimate Weibull parameters for wind energy applications.* Energy Conversion and Management *50* (2009), No. 7, 1761–1766.

[31] T. P. Chang: *Performance comparison of six numerical methods in estimating Weibull parameters for wind energy application.* Applied Energy *88* (2011), No. 1, 272–282.

[32] M. Islam, R. Saidur, N. Rahim: *Assessment of wind energy potentiality at Kudat and Labuan, Malaysia using Weibull distribution function.* Energy *36* (2011), No. 2, 985–992.

[33] M. Shahbaz, M. Zeshan, T. Afza: *Is energy consumption effective to spur economic growth in Pakistan? New evidence from bounds test to level relationships and Granger causality tests.* Economic Modelling *29* (2012), No. 6, 2310–2319.

[34] J. Anwar: *Analysis of energy security, environmental emission and fuel import costs under energy import reduction targets: A case of Pakistan.* Renewable and Sustainable Energy Reviews *65* (2016), 1065–1078.

[35] K. Harijan, M. A. Uqaili, M. Memon, U. K. Mirza: *Forecasting the diffusion of wind power in Pakistan.* Energy *36* (2011), No. 10, 6068–6073.

[36] K. Zaman, I. Abdullah, M. Ali: *Decomposing the linkages between energy consumption, air pollution, climate change, and natural resource depletion in Pakistan.* Environmental Progress & Sustainable Energy *36* (2017), No. 2, 638–648.

[37] Change IPCC: *Climate Change 2014: Impacts, Adaptation, and Vulnerability.* IPCC WGII AR5 Summary for Policymakers, Regional Aspects: Cambridge University Press.

[38] V. Chaturvedi, L. Clarke, J. Edmonds, K. Calvin, P. Kyle: *Capital investment requirements for greenhouse gas emissions mitigation in power generation on near term to century time scales and global to regional spatial scales.* Energy Economics *46* (2014), 267–278.

[39] A. W. Bhutto, A. A. Bazmi, G. Zahedi, J. J. Klemeš: *A review of progress in renewable energy implementation in the Gulf Cooperation Council countries.* Journal of Cleaner Production *71* (2014), 168–180.

[40] E. K. Stigka, J. A. Paravantis, G. K. Mihalakakou: *Social acceptance of renewable energy sources: A review of contingent valuation applications.* Renewable and Sustainable Energy Reviews *32* (2014), 100–106.

[41] M. Hosenuzzaman, N. A. Rahim, J. Selvaraj, M. Hasanuzzaman, A. B. M. A. Malek, A. Nahar: *Global prospects, progress, policies, and environmental impact of solar photovoltaic power generation.* Renewable and Sustainable Energy Reviews *41* (2015), 284–297.

[42] C. Özkale, C. Celik, A. C. Turkmen, E. S. Cakmaz: *Decision analysis application intended for selection of a power plant running on renewable energy sources.* Renewable and Sustainable Energy Reviews *70* (2017), 1011–1021.

[43] H. Dai, D. S. Herran, S. Fujimori, T. Masui: *Key factors affecting long-term penetration of global onshore wind energy integrating top-down and bottom-up approaches.* Renewable Energy *85* (2016), No. 7, 19–30.

[44] GWEC-Global Wind Energy Council: *Global statistics 2017.* From http://www.gwec.net/global-figures/graphs/.

[45] Y. Kumar, J. Ringenberg, S. S. Depuru, V. K. Devabhaktuni, J. W. Lee, E. Nikolaidis, B. Andersen, A. Afjeh: *Wind energy: Trends and enabling technologies.* Renewable and Sustainable Energy Reviews *53* (2016), 209–224.

[46] GWEC-Global Wind Energy Council: *Global Wind Report 2015 – Annual market update.* From http://www.gwec.net/publications/global-wind-report-2/global-wind-report-2015-annual-market-update/.

[47] M. M. Aman, G. B. Jasmon, A. Ghufran, A. H. A. Bakar, H. Mokhlis: *Investigating possible wind energy potential to meet the power shortage in Karachi.* Renewable and Sustainable Energy Reviews *18* (2013), 528–542.

[48] K. Harijan, M. A. Uqaili, M. Memon, U. K. Mirza: *Potential of on-shore wind power in the Coastal Areas of Balochistan, Pakistan.* Wind Engineering *34* (2010), No. 2, 167–179.

[49] S. F. Khahro, K. Tabbassum, A. M. Soomro, X. Liao, M. B. Alvi, L. Dong, M. F. Manzoor: *Techno-economical evaluation of wind energy potential and analysis of power generation from wind at Gharo, Sindh Pakistan.* Renewable and Sustainable Energy Reviews *35* (2014), 460–474.

[50] C. D. Lai, M. Xie, D. N. P. Murthy: *A modified Weibull distribution.* IEEE Transactions on Reliability *52* (2003), No. 1, 33–37.

[51] G. O. Silva, E. M. Ortega, G. M. Cordeiro: *The beta modified Weibull distribution.* Lifetime data analysis *16* (2010), No. 3, 409–430.

[52] S. Pishgar–Komleh, A. Keyhani, P. Sefeedpari: *Wind speed and power density analysis based on Weibull and Rayleigh distributions (a case study: Firouzkooh county of Iran).* Renewable and Sustainable Energy Reviews *42* (2015), 313–322.

[53] S. Pishgar-Komleh, A. Keyhani, P. Sefeedpari: *Wind speed and power density analysis based on Weibull and Rayleigh distributions (a case study: Firouzkooh county of Iran).* Renewable and Sustainable Energy Reviews *42* (2015), 313–322.

[54] M. Jamil: *Wind power statistics and evaluation of wind energy density.* Wind Engineering *18* (1994), No. 5, 227–240.

[55] F. Pimenta, W. Kempton, R. Garvine: *Combining meteorological stations and satellite data to evaluate the offshore wind power resource of Southeastern Brazil.* Renewable Energy *33* (2008), No. 11, 2375–2387.

[56] H. W. Teetz, T. M. Harms, T. W. von Backström: *Assessment of the wind power potential at SANAE IV base, Antarctica: A technical and economic feasibility study.* Renewable Energy *28* (2003), No. 13, 2037–2061.

[57] A. Keyhani, M. Ghasemi-Varnamkhasti, M. Khanali, R. Abbaszadeh: *An assessment of wind energy potential as a power generation source in the capital of Iran, Tehran.* Energy *35* (2010), No. 1, 188–201.

[58] T. C. Carneiro, S. P. Melo, P. C. M. Carvalho, A. P. D. S. Braga: *Particle Swarm Optimization method for estimation of Weibull parameters: A case study for the Brazilian northeast region.* Renewable Energy *86* (2016), 751–759.

Received March 16, 2018

Acta Technica *63* No. 6/2018, 877–886

Circularly polarized S-band patch antenna for small satellite applications

Md. Samsuzzaman[1], F. K. Shawon[1], Mohammad Tariqul Islam[2], Md. Zulfiker Mahmud[2]

Abstract. In this paper, a circularly polarized compact printed antenna is adduced for small satellite communication system. Due to low profile and lightweight property of microstrip antenna it has been selected for satellite communication. For the analysis process Computer Simulation Software (CST) microwave studio and High Frequency Structural Simulator (HFSS) have been used and their working procedure is Finite Integration Technique (FIT) as well as Finite Element Method (FEM). The anticipated antenna consists of a truncated corner cut patch with a T-shaped slot in the ground plane. Both CST and HFSS packages of simulation software have been justified to find the axial ratio and reflection coefficient result. The CST and HFSS simulated results show that the obtained impedance bandwidths are 130 MHz (2.30–2.43 GHz) and 140 MHz (2.28–2.43 GHz) respectively, good enough for S-band satellite applications. Substrate material FR-4 (lossy) with dielectric constant of 4.6 with a height of 1.6 mm has been used to print the antenna. An axial ratio of 3 dB beam width more than 160 ° was displayed by the proposed antenna. The simulation and measured result are very much identical.

Key words. Circular polarization, small antenna, satellite application..

1. Introduction

Most of the application like Global positioning and radar system as well as wireless local area network currently use circular polarization which has made this polarization one of the preferred kinds of polarization. A major system for circular polarization is not different though there are various kinds of circularly polarized antennas. Circular polarization for small satellite system is very much desirable to ease any orientation-relevant affairs of the acquiring base-station antennas [1]. In addition, small satellite which is an invention of miniaturization technology without degrading performance, has created an era in the satellite industry.

[1]Computer Science and Engineering, Patuakhali Science and Technology University, Patuakhali, Bangladesh; e-mail addresses: sobuz@pstu.ac.bd,shawon.kayes@gmail.com

[2]Department of Electrical Electronic and Systems Engineering, Universiti Kebangsaan Malaysia, Malaysia; e-mail addresses: tariqul@ukm.edu.my,zulfikerm@siswa.ukm.edu.my

In the last decades, many studies have been developed for the small satellite antenna. With a fractional bandwidth of 1.5 % and frequency at 2.225 GHz, a planar antenna for small satellites is developed in [2]. With the satellite size of $60 \times 60 \times 70\,\mathrm{mm}^3$, another CP planer antenna whose profile and gain is lower at 2.4 GHz, was developed for an SSETI-Express minisatellite [3]. For small satellite applications, a CP circular patch antenna fed by a coaxial probe operating within a tuneable frequency range of 2.0–2.5 GHz was proposed in [4]. A patch antenna which is a compact single layer co-axial probe-fed circularly polarized high-gain antenna is designed for HORYU-4 nanosatellites S-band communication is presented in [5]. A circularly polarized S-band antenna for satellite application with parasitic elements around the main radiator is introduced in [6] and the antenna design has a wide-ranging 5 dB AR bandwidth of 12.3 % as well as stable peak gain of 7.6 dBi. In [7], a modification of circular shape patch by cutting circular shape slots for a highly directional circular polarized S-band small patch antenna for satellite application was proposed. Simulation result shows the impedance bandwidth of 55 MHz (2.380–2.435 GHz) and an axial ratio less than 3 dB appears at about 35 MHz (2.410–2.445 GHz). A new compact single-feed circularly polarized S-band antenna for Nanosatellite Telemetry and Telecommand applications has been introduced where the reflector is composed of an Artificial Magnetic Conductor (AMC) in order to decrease the size of the structure[8].

A circularly polarized S-band antenna for small satellite is presented in this article, which is easy to fabricate and less expensive. Axial ratio bandwidth achieved from the antenna of 22 MHz with ±80-degree beam width. This paper is formatted as follows: Antenna description is given in Section II. Section III represents result and discussion. Finally, the conclusion of this paper is given in Section IV.

2. Antenna geometry

Implementation of the equations from the transmission line model (TEM), the primary geometry of the proposed patch antenna was first designed. In the noted reference [9], below equations can demonstrate the width and length of the patch antenna in relation to the detailed central frequency:

$$\frac{c}{2f_0}\sqrt{\frac{\varepsilon_\mathrm{r}+1}{2}}\,, \tag{1}$$

$$L = \frac{c}{2f_0\sqrt{\varepsilon_\mathrm{e}}} - 2\Delta l\,, \tag{2}$$

where L and W are the length and width of the patch respectively, f_0 is the target resonance frequency, c means the speed of light in vacuum and the relative permittivity ε_e can be measured by the equation

$$\varepsilon_\mathrm{e} = \frac{\varepsilon_\mathrm{r}+1}{2} + \frac{\varepsilon_\mathrm{r}+1}{2}\sqrt{(1+\frac{10h}{W})}\,, \tag{3}$$

where the substrate width is h and ε_{r} is the dielectric constant of the substrate. The antenna looks larger electrically comparing to physical dimensions due to the adjoining field around the boundary of the patch. Considering this result, Δl can be stated as

$$\Delta l = 0.412h\frac{(\varepsilon_{\mathrm{r}}+0.3)(\frac{W}{h}+0.264)}{(\varepsilon_{\mathrm{e}}-0.258)(\frac{W}{h}+0.8)}\,. \tag{4}$$

The length of the probe feed is also measured as the antenna is fed through it. Probe feed line and the input impedance of the antenna should be matched. The antenna is firstly considered to operate in single frequency at S-band in account the design necessities such as dielectric constant and bandwidth and subsequently adjusted to achieve the most desirable size of the patch using HFSS and CST simulator.

The design challenges for such applications differ from other modern wireless communications systems in that power consumption and size of the node are serious issues [10]. These limitations place strict requirements on the communication system; the system frequency should be high in order to minimize the antenna size.

Proposed antenna's geometric layout is exposed in Fig. 1. On FR-4 substrate material, the antenna is designed. Substrate height is 1.6 mm, relative permittivity is 4.6 and dielectric loss is 0.024. The antenna contains a square patch with two square slots in the one side of the substrate. One square slot is etched out from the top right corner with length L_{s} and another slot is etched out from the down left corner with the same length. These two slots is responsible for creating resonance frequency on the particular frequency. On the other hand, a square ground plane with opposite T-shaped slot was etched out from the center of the ground plane. The optimized antenna parameters are given in Table 1 with their values.

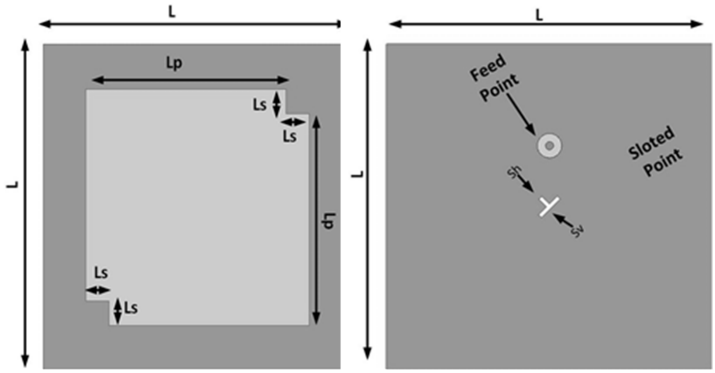

Fig. 1. Geometry layout of presented antenna

3. Results and discussion

To design a circularly polarized S-band patch antenna, a comprehensive parametric research of the antenna is accompanied. The ground slot of the proposed antenna

is responsible for desired frequency. The variation of reflection coefficient and axial ratio for different position and different size of slot is observed. The variation for different types of slot in the ground is depicted in Fig. 2, which indicates that the maximum reflection coefficient with minimum value of (–31.6643 dB) at 2.36 GHz is obtained by the proposed T slot antenna.

Table 1. Proposed antenna specification with particular parameters

Parameters	Dimensions (mm)	Description
L	40	Length of ground plane
Lp	26	Length of patch
Ls	3	Length of area etched from patch
h	1.6	Height of substrate
Sh	1.15	Horizontal slot
Sv	1.13	Vertical slot
r	1.5	Radius of circle

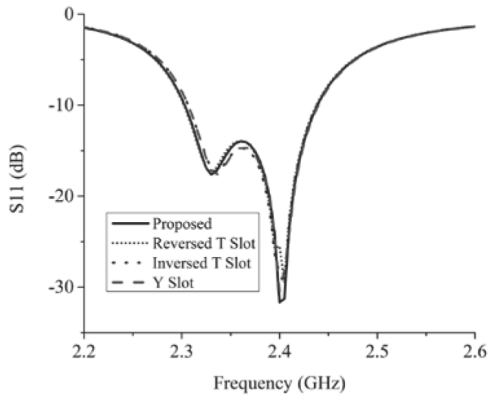

Fig. 2. Variation of reflection coefficient with frequency for different slots

The axial ratio value, which should be 0 for pure circular polarization, is varied for different types of slot in the ground plane, which is presented in Fig. 3. From this figure it can be observed that the maximum axial ratio bandwidth (1.298 %) with minimum axial ratio value (1.3358 dB) is attained. For other types of slot in the ground the value of the axial ratio increases.

The proposed antenna has been designed and studied by High-Frequency Structural Simulator (HFSS) and Computer Simulation Software (CST) microwave studio. The working procedure of this two software is Finite Integration Technique (FIT) based on the finite element method as well.

Figure 4 represents the reflection coefficient of the proposed antenna. It shows simulated and measured result of impedance bandwidth. HFSS and CST software are used to get the S_{11} values and the result are 100 MHz (2.30–2.40 GHz) and 120 MHz (2.28–2.40 GHz), respectively. The measured result of reflection coefficient

also meets an agreement with the simulation result and all of them are less than –10 dB. Smith chart is used to detect all prospective impedances on the sphere of presence of the reflection coefficient.

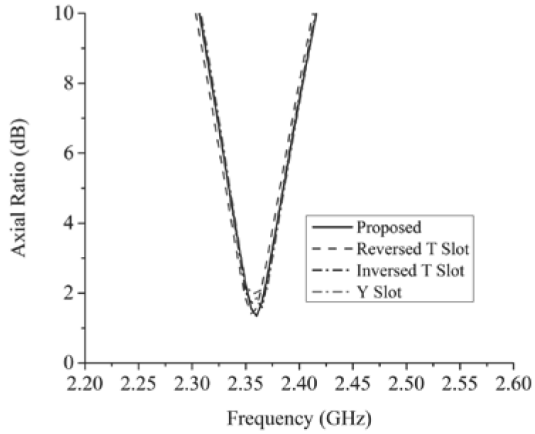

Fig. 3. Variation of axial ratio with frequency for different slots

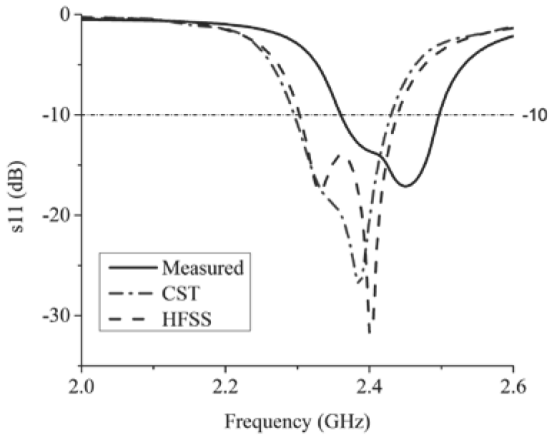

Fig. 4. Simulated and measured reflection coefficient of the proposed antenna

For impendance matching the Smith chart of the presented antenna has been evaluated and this is given in Fig. 5. The simulated and measured axial ratio of the proposed antenna is described in Fig. 6. The axial ratio presents the antenna polarization. The simulation result shows that the axial ratio of the presented antenna is less than 3 dB, which indicates that the antenna polarization is circular. The antenna displays 30 MHz of 3 dB axial ratio bandwidth. The measured axial ratio is consistent with the simulation result. This represent the antenna signal is more resistance due to atmospheric condition. Proposed antenna's current distribution has experimented at 2.36 GHz.

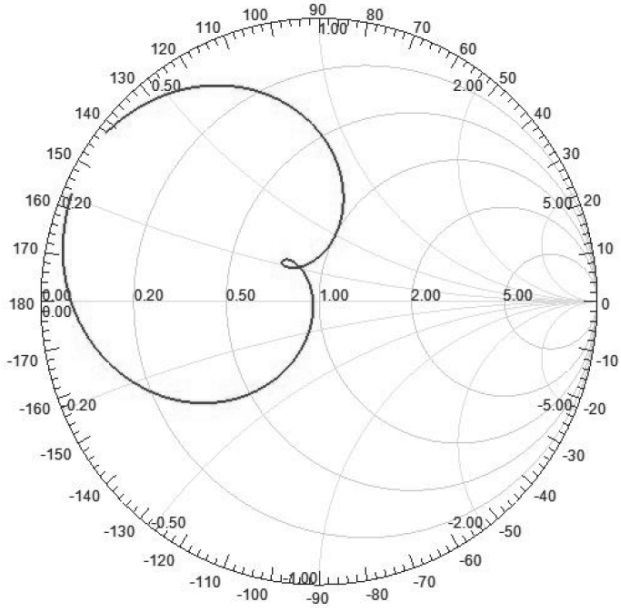

Fig. 5. Simulated Smith chart of the proposed antenna

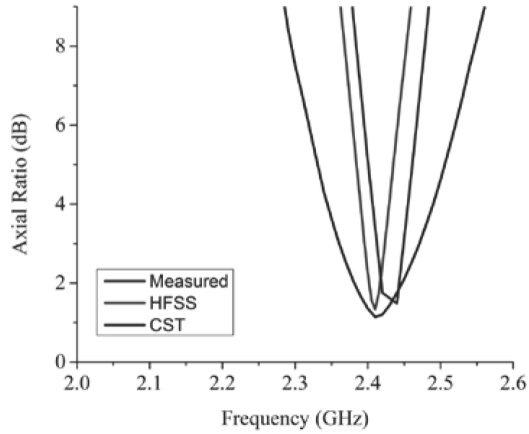

Fig. 6. Simulated and measured axial ratio of the proposed antenna

The current spreading experiments at four phase 0°, 90°, 180° and 270° are illustrated in Fig. 7. The 0° phase reference shows that the dominant radiating currents are in $-Y$ direction. The dominating currents flow for 90° phase is in the $+X$ direction. For 180° phase, the principal current movement is in the opposite current phase direction to 0° phase reference. Finally, for the 270° phase, the currents are directed in $-X$. Surface current distribution movement is anti-clockwise. Right-hand circular polarization (RHCP) has been observed from the behavior it shows.

Figure 8 shows the prototype of the antenna and Fig. 9 illustrates the elevation angle scope regarding lower 3-dB axial ratio for two different values of Φ and the value is 0 an 90, respectively, at 2.36 GHz. For $\Phi = 0$ the lower 3-dB axial ratio is -80 degrees and for $\Phi = 90$ the value is $+80$ degrees. The simulation and measured axial ratio pattern shows the similarity of the proposed antenna.

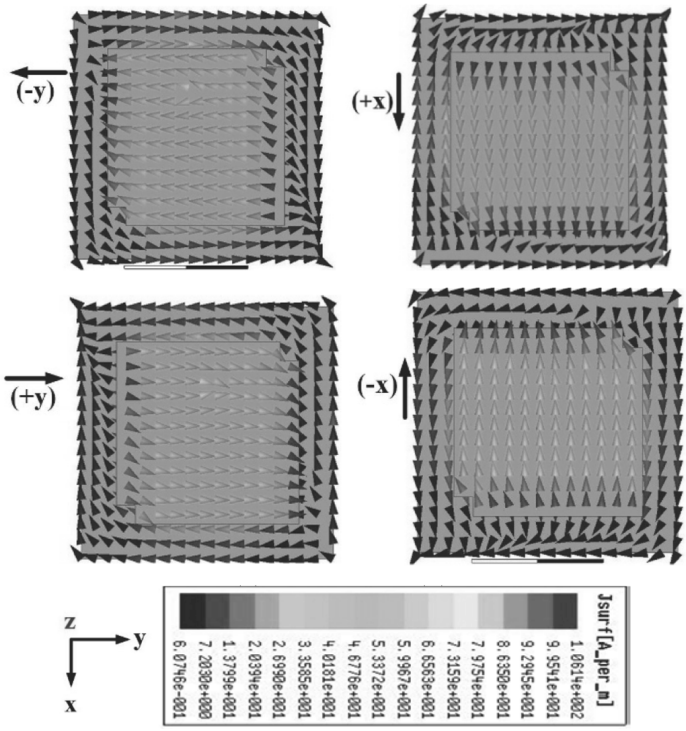

Fig. 7. Simulated surface current distribution at 2.36 GHz for altered phases top left–0°, top right–90°, bottom left–180° and bottom right–270°

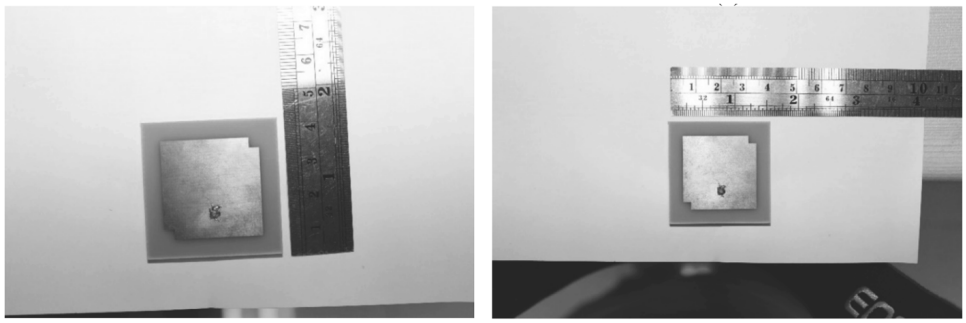

Fig. 8. Prototype of the antenna after fabrication from two different views

If the VSWR is lower than 2, the antenna match is considered very good and little would be gained by impedance matching. Figure 10 illustrates the VSWR curve of the proposed antenna which indicates the frequency range from 2.30 to 2.43 GHz. Here, the calculated impedance bandwidth is below 2. The simulated and measured VSWRs are very similar.

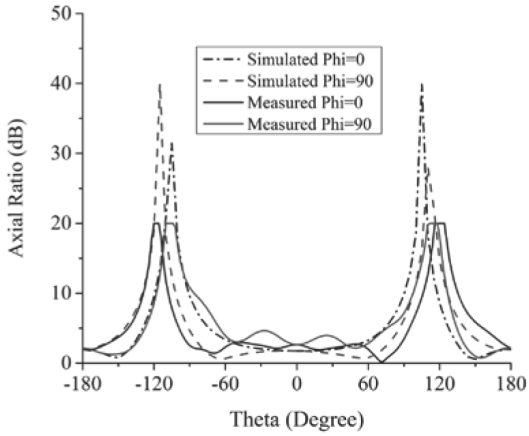

Fig. 9. Simulated axial ratio patterns of the proposed antenna

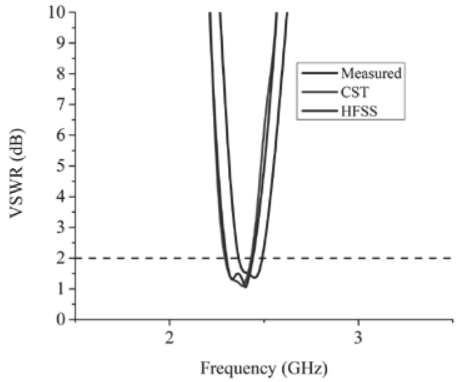

Fig. 10. Simulated VSWR of the proposed antenna

The simulated and measured RHCP and LHCP performance of the antenna are shown in Fig. at 2.4 GHz for phi 0 and 90 degrees, respectively. 2D radiation pattern of the proposed antenna displays a larger RHCP comparing to LHCP. The measured and simulated results are almost similar. Measured 3D radiation pattern shows the RHCP and LHCP performances in Fig. 12.

Figure 13 depicts the plot of simulated and measured peak gains of the presented antenna. The maximum gain 2.76 dBi in the frequency band, which remains consistent over the frequency band.

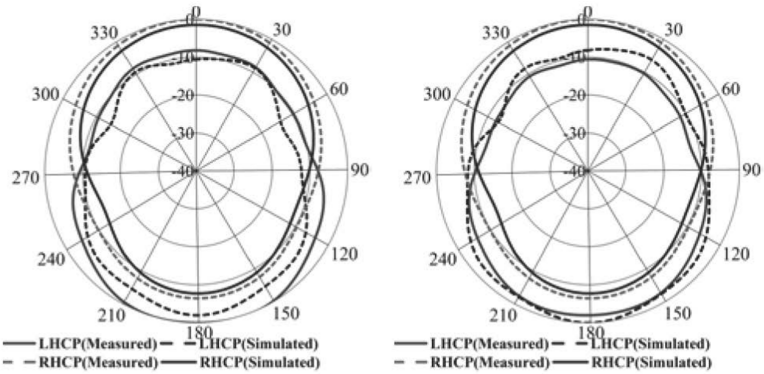

Fig. 11. 2D radiation pattern of the proposed antenna at 2.36 GHz: left–$\Phi = 0°$, right–$\Phi = 90°$

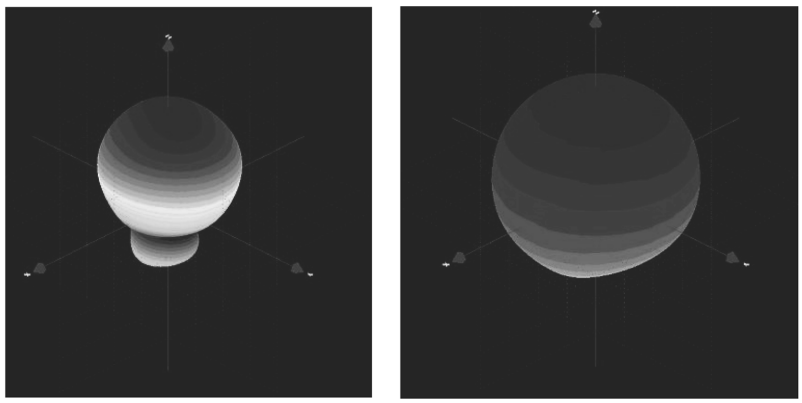

Fig. 12. Simulated 3D radiation pattern at 2.36 GHz: left–LHCP, right–RHCP

4. Conclusion

A circularly polarized patch antenna for S-band satellite application system has been introduced and designed. Simulation results, measured results and its implementation is presented in this paper. The antenna is easy to fabricate, less expensive, and can be stated as circular polarized as it shows that the value of axial ratio is less than 3 dB. The proposed antenna demonstrates 3 dB AR bandwidth of 30 MHz with an elevation angle of ±80 degrees. From this result, it can be indicated that the proposed antenna is circular polarized. This antenna was found to have an S_{11} of 4.26 % at 2.36 GHz. This type of antenna is capable of transmitting at high gain with maintaining its low-profile structure, which is very much desirable for a small satellite. Therefore, for the respective satellite application, the proposed antenna can be worth enough and can also be used for another frequency as well. In the future, the proposed antenna simulation effect with the actual satellite will be examined in the same condition in space.

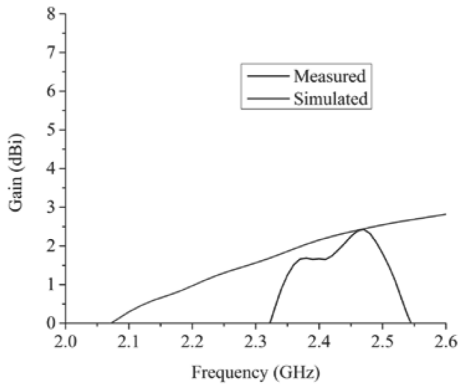

Fig. 13. Simulated and measured gains of the antenna

References

[1] W. A. Imbriale, S. Gao, L. Boccia: *Space antenna handbook*. John Wiley & Sons, Ltd (2012).

[2] M. Tanaka, Y. Suzuki, K. Araki, R. Suzuki: *Microstrip antenna with solar cells for microsatellites*. Electronics Letters *31* (1995), No. 1, 5–6.

[3] R. Holmberg, J. C. Slater: *Powered caster wheel module for use on omnidirectional drive systems*. Google Patents US6491127B1 (2002).

[4] S. Gao, K. Clark, M. Unwin, J. Zackrisson, W. A. Shiroma, J. M. Akagi, K. Maynard, P. Garner, L. Boccia, G. Amendola, G. Massa, C. Underwood, M. Brenchley, M. Pointer, M. N. Sweeting: *Antennas for modern small satellites*. IEEE Antennas and Propagation Magazine *51* (2009), No. 4, 40–56.

[5] M. T. Islam, M. Cho, M. Samsuzzaman, S. Kibria: *Compact antenna for small satellite applications [Antenna applications Corner]*. IEEE Antennas and Propagation Magazine *57* (2015), No. 2, 30–36.

[6] E. C. Choi, J. W. Lee, T. K. Lee, W. K. Lee: *Circularly polarized S-band satellite antenna with parasitic elements and its arrays*. IEEE Antennas and Wireless Propagation Letters *13* (2014), 1689–1692.

[7] M. Samsuzzaman, M. T. Islam, M. K. Nahar, J. S. Mandeep, F. Mansor, M. M. Islam: *Circularly polarized high gain S band antenna for nanosatellite*. International Journal of Applied Electromagnetics and Mechanics *47* (2015), No. 4, 1039–1049.

[8] A. Bellion, K. Elis, S. De Gaetano: *New compact S-band antenna for Nanosatellite TeleMetry and TeleCommand applications - EyeSat program*. European Conference on Antennas and Propagation (EuCAP), 10–15 April 2016, Davos, Switzerland, Publisher: IEEE (2016).

[9] P. Bhartia, I. Bahl, R. Garg, A. Ittipiboon: *Microstrip Antenna Design Handbook*. Artech House Publishers, Series: Artech House Antennas and Propagation Library (2001).

[10] G. Whyte, N. Buchanan, I. Thayne: *An omnidirectional, low cost, low profile, 2.45 GHz microstrip fed rectaxial antenna for WSN applications*. IEE and IEEE Conference, Loughborough Antennas and Propagation Conference (LAPC), 1–1 Marc 2006, Loughborough, UK (2006), 73–76.

Received April 15, 2018

Acta Technica *63* No. 6/2018, 887–896

Study on PID control and Fuzzy-PID control of magnetic fluid semi-active suspension[1]

Weichi Pei[2], Jianwei Dong[2], Haiyang Long[2], Yaogang Li[2], Hongchao Ji[2,3]

Abstract. Automotive semi-active suspension of adjustable damping force, under the control strategy based on real-time dynamic adjusting damping characteristics roads and cars, reducing vehicle vibration, in order to improve the vehicle comfort and stability. The magnetorheological (MR) damper is an ideal element for vehicle suspension semi-active control. In this paper, the MR damper is used as the adjustable damping force device, and the mechanical properties of the MR damper are obtained by the test, and the conventional PID control and Fuzzy-PID control are designed for the semi-active suspension respectively. To as random road excitation are simulated, the simulation results show that compared with the passive suspension, two control schemes are make the suspension performance has improved, but the Fuzzy-PID control of suspension performance improvement is better than PID control.

Key words. MR, semi-active suspension, PID control, fuzzy-PID control, simulation.

1. Introduction

The safety and comfort of a car is an important requirement for its driving [1]. The smoothness and stability of the vehicle in the driving process depend on the adjustment of the characteristics of the suspension system [2]. Suspension as the influence of vehicle comprehensive performance of the key components, connect the body and the axle, plays a relief when the vehicles running on the road because of the uneven road, engine vibration and turn itself the role of the braking and

[1]This work is supported by the National Natural Science Foundation of China (Grant No. 50975076). This work is also supported by Hebei Province Science Foundation for Youths (Grant No.E2017209059).

[2]School of Mechanical Engineering, North China University of Science and Technology, Tangshan Hebei, 063210, China

[3]Corresponding author

[4]Workshop 3; e-mail: jihongchao666@163.com

other operation caused by vehicle vibration [3]. Traditional passive suspension has limited the performance of the car by its inherent defects, the controllable suspension has become the development direction of vehicle suspension technology [4]. The semi-active suspension has the advantages of both passive suspension and active suspension, and it can reach the control effect of the active suspension, which is the most promising controllable suspension form [5]. The semi-active suspension system exists in the adjustable damping force, through studying the characteristics of damper, control strategy and design dynamic adjust the damping force to reduce vehicle vibration, in order to improve the ride comfort and operation stability [6]. Pan [7] combines PID control with fuzzy control [8], the fuzzy-PID switching control system of semi-active suspension with MR damper is designed, and the simulation results show that the method has good damping effect. Reference [9] combines adaptive fuzzy reasoning system (ANFIS) and PID control, an ANFIS-PID controller was designed for a quarter of a semi-active MR damper. The simulation proved that the strategy was superior to the conventional PID control.

This paper combines conventional PID control with fuzzy control, the fuzzy controller is used to realize the dynamic adjustment of the parameters to deal with the nonlinear and time-varying characteristics of the semi-active suspension. Based on the above two control methods, the conventional PID control and fuzzy-PID control strategy of semi-active suspension are designed respectively. Based on the performance of passive suspension, the improvement of suspension performance is compared.

2. A quarter of the semi-active suspension

The kinetic differential equation has the form

$$\begin{cases} m_2\ddot{z}_2 + c(\dot{z}_2 - \dot{z}_1) + k_2(z_2 - z_1) - F = 0, \\ \\ m_1\ddot{z}_1 - c(\dot{z}_2 - \dot{z}_1) - k_2(z_2 - z_1) + k_1(z_1 - q) + F = 0, \end{cases} \tag{1}$$

where m_1 is the tire mass, m_2 is the body mass, z_2 is the vertical displacement of the body, z_1 is the vertical displacement of tire, k_1 is tire stiffness, k_2 is the suspension stiffness coefficient, c is the suspension damping spring stiffness, q is the road input and F is the adjustable damping force, which is also the research object of semi-active control strategy to realize dynamic regulation to improve suspension performance.

In the evaluation indexes of suspension performance, the most important is the vertical acceleration, suspension dynamic deflection and tire load, respectively corresponding to the $\ddot{z}_2$, $z_2 - z_1$ and $k_1(z_1 - q)$ in (1).

In Simulink, the simulation model as shown in Fig. 1 is created by using the semi-active suspension differential equation of a quarter of the car shown in (1). After removing the adjustable damping force F, the model becomes a passive suspension simulation model. The damper used in this paper is the RD-8041-1 MR damper of American lade company. The selection of the model suspension parameters: $m_1 =$

30 kg, $m_2 = 264$ kg, $k_1 = 160000$ N/m, $k_2 = 16000$ N/m, $c = 1100$ N.s/m.

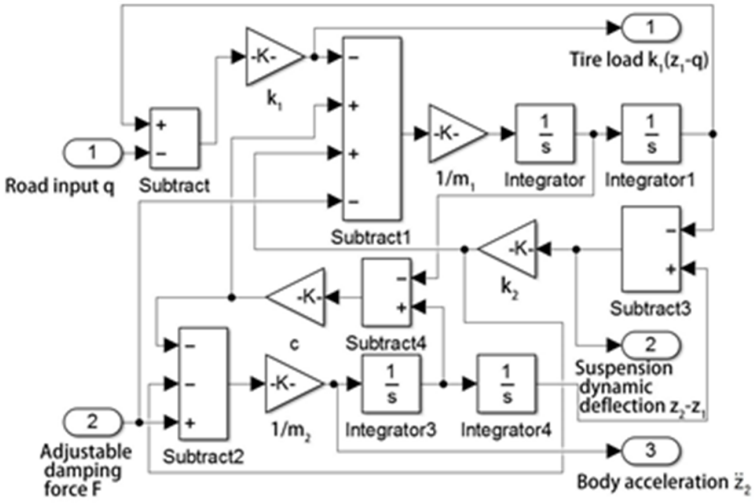

Fig. 1. Semi-active suspension simulation model

During the moving process, the vehicle will be subjected to the vibration of the body caused by the change of the ground, the vibration of the engine itself, and the turn braking. In this paper, the rough pavement excitation is the most important incentive. In the study of the dynamic performance of automotive suspension, an effective pavement input model must be established.

In the simulation of suspension performance, the pavement input usually adopts the simple harmonic signal and the white noise signal. In this paper, the white noise method is used to simulate the surface input, and its differential equation is shown in (2).

$$\dot{q}(t) = 2\pi n_0 \sqrt{VGq(n_0)}w(t) - 2\pi f_0 q(t)\,, \tag{2}$$

where $q(t)$ is a random road incentive, $w(t)$ is the Gaussian white noise signal, n_0 is the reference space frequency, V for vehicle speed (m/s), Gqn_0 is the pavement spectrum value, which can query the national standard, and f_0 is the space cutoff frequency.

By equation (2), a random road simulation model is established in Simulink, as shown in Fig. 2.

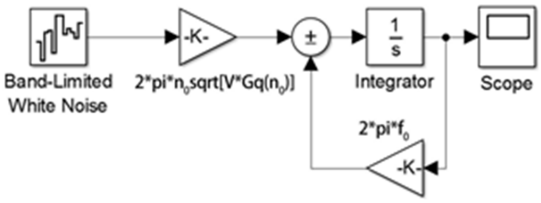

Fig. 2. Input model of road

3. Mechanical experiment and modeling of MRD

The adjustable damping force of semi-active suspension is the RD-8041-1 MR damper of the U.S. The instrument used in the test is the dampers test system produced by Hangzhou YiHeng science and technology. The loading method is loaded by the displacement control sine wave, the loading current is 0 A, 0.3 A, 0.6 A and 0.9 A, the loading frequency is 0.5 Hz, 1.0 Hz, 1.5 Hz, and the amplitude is 5 mm, 10 mm and 15 mm respectively. The experiment of $4 \times 3 \times 3 = 36$ working conditions was carried out.

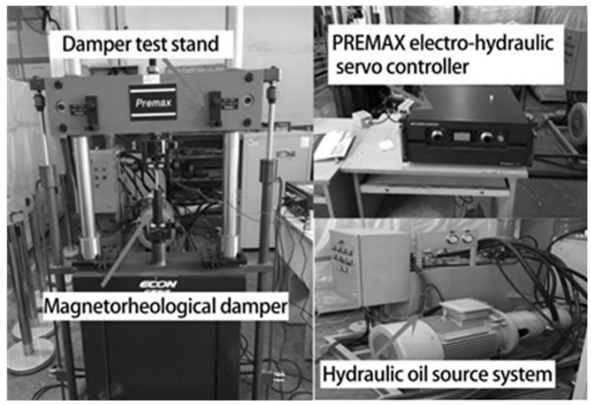

Fig. 3. Damper test system

When the excitation frequency is 1.5 Hz and the amplitude is 15 mm, the real-time damping force-velocity and damping force-displacement curve of 0 A, 0.3 A, 0.6 A and 0.9 A are shown in Fig. 4. As can be seen from Fig. 4, right part, the damping force–displacement curve is approximately square, and the damping force-velocity curve has a noticeable hysteresis characteristic. In the same vibration displacement or velocity, the larger the current, the greater the damping force.

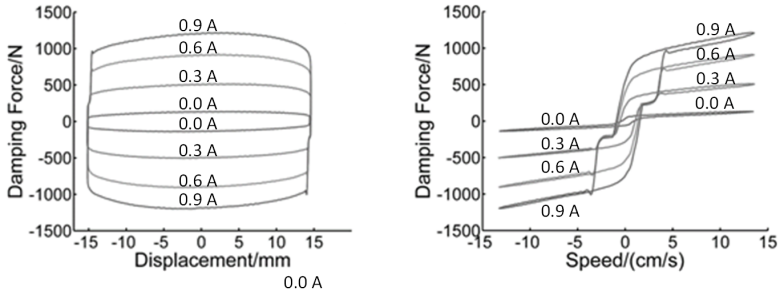

Fig. 4. Mechanical property curve of damper

The MR damper has a variety of mechanical models, and the modified Dahl model has fewer parameters and can well describe the hysteresis characteristics of

the dampers. The model expression is

$$\begin{cases} F = K_0 x + C_0 \dot{x} + F_{\mathrm{d}} Z - f_0, \\ \dot{Z} = A\dot{x}\left[1 - Z\,\mathrm{sgn}(\dot{x})\right], \end{cases} \tag{3}$$

where K_0 is the stiffness coefficient, C_0 is the viscous damping coefficient, f_0 is the initial force, F_{d} is the adjustable coulomb friction force, A is the shape parameter of hysteresis curve, x is the relative displacement of the piston and cylinder body, and Z is the delayed displacement. In addition, there is a linear relationship between C_0, F_d and current in the form

$$\begin{cases} C_0 = C_{0\mathrm{s}} + C_{0\mathrm{d}} I, \\ F_{\mathrm{d}} = F_{\mathrm{ds}} + F_{\mathrm{dd}} I. \end{cases} \tag{4}$$

As can be seen from Table 1, the parameters change with current. In the further description of parameters and current relationship, if all parameters are taken into account, it can improve the precision of mechanical model, but it will increase the number of parameters and increase the identification complexity. The force F_{d} and C_0 of the redefined parameters after fixing the above parameters are as Table 2. Using Matlab to fit the relationship between F_{d}, C_0 and current I, the conclusion was drawn that F_{d} and C_0 were shown in a linear relationship as shown in (4).

Table 1. Results of each current parameter identification

I	C_0	A	f_0	F_{d}	K_0
0	0.627	51.076	1.933	50.828	1.011
0.3	1.638	25.390	2.213	296.779	1.397
0.6	2.893	10.572	7.864	541.569	2.028
0.9	3.695	6.977	12.600	734.848	2.217

Table 2. F_{d} and C_0 identification results

I	C_0	F_{d}
0	0.652	48.313
0.3	1.647	295.943
0.6	3.027	524.954
0.9	4.069	688.653

The total parameters of Dahl model with the modified Dahl model for the experimental magnetic MR dampers are shown in Table 3.

By identifying the parameters, the modified Dahl model of (3) can accurately describe the mechanical properties of the dampers used in the experiment, and describes the hysteresis characteristics of the MR damper. This expression reflects the relationship between the current and the output damping force in different states.

The damping force of the semi-active suspension can be obtained by adjusting the control current in the MR damper with the current generator.

Table 3. Modified Dahl model parameter identification results

Parameter	Numerical	Parameter	Numerical
A	23.504	C_{0s}	0.604
f_0	6.152	F_{dd}	716.677
K_0	1.663	F_{ds}	66.961
C_{0d}	3.878		

4. Semi-active suspension Fuzzy-PID control

The semi-active suspension system as a nonlinear time-varying systems, the conventional PID control parameters presented the dynamic adjustment shortcoming, thus the PID control and compound control method combined with other control methods. This study combines PID control with Fuzzy control to form Fuzzy-PID control. The principle is shown in Fig. 5, and the real-time correction of PID control parameters is realized by Fuzzy theory to meet the time-varying characteristics of the suspension system so as to achieve better control effect.

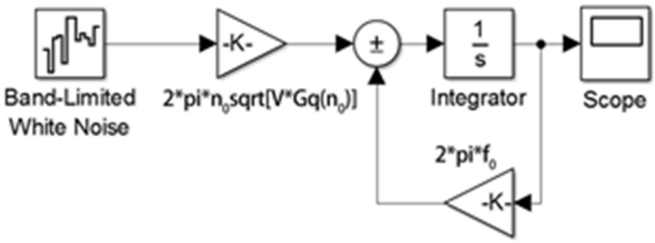

Fig. 5. Schematic diagram of Fuzzy-PID control

In this suspension Fuzzy-PID control, the difference between the real value and the default value of the body vertical velocity is selected as e, and the change rate is input to the Fuzzy controller as ec. Set the preset value to zero, at this point, e is the vertical speed of the body, ec is the vertical acceleration of the body. The output of fuzzy controller is the adjustment of the three parameters of PID controller, Δk_{p}, Δk_{i}, Δk_{d}, and through PID controller, the final k_{p}, k_{i} and k_{d} are obtained, and the output is adjustable damping force F. The relationship between k_{p}, k_{i}, k_{d} and Δk_{p}, Δk_{i} and Δk_{d} is shown in (5).

$$k_{\mathrm{p}} = k_{\mathrm{p0}} + \Delta k_{\mathrm{p}},\ k_{\mathrm{i}} = k_{\mathrm{i0}} + \Delta k_{\mathrm{i}},\ k_{\mathrm{d}} = k_{\mathrm{d0}} + \Delta k_{\mathrm{d}} \tag{5}$$

where k_{p0}, k_{rmi0}, k_{d0} are the initial parameters before the whole setting. The parameters of conventional PID control are selected, Δk_{p}, Δk_{i} and Δk_{d} are proportional, integral and differential coefficient adjustment k_{p}, k_{i} and k_{d} are the final PID controller parameters. In real life, the approximate range of the vertical velocity of the

body is [-0.3, 0.3] m/s, and the vertical acceleration of the body is [-3, 3] m/s^2. The fuzzy field of input and output is as follows:

$$E,\ ec = [-3, -2, -1, 0, 1, 2, 3]\Delta k_{\mathrm{p}},\ \Delta k_{\mathrm{i}},\ \Delta k_{\mathrm{d}} = [0, 1, 2, 3]\,.$$

The input and output variables are selected by the triangle membership function. Fuzzy reasoning using Mamdani method, a total of 3×49 control rules are established. The solution to blur is to use the center of gravity method, create a simulation model based on the above design, as shown in Fig. 6.

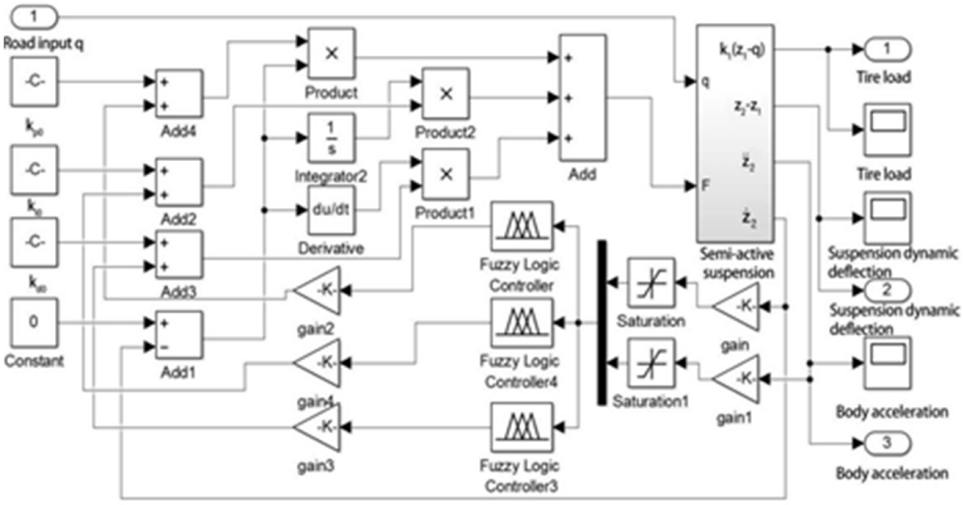

Fig. 6. Semi-active suspension Fuzzy-PID simulation model

5. Simulation analysis

From Fig. 7 and Table 4, when the vehicle travels with velocity of 25 m/s along B level road compared with the passive suspension, the performance response curve of semi-active suspension under the control of conventional PID control and fuzzy-PID control has dropped. Tyre dynamic load body vertical acceleration, suspension dynamic deflection and the root mean square of the conventional PID control was reduced by 4.8 %, 8.6 % and 9.3 %, respectively, Fuzzy-PID control makes the suspension performance indexes reduce by 13.5 %, 26.5 % and 13.5 % respectively.

6. Conclusion

In this paper, the vehicle semi-active suspension is simplified to obtain a two-degree of freedom and one-fourth vehicle dynamics model, and the road input model is established by using the integral white noise method. Then the mechanical test and the mechanical model of the adjustable damping force device of the semi-active

suspension is studied. Then in order to reduce the suspension key performance indicators that tyre dynamic load body vertical acceleration, suspension dynamic deflection, for the purpose of the semi-active suspension design PID control and Fuzzy-PID control method, with simulation as an incentive for random road, compared with passive suspension at the same time, simulation experiment is carried out under the same roads in perfect condition. The results show that PID control and Fuzzy-PID control can improve the performance of semi-active suspension. Fuzzy-PID control is better than PID control for suspension performance, and provides reference for future research of automotive suspension.

Table 4. The root-mean-square of suspension performance

Control scheme	Body vertical acceleration m/s^2	Suspension dynamic deflection (m)	Tire load (N)
Passive suspension	1.365	0.007799	550.6
PID control	1.238	0.007129	524.2
Fuzzy PID control	0.9937	0.005731	476.3

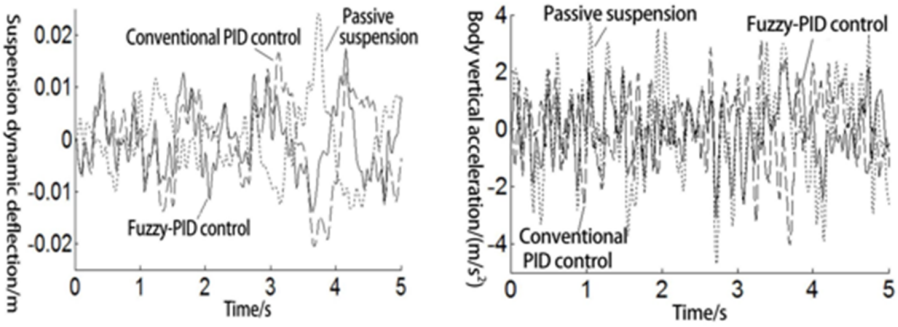

(a) Suspension deflection **(b) Body vertical acceleration**

Fig. 7. Simulation results of suspension three indicators

References

[1] Z. Z. Peng, J. Q. Zhang, J. Yue, L. Zhang, D. Huang: *Design and analysis of magnetorheological damper with parallel normal holes.* Journal of mechanical engineering (2015), No. 8, 172–177.

[2] Z. L. Yang: *Analysis of PID control of semi-active suspension stability of automobile.* Journal of Chongqing University of Science and Technology (Natural Science Edition) *19* (2015), No. 5, 102–104.

[3] X. P. Wang, X. P. Chen, L. N. Ji, L. Wu: *Simulation study on two-degree-of-freedom semi-active suspension based on fuzzy PID control strategy.* Journal of Guangxi university of science and technology *28* (2015), No. 2, 35–41.

[4] J. H. Zhang, L. S. Hong, W. Z. Yang, et al.: *Overview of vehicle suspension system and its performance evaluation.* Mechanical design and research (2015), No. 6, 147–153.

[5] H. E. Tseng, D. Hrovat: *State of the art survey: Active and semi-active suspension control.* International Journal of Vehicle Mechanics and Mobility *53* (2015), No. 7, 1034–1062.

[6] M. Kaldas, K. Caliskan, R. Henze, F. Kücükay: *Rule optimized fuzzy logic controller for full vehicle semi-active suspension.* SAE International Journal of Passenger Cars - Mechanical Systems *6* (2013), No. 1, 332–344.

[7] D. Y. Pan, Y. Tang, P. C. Shi, et al.: *Application of fuzzy-PID switching control in magnetorheological semi-active suspension system.* Mechanical Science and Technology (2017), No. 2, 292–297.

[8] M. Gh. Morteza, M. k. Mahmoodi: *Development a new power management strategy for power split hybrid electric vehicles.* Transportation Research Part D: Transport and Environment *37* (2015), 79–96.

[9] J. Marzbanrad, G. Soleimani, M. k. Mahmoodi, A. H. Rabiee: *Development of fuzzy anti-roll bar controller for improving vehicle stability.* Journal of Vibroengineering *17* (2015), No. 7, 3856–3864.

Received June 17, 2018

Acta Technica *63* No. 6/2018, 897–902

Simulation and study of optical systems based on LEDs

Vitaly Baynev[1 2], Sergey Fedosin[2]

Abstract. The paper considers the problems and the ways of reaching energy efficiency in lighting. The features of lighting engineering calculation and the computer modeling of modern light devices based on light-emitting diodes and their optical systems are also considered. The development of modern LED lighting systems is associated with the use of software. The article describes the developed software system that allows developing the models of optical systems to perform ray tracing and to design the spatial distribution of light flux. Modeling of optical systems is described using the example of secondary LED optics for street lighting fixtures. An experimental study of the main lighting and thermotechnical characteristics of lens systems, created by 3D prototyping is also carried out.

Key words. Modeling, optical system, lighting device, secondary optics, LED, lens, photometric body, program, tracing.

1. Introduction

The problems of industrial product quality provision and energy efficiency increase have one of the highest priorities in Russia and in the world [1]. This fully applies to modern lighting, which currently consumes about 20 % of the world electricity consumption, and it will only increase due to ever-increasing needs. The increase of energy saving and energy efficiency in the field of lighting is aimed primarily at the prohibition of incandescent lamp production and consumption, the modernization of lighting systems and an active introduction of LED technologies [2–3]. Energy saving is also very important in the production of many possible optical and electronic devices and has become the focus of attention recently [4]. LED lighting systems allow to implement many tasks in the field of modern artificial lighting. The use of LEDs for outdoor, industrial and architectural lighting will grow at higher rates than in other areas of their traditional use (indications, lighting

[1]Department of Automated information processing systems and Management, Institute of Electronic and Light Engineering, National Research Ogarev Mordovia State University, Saransk
[2]Corresponding author; e-mail: bw14@mail.ru

systems, etc.). The main trends for LED lighting equipment improvement is the increase of light output and service life at cost reduction. A wide application of LED makes relevant the calculation and the design of lighting systems that have high light efficiency and wide possibilities of lighting technical characteristics control.

In modern lighting engineering, the calculation and the modeling of LED lighting characteristics of lighting devices (LD) is an actual task. The results of this calculation largely determine the shape and the dimensions of an optical system and an entire LD, as well as its lighting parameters, which in its turn depend on the field of a device application [5–7]. The calculation of an optical system (OS) is the main stage in LD development, the result of which is its overall and photometric characteristics determination. Light engineering calculation of optical systems is based on a sequence of direct problem solution for LD calculation, i.e. the determination of LD light distribution under known LD and light source parameters. There are various methods for this problem solution, based on the methods of elementary imaging, the balance of flows, the numerical-ray methods, etc. [2]. In many cases, when a LD is used in lighting systems, a special secondary optics is needed. It serves to develop a set light distribution [4]. Nowadays, secondary optics are produced with a variety of light intensity curves (LIC) influenced by the type of surface and optics geometry and the characteristics of LED (luminescence power, size and angle).

2. Method

The calculation of OS elements consists of several stages. First, a light source model is created, a light distribution is set, a choice or a development of an optical element form and design is performed. Then, the simulation and the optimization of an obtained system are carried out by characteristic analysis, parameter adjustment and a direct optimization to obtain a final result [8]. The use of computer technology makes it possible to avoid labor-intensive manual calculations and a large amount of computational and graphic works. And many stages of their development can be fully automated with the use of a specialized software for modeling, the analysis and the optimization of optical systems.

The mathematical model is developed, which is used as the basis for LightModeling software package developed for modeling purposes. This program allows you to create three-dimensional models of optical systems and conduct the analysis of illumination distribution, taking into account the reflection, the absorption and the diffraction of light. Special elements of secondary optics have been developed for the use in street and road lighting relatively recently. The use of such lenses can greatly simplify the task of LED fixture design for street and road lighting, while they can be installed instead of conventional ones with discharge lamps, without any change of the support configuration.

3. Results

It is very important that the elements of the secondary optics are accessible with the required parameters of a selected type of LED for the manufacturers of LED outdoor lighting. Street lighting, as a rule, requires the development of a specific LIC, a typical shape of lenses and their LIC for such lighting are shown in Fig. 1. A similar function is performed by the LD with multilenses.

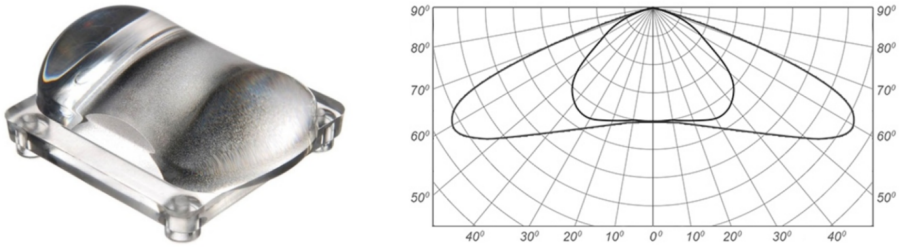

Fig. 1. Typical forms of lenses and LIC for outdoor lighting fixtures

The algorithm of OS modeling by the use of the software package was described in [5]. Figures 2–3 show the process of LED optics design for a street lighting fixture. The following is shown here: the working window of the program with the LED module (LM) and the functional of specifications for used materials (Fig. 2), SD model with secondary optics, its photometric body and LIC (Fig. 3) and LM assembly model (Fig. 4).

3.1. LED module prototyping

In order to test the adequacy of the developed LM for the LED road lighting fixture, the prototyping was carried out (the creation of prototypes or a system running model to test the feasibility of their implementation). One of the most common formats for a prototype model provision is STL format, which is used for 3D modeling and the use in 3D printers. The developed software allows exporting the calculated data to many formats, including OBJ format for standardized files containing 3D objects. Further design was carried out in 3DS Max program, namely, the export to the previously described STL format for a 3D printer. The final LM model for prototyping has the following overall dimensions: $18.8 \times 11.2 \times 6.35$ mm. A rapid unit (3D printer) ULTRA 3SP was used for prototyping. A key feature of this 3D printer is the ability to use transparent E-Glass material, which allows prototyping transparent lighting components (protective glass of complex shape, lenses, optical elements, etc.). After the performed works, the model obtained through the use of 3D printing, is completely ready for the production of a silicone mold with the subsequent pouring of polyurethane into it.

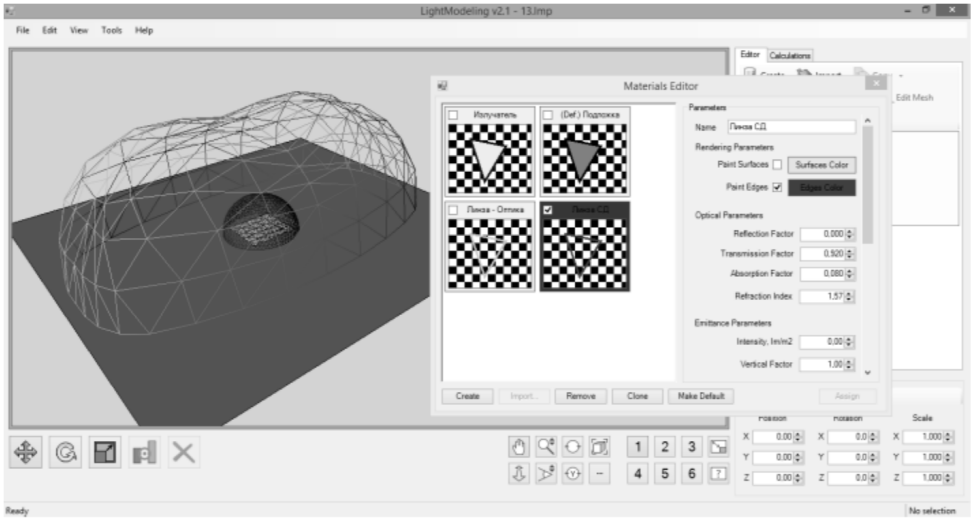

Fig. 2. Projecting of material characteristics in design process

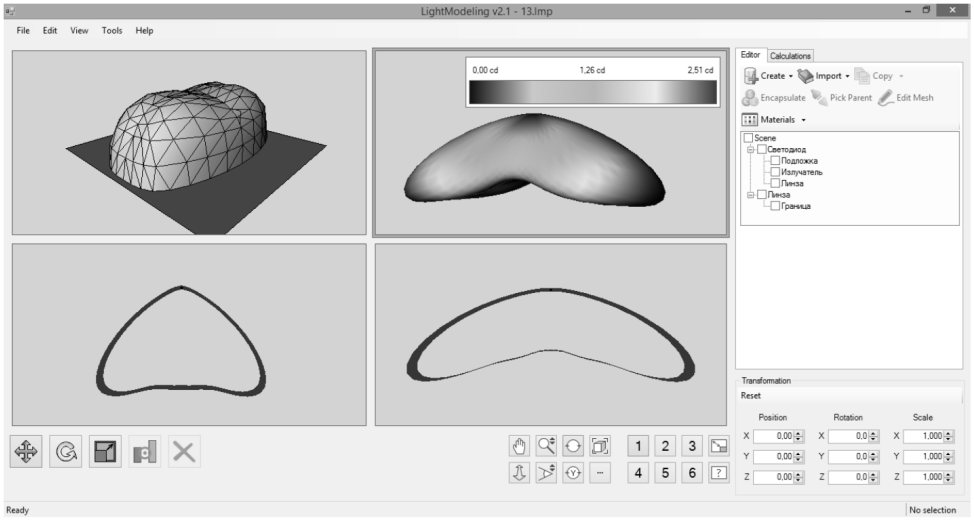

Fig. 3. Light distribution modeling from LM

3.2. Experimental study of LED module lighting characteristics

The most significant characteristics of LM are light distribution and thermal mode. The measurement of light intensity and luminous flux spatial distribution as a derivative can be performed with a goniophotometer (GO-2000A distribution photometer) most accurately. The processing of test results is performed using the supplied software GOSoft V2.0 in an automatic mode, which is displayed in real time. The result of the experimental LM measurement on a goniophotometer was a

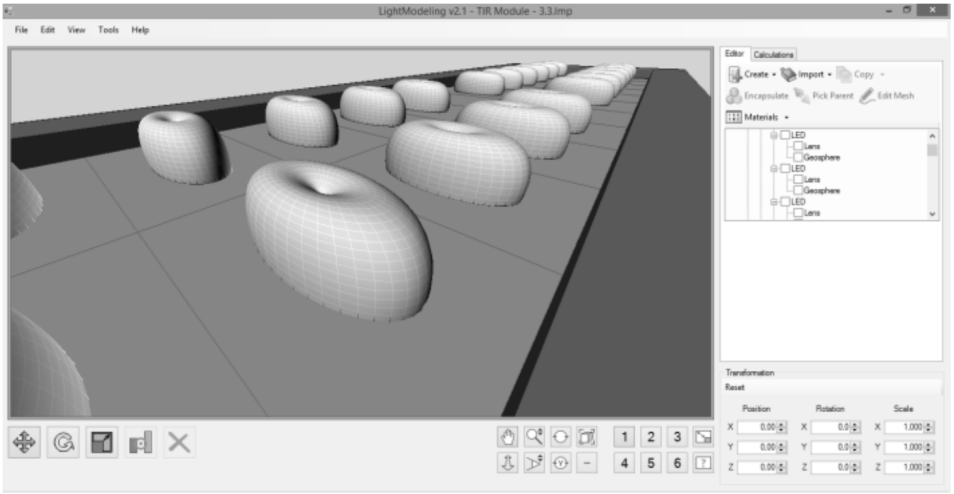

Fig. 4. LM assembly

photometric body and LIC (Fig. 5), which meets the requirements of street lighting.

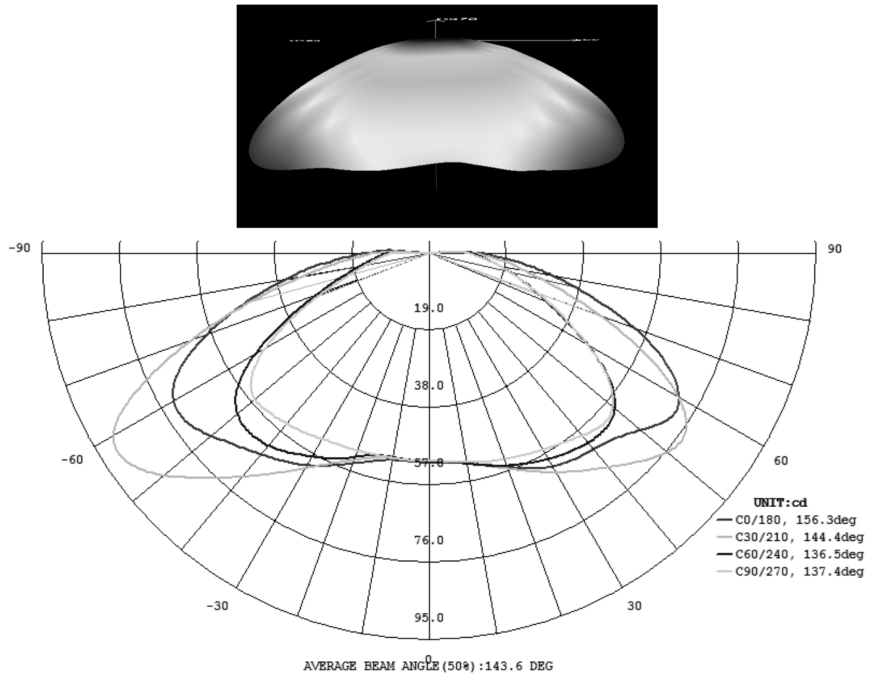

Fig. 5. The photometric body and the LIC of LED module

The maximum luminous intensity for this sample was 104 cd, the luminous flux was 312 lm, the light output was 155 lm/W, and the emission angle was 150°. The

evaluation of the experimental LIC conformity with the calculated ones was estimated by their superimposing them and visual comparison, as well as by a standard deviation determination, which was 3.5 cd (approximately 4 % of the luminous intensity maximum value). In order to determine the temperature distribution over the developed lens surface, the temperature was measured with Testo 881 thermal imager. The maximum temperature on the lens surface is 78.7 °, which does not exceed values typical for similar systems.

4. Conclusion

In modern lighting equipment, the calculation and modeling of the LED modules and LD lighting characteristics is an actual task. The developed software package makes it possible to simplify the process of optical LED system design and to improve their quality significantly. In this complex, a LD as a complex product is viewed as a hierarchical structure in the form of parent and child nodes, the geometry of which is modeled with triangulation grids. The computer simulation of LED and its optical system is performed in the form of a free-form lens and a LED module assembly. Its 3D models, the photometric body and light power curves were obtained in two planes. On the basis of 3D-prototyping technology, the experimental samples of LED modules were made and their lighting and thermal characteristics were studied. The results obtained from the measurements show a very good agreement with the calculated ones, which indicate a great potential of such programs. This software package allows studying visually the processes in optical systems without resorting to expensive experiments, which allows recommending it for practical use.

References

[1] S. B. Baurina, E. V. Nazarova, E. O. Savchenko: *The problem of ensuring industrial products quality in Russia.* Journal of Business and Retail Management Research (JBRMR) *12* (2017), No. 1, 206–214.

[2] I. I. Bayneva: *Concerns of design of the energy-efficient fixtures.* International Journal of Applied Engineering Research *10* (2015), No. 3, 6479–6487.

[3] Z. Hemmat, R. Faez, S. Amiri: *Simulation and investigation of a back-triggered 6H-SiC high power photoconductive switch.* Power Electronics, Drive Systems & Technologies Conference (PEDSTC2015), 3–4 Februar 2015, Tehran, Iran, IEEE Conferences (2015), 253–256.

[4] V. V. Bainev, I. I. Bayneva: *Optical systems for light-emitting diodes.* Photonics *56* (2016), No. 2, 84–93.

[5] V. V. Bainev: *Calculation and design of LED optical systems.* Semiconductor lighting equipment *45* (2017), No. 1, 38–41.

[6] F. Rasouli, Z. Hemmat: *Simulation of InGaN-based near-ultraviolet/visible dual-band photodetector.* Optical and Quantum Electronics *48* (2016), No. 1, p. 23.

[7] I. I. Bayneva: *Computer modeling and design of a LED lamp with an autonomous power supply.* Assembling in machine building and instrument making (2017), No. 10, 466–473.

Received June 14, 2018

Acta Technica *63* No. 6/2018, 903–908

Design of new small water passing structures at roads

Michail V. Nemchinov[1], Igor V. Chistiakov[1], Tatiana A. Suetina[1], Nikita V. Borisuk[1], Anna G. Ivanova[1]

Abstract. A new type of a small water passing structures for roads is offered. Need of construction of new type small water passing structures is caused by the considerable height of a road bed in places of their construction that leads to unfairly high embankments on roads, big need for soil for construction, pits for production of soil and excessively high cost of construction of a road bed. If to proceed from need of new construction for Russia about 900 thousand kilometers of roads (at the general need of the country for a network of roads of national federal and regional value in 1.5 million kilometers, apart from local roads which it is necessary to construct about 850 thousand more kilometers), with a "brought by snow" height of an embankment 2 meters and the minimum width of a road bed on top 17.5 meters, will be required at least 35.1 cubic kilometers of the good soil suitable for a road bed. In article features of design of new type of a small water passing structures of "split" type are stated. Theoretical calculations and data of hydraulic laboratory researches are submitted, and also recommendations about design of the offered small water passing structures of new type are provided.

Key words. Waterway, waterless valley, water throughput construction, expansion of a stream, expansion site length, stream speed, stream expense, model, criteria of modeling, hydraulic experiment.

1. Introduction

The crossing of small watercourses and dry land (temporary watercourses) by a road requires the construction of small-sized discharge facility—small bridges, culverts and other types of road hydraulic structures. Their number is great not only on a crossed, but also on a flat terrain—at least one per kilometer of road. In the design process, the control points of the project line position are determined concerning a longitudinal road profile [1]. An example of such control points are the elevation marks of a roadbed over small culverts. These elevation marks are determined by

[1]Moscow Automobile and Road Construction State Technical University (MADI) 64, Leningradsky Prospect, Moscow, 125319; e-mail: Madi-bnv@mail.ru

the sum of the log bottom marks, the height of a structure (a culvert) and the height of a soil backfill above a pipe. Usually the minimum internal diameter of a water discharge pipe is 1 m, the outer one makes 1.2 ... 1.3 m, the thickness of a soil layer above a pipe makes at least 0.5 m [2]. In total, this gives an embankment height of 2 meters at least. Thus, the roadbed of a road is formed in an embankment without an actually justified height [3]. The issue of snowdrifts requires special consideration.

The construction of roads in embankments requires a huge amount of soil and a variety of soil quarries [4]. Therefore, it is necessary to look for the ways reducing the height of mounds on flat areas. One of them is the construction height decrease of a roadbed at the location of small culverts.

2. Research method

The expansion of a water flow in front of a roadbed means the construction of a small culvert with an opening equal to the width of a water flow. If the capacity is maintained, this means that it is possible to reduce the height of a hole and, correspondingly, the height of an embankment. Let us call it a sprawling structure.

The change of a small culvert design principle requires certain changes in the construction associated with the hydraulic pattern of a water flow. In this case, the leading log located near the roadbed of the road requires a culvert expansion to the desired width. The decrease of the culvert height is limited by the requirements of its cleaning possibility from the deposits from a water stream [5, 6]. Small longitudinal slopes of small logs in combination with the presence of vegetation reduce the speed of water flow and, thus, the carrying capacity of the water flow [7]. Large pollution in accordance with the rules of small culvert operation (maintenance) should be removed by the road maintenance service [6]. Thus, a minimum height of a culvert can be set in the range of 0.3–0.4 m.

An extended discharge facility can work in a non-pressure (preferably) or in a pressure regime. The latter is worse because of backwater and roadbed flooding emergence, the in-crease of water flow at the exit from the structure [3].

One can achieve a situation when the speed of the water flow reaches the value of "non erosive" for the soil. The length of a log section widening should be sufficient for a smooth expansion of a water flow to the magnitude of broadening [8].

With a sufficient degree of accuracy, the specific energy of the flow E can be deter-mined from the formula for the cross section of a water flow outlet from a natural log to an expansion site:

$$E = \beta h_{\text{out}} + \alpha V_{\text{out}}^2 \approx 2g\,, \tag{1}$$

where β is the coefficient of potential energy, taking into account the non-hydrostatic distribution of pressure in an outlet section, and h_{out}, V_{out} are the depth and velocity of the water flow in an outlet section, respectively. At the form of a log channel part cross section, which is close in shape to a circular one (as in the case of a pipe), the coefficient β at non-pressure and channel filling $h_0/D = 0 - 0.5$ is assumed to be [0.5–0,6] (D is the diameter of an equivalent pipe and h_0 is the of flow in a log bed).

Like with the calculation of small bridges, the depth of the flow in the outlet section is determined from the Bernoulli equation. According to numerous studies the section of the surface water level reduction is formed before the cross section of the water flow outlet transits from the log to its widened part ($l_{\text{out}} = [3-4]h_{\text{out}}$).

For this section, neglecting (in view of smallness) the variation of a slope and the forces of friction within its limits, we can put down the following

$$h_1 + \alpha V_1^2 \approx 2g = \beta h_{\text{out}} + \alpha V_{\text{out}}^2 \approx 2g\,, \tag{2}$$

$$\eta_1 = \left[1 - \frac{\Pi\kappa_1}{2}\left(1 - \frac{w_1^2}{w_{\text{out}}^2}\right)\right]. \tag{3}$$

Here, $\Pi\kappa_1 = \alpha V_1^2 \approx g h_1$, the ratio w_1^2/w_{out}^2 is replaced by ratio $V_{\text{out}}^2/V_1^2 \times \eta = h_{\text{out}}/h_1$. Symbol w denotes the cross-sectional area of the flow in the corresponding section.

The values of h_1 and $\Pi\kappa_1$ for the slopes of the log $i_0 > i_k$ for the considered case are taken equal to $h_1 = h_0$, $\Pi\kappa_0 = \text{Fr}^2$ (taking into account a relatively large length of the log), where $\text{Fr} = V^2/(2g)$ is the Froude number for the section 1.

3. Results

When we calculate a flow spreading, we use Fig. 1. We also determine $\text{Fr}_{\text{out}} = V_{\text{out}}/(\sqrt{g}h_{\text{out}})$ for the axis of the flow (X-axis). By means of Table 1 [2] we find also the ratio $X\text{Fr}_{\text{out}}/b$ for the depths of the flow at a different distance from a cross section exit.

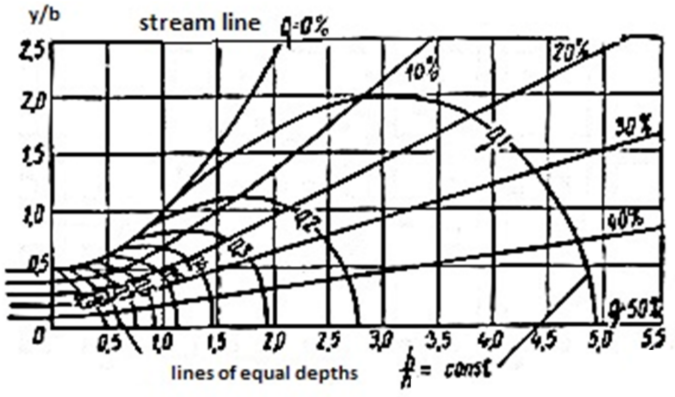

Fig. 1. The graph of current lines and the lines of equal depths

Table 1. The value of current line coordinates and the lines of equal depths (h/h_0) for the graph in Fig. 1.

Q (%)	Coord.	The lines of equal depths h/h_0 = const								
		0.9	0.8	0.7	0.6	0.5	0.4	0.3	0.2	0.1
0	$x/b\,\mathrm{Fr}$	0.050	0.150	0.280	0.400	0.500	0.600	0.730	0.860	0.110
	y/b	0.503	0.510	0.530	0.565	0.620	0.675	0.760	0.870	0.100
10	$x/b\,\mathrm{Fr}$	0.165	0.205	0.460	0.610	0.790	1.000	1.210	1.660	2.770
	y/b	0.405	0.420	0.450	0.500	0.575	0.690	0.820	1.110	1.980
20	$x/b\,\mathrm{Fr}$	0.270	0.430	0.610	0.780	0.970	1.220	1.590	2.140	3.790
	y/b	0.310	0.330	0.360	0.410	0.480	0.580	0.750	1.020	1.840
30	$x/b\,\mathrm{Fr}$	0.370	0.530	0.710	0.880	1.060	1.360	1.800	2.460	4.370
	y/b	0.210	0.230	0.250	0.290	0.350	0.440	0.560	0.770	1.360
40	$x/b\,\mathrm{Fr}$	0.450	0.590	0.750	0.920	1.120	1.430	1.910	2.690	4.770
	y/b	0.115	0.125	0.140	0.160	0.190	0.230	0.300	0.410	0.760
50	$x/b\,\mathrm{Fr}$	0.480	0.610	0.770	0.940	1.130	1.450	1.950	2.760	4.940
	y/b	0.0	0.0	0.0	0.0	0.0	0.0	0.0	0.0	0.0

Note: here, $\mathrm{Fr} = \mathrm{Fr}_{\mathrm{out}}$, b is the width of the stream (the log channel) in the section of its exit to an expansion site, x is the distance along the flow, and y is the distance across the flow.

The above mentioned provisions show that by this way it is possible to design the required conditions of a water flow flowing in the area of approach to a water-pipe construction.

At the outlet of a culvert, the width of a channel is equal to the width of its opening. The speed of water flow in a single-span structure is almost equal to the flow rate of water at an inlet. This speed is lowered due to a flow expansion. Therefore, no further spreading of a flow is required. With the corresponding soils of a log channel, the value of the non-eroding velocity can be achieved at the exit from a structure [4].

4. Experimental research

For the purpose of flow spread visual estimation on the leading section of a log, an experiment was performed on a hydraulic tray. The scale of the geometric modeling is –1:2 [8]. The width of the supply channel was 0.60 m on the model; the speed of water flow in the exit section makes 0.860 m/s, the flow rate makes $0.01548\,\mathrm{m}^3/\mathrm{s}$. During the modeling according to the Froude model this is equivalent to a full-scale stream with the width of 1.2 m in an output section with the water flow rate of 1.216 m/s ($V_{\mathrm{M}}^2 = V_{\mathrm{N}}^2 \times h_{\mathrm{N}}/h_{\mathrm{M}}$) and the flow discharge of $1.459\,\mathrm{m}^3/\mathrm{s}$.

The length of the flow spreading section (l_{p}) was 1.05 m on the model, which corresponds to the length of 2.10 m for the natural flow [8]. Thus, according to the dependencies shown on the graphs (Fig. 3), the length of the log channel expansion section before entering a small culvert should make at least the sum of distances $l_{\mathrm{p}} + l_{\mathrm{k}}$.

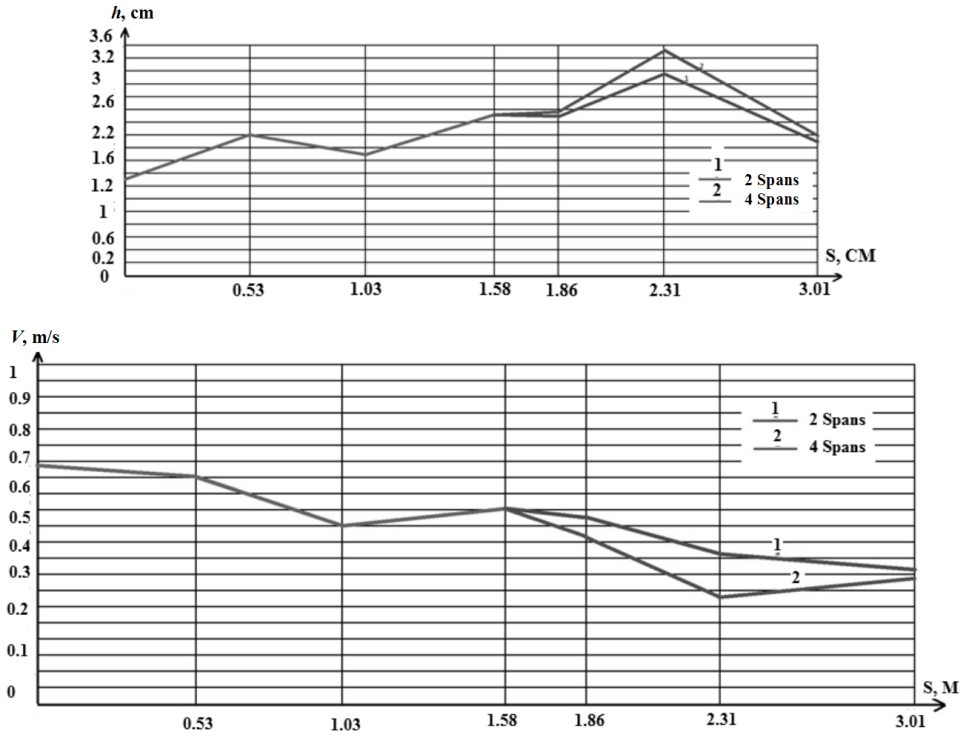

Fig. 2. Graphs of the level change concerning free surface of water and the flow velocity along the axis of flow on the area of its expansion

5. Conclusion

Theoretical and experimental studies allow us drawing the following conclusions:

1. A new principle is proposed for the construction of small culverts. the essence of which is to expand a channel on the way to a structure (instead of compression). This requires a hydraulic calculation of water flow parameters in each specific case. the collection of hydrological data on the development of a water flow during the flood period. conditioned by the need of a supply channel development (expansion).

2. The use of extended culverts in projects requires the revision of surface runoff diversion system flowing to a road: the usual construction of side drainage canals should be supplemented by the development of a spatial system for surface runoff receiving and discharging from the roadbed of a motor road; when such a drainage system is being developed on the territory adjoining a road, watercourses, dry valleys, and low places are fixed, where surface runoff can be redirected during the flood period instead of building a culvert on a plain. A small, extended culvert can be constructed without a reinforcing channel construction (except for natural or artificial vegetation)—if by the expansion of a supply channel (and, consequently, an outflow one)—the speed of the water flow can be reduced to the channel value that does not erode channel soil.

3. The construction of small-sized extended culverts of water discharge facilities due to the reduction of their height allows to reduce significantly the need in imported soil for the construction of earthen cloth, which reduces the cost of the road building.

References

[1] M. V. Nemchinov, A. G. Vasilieva: *The ways of excavation work volume reduction during the construction of highways.* Bulletin of Moscow Automobile and Highway Technical University (MADI) *45* (2016), No. 2, 62–70.

[2] M. V. Nemchinovh: *The protection of small artificial structures from local erosion.* Scientific and technical report No. 745, Moscow, MADI (1964).

[3] R. Luo, Z. Liu, T. Huang, C. Tu: *Water vapor passing through asphalt mixtures under different relative humidity differentials.* Construction and Building Materials *165* (2018), 920–930.

[4] P. Kolisoja, A. Kalliainen: *Modelling of plastic culvert and road embankment interaction in 3D.* Procedia Engineering *143* (2016), 427–434.

[5] V. I. Altunin, T. A. Suetina, O. N. Chernykh: *Hydraulic calculations of culverts on motor roads*, Master Thesis, Kazan University (2016).

[6] J. Li, Z. Fu, W. Chen: *Numerical investigation on the obliquely incident water wave passing through the submerged breakwater by singular boundary method.* Computers & Mathematics with Applications *71* (2016), No. 1, 381–390.

[7] *The manual on hydraulic calculations of small culverts.* VNII of transport construction (TSNIIS), Chief editor G. Ya. Volchenko, 1992.

[8] C. S. Duncan: *Revenue for highway construction and maintenance.* Annals of the American Academy of Political and Social Science *171* (1934), No. 1, 244–252.

Received June 15, 2018

Acta Technica *63* No. 6/2018, 909–914

Deceptive call recognition in a network using machine learning[1]

V. A. Narayana[2], Abhinav Chamakura[2], Ramakrishna Gandi[2]

Abstract. This paper considers the construction of an effective beam finite element for the blade as the component of cyclic symmetric system. Spontaneously sensing and thwarting deceitful calls on a network. The call history on the network is collected for a given time span, call topographies for each of the collected call history by recipient number and using machine learning to make choices for identifying whether recipient number and a call to recipient number may be deceitful. The choice model may be incorporated on network to sense and thwart deceitful calls.

Key words. Network, deceptive call recognition, machine learning.

1. Introduction

The task of ensuring the vibration reliability concerning the rotor systems of turbomachines and their elements is accompanied by the implementation of a large amount of computational studies for the set of design models. The telecommunication industry is facing lot of challenges in terms of deceptive calls communication among the network. The worldwide yearly damages due to deceptive calls or deceptive activities increasing to US$40 billion according to various survey instruments. The losses are increasing faster than the profits in small and medium sized telecom industry. To monitor full time deceptive activities, it is an overhead on the Government and non-Government organizations. To overcome this challenge an attempt made in this paper to address the problem using decision tree generation using clustering analysis and machine learning module in a cost effective way.

[1]This work was supported by the Management of CMR College of Engineering & Technology.
[2]CMR College of Engineering & Technology, Hyderabad-501401, India

2. Related work

Niall J. Conroy [2] proposes linguistic and network analysis methods deceitful counterfeit news indicator system. Linguistic methods where the content of deceptive posts is mined and examined to associated language patterns with deception and network methods likewise post meta data or organized network inquiries will be coupled to provide collective deception actions.

Anton Wiens [3] proposes user profiles are used to train for sensing deceit calls by the values of each profiles. Lacking labeling data only some algorithms can be used for deceit call sensing using supervised methods.

Iulia Lefter [4] proposes enunciation on every stage in the growth of an sentiment recognition system from the existing databases, the sentiment specific topographies which are pertinent for sentiment recognition and machine learning approaches used. Support Vector Machines(SVM) classifiers in dialogue sentiment recognition used. SVM will regulate a hyper plane exploits the boundary of the two datasets, and the trials that lie on the boundary are called support vectors to create orator sovereign cross justification framework.

Gideon Mendels [5] proposes repeatedly sensing deception from dialog. CXD exploited large-scale corpus of deceptive and non-deceptive dialog for training and assessing spectral, lexical feature sets and acoustic-prosodic, by various machine learning modules. Design a sole hybrid deep model for together acoustic and lexical topographies trained together to achieve advanced outcomes on the CXD corpus.

Larcker, D. [6] proposes estimation linguistic-based classification modules of deceptive calls during conference calls. Prediction modules are established with word groups that are revealed by earlier psychosomatic and linguistic research related to deception.

Baohua Wang [7] assessed classification modules of deceptive calls during conference calls, the model is established through word types related toward deception and by conventional arithmetical examinations. Nonetheless their performance is 60 %–70 % of linguistic topographies are useful to recognize deceptive calls.

Graaff A. J. [8] proposes finding deceptive calls from the average set of calls period and extended call period over calls by client are brief and equated to a determined threshold. A machine learning approach is used to train the best possible threshold levels. Thereby every client has own rules for prediction to sense deceptive calls.

"Life cycle of a phone fraud" proposes to produce machine learning modules to recognize the genuine type of machine/device used to make a call, the geography a call is identifies by its phone print.

Tata Communications technology software monitors to prevent deceitful activities. The software deals with fraud fighting technologies, including machine learning, big data analytics, subscriber alerts, real-time monitoring, crowd sourcing and automated reporting. When the fraud fighting software identifies a deceitful call, blocks the number across whole world wide network avoiding further deceitful activity.

David Lary [11] proposed automated detection & reporting of online auction seller deception risk using call through API interface and web site GUI data harvesting application feedback collection application for data cleaning & analysis module to

get cleaned data applying machine-learning algorithm and decision support system.

3. Proposed system

Sensing deceptive activities on a network, by collecting call history on a network for a specified time frame, each call history comprising a plurality of call topographies for a call to a recipient number, call topographies from each of the poised call history by recipient number, resulting in a combination of call features for each recipient number. Resultant data points obtained from set of data points transmuting from call features by dimension reduction, each data point signifying a particular call features for recipient number. The flowchart of the proposed system is depicted in Fig. 1.

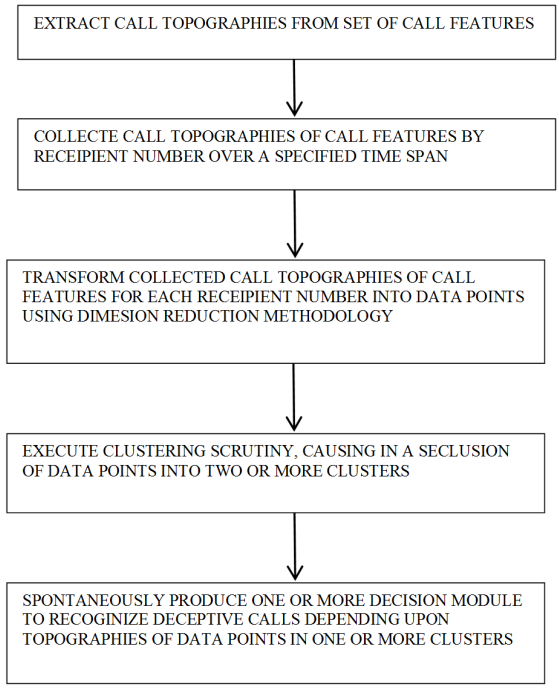

Fig. 1. Representation of deceptive calls recognition: approach

Execution of clustering analysis that is formed out of set of data points into two-or more clusters and tagging call features as deceptive or non-deceptive built on cluster of each particular data point. Execution of supervised learning module on each tagged call features as a trained information to produce at least one or more decision module to recognize deceptive calls. Recognizing deceptive calls on the network using at least one decision module and triggering a programmed action based on recognition.

Two types of features are proposed, one is arithmetical and other is categorical features, arithmetical columns containing numbers and categorical columns containing non-numbers features. The deceptive module may smear a one-hot transformation transforms a categorical call feature into an arithmetic number and that they are homogeneous contingent on the machine learning module. The deceptive analysis module smears a supervised learning module to the total dataset to obtain a decision module for identifying whether a call is deceptive. One category of decision module is decision tree. The deceptive analysis module uses a cross validation model to pick up training data points to produce a decision tree module for forecasting about deceptive calls. The major benefits of decision tree module are the forecasting module, which visually describes decision methodology process.

4. Conclusion

Traditional research approaches of discovery of deceptive calls is modest. Trained professionals are anticipated to sense such maneuvers. The study displays that individuals are untruth indicators are scarcely improved than devices on sensing deception communication.

One of major disadvantage of these research findings is that they depend on the arithmetic credibility and they ignored the deceptive communication that escorts the deceitful. The proposed system deals in recognizing deceitful calls in a network using machine learning approach.

References

[1] S. Falaleev, A. Vinogradov, P. Bondarchuk: *Influence research of extreme operate conditions on the face gas dynamic seal characteristics.* Technische Akademie Esslingen International Tribology Colloquium Proceedings *15* (2006), p.208.

[2] N. Conroy, V. L. Rubin, Y. Chen: *Automatic deception detection: Methods for finding fake news.* ASIS&T Annual Meeting: Information Science with Impact: Research in and for the Community, 6–10 November 2015, St. Louis, Missouri, USA, Proceeding ASIST'15 (2015), Article No. 82.

[3] A. Wiens, T. Wiens, M. Massoth: *A new unsupervised user profiling approach for detecting toll fraud in VoIP networks.* Advanced International Conference on Telecommunications, 20–24 July 2014, Paris, France, Presented during AICT (2014).

[4] I. Lefter, L. J. M. Rothkrantz, D. van Leeuwen, P. Wiggers: *Automatic stress detection in emergency (telephone) calls.* International Journal of Intelligent Defence Support Systems *4* (2011), No. 2, 148–168.

[5] G. Mendels, S. I. Levitan, K. Z. Lee, J. Hirschberg: *Hybrid acoustic-lexical deep learning approach for deception detection.* Interspeech, 20–24 August 2017, Stockholm, Sweden, Proc. Interspeech (2017), 1472–1476.

[6] D. F. Larcker, A. A. Zakolyukina: *Detecting deceptive discussions in conference calls.* Journal of Accounting Research *50* (2012), No. 2, 495–540.

[7] B. H. Wang, X. L. Wang: *Deceptive financial reporting detection: A hierarchical clustering approach based on linguistic features.* 2012 International Workshop on Information and Electronics Engineering, Published Procedia Engineering *29* (2012), 3392–3396.

[8] A. J. Graaff, A. P. Engelbrecht: *An overview of models to detect and analyze fraud in the telecommunications environment.* School of Information Technology, University of Pretoria, South Africa (2002).

[9] M. Ott, Y. Choi, C. Cardie, J. T. Hancock: *Finding deceptive opinion spam by any stretch of the imagination.* Annual Meeting of the Association for Computational Linguistics: Human Language Technologies, 19–24 June 2011, Portland, Oregon, USA, HLT'11 Proceedings (2011), No. 1, 309–319.

[10] V. Balasubramaniyan, R. Bandyopadhyay, T. Calhoun: *Lifecycle of a phone fraudster: Exposing fraud activity from account reconnaissance to takeover using graph analysis and acoustical anomalies.* In Black Hat USA (2014), "Fraud Protection Toolkit", Tata Communications Ltd.

[11] D. J. Lary, A. Nikitkov, D. Stone: *Which machine-learning models best predict online auction seller deception risk?.* National Aeronautics and Space Administration (NASA) Goddard Space Flight Center (2010).

Received June 18, 2018

Acta Technica *63* No. 6/2018, 915–920

Assessment of the level of ultra-high temperature effects on structural elements

Elena Karpanina[1], Anna Leonova[1], Olga Sirotina[1], Dmitry Gura [1]

Abstract. The article presents the study of the level of fire effects on structures based on their material, size, temperature and duration of the fire. The necessity of technical inspection of affected buildings as an important factor for decision-making on the use of structures subjected to fire exposure is shown. The goal of the technical inspection is the determination of the residual bearing capacity of the fire-damaged structures.

Key words. Bearing capacity, fire exposure, calculated resistance, building constructions, technical inspection.

1. Introduction

As a result of fires in buildings their constructions are damaged up to final destruction. Extent of fire impact on building constructions depends on their material, sizes, temperature and duration of the fire. Let us consider each of them:

1.1. Wooden constructions

At fire impact on wooden constructions combustible gases emitted from them burn down out of wood. Under the influence of distillation wood heats up and becomes charred.

Humidity of wood decreases and durability of construction uncharred layers increases. While putting out a fire with water the wood is moistened and its durability becomes equal to that it had before the fire.

At restoration of the wooden burned construction all charred layer of wood has to be removed since it keeps an unpleasant smell for a long time.

[1]Kuban State Technological University, Krasnodar

In wooden constructions the cross section of the elements minus the thickness of the charring is defined.

Design resistance of wood is accepted the same as for the wood which has not undergone fire impact [1].

1.2. Steel constructions

Steel constructions are made of low-carbon steel. When heating steel elements above 600 °C they receive big deformations and cannot be used as intended [1].

Strengthening of the steel constructions which have undergone fire effect is made by the same methods as of the constructions not damaged by the fire.

In steel elements there is determined their cross section considering time of the building erection. Deflections in the vertical and horizontal plane are defined.

Design resistance of steel is accepted depending on time of rolled steel production without fire effect. At the same time axis bending existence of the damaged element is taken into consideration.

1.3. Stone constructions

Stone constructions (walls, columns, arches) are damaged from a surface. Damages are expressed by brick peeling depth. Yet constructions from a silicate brick sustain deeper damage in comparison with those from a ceramic brick.

As a result of thermal effect in case of fire stone walls and arches can receive big deformations leading to cracks formation. The stone constructions damaged in a fire are strengthened in the same way as those which have not undergone fire effect [2].

The residual bearing capacity of a stone masonry also depends on temperature and duration of the fire. Stones of masonry and mortar are damaged only on its surface. In calculations of the residual bearing ability it is necessary to consider existence of cracks in a laying.

1.4. Reinforced concrete constructions

The most stratifiable is the accounting of fire damage extent of reinforced concrete constructions in a fire. Heterogeneity of the materials forming reinforced concrete when heating leads to different temperature deformations and bond breaks between cement stone, large and small fillers and reinforcing.

In reinforced concrete elements irreversible changes of mechanical properties, decrease in durability on compression and stretching, additional deflections result.

Changes of mechanical properties of concrete when heating and subsequently cooling are estimated very much approximately now.

It complicates definition of the bearing capacity of the reinforced concrete elements subjected to fire and subsequent cooling, particularly for the compressed elements.

2. Research method

When calculating the residual bearing capacity of reinforced concrete elements the cross section of an element is divided into strips of different thickness depending on the element cross section sizes, 50. . . 100 mm.

Design resistance of concrete is defined by multiplication of design resistance of the undamaged concrete by the decreasing coefficients calculated according to tables and schedules.

When heating concrete reaches over 500 °C, its resistance to compression and resistance of fittings located in it are accepted equal to zero. The stretched fittings of the class A-240, A-300, A-400 and A-500, heated to temperature above 600 °C, also are not considered in calculations [3].

Design resistance of concrete is defined by multiplication of design resistance of the undamaged concrete by the decreasing coefficients calculated according to tables and schedules.

Design resistance R_{bI} to compression of the concrete layers damaged by fire after cooling can be determined by a formula [2]

$$R_{\mathrm{bI}} = \gamma_{\mathrm{bI}} R_{\mathrm{b}} \,, \tag{1}$$

where γ_{bI} is a coefficient of decrease in design resistance of concrete to compression after cooling depending on heating temperature and R_{b} is the initial resistance.

Design resistance $R_{\mathrm{bt.I}}$ at stretching of the concrete layers damaged by fire is determined by the formula

$$R_{\mathrm{bt.I}} = \gamma_{\mathrm{bt.I}} R_{\mathrm{bt}} \tag{2}$$

where $\gamma_{\mathrm{bt.I}} = \gamma_{\mathrm{bI}} - 0.2(1 + 0.1t)$, t being the concrete heating temperature.

The initial modulus of elasticity E_{bI} of concrete which was exposed to heating and the subsequent cooling is determined by the formula [3]

$$E_{\mathrm{bI}} = \beta_{\mathrm{b}} E_{\mathrm{b}} \,, \tag{3}$$

where β_{b} is the coefficient of decrease of the concrete modulus of elasticity and E_{b} is the initial module. Here,

$$\beta_{\mathrm{b}} = 1 - kt \,, \tag{4}$$

where the coefficient k for heavy concrete is equal to $0.17 \cdot 10^{-2}$, for haydite concrete it is $0.10 \cdot 10^{-2}$. Decrease in the modulus of elasticity of concrete when heating is irreversible after cooling.

When heating concrete over 500 °C, the module of elasticity is not considered in calculations of durability and construction deformation.

The values of design resistance R_{sI} of reinforcing to stretching when heating and the subsequent cooling are determined by the formula

$$R_{\mathrm{sI}} = \gamma_{\mathrm{sI}} R_{\mathrm{s}} \,, \tag{5}$$

where γ_{sI} is the coefficient of decrease in design resistance of reinforcing to stretching

depending on heating temperature and R_{s} is the initial value.

3. Results

For the reinforcing steel of the classes A-240, A-300, A-400 located in the stretched zone at the size of the smaller side of an element section more than 300 mm and temperature of fittings heating up to 600 °C, and the size of the smaller side of an element section less than 300 mm and temperature of heating up to 600°C, $\gamma_{\mathrm{sI}} = 1$ [3].

At the smaller size of an element section side more than 300 mm and temperature of fittings heating more than 500 °C, and smaller size of the side of an element section less than 300 mm, and temperature of fittings heating more than 600 °C $\gamma_{\mathrm{sI}} = 0$.

For reinforcing steel of the class A-500, A-600 at temperature of fittings heating to 400 °C, and at temperature of fittings heating more than 400 °C $\gamma_{\mathrm{sI}} = 0$.

The values of design resistance R_{sc} of reinforcing to compression can be determined by the formula

$$R_{\mathrm{sc}} = \gamma_{\mathrm{sI}}\gamma_{\mathrm{s2}}R_{\mathrm{s}}\,, \tag{6}$$

where γ_{s2} is the coefficient considering decrease in bond of fittings with concrete after heating and cooling.

For smooth hot-rolled reinforcing rods

$$\gamma_{\mathrm{s2}} = 1 - 0.001t\,. \tag{7}$$

For hot-rolled reinforcing rods of a periodic profile

$$\gamma_{\mathrm{s2}} = 1 - 0.001(0.1 + 0.001t\,. \tag{8}$$

The module of reinforcing steel deformation after heating and the subsequent cooling is accepted at $\gamma_{\mathrm{sI}} = 1$ as for fittings which have not undergone heating.

The depth of concrete warming up depending on warming up temperature of a construction surface and high temperatures impact duration can be determined by Fig. 1.

When considering irregularity in distribution of the concrete strength on the thickness of the element which has been subjected to fire, reduction of the unequally heated layers of concrete to a homogeneous material is made.

The reduction coefficient of parts (concrete layers) of the section of the element damaged by fire $\alpha_{\mathrm{bt.I}}$ should be accepted proportional to the ratio of concrete strength of the considered layer $R_{\mathrm{bt.I}}$ to the strength of the base layer $R_{\mathrm{b\,loc}}$

$$\alpha_{\mathrm{bt.I}} = \frac{R_{\mathrm{bt.I}}}{R_{\mathrm{b\,loc}}} \tag{9}$$

For decision-making on the use of constructions subjected to fire exposure in case of fire, a technical inspection of affected buildings is made. The purpose of the technical inspection is to determine the residual bearing capacity of the fire-damaged constructions.

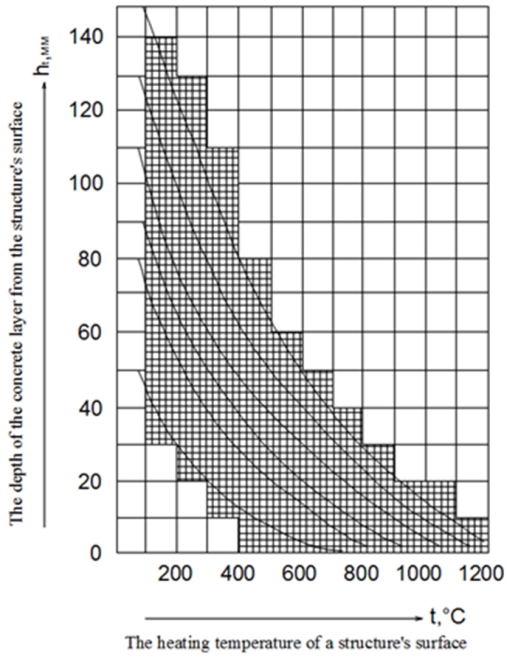

Fig. 1. Dependence of temperature distribution in concrete layers [2]

For decision-making on the use of constructions subjected to fire exposure in case of fire, a technical inspection of affected buildings is made. The purpose of the technical inspection is to determine the residual bearing capacity of the fire-damaged constructions.

Usually after the fire there is no accurate data on heating temperature of constructions and duration of the fire. It reduces the accuracy of determination of residual strength of reinforced concrete elements after the fire. Assessment of key parameters of the fire is made by two methods.

The theoretical method is based on dependence of the design parameters of the fire on the type of the room, the size of window and door openings and ventilation conditions.

While there are factors characterizing the constructions and the factors that determine burning conditions. Changes in these factors affect the development of fires characterized by time, intensity of development and the thermal effects on the protecting structures of the room.

4. Conclusion

In the calculations the parameters are given to the standard mode, which explore the limits of fire resistance of building structures. The calculations for fires parameters in buildings with building structures made of insulating combustible and

non-combustible materials are produced according to the dependencies allowing to evaluate the integral thermal parameters of the freely developing fire such as the temperature of the gaseous medium in the fire center, the temperature of the walls and floors, the density of the heat flow.

Temperature mode of the three-dimensional fire regulated by ventilation when burning, is calculated provided that the fire load is uniformly distributed over the floor area, window openings during the fire and open area ratio of openings to floor area is 2.5–35 %. The minimum duration of the initial stage of the fire is calculated provided that openings of the premises are closed until the moment of the flash defined by the temperature of the flash [4].

The experimental and theoretical evaluation method is based on determination of the fire temperature when analyzing the appearance, condition and color of various materials located in a fire zone. Data on changes in the external parameters of bearing and enclosing structures, as well as materials located in the fire area at high temperatures are presented in the normative literature [5]. By the results of inspection constructions are classified by a damage rate and, if necessary, detailed inspection of the bearing structures by the destructive and nondestructive methods for determination of the residual bearing capacity of the fire-damaged structures is appointed.

References

[1] V. T. Grozdov: *Technical inspection of building structures and constructions.* SPb., 2014, p. 71.

[2] S. J. Barnett, J. F. Lataste, T. Parry, S. G. Millard, M. N. Soutsos: *Assessment of fibre orientation in ultra-high performance fibre reinforced concrete and its effect on flexural strength.* Materials and Structures *43* (2010), 1009–1023.

[3] S. Vaishnavi, B. S. Suresh Chandra: *Effect of varying temperature load on RCC structure by seismic analysis.* International Research Journal of Engineering and Technology (IRJET) *05* (2018), No. 5, 666–671.

[4] T. Leutbecher, E. Fehling: *Structural behaviour of UHPC under tensile stress and biaxial loading).* Proc. International Symposium on Ultra High Performance Concrete, 13–15 September 2004, Kassel, Germany, 435–448.

[5] M. Seif, J. Main, J. Weigand, T. P. McAllister, W. Luecke: *Finite element modeling of structural steel component failure at elevated temperatures.* Structures *6* (2016), 134–145.

Received June 15, 2018

Acta Technica *63* No. 6/2018, 921–926

Research on clearance provisions of airport terminal clearance zone under the takeoff climbing model

Yu Qingkun[1], Cai Liangcai[1], Geng Hao[1]

Abstract. In order to make the clearance provisions of the Airport Terminal Clearance Zone (ATCZ) more scientific, safe, and reasonable, we need to analyze the takeoff climbing trajectory of the aircraft using fight dynamics theory. We design the calculation program to make the model calculation process simpler. Through the examples, the calculation results of the takeoff climbing model and the measured results are comparatively analyzed to verify the validity and rationality of the takeoff climbing model. We provide the calculation method and theoretical basis to ensure the flight safety of the aircraft in the ATCZ and to make the ATCZ provisions more scientific.

Key words. ATCZ, takeoff climbing, flight dynamics, numerical analysis.

1. Introduction

As an important part of airport clearance zone, the ATCZ' obstacle limitation provisions is the most important safety measure to ensure the aircraft takeoff, leave, approach, land, fly and other flight activities [1].During the aircraft takeoff climbing, the magnitude of the climbing angle has a decisive impact on the height limit of the ATCZ [2].

Some scholars have conducted some research on takeoff climbing performance of aircrafts. Robinson and Loomis adopt the indirect method and gradient method to find the optimal flight control, and discuss the advantages and disadvantages of the two methods [3]. Slater adjust the engine thrust by energy rate based on observation and calculation in aircraft rise stages to improve the prediction of the aircraft climb performance [4]. Cavcar adopt four equations to calculate the piston propeller plane's optimal angular velocity and maximum climb rate [5]. We select the takeoff climbing trajectory as the research object, and establish the takeoff climbing angle calculation model under the influence of atmospheric conditions, which is used to analyze the climbing's influence on the ATCZ provisions, so as to provide scientific

[1]Air Force Engineering University, Xian 710038, China

calculation method and theoretical basis to determine the ATCZ obstacle limitation surface.

2. Aircraft takeoff climbing process division

The aircraft takeoff climbing starts from the departure point, and ends up with the state of the aircraft's clean configuration. In the process, the pilot will operate the aircraft according to the prescribed driving technique, constantly adjust the thrust of the engine, and change the aircraft's configuration and cruise in the fixed flight route. The takeoff climbing process of aircraft can be divided into 4 segments: Airborne phase, Wheel up, Flap up and Clean configuration, which are denoted as the jth climb mission segment ($j = 1, 2, 3, 4$) in turn, as shown in Fig. 1.

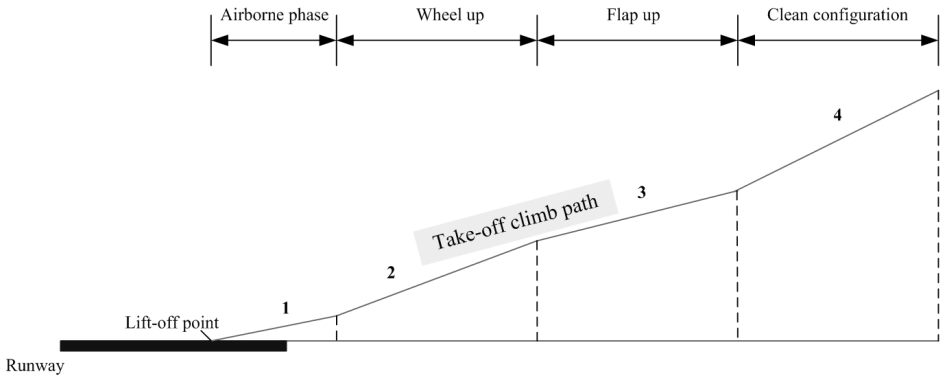

Fig. 1. Typical schematic diagram of aircraft takeoff climbing process

3. Equations of motion for takeoff climbing

In the ATCZ, the takeoff climbing trajectory of the aircraft can be determined by using the equations of the aircraft climbing motion in the vertical plane in the track coordinate system, as shown in (1)–(4)

$$P\cos(\alpha+\varphi_{\mathrm{p}}) - \frac{1}{2}C_{\mathrm{D}}\rho S V^2 - G\sin\gamma = \frac{G}{g}\frac{\mathrm{d}V}{\mathrm{d}t}\,, \tag{1}$$

$$P\sin(\alpha+\varphi_{\mathrm{p}}) + \frac{1}{2}C_{\mathrm{L}}\rho S V^2 - G\cos\gamma = \frac{G}{g}V\frac{\mathrm{d}\gamma}{\mathrm{d}t}\,, \tag{2}$$

$$\frac{\mathrm{d}h}{\mathrm{d}t} = (V \pm V_{\mathrm{w}})\sin\theta\,, \tag{3}$$

$$\frac{\mathrm{d}L}{\mathrm{d}t} = (V \pm V_{\mathrm{w}})\cos\theta\,. \tag{4}$$

Here, G is the weight of the aircraft (N), g is the acceleration of gravity (m/s^2), V is the aircraft vacuum speed (m/s), t is the time (s), γ is the aircraft climbing angle (rad), P is the engine thrust (N), α is the angle of attack (rad), φ_{p} is the engine mounting angle (rad), C_{D} is the resistance coefficient, ρ is the actual air density (kg/m^3), S is the wing area(m^2), C_{L} is the lift coefficient, l is the aircraft climbing horizontal distance (m), h is the aircraft climbing vertical geometric height, relative to the airport elevation (m), and V_{w} is the wind speed (m/s): with the flowing wind the coefficient is positive, and with the head wind, the coefficient is negative.

4. Example analyses

4.1. Takeoff climbing model program

The basic idea of programming is as follows:

(1) Discretize the chart data of different types of aircraft for storage and establish a database.

(2) Set input parameters of the program interface according to the calculation principle of takeoff climbing angle model, including airports, aircrafts and other relevant parameters.

(3) The input parameters are linked to the database, and the takeoff climbing angle of each equal pressure height segment is calculated.

(4) The calculation results are stored, analyzed, and exported, with the output parameters including an aircraft's total time of flight, flight distance, the minimum angle of climb, the airport terminal clearance each takeoff climbing mission segment's slope and terminal height.

4.2. Validation of takeoff climbing model

For example, the elevation of an airport is 19 m, and the actual environmental temperature is 15 °C. The airport has A-type aircraft with 2 engines, the engine reduction factor is 0.9, and the engine installation angle is ignored. When the aircraft takes off, the aircraft takeoff mass is 24100 kg, with the onboard fuel 1900 kg.

The above known conditions are used as the input parameters of the program to calculate and analyze the takeoff climb process, and the output calculation results are shown in Figs. 2 and 3.

In order to verify the accuracy and rationality of the model results, the takeoff climbing track data [4] is obtained by field test which are compared with the calculated results, as shown in Fig. 4.

It can be seen from Fig. 4 that the model calculation results coincide well with the measured results. At the beginning of takeoff climbing, the calculated track is in good agreement with the measured track. However, there is a big error at the end of takeoff climbing process. At the horizontal distance, the maximum error between the measured track and the calculated track does not exceed 200 m. In the height direction of climb, the maximum error between the measured actual track and the calculated track does not exceed 100 m. It is mainly due to the fact that

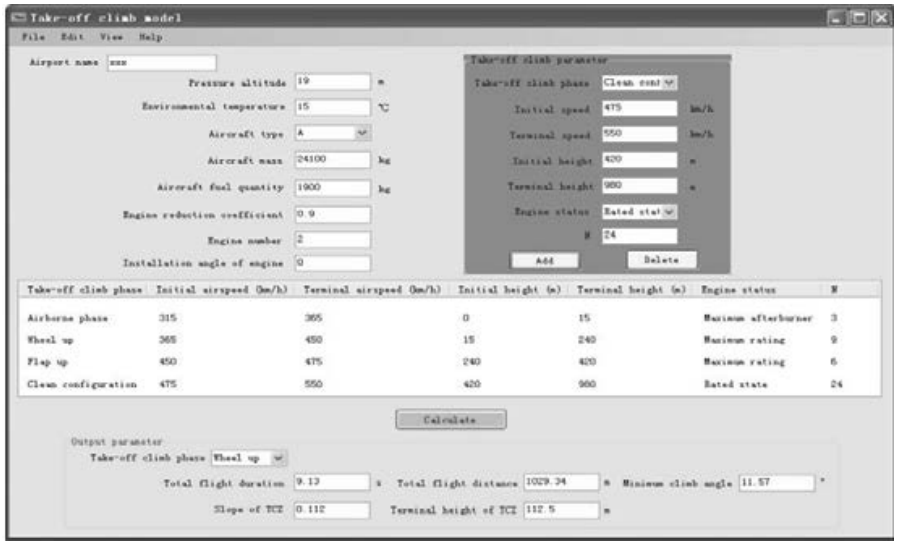

Fig. 2. Program interface of takeoff climbing model

Pressure altitude(m)	True airspeed (km/h)	Angle of attack (°)	Climb angle (°)
18.99	315.35	6.548	0.000
23.99	335.34	7.888	3.164
28.99	350.26	8.262	3.009
33.99	365.67	7.668	2.874
58.97	380.41	7.185	13.924
83.96	387.19	6.394	13.546
108.95	398.50	5.273	13.234
133.94	406.09	5.427	12.917
158.93	417.50	5.977	12.614
183.92	425.27	2.747	12.333
208.91	435.00	3.186	12.078
233.90	443.14	3.120	11.823
258.89	455.74	3.120	11.570

Fig. 3. Results calculated by the program

the actual track is less affected by external factors at the beginning of climb. As the takeoff climbing process continues, due to the accumulation of navigation errors or uncertain wind shear and other effects, the actual track and the calculated track deviations have occurred. However, for the determination of the takeoff climbing clearance provisions, the results of this model are biased towards safety. Therefore, this model can basically reflect the actual climbing situation of A-type aircraft and can be used in the analysis of the takeoff climbing clearance provisions.

The takeoff climbing model is used to obtain the takeoff climbing tracks under Case 1 and Case 2 respectively, as shown in Fig. 5. Considering the takeoff climbing clearance provisions of each takeoff climbing mission segment in the two cases, select the lower takeoff climbing track combination, in order to more safely meet the A-type aircraft takeoff climbing clearance requirements. Finally, the ACTZ clearance provisions are shown in Table 1.

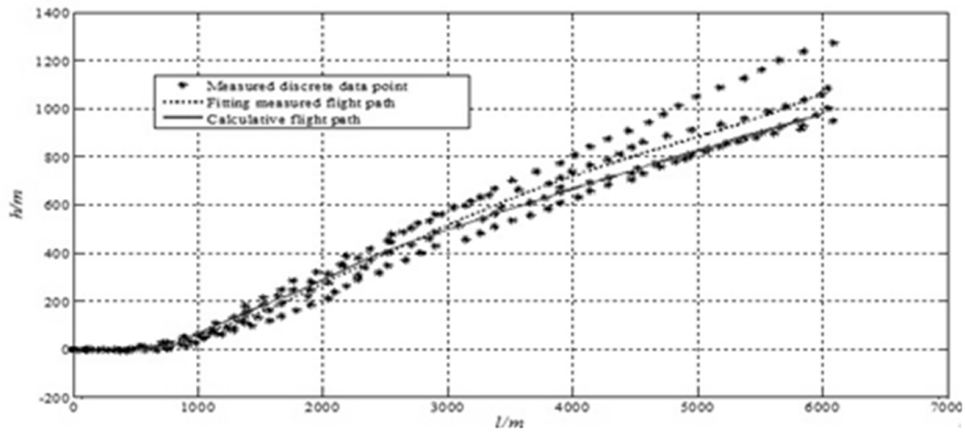

Fig. 4. Results calculated by the program

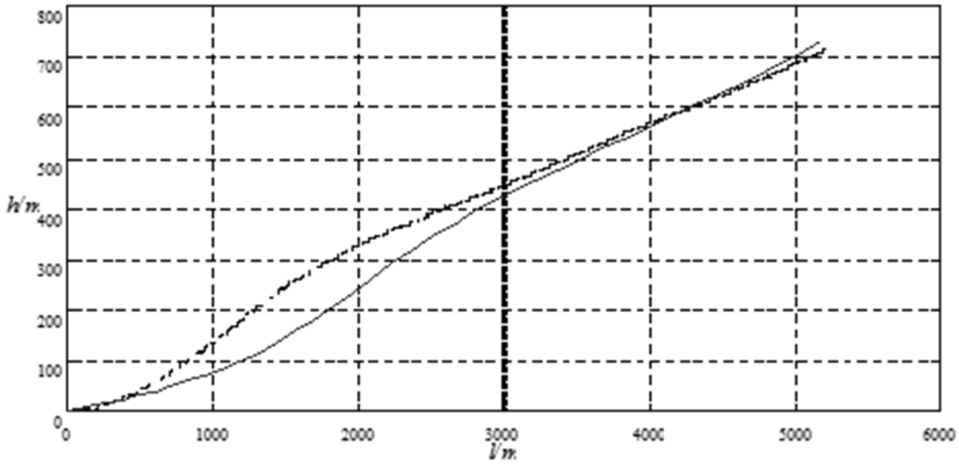

Fig. 5. The takeoff climbing track of Case 1 and Case 2

Table 1. A-type aircraft takeoff climbing clearance provisions

Takeoff climb section	Terminal clearance slope	Terminal clearance tip height (m)
Airborne phase	0.0263	7.5
Wheel up	0.112	120
Flap up	0.118	210
Clean configuration	0.081	490

5. Conclusion

The takeoff climbing angle of the aircraft plays a decisive role in limiting the height of obstacles in the ARCZ and becomes the basis for formulating the ATCZ clearance provisions. Therefore, we firstly define the speed correction coefficient and height correction coefficient. Secondly, the calculation formula of the takeoff climbing performance applicable to the actual atmospheric conditions is converted into the standard atmospheric conditions, and then applies to the ATCZ takeoff climbing model. Based on the established takeoff climbing model, the simulation of aircraft takeoff climbing track is realized. Compared with the measured data, the track calculated by the model basically reflects the takeoff climbing track of the aircraft, which can provide computational analysis and theoretical basis to determine the takeoff climbing obstacle limitation surfaces. Although the calculation results of the takeoff climbing model are similar to the measured results, a large number of measured data of the takeoff climbing trajectory are needed in the follow-up work, so as to further correct the ATCZ takeoff climbing model which becomes more scientific and reasonable to determine the airport clearance provisions.

References

[1] L. C. Cai, X. L. Chong, R. H. Zheng, B. Shao: *Analysis of confirmation to obstruction restrict in airfield clearance*. Journal of Air Force Engineering University (Natural Science Edition) *6* (2005), No. 6, 1–3.

[2] M. Delisle, T. T. Takahashi: *Speed stability and obstacle clearance during engine inoperative takeoff*. Proc. 2018 Aviation Technology, Integration, and Operations Conference, 25–29 June 2018, Atlanta (2018), USA, 3502.

[3] A. C. Robinson, J. P. Loomis: *Optimal longitudinal control for obstacle clearance on takeoff*. Guidance, Control and Flight Mechanics Conference, 17–19 August 1970, Santa Barbara, CA, USA, AIAA Meeting papers 1–11.

[4] G. L. Slater: *Adaptive improvement of aircraft climb performance for air traffic control applications*. IEEE International Symposium on Intelligent Control, 30–30 October 2002, Vancouver, BC, Canada, Proceedings (2002), 602–607.

[5] A. Cavcar: *Climb performance of piston-propeller airplane with cambered wing and variable propeller efficiency*. Journal of Aircraft *48* (2011), No. 5, 1701–1707.

Received June 16, 2018